Magnetic resonance imaging (MRI) guided radiotherapy for prostate cancer

Dr Angela Uma Pathmanathan

Institute of Cancer Research

and

The Royal Marsden NHS Foundation Trust

A thesis submitted to the University of London for the degree of Doctor of Medicine, MD(Res)

Volume 1 of 1

March 2020

Author's declaration

I declare as sole author of this thesis that the work presented here represents my personal research conducted as a clinical research fellow at the Institute of Cancer Research and The Royal Marsden NHS Foundation Trust between 2015 and 2020. Tables and figures contained herein are my own work unless credited otherwise

Angela Pathmanathan

March 2020

Abstract

Radiotherapy to the prostate involves increasingly sophisticated delivery techniques and changing fractionation schedules. Magnetic resonance imaging (MRI) guided radiotherapy allows daily adaptive replanning and can improve accuracy. Integrating an MRI scanner and linear accelerator (linac) for the MR-Linac harnesses the advantages of MRI for intrafractional imaging with the potential for tumour tracking, gated treatment and adaptive radiotherapy.

I initially focus on pre-clinical research to model the benefits of the addition of MRI in radiotherapy planning and treatment. I firstly examine prostate motion, as assessed by automatic tracking of fiducials, confirming previously published data on the intrafraction motion of the prostate and setting the scene for the need for adaptive radiotherapy.

Further work concentrates on the stages of adaptive treatment and the challenges involved. With more data emerging on the safety and benefits of extreme hypofractionated prostate schedules, I test the feasibility of planning prostate SBRT for the MR-Linac. I assess the factors required for online and real-time imaging including the optimisation of MRI sequences and autosegmentation.

My final two chapters focus on the clinical MR-Linac workflow. I describe the first in-man study 'Prostate Radiotherapy Integrated with Simultaneous MRI' (PRISM) trial, treating patients requiring radical prostate radiotherapy on the

MR-Linac. There is a complex workflow involved in delivering online adaptive imaging based on the daily anatomy, which has been feasible and in the limited number of patients discussed, not associated with increased toxicity compared to standard treatment. Finally, looking ahead to the changes required to make the workflow more efficient whilst maintaining accuracy, I present data on the accuracy of treatment radiographer and automated propagated contours.

This thesis takes each of these steps in turn to assess the feasibility of this novel treatment delivery, which has the potential to optimise fractionation schedules and improve target dose whilst reducing toxicity from treatment.

Table of Contents

Table of figures

Table of Tables

Abbreviations

ADC	Apparent diffusion co-efficient
ADT	Androgen deprivation therapy
ART	Adaptive radiotherapy
ATP	Adapt to position
ATS	Adapt to shape
BED	Biologically effective dose
bSSFP	Balanced steady-state free precession
CBCT	Cone beam computed tomography
CI	Conformity index
COM	Centre of mass
CT	Computed tomography
CTCAE	Common Terminology Criteria of Adverse Events
CTV	Clinical target volume
DIL	Dominant intraprostatic lesion
DIR	Deformable image registration
DSC	Dice similarity co-efficient
DVH	Dose volume histogram
DWI	Diffusion weighted imaging
EBRT	External beam radiotherapy
FM	Fiducial marker
FSE	Fast spin echo
GI	Gastrointestinal
GTV	Gross tumour volume
GU	Genitourinary
Gy	Gray
HD	Hausdorff distance
HDR-BT	High-dose-rate brachytherapy
ICR	Institute of Cancer Research
IGRT	Image guided radiotherapy
IMRT	Intensity modulated radiotherapy
IPSS	International prostate symptom score
IOV	Interobserver variability
kV	kilovoltage
MAS	Multi-atlas segmentation
MLC	Multi-leaf collimator
MRI	Magnetic resonance imaging
mV	megavoltage
OAR	Organs at risk
PSA	Prostate specific antigen
PTV	Planning target volume
RMH	Royal Marsden Hospital NHS Foundation Trust
RTOG	Radiotherapy Oncology Group
SBRT	Stereotactic body radiotherapy
SD	Standard deviation

SSO	Segment shape optimisation
STAPLE	Simultaneous Truth and Performance Level Estimate
SV	Seminal vesicles
T2W	T2-weighted (MRI sequence)
T2*W	T2*-weighted (MRI sequence)
TE	Echo time
TPS	Treatment planning system
TSG	Tumour site group
UK	United Kingdom
VMAT	Volumetric modulated arc therapy
2D	Two dimensional
3D	Three dimensional

Acknowledgements

I am very grateful to a large number of people who gave me their support, expertise and encouragement during the preparation of this thesis.

Firstly I would like to thank my supervisors Robert Huddart, Alison Tree and David Dearnaley. I have been privileged to have a team of such renowned experts, bringing so much experience and being the best examples of how research should be conducted. I very much appreciate the invaluable guidance you have given me, the time you have spent with me discussing and keeping the thesis on track.

I would particularly like to thank Alison Tree for gently guiding me through the minefield of research and providing me with a great deal of opportunities during this time, extending far above and beyond the work that is encompassed by this thesis.

I was lucky enough to be part of the incredible MR-Linac team, the journey before and since treating the first patient has been a highlight of my work. This is a truly multi-professional team and I thank the clinicians, treatment radiographers and physicists.

I received a great deal of support and advice from the ICR/RMH physics department and fully appreciate their unrelenting patience while I navigated this unfamiliar territory. With special mention to Simeon Nill, Uwe Oelfke, Alex Dunlop, Adam Mitchell and Martin Menten for your swift replies to my 'SOS' emails.

I am grateful to our MR-Linac radiographers and the urology specialist radiographers for their time and contributions to our projects. With special

thanks to Helen McNair and Trina Herbert, for their advice and input from the very start of my research journey.

As part of the MR-Linac consortium prostate tumour site group, I participated in a number of international collaborations. I very much appreciate the opportunities I was given and would particularly like to thank John Christodouleas as well as the team from University Medical Centre Utrecht.

I gratefully acknowledge Elekta and NIHR Biomedical Research Centre at RMH and ICR for funding my research time.

My time in research was thoroughly enjoyable, I had particularly fun times with our group of research fellows who provided a great deal of support, discussions and were a constant sounding board for ideas. I take away many fond memories from ESTRO, and from our tea and cake sessions. Extra special Thanks to Ingrid White, Alison Ranger, Hannah Bainbridge and Naomi Lavan.

My journey through Clinical Oncology training and research would not have been nearly as successful or enjoyable without the support of friend and colleague Julia Murray. You are my biggest cheerleader and I am fortunate to have you by my side.

For my parents and sister Latha, thank you for your never-ending support and for always pushing me to be my best.

For my husband Steve, thank you for your courageous attempts at understanding my research, as well as proudly explaining it to your friends. I am hugely grateful for the support you have shown in so many ways.

Finally for my darling Janan and Anya, who still think I go to work to “put plasters on patients to make them feel better”. Thank you for your hugs and kisses that fuel my days.

The MR-Linac team, 18th September 2018

Following the first ever MRI-guided radiotherapy treatment in the United Kingdom within the PRISM trial

Chapter 1- Introduction

Sections of this chapter have been taken from the following publications;

Magnetic resonance imaging-guided adaptive radiation therapy: A "game-changer" for prostate treatment? Pathmanathan A, van As N, Kerkmeijer L, Christodouleas J et al. International Journal of Radiation Oncology Biology and Physics 2018; 100(2):361

The delineation of intra-prostatic boost regions for radiotherapy using multi-modality imaging- Pathmanathan A, Alexander E, Huddart R, Tree A. Future Oncology 2016;12(21):2495-25112015

1.1 Prostate radiotherapy- past, present and future

Prostate cancer is the most common non-cutaneous malignancy in men, with over 40,000 new cases in the England in 2017 [1] and increasing incidence, particularly early stage disease, as a result of more common prostate specific antigen (PSA) testing. Localised disease, where cancer is isolated to the prostate gland, can be treated with several options including active surveillance, radical radiotherapy, radical prostatectomy and brachytherapy. None of these have been shown to be more effective compared to the others [2], the modality of treatment selected is therefore dependent on the risk group of disease, staging, patient fitness, comorbidities and patient choice.

External beam radiotherapy (EBRT) to the prostate is effective but associated in particular with acute and chronic gastrointestinal (GI) and genitourinary (GU) toxicity. The priority is therefore to achieve biochemical control whilst minimising toxicity.

1.1.1 The evolution of radiotherapy

Prostate radiotherapy techniques have undergone a metamorphosis over the last two decades. We have transitioned from two-dimensional (2D) to three-dimensional (3D) techniques, subsequently to intensity-modulated radiotherapy (IMRT), image-guided radiotherapy (IGRT) and, more recently, stereotactic body radiotherapy (SBRT). Localization strategies have evolved from external skin markings, to 2D/megavoltage (MV) based bony localization, to complex techniques allowing localization of the target through implanted fiducials, electromagnetic beacons or 3D/kilovoltage (kV) volumetric imaging with soft

tissue capabilities of in-room computed tomography (CT) or cone-beam CT (CBCT).

The improvement in precision delivered by these technical changes has synchronised with a change in our radiotherapy fractionation. As the alpha/beta ratio of prostate cancer is thought to be low [3-6], hypofractionation should improve the therapeutic ratio. Moderate and extreme hypofractionated schedules are discussed further below in Section 1.3.

1.1.2 Prostate motion and IGRT

Prostate motion, both interfractional and intrafractional, has been well documented [7-10]. In particular, the use of cine-MR images can be used to reflect the prostate motion during a treatment fraction with previous studies using defined points of interest [11-14], the prostate edge [15] or measurement of movement compared to a baseline contour [16]. These provide data on general drift of the prostate as well as transient movements of varying magnitude, however do not consider the entire prostate volume. Continuous motion data during radiotherapy treatment itself is provided by tracking electromagnetic markers [17] and reporting the frequency and magnitude of displacements using the geometric centre of the markers.

The addition of a margin to the clinical target volume (CTV) must take into account any translational movements, rotations and change in size of the prostate. IGRT, whereby imaging is used to adjust subsequent treatment, comprises of a spectrum. At present, images taken prior to treatment, typically

cone-beam CT imaging, are used to locate the target and adjust treatment for that fraction of treatment, usually by adjusting patient positioning. This only takes into account interfractional variation, whereas adjusting for intrafractional motion can further improve target coverage [18-20] and reduce the toxicity of treatment [21, 22].

The implantation of fiducial markers (FM) prior to prostate radiotherapy allows more accurate patient set-up verification prior to each fraction of treatment [23, 24]. Although IGRT with FM permits margin reduction [24, 25], online images acquired prior to the radiotherapy fraction do not adjust for intrafractional movement of the prostate, which can be significant and is dependent on patient movement, bladder and rectal filling [11, 13, 15, 16].

Off-line adaptive radiotherapy (ART), whereby images are acquired prior to treatment can be helpful where there are systematic changes in anatomy such as response in the target or weight loss. However, again, off-line ART does not take into account intrafractional motion and the new plan generated 'off-line' does not influence treatment delivery on the same day.

The ultimate goal would be 'real-time' adaptive radiotherapy, utilising images obtained during treatment delivery to change the treatment plan according to the position of the prostate. This is not yet a reality, however with significant advances in the speed of Monte-Carlo dose calculations [26] , the quality assurance of newly adapted plans [27], multi-leaf collimator (MLC) tracking [28] and intrafractional dose accumulation [29], this would be possible in the future.

1.2 The use of MRI in prostate radiotherapy

1.2.1 Advantages of magnetic resonance imaging

Magnetic resonance imaging (MRI) in radiotherapy planning provides superior soft tissue differentiation with the added potential for functional imaging sequences. Diagnostic MRI for manual delineation of the prostate has shown a reduction in inter-observer variability, particularly at the prostatic apex [30, 31] and distinction anteriorly from the venous plexus. In addition, the volume of the MRI-defined prostate can be up to 40% lower compared to CT, translating to a lower rectal dose [31, 32].

The radiotherapy planning pathway typically involves an initial planning CT scan used for delineating the targets- CTV and planning target volume (PTV); and organs at risk (OAR). The CT provides the relevant electron density information required for dose calculations and can be used to construct digitally reconstructed radiograph for the verification process during treatment.

However, the improved soft tissue contrast of MRI allows more accurate outlining of these structures with reduced interobserver variability and a reduction in the prostate volume delineated [31]. Another significant benefit of MRI includes the lack of radiation exposure with MRI, particularly important for any imaging to be used for verification or intrafractional tracking.

1.2.2 Multiparametric imaging

The accuracy of MRI in staging prostate cancer has been extensively studied. Conventional MRI consists of anatomical T2 weighted images (T2W) with prostate cancer exhibiting low T2 signal intensity. The T2W sequence is based on fast spin-echoes and allows visualisation of internal structure of the prostate (central and peripheral zone and urethra).

Multiparametric MRI includes functional data from dynamic contrast-enhanced (DCE), MR spectroscopy (MRS) and/or diffusion weighted imaging (DWI), which can all provide additional information on the tumour to improve the sensitivity and specificity of tumour detection [33-38].

DCE-MRI acquires images whilst contrast is administered and therefore provides information on the perfusion and vascular permeability of a tumour. DWI assesses the motion of water molecules, with tumours showing a restricted diffusion due to increased cellularity. This restriction of diffusion is expressed as the apparent diffusion coefficient (ADC) and has been found to be a predictor of the aggressiveness of a prostate cancer [39, 40]. MRS is a form of metabolic imaging that detects prostate cancer due to the lower levels of intracellular citrate and higher levels of choline compared to benign prostate tissue. There is increased sensitivity for detection of prostate cancer with the addition of MRS [35], however spatial resolution is poor, limiting accurate tumour delineation.

Combining modalities improves the sensitivity compared to T2W images alone [36-38]. Pooled results from studies using the combination of T2W, DWI and DCE-MRI show a sensitivity of 0.74 (95% CI, 0.66–0.81) with specificity of 0.88

(95% CI, 0.82–0.92) [41]. Of the three multiparametric modalities (DWI, MRS and DCE), two appear to be sufficient for maximal sensitivity and adding in the third modality may not be of additional benefit [42]. Current recommendations suggest the use of two functional MRI techniques in addition to standard T2 weighted images [43].

The reported accuracy of MRI for IPL delineation is variable and dependent on a number of imaging factors as well as tumour characteristics. Technical factors include field strength, b values (which assess the strength of the gradients for DWI), signal- to-noise ratio and whether an endorectal coil is used. The latter improves the spatial resolution and has been found to improve the sensitivity, specificity and staging accuracy of prostate cancer [44] but the presence of the coil causes distortion of the prostate, which limits its use in planning radiotherapy. Low signal on T2W can be seen with prostatitis, haemorrhage, post radiotherapy change and scarring, and distinguishing these from tumour nodules can be challenging.

MRI is limited in the detection of small volume tumours e.g. $<0.5cm^3$ [45], particularly those of lower Gleason score. This is due to histological characteristics of the tumour focus, such as the ratio of malignant epithelium-to-stroma, which are inherently different in lesions picked up on MRI compared to those that are not detected [46, 47].

1.2.3 The use of fiducial markers

Accurate co-registration of MRI and CT images is essential in radiotherapy planning using both modalities. As CT and MRI examinations take place at

different times and over different timescales, co-registration is more accurate with the use of FM [48]. In addition, the implantation of FM prior to prostate radiotherapy allows more accurate patient set-up verification prior to each fraction of treatment [23, 24].

FM's create a high signal on CT images [49] and are therefore easily identified, however, specific sequences are required to enhance the visibility of the signal void on MR images, such as spin echo, gradient echo and balanced steady-state free precession sequence (bSSFP) [50] imaging. There have been a number of studies investigating dedicated MRI sequences for FM detection [50-55]. Both balanced steady-state free precession sequences [50] and sequences based on spoiled gradient-echoes have been employed in 2D [50-53] and 3D [54, 55] acquisitions, relying on T2*-related signal loss to create a detectable signal void in the vicinity of the FM.

The averaging of consecutive echoes in multi-echo recalled sequences, such as the T2*-weighted 'medic' sequence studied further in Chapter 4, is an attractive mechanism for increasing the signal-to-noise ratio. It is gradient-echo-based thereby maximising the signal loss surrounding the fiducial markers. This is achieved by combining several gradient-echo signals, with a range of echo-times, into one single image. This strategy maintains the signal-to-noise ratio and has been used for other clinical applications [56, 57]. In addition, the absence of geometric distortions has been demonstrated for this sequence [58] which would otherwise lead to systematic registration errors.

The accuracy of fiducial detection is paramount and can be either manual [51] or automatic [50, 52-55]. However, ultimately, this must be performed automatically, especially if intrafractional imaging is to be used. Different methods have been described for automatic algorithms including feature extraction [50, 53], template matching [54, 55] or even a combination of approaches [52]. The fiducial detection is dependent on the signal loss, which varies with factors including seed orientation and echo time [59, 60]. In Chapter 2, a dataset of bSSFP cine-MRI scans is used to assess the accuracy of an automatic fiducial detection method. In turn, this is used to assess the characteristics of prostate motion including rotations.

Calcifications within the prostate are a common source of signal voids in T2*W images, and they have been shown to mimic fiducial voids [61]. Although Gustafsson et al proposed to detect fiducials automatically by considering images at different echo times and the progressive increase in signal loss in multiple-echo pulse sequences, it is unclear whether calcifications will be a significant confounding factor [53]. Further investigation is required to determine whether false positive detection as a result of calcifications is a significant issue and whether calcifications can contribute towards MR-CT co-registration [61].

1.2.4 Dose escalation to the dominant intraprostatic lesion

Although prostate cancer tends to be multifocal, histopathology from prostatectomy specimens commonly reveals a larger focus or intraprostatic lesion, also referred to as the dominant intraprostatic lesion (DIL). To enhance personalised treatment, the dose can be escalated to the DIL, which is the most

common site of local recurrence [62, 63]. A higher dose to the DIL may reduce biochemical PSA failure and it is suggested that improving local control may translate into a reduction in distant metastases [64].

The demonstration of disease recurrence within the DIL has led to the proposal of boosting this region, whilst maintaining a standard dose to the rest of the prostate, in order to improve the therapeutic ratio [65]. The boost dose needs to be at least 80-90Gy in 2 Gray fractions, to reach the top of the tumour control probability (TCP) curve [66, 67]. The aim of treatment would be to increase the TCP without increasing the normal tissue complication probability (NTCP) for the bladder and rectum.

Dominant nodules may be easily defined on initial diagnostic imaging, however most patients then receive androgren deprivation therapy (ADT) which decreases the size of the IPL, and reduces tumour conspicuity [68]. Imaging for DIL delineation for radiotherapy planning could therefore be acquired prior to starting ADT with immediate irradiation, thus necessitating a change in the treatment paradigm. Alternatively, the information from pre-ADT imaging can be ‘mapped’ onto post-ADT imaging using deformable registration techniques. An additional unknown is whether the optimal target is in fact the pre- or post-ADT lesion. The latter would require further investigation into the effect of ADT on mp-MRI images and may become clearer when the exact benefits of a DIL boost are confirmed.

There are challenges involved in delineating the DIL, however a number of studies have shown this is feasible and safely delivered [69]. More recently, this has been tested in the FLAME trial NCT01168479 [70] with no significant difference in GU or GI toxicity at 2 years for patients receiving an integrated boost to the DIL compared to standard treatment [71], with outcome data awaited. The Hypo-FLAME study NCT02853110 (www.clinicaltrials.gov) is a Phase II study investigating a simultaneous integrated boost of up to 50 Gy in patients receiving whole gland SBRT of 35Gy in 5 fractions, toxicity data is not as yet reported.

1.2.5 Assessing tumour response with MRI

MRI sequences can be used as an indicator of tumour response. Preliminary results of DWI with MR-guided radiotherapy have been published [72], although there are currently no validated MRI biomarkers for prostate radiotherapy. MR images acquired throughout a course of MRgRT could allow the dose distribution to be adjusted based on tumour response. The concept of 'biological conformality' [73] uses the additional information from functional sequences to target dose to the area most likely to benefit from dose escalation. In particular, DWI imaging can be used to generate apparent ADC maps to identify more aggressive disease, which may benefit from boosting [39, 69, 74].

There is currently a paucity of data assessing imaging changes during and directly after treatment, however studies have shown that the ADC values from

DWI increase following treatment [75-77] with the greatest changes seen in patients with a better outcome [76].

1.2.6 Challenges and hurdles

The integration of MRI into the different stages of radiotherapy from target identification, to planning, to delivery is clearly attractive. There are, however, limitations including limited availability of MR scanners, medical contra-indications to MRI and the relatively reduced familiarity of MR imaging by radiation oncologists compared with CT images. MRI is also complicated by patient and machine related factors, which introduce distortions that must be corrected for [78].

In addition, MRI introduces technical hurdles within the planning process including lack of direct electron density information, organ motion between CT and MR scan and geometric distortion. Conventional immobilization with MR receiver coils presents additional challenges. Obstacles also include culture changes when a radiation oncology department houses a MRI scanner. Although integration of MR simulators is becoming more commonplace in radiation oncology departments, the need to incorporate MRI safety poses unique challenges.

At present, when MRI is used during the planning process, co-registration of images is required which can introduce a systematic error. To remove this step would require an MR-only workflow, with a number of challenges involved [79-82]. This is discussed further in Section 1.8.

1.3 Hypofractionation- How low do we go?

Although the ideal dose and fractionation of radiotherapy, allowing for maximum tumour control with acceptable toxicity, is far from certain, hypofractionation is increasingly favoured [66, 67, 83]. The alpha/beta ratio for prostate cancer is estimated to be as low as 1.5 Gy [3, 84-86], suggesting that moderate hypofractionation can be as effective as standard fractionation for prostate radiotherapy. Until 2016, patients in the United Kingdom (UK) attended hospital for 37 fractions of treatment over 7-8 weeks. As the alpha-beta ratio of prostate cancer is reported to be as low at 1.5 [5, 84-86], we would therefore expect a larger dose per fraction to be beneficial. This has been confirmed in several randomised studies [84, 87, 88] investigating moderate hypofractionation.

1.3.1 Moderate hypofractionation

The CHHiP trial [84] has resulted in many UK centres using a 20 fraction schedule. In this Phase III, non-inferiority study, patients were randomised between three schedules of 74 Gray (Gy) in 37 fractions, 60 Gy in 20 fractions and 57 Gy in 19 fractions with the 5-year biochemical and clinical failure free rates of 88.3%, 90.6% and 85.9% respectively. The 60 Gy group was non-inferior to the 74 Gy group, although non-inferiority was not shown for the 57 Gy group. There was no significant difference in the side effects reported at 5 years; reported acute RTOG $\geq$ grade 2 GI toxicity was 25% and 38% and acute RTOG $\geq$ grade 2 GU toxicity was 46% and 49% respectively for the 74Gy and 60Gy group. Late toxicity at 2 years was reported as RTOG $\geq$ Grade 2 GI toxicity was 4% and 3% and RTOG $\geq$ grade 2 GU toxicity 1% and 2% for the 74 Gy and 60 Gy group respectively.

1.3.2 Extreme hypofractionation

Extreme hypofractionation, using SBRT doses per fraction of ≥7.0 Gy, has many potential advantages including an improved clinical outcome and fewer attendances, with associated improved quality of life and significant reduction in healthcare costs [89]. Prospective phase II studies of SBRT have focussed on low and intermediate risk patients but report favourable biochemical outcomes for all risk groups [90, 91] and report acceptable toxicity [90-94]. The Phase III PACE trial is testing 5 fraction SBRT against standard fractionation, to establish if the abbreviated schedule is non-inferior. In advance of the randomised evidence, SBRT in 5 fractions appears to have promising efficacy and side effect profile. For these studies, the CTV is defined as the prostate or prostate plus the proximal SV with a CTV to PTV margin of 3 to 5 mm. Favourable outcomes have been confirmed by a pooled multi-institutional analysis from 8 institutions including 1100 patients with 58% high-risk, 30% intermediate-risk and 11% low-risk disease [95]. Treatment delivery was with CyberKnife (Accuracy Inc., Sunnyvale CA) using fiducials with a median dose of 36.25 Gy in 4-5 fractions and biochemical relapse free survival reported as 95%, 84% and 81% for low, intermediate and high risk disease respectively.

Preliminary outcome data and updated toxicity was reported from the Scandinavian HYPO-RT-PC study [96]. This Phase III, randomised non-inferiority study randomised 1200 patients with intermediate or high-risk prostate cancer between conventional fractionation schedule of 78 Gy in 39 fractions or 42.7 Gy in 7 fractions without ADT. Fiducial based IGRT was utilised with treatment to the prostate alone using a 7 mm margin. With a

median follow up of 59.7 months, the biochemical or clinical failure free rate at 5 years was 83.8% and 83.7% for the conventional fractionated and ultra-hypofractionated groups respectively. In this updated toxicity data, there was no significant difference between groups for physician reported toxicity although their previous data had reported a significantly worse patient reported outcome measure (PROM) for bowel function at the end of radiotherapy for the ultra-hypofractionated regimen, with this difference no longer apparent at three months [97]. More recently, acute toxicity data has been reported from the randomised controlled trial Prostate Advances in Comparative Evidence (PACE) trial (NCT01584258), with PACE-B comparing 5 fraction SBRT, 36.25Gy in 5 fractions over 1-2 weeks, against standard conventional or moderately fractionated schedules [98]. The worst reported acute RTOG $\geq$ grade 2 GI toxicity was 12% and 10% and acute RTOG $\geq$ grade 2 GU toxicity was 27% and 23% respectively for the standard versus the SBRT arm. These are lower than the toxicity rates summarised above for the CHHiP trial, interpreted to be due to a combination of mandated IGRT, smaller margins and more conformal planning techniques within the PACE-B trial.

1.3.3 How low can we go?

The direction of travel is for progressively more abbreviated radiotherapy schedules, and if 5 fraction SBRT is safe and effective, it raises the question – how low can we go?

Given the potential for extreme hypofractionation, there is the possibility of reducing the number of fractions even further, which has been demonstrated

with brachytherapy. Hoskin et al reported the longer-term outcome for patients treated with high-dose-rate brachytherapy (HDR-BT) alone for mainly intermediate and high risk patients [99, 100]. A dose of either 3 fractions at 10.5 Gy or 2 fractions of 13 Gy gave acceptable toxicity rates with 91-93% free from biochemical relapse at 4 years [100]. The same group published early toxicity data showing single fraction prostate HDR-BT with 19 Gy is tolerable, although a significant increase in the need for catheterisation was seen compared to the two fraction cohort, particularly when 20 Gy was delivered to the whole gland [101]. However, late toxicity and biochemical control were similar for a single 19-20 Gy fraction compared to 2-3 fractions [100]. Other groups have reported favourable toxicity rates with single fraction HDR-BT [102, 103]. Prada et al reported low morbidity in patients treated with single fraction 19 Gy HDR-BT monotherapy [102] with injections of transperineal hyaluronic acid into the peri-rectal fat. However, no margin was added to the prostate for the PTV and the biochemical control was 66% at six years. Urethral dose can be a limiting factor to the total dose achieved, as seen when HDR-BT is used to plan an intraprostatic boost [104].

Despite the favourable toxicity profiles reported for single dose HDR-BT, data from several groups suggest a higher local failure rate and poorer outcomes compared to multifraction treatment [105-107]. The largest patient group so far, a UK national cohort study [106] from seven centres delivering 19 Gy to the PTV, reported a three year biochemical relapse free survival of 88% overall, subdivided into 100% in low risk, 86% in intermediate risk and 75% in high risk patients. Morton et al have reported data from a Phase II randomised trial with a

significantly inferior 5-year biochemical disease-free survival of 73.5% in the single fraction arm compared to 95% in the two fraction arm [107].

Low-dose-rate brachytherapy (LDR-BT) is also an option for dose escalation with low toxicity rates and excellent biochemical control [108, 109], without the need for a shielded room as for HDR-BT. In the ASCENDE-RT trial, the use of LDR-BT as a boost improved biochemical progression-free survival compared to dose-escalated external EBRT alone [110], however, this was at the cost of higher genitourinary toxicity [111].

Although brachytherapy may be considered the ultimate in conformal treatment, it is invasive and requires patients to meet anatomic criteria and is therefore not broadly available to all patients. In contrast, linac-based treatment with fewer fractions would potentially be feasible across the globe. It may even offer cost effective benefits over brachytherapy or multiple-fraction treatment and allow a higher patient throughput on a single machine. It is technically feasible to deliver similar target doses and meet the same constraints of HDR-BT with EBRT [112]. SBRT can be used to deliver an equivalent biologically effective dose without the need for a surgical procedure, general anaesthesia and associated potential complications. This has been assessed within the Phase II PROSINT trial (NCT02570919) randomising between 45 Gy in 5 fractions or a single 24 Gy fraction. However, given the inferior outcome data from single fraction HDR-BT, further SBRT studies employing schedules with fewer fractions must be cautiously designed with the data suggesting that two fractions should be the minimum.

Given the higher dose per fraction, highly conformal dose distribution and steep dose gradient seen with SBRT, accurate delivery using direct tumour motion monitoring and online adaptive radiotherapy (ART) methods becomes ever more important. The ideal delivery system would consist of optimal image guidance (pre-treatment and intrafraction MRI), rapid delivery, and intrafraction ART.

1.4 The future of image-guided radiotherapy

1.4.1 MRI guided radiotherapy platforms

MRI guided radiotherapy systems provide what has long been considered the 'holy-grail' of radiotherapy delivery, the integration of a MRI scanner that can provide clinical-quality imaging with a modern linear accelerator [113]. There are several systems in development for clinical use [114-117], summarised in Table 1.1. Not only can the improved soft tissue contrast of MR improve patient positioning prior to radiotherapy 'on-line', but 'real-time' imaging during the treatment delivery itself can also help to detect tumour and normal tissue position and deliver radiation dose more precisely.

	Type of system	Magnetic Field Orientation	Research/Clinical Status	Adaptive capabilities
Elekta MR-Linac research system [114]	1.5T 7MV 70cm closed bore Single-focused Agility MLC providing 5 mm resolution for nominal 100 cm SSD, projecting to 7 mm at Unity's isocentre	B_0 magnetic field perpendicular to delivery	First patient treated May 2017 in Utrecht as part of First In Man protocol First patient treated in the UK at RMH/ICR in September 2018 within the PRISM trial	ART capabilities include: 1. Shifting plan to overlay anatomy—simple dose shift 2. Offline ART 3. Library of plans 4. Online ART- segment-weight optimization and full re-optimization available 5. Visual tracking of target
ViewRay MRIdian Cobalt-60 system [115] **ViewRay MRIdian Linac system**	0.35T cobalt system Three cobalt-60 heads on rotating gantry ring Split magnet 70cm closed bore Newer system with 6MV linac Split magnet 70cm bore 'Razor' MLC is a double-stacked, double-focused MLC of 8 mm leaf width, providing 4 mm resolution and allowing field sizes down to 2 mm by 4 mm	B_0 magnetic field perpendicular to delivery	FDA 510(k) cleared for cobalt and linac systems Treated patients since 2014 (on cobalt system) and 2017 (on linac system)	ART capabilities include: 1. Shifting plan to overlay anatomy—couch shift 2. Offline ART 3. Library of plans 4. Online ART –segment-weight optimization and full re-optimization available 5. Tracking with exception gating for target
Sydney Inline Australian MRI-LINAC system [116]	1.0T 6MV 82cm open bore	B_0 magnetic field perpendicular and parallel to delivery	Currently research system	
MagnetTx Aurora RT™ Linac-MR [117]	0.5T 6MV	B_0 magnetic field parallel to delivery	Currently research system	

Table 1.1- MR guided radiation platforms existing or in development

MRI in radiotherapy planning provides superior soft tissue differentiation with the added capability of functional imaging. Improved image contrast has also been demonstrated with MR-guided radiotherapy systems, where even low field strength from an on-board 0.35 T MRI can give improved anatomical visualisation compared to on-board CT [118], with a reduction in radiation exposure.

The MRIdian system (ViewRay Inc., Oakwood Village, OH), initially integrated with tri-cobalt-60, more recently with a 6 MV linac, has been treating patients since 2014. The first patient was treated using Elekta's MR-Linac research system (Elekta Inc., Crawley, UK) in May 2017. Despite the potential effect on dose distribution by the magnetic field [119], which increases with higher field strength [120], treatment plan quality equivalency to standard linacs is achievable [121, 122]. The dosimetric impact of the Lorentz force can be accounted for and mitigated through Monte Carlo dose calculations and inverse planning techniques.

1.4.2 The MR-Linac: Elekta Unity

The MR-Linac, named Elekta Unity (Figure 1.1), is a new technology that combines an MR scanner and linear accelerator (or 'linac') [114, 123] which would allow the benefits of MRI to be harnessed at all stages from planning to patient set-up and continuous imaging during treatment delivery to allow tracking of the targets and organs at risk.

Figure 1.1- Photo of the MR-Linac or 'Elekta Unity'. The 70 cm bore is seen centrally. Housed within the unit is the integrated MRI scanner and linear accelerator. All positioning devices are MRI compatible.

The Royal Marsden Hospital together with the Institute of Cancer Research are one of just seven 'early adopter' centres worldwide forming part of the MR-Linac global research consortium. The aim of this consortium is to ensure evidence-based introduction of this new technology by standardising radiotherapy planning, collecting data within an umbrella registry, and enabling collaborations [124]. Within the consortium, research initially focussed on nine tumour sites, with specialists from each centre forming a tumour site group (TSG) to co-ordinate research within the pre-clinical and clinical studies. In my thesis, I have included work that has built upon the collaborations within the prostate TSG. Following the clinical use of the Elekta Unity (see Chapter 6), more centres

internationally have joined the consortium and additional TSGs have been initiated.

Following installation of the Elekta Unity, the first step was acquiring images utilising a range of sequences and to ensure that the pre-specified parameters would provide imaging of sufficient quality for the MR-guided workflow. At our centre, this was achieved within the 'Development of daily online magnetic resonance imaging for magnetic resonance image guided radiotherapy' (PRIMER) study (chief investigator Robert Huddart). The study is summarised in Figure 1.2.

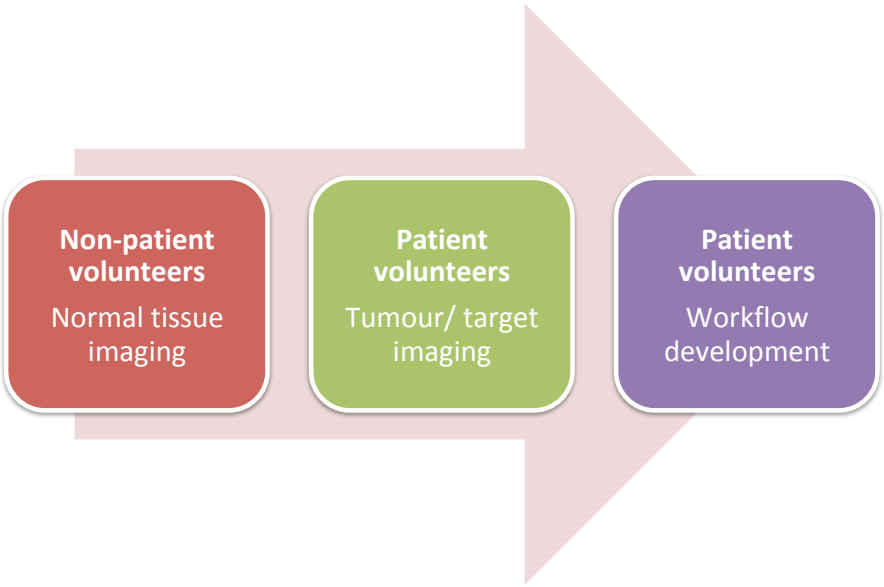

Figure 1.2- Summary of the phases within the PRIMER study to assess the suitability and development of MRI sequences for the MR-Linac.

During the first phase of this study, imaging is acquired in healthy non-patient volunteers and graded by a combination of clinicians and treatment radiographers, as to the quality of the appearances of the normal tissues that is

the organs at risk. For example, the prostate team would rate the images for femoral heads, rectum, bladder and bowel. The targets, that is, prostate and SV were assessed within the second phase of the study within patient volunteers, although 'tumour' assessment is less relevant for prostate radiotherapy compared to other tumour types.

As will be discussed in Chapter 6, this is pertinent when deciding the imaging for use within the MR-Linac online workflow. Within the PRIMER study, the 2 minute T2W sequence was determined just as sufficient as the 6 minute T2W sequence (see Figure 1.3) without the additional time penalty. The third phase involves ongoing adjustments to the parameters, acquisition of these sequences and further review of the suitability of the imaging.

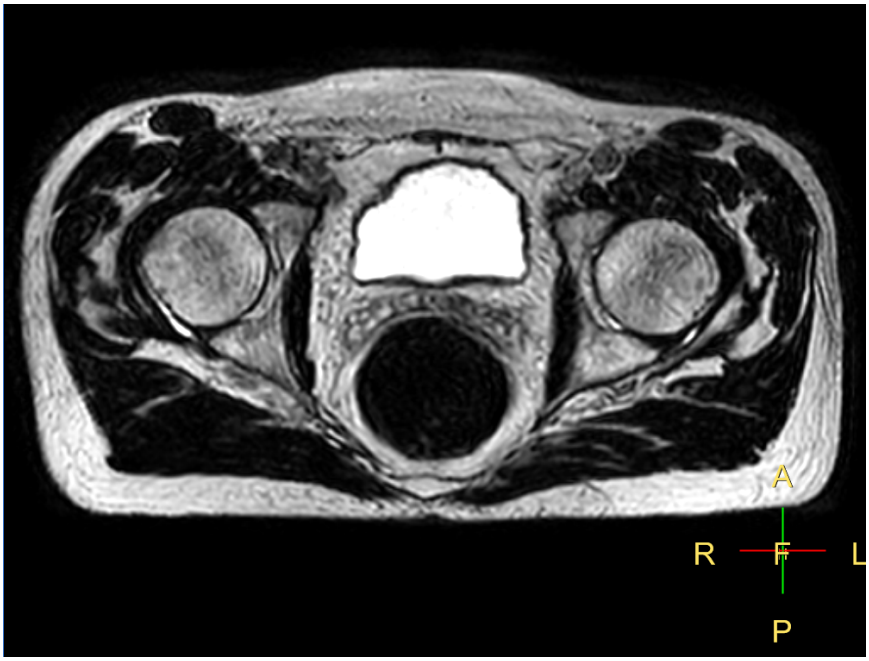

Figure 1.3- An example of an axial slice from the MR-Linac 6 minute pelvis T2W sequence, as acquired within the PRIMER study.

1.4.3 Applications for MR-guided radiotherapy

I have discussed the role of hypofractionated schedules (Section 1.3) and dose escalation to the DIL (Section 1.2.4). To deliver this dose accurately and improve the therapeutic ratio, prostate movement needs to be accounted for by IGRT, ideally with at least online ART.

For MR-guided radiotherapy, a realistic assessment of prostate motion is required to guide the margins added to the prostate CTV. Margin reduction, even in the presence of image guidance may lead to geographical miss with negative impact [125], however an overestimated margin will increase the dose to the OAR and counteract any benefit from MR guidance. In Chapter 2, using a method for automatic fiducial marker detection, I look at data for prostate motion, assessed using cine-MRI.

Although real-time ART with prostate tracking is not currently possible on the MR-Linac, on-line ART is being utilised, discussed further in Chapter 6. The next step would be online ART prior to treatment delivery followed by prostate tracking for exception gating, which would correct for both interfractional and intrafractional motion. In this workflow, MR imaging taken just prior to a fraction of treatment is matched to the reference imaging. Following this, deformable image registration is used to match the new anatomy to the initial treatment plan, with re-contouring where required, for re-optimisation of a new plan [126, 127] using the ‘adapt to shape’ method. This workflow is discussed in further detail in Chapter 6. Prior to treatment delivery, as repositioning of the patient is limited within the bore of the MR-Linac, a ‘virtual couch shift’ is used to shift the

plan to the new daily anatomy [128], also known as the 'adapt to position' method.

Although not yet available with the MR-Linac, this new plan could be delivered using continuous MR imaging with exception gating, that is, if the prostate moves out of pre-defined thresholds, treatment is paused until the prostate returns to within margins [20, 129, 130] or a further virtual couch shift could be applied. Exception gating has been clinically applied with the MRIdian system [131]. The optimal combination would be online ART to create a new daily plan, followed by delivery using real-time plan adaptation during radiation delivery.

1.5 Daily adaptive re-planning

1.5.1 Benefits of daily adaptive re-planning

With standard IGRT, there is no method to compensate for the independent movements of the four potential radiotherapy targets- prostate, seminal vesicles (SV), pelvic nodes and intraprostatic boost. Radiotherapy can induce an initial increase in size of the prostate followed by constriction at the end of radiotherapy [132, 133]. With SBRT, the swelling can persist even at the end of treatment [134].

Despite daily IGRT to compensate for interfractional movement, residual deformation of the prostate and the organs at risk (OAR) [133, 135] with ongoing intrafractional motion of the prostate continues to be a challenge [10]. Offline adaptation can adjust for systematic changes, but Peng et al [136]

showed when the original treatment plan is superimposed on daily in-room CT scans, approximately a third of fractions would need online re-planning due to the discrepancy in planned and delivered dose.

The implications of this disparity become more significant with a shorter ultra-fractionated treatment course. On-table, online ART is now feasible with MRgRT and represents an attractive solution for ultra-hypofractionated prostate radiotherapy. Online ART has the ability to account for not only systematic anatomical changes of prostate swelling, but also random anatomical changes, such as inter/intra-fraction bladder and rectal filling, in addition to independent movements and deformations of multiple targets.

1.5.2 Daily adaptive re-planning – obstacles and solutions

The solution for optimal delivery of planned dose is real-time planning and daily online adaptation. There are a number of steps involved in utilising the newly acquired images adjusting for a change in anatomy.

There are six strategies of ART:

1. Shifting the plan to overlay anatomy: Dose is adapted by shifting the plan relative to the anatomy (3D or 6D correction) or vice-versa. This is equivalent to standard IGRT.
2. Dynamic shifting of a plan with tracking: Requires intrafraction motion monitoring, and has been shown to be feasible with in prostate cancer with Calypso beacons [137].

3. Offline ART: Correct for systematic deformations of the target(s) [138] or OAR that occur slowly over the radiotherapy course, plus shifting plan on the day as above.
4. Library of plans: Select from plans for varying patient anatomy and deliver the best fit for the anatomy of the day [139, 140].
5. Online ART: Adapt the plan on a daily basis after imaging and re-optimising/recreating a treatment plan
6. Real-time (intrafraction) ART: Adapt the planned dose during a radiotherapy fraction.

The strategies most relevant to prostate MRgRT (#1, #5 and #6) are discussed below and summarised in Figure 1.4. Note offline strategies #3 and #4 may be performed in lieu of strategy #5, when departmental resources limit ability to perform on-table ART. All above strategies could be carried out with MRgRT gating in the presence of accurate beam-on imaging.

Figure 1.4- Flow chart summarising the spectrum of adaptive radiotherapy. Figure previously published in my review article (157).

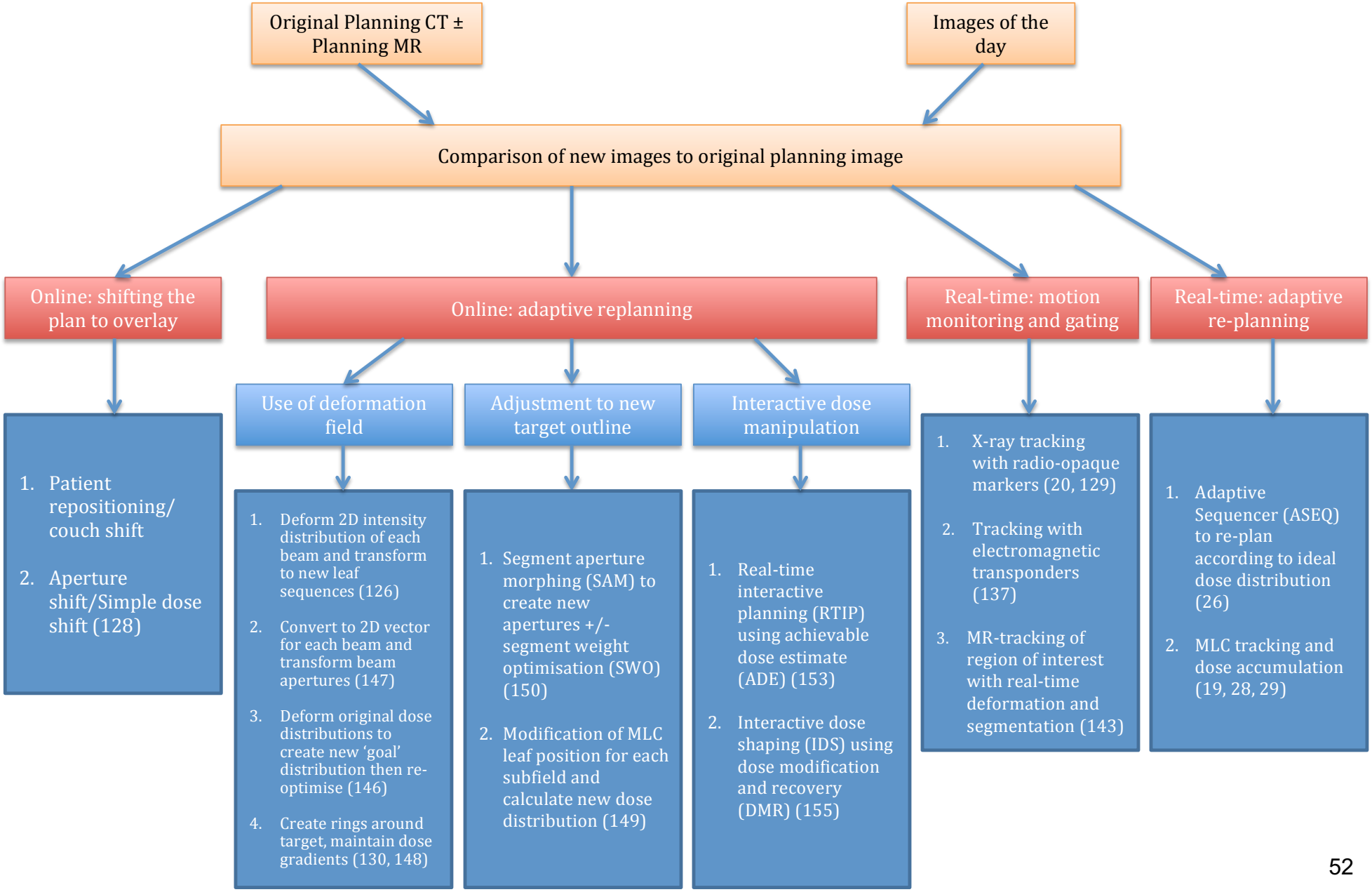

1.5.3 Shifting the plan to overlay anatomy

***IGRT repositioning**:* Online approaches [141] adjust for interfractional displacements of one selected radiotherapy target using a couch shift technique, keeping the treatment plan the same.

***Simple dose shift**:* The pre-treatment dose distribution itself is translated and rotated according to the change in anatomy [128]. This method does not require full re-optimisation of a plan and is therefore a rapid IGRT solution. A similar method has been described for online rotational correction by adjusting gantry and collimator angles [142].

1.5.4 Real-time imaging with gated delivery

The challenge of intrafraction motion can be mitigated using gating strategies, whereby tumour motion monitoring is used in conjunction with visual inspection or an automated algorithm to adjust treatment delivery. 'Exception gating' utilises a specified threshold, for example with a 2mm/5 second threshold, if the movement of the prostate exceeds 2mm from baseline for over 5 seconds, treatment delivery is paused to allow return of the prostate to the initial position, adaptation of patient position or simple dose shift.

At the present time prostate motion can be monitored using x-ray tracking of implanted radio-opaque markers (seeds) [20, 129], or the Calypso system using electromagnetic transponders [137]. Continuous MR imaging does not involve additional radiation exposure and ultimately, an MR-workflow would not require

the implantation of seeds if soft tissue imaging accurately reflects the target position and motion. The accuracy of target localisation is dependent on the speed of image acquisition. Gating through MR in a clinical setting has been demonstrated with the MRIdian system, where motion monitoring is performed on a sagittal plane acquired at four frames per second, followed by real-time deformation and segmentation of the region of interest [143]. However this would be further improved using 3D imaging and patient individualisation of the threshold margin, which may include motion prediction algorithms [144].

1.5.5 Online adaptive re-planning

There are a number of methods with various levels of complexity for adaptive re-planning. Most studies so far have used CBCT for daily imaging, which provides a poorer image quality (compared with planning CT and MRI) for new contours, followed by plan adaptation.

The ‘Blue Sky’ aim would be eventually to dispense with pre-treatment planning completely, and create an online plan from scratch each day, to reflect the current anatomy. This can be in tandem with dose painting based on the distribution of tumour load as described earlier [145]. Online MRgRT has been demonstrated clinically with daily MRI by re-optimising using the original beam angles and objectives used if constraints were not met [127]. Just over half of the fractions were treated using an adapted plan. The median time for ART was 26 minutes and was well tolerated.

As this process needs to be completed in a timely manner, several approaches have described adjusting the initial plan, without full optimisation, for expediency. Rapid re-planning is particularly important as increased organ motion over time could negate any benefit from ART.

***Use of the deformation field**:* The deformation matrix created by registering the daily verification images to the planning images can be used to alter the original plan accordingly. Comparison of the whole target or points on the target [146] in the beam's eye view (BEV) can be used to modify each segment [126] or beam aperture [147]. Alternatively, the method of gradient maintenance [148], creates a series of partial concentric rings (PCRs) around the target with the aim of retaining the dose gradients towards each OAR. A similar method has been described with the MRIdian system whereby rings control gradients and auto-segmentation through deformation, to minimize the re-contouring required [130].

Adjustment to new target outline: In order to avoid the complexities of deformable image registration (DIR), there are methods simply comparing the target outline [149, 150]. Segment aperture morphing (SAM) can adjust the segment shapes to the new target contour [151] with a further step of segment weight optimisation (SWO) for larger deformations. Online re-planning methods that are suitable for implementation with the MR-Linac have also been reported [150, 152].

Interactive dose manipulation: This approach enables the clinician to use tools to click on or select part of the plan and 'drag' the isodose curves or dose-volume histogram and view the updated dose distribution [153-155]. Constraints can be defined that should not be violated, to preserve, for example, a minimum dose to the target [153]. In the future, these could allow real-time automated modification of a plan to the anatomy of the day both before and during treatment.

1.5.6 Real-time adaptive re-planning

The methods described so far mainly focus on the target outline alone, and although they can improve target coverage compared to patient repositioning alone [126, 147, 149], ultimately re-planning from scratch yields the best dosimetry. Real-time ART can improve dose accuracy regardless of the delivery system [156]. The only way this can be achieved is by continuous imaging with constant re-planning, including re-optimisation. Treatment planning systems are already capable of rapid dose calculations using cloud computing.

The ultimate goal of adaptive re-planning will be to adapt a plan *during* beam delivery. Kontaxis et al have described a graphics processing unit (GPU) Monte Carlo dose engine, inverse dose optimisation algorithm and an Adaptive Sequencer (ASEQ) to calculate deliverable IMRT plans [26]. New images are fed into this system in real time. Starting with an ideal dose, the sequencer calculates each segment and the dose that it will deliver, subtracting this from the initially calculated 'ideal' dose distribution. This step is repeated with multiple iterations to achieve the ideal dose. Treatment can start before the final

dose calculation is complete, therefore allowing the constantly changing anatomy to affect the optimisation and preventing a delay in treatment. At the end of each fraction, the actual dose delivered is used to calculate any excess in dose or shortfall, which is then compensated for by adjusting the dose calculations in subsequent fractions.

Real-time MLC tracking has been demonstrated to improve dose delivery in a clinical setting for prostate patients using the Calypso localisation system [19]. If accurate online dose reconstruction is available, this can provide a rapid calculation of the dose delivered so far within a fraction to adjust the dose for the remaining fraction delivery time and allow intrafractional re-planning. This has been described for dynamic MLC tracking [28] and can be used to re-optimise a plan in the time taken for the gantry to rotate between beams for uninterrupted treatment [29].

Although such solutions are attractive, they assume that DIR is a well-solved problem. However, bladder, rectum and prostate deform in a non-uniform manner. This makes the quality assurance (QA) of accurately documenting delivered dose challenging and novel methods of time efficient QA are required [27].

Before adaptive intrafraction re-planning becomes a reality, efforts are currently focussed on expediting imaging, re-planning and beam-on times such that intra-fraction adaptation is less prominent [157].

1.6 Contour Variability

With the evolution of more conformal treatment techniques, the need for accurate target and OAR delineation especially becomes important. Contouring has understandably been described as 'the weakest link' [158].

Radiotherapy planning of a prescribed dose with dose constraints is heavily dependent on a consistent target and OAR contours. 'Intraobserver' variability for contouring is the variability seen when a single individual's contours vary when presented with the same imaging more than once. 'Interobserver' variability describes the difference between several observers asked to delineate a particular structure on the same image. There are a number of factors affecting this image interpretation including imaging modality, anatomy, observers' institution, training including the use of contouring guidelines and experience. In Chapter 4 I discuss the **consistency** of individual contours where there is reduced interobserver variability. Although there may be high agreement between observers, this does not automatically translate to accuracy. However in the absence of a ground truth for the accurate contour, the interobserver variability still provides vital information with high variability indicating more individuals are incorrect. There have been a number of studies assessing interobserver variability [30, 31, 48, 159-174] in outlining the prostate, with some looking at single imaging modalities (summarised in Table 1.2) and others comparing different imaging modalities (Table 1.3). As discussed in the Introduction Section 1.2.1, MRI appears to reduce interobserver variability [30, 31, 171, 173] although this is also affected by the experience of the observers.

Publication	Methods	Results- overlap measures	Results- distance measurements
Pasquier et al, 2016 [161]	1 patient for prostate CTV 14 observers (physicians across 11 centres) CT imaging	DSC Initial 0.83 ± 0.06 Post discussion and guidelines 0.83 ± 0.08	None reported
Shahedi et al, 2014 [162]	10 patients 3 observers (two radiologists, one radiation oncologist) T2W fast spin echo MRI	Comparison to STAPLE DSC Whole gland range 78-98	Mean absolute distance (MAD) Whole gland range 0.2-3.1
Langmack et al, 2014 [163]	8 patients 2 sets of contours (each contoured by a combination of a radiation oncologist and dosimetrist) Fused CT/T2W MRI	DSC mean (sd) Prostate 0.70 (0.08) SV 0.58 (0.10) Rectum 0.76 (0.11) Bladder 0.88 (0.05) L fem head 0.89 (0.03), R fem head 0.91 (0.02)	Mean distance to conformity (MDC) (mm) Prostate 3.1 (0.7) SV 3.4 (0.9) Rectum 4.8 (2.4) Bladder 2.2 (0.3) L fem head 3.0 (1.0), R fem head 2.6 (0.8)
Nyholm et al, 2013 [164]	25 patients 10 observers from five centres (radiation oncologists) T2W MRI (from five centres)	None reported	Range of median distance from joint centre of mass (mm) Prostate 0.8 (posterior) to 2.5mm (inferior) SV 2.0 (posterior) to 3.7 (left)
Simmat et al, 2012 [175]	5 patients 7 observers (same institution) Planning CT and CBCT	DSC for planning CT Prostate 0.79 Rectum 0.85 Bladder 0.94	None reported
Choi et al, 2011 [166]	10 patients 3 observers (physicians) Anatomical training session beforehand. Planning CT and CBCT,MRI on separate monitor	CIgen mean for planning CT (range) Prostate 0.74 (0.66 to 0.81)	Difference between COM and average COM Prostate 1.23 (0.18 to 2.98)
White et al, 2009 [168]	5 patients 5 observers (radiation oncologists) CBCT	None reported	Standard deviation of centre of mass placement Right-left 0.07 Anterior-posterior 0.18 Superior-inferior 0.28
Gao et al, 2007 [169]	1 patient 6 observers CT imaging	None reported	Standard deviation of the mean gaps between observer and gold standard contour for each quadrant (mm) Left 0.5, Right 1.5 Posterior 0.5, Anterior 2.0
Song et al, 2006 [170]	5 patients 7 observers (4 radiation oncologists, 1 physicist, 2 radiation therapists) Kilovoltage CT (KVCT) and megavoltage CT (MVCT)	Volume variability (CV-EV/EV) x100% Higher value indicates increasing IOV Prostate KVCT 59.7, MVCT 76.2% SV KVCT 73.1, MVCT 85.6% Prostate KVCT ant-post z(com) 0.12	Distance measurements by intersecting a ray from COM Prostate KVCT lateral x(com) 0.05 Prostate KVCT sup-inf y(com) 0.20
Fiorino et al, 1998 [172]	6 patients 5 observers (radiation oncologists) CT	None reported	SD of relative difference from mean contour (mm) Prostate 1.4-7.1mm SV 1.5-2.8mm
Cazzaniga et al, 1998 [173]	3 patients 6 observers (radiation oncologists) CT	None reported	Square root of variance by measuring distance from centre of the contour in 12 directions Prostate apex 1.99 Middle prostate 2.90 SV 4.98

Table 1.2- A summary of publications assessing interobserver variability (IOV) of prostate contours on one imaging modality. Overlap measures range from 0-1.0 unless where stated. CIgen- Conformity index, COM- centre of mass, DSC- Dice similarity co-efficient, L-left, R-right

Publication	Methods	Results- overlap measures	Results- distance measures
Alasti et al, 2017 [160]	10 patients 5 observers (radiation oncologists) Conventional helical CT (CCT), high dose volumetric CT (HDVCT), T2W MRI	Jaccard index CCT 0.55 ± 0.07 HDVCT 0.59 ± 0.06 MRI 0.60 ± 0.11	Standard deviation of the 5 observations for each sample point (total of 552 for each image) CCT 2.0 ± 0.6 mm HDVCT 1.9 ± 0.4 mm MRI 1.8 ± 0.4 mm
Lutgendorf-Caucig et al, 2011 [159]	8 patients 7 observers (radiation oncologists) MRI, CT, CBCT	Conformity index (CIgen) CBCT 0.57 ± 0.09 CT 0.72 ± 0.07 MRI 0.66 ± 0.12	None reported
Khoo et al, 2012 [174]	3 patients 5 observers (radiation oncologists) CT and T2W MRI Assessed before and after educational programme	Encompassing volume (EV)/common volume (CV) Higher value indicates increasing IOV CT 2.74 (before education), 2.38 (after) MRI 2.38 (before education), 1.41 (after)	None reported
Rosewall et al, 2009 [167]	7 patients All with bilateral hip replacements CT and T2W images	Encompassing volume (EV)/common volume (CV) Higher value indicates increasing IOV MRI mean EV/CV 1.71 CT mean EV/CV 1.95 Not significantly different	None reported
Villeirs et al, 2005 [30]	13 patients 3 observers (radiation oncologists) One day training in pelvic anatomy (CT and MRI) at start of study CT alone then CT+MRI (and radiologist input)	Volume comparison for CT+MRI Prostate 5.21% reduction compared to CT alone SV 10.47% reduction compared to CT alone Delineation uncertainty index Ratio between delineated volume and intersecting volume- higher value indicates increasing IOV Prostate CT 1.16, CT+MRI 1.10 SV CT 1.20, CT+MRI 1.07	Interobserver mean SD of prostatic margin position Anterior CT 1.9-3.2, MRI 1.6-2% Posterior CT 2.0-2.3, MRI 1.4-1.7% Right CT 2.1-2.8, MRI 1.1-1.5% Left CT 1.4-2.6, MRI 1.0-1.4% Sup/inf CT 2.1-4.4, MRI 1.6-2.2%
Parker et al, 2003 [48]	6 patients 3 observers (radiation oncologists) CT and MRI (independently)	Scan encompassing volume (SEV)/Scan common volume (SCV) Higher value indicates increasing IOV CT 1.58 MRI 1.37 Significant difference	None reported
Debois et al, 1999 [31]	10 patients 3 observers (radiation oncologists) CT and MRI independently	None reported	IOV of sup-inf prostatic apex position CT 0.5-1.0, axial MR 0.4-0.6, coronal MR 0.2-0.3cm
Rasch et al, 1999 [171]	18 patients 3 observers (radiation oncologists) CT, axial/coronal/sagittal MRI independently	Scan encompassing volume (SEV)/Scan common volume (SCV) CT 1.5, axial MR 1.5, coronal MR 1.5, sagittal MR 1.7	Overall observer variation (1 SD)(mm) CT 3.5, axial MRI 2.8, coronal MRI 2.5, sagittal MRI 5mm

Table 1.3- A summary of publications comparing interobserver variability (IOV) of prostate contours on different imaging modalities. Overlap measures range from 0-1.0 unless where stated. Higher distance values indicate poorer IOV. CIgen- Conformity index, COM- centre of mass, DSC- Dice similarity co-efficient, L- left, R-right

In addition, in Chapters 4, 5 and 7, I consider the **accuracy** where the contours in question are compared to a 'gold standard' or 'reference' contour. Again, in the absence of the ground truth, this can be defined based on a single clinician contour, a radiologist contour [176], a combination of clinician contours [161, 162, 177, 178] or a consensus contour [179]. To avoid bias by a single observer and take into account interobserver variability here, I use a combination of several clinician contours or the Simultaneous Truth and Performance Level Estimate (STAPLE) contour [180]. This is a more sophisticated way compared to simply 'averaging' contours, which would assume that each contour is equally correct. Instead, the STAPLE calculates an estimate of the 'true' segmentation by weighting each individual segmentation based on the calculated performance quality of that contour.

Assessing contouring consistency and accuracy are particularly relevant in this thesis for a number of reasons. Firstly, contours will vary depending on the imaging modality used and the impact of MRI on contouring has already been discussed in Section 1.2.1. Secondly, with the introduction of MRI in all stages of the radiotherapy workflow, contouring guidelines for the prostate, SV and OAR can help to standardise contouring [181]. Thirdly, with the progression of adaptive radiotherapy, new contours will initially be reviewed and amended by clinicians but it is not feasible to maintain this long term as increasing patient workload will impact on other clinical duties, therefore, this step is more practically achieved by other members of the interprofessional team notably treatment radiographers. Finally, as delineation is a time consuming process, there have been huge developments in automatic contouring software, with the

potential to save time and reduce interobserver variability [182]. This is assessed further in Chapter 5.

1.6.1 Contour comparison measurements

There are multiple comparison metrics available with no consensus on the most appropriate ones [183-185]. This is demonstrated in Table 1.2, where there are a wide variety of measurements used for evaluation. As each type of metric provides information on just one aspect of the structure, a combination of metrics is more likely to give a spatial representation. Some studies describe the absolute volume of a structure, however, this is not useful when used alone, as two structures may have the same volume without overlapping at all. In studies where other metrics have been reported however, this can be a useful additional value.

Analysis of the centre of mass (COM) or centre of volume (COV) can describe the distance between two contours but gives an indication of displacement rather than the shape of the volume itself as two volumes with completely different volumes and shapes can have the same COM/COV.

The contour comparisons reported in Chapters 4-7 are calculated using research versions of Monaco ADMIRE (version 2.0, Elekta AB, Stockholm, Sweden), although this is primarily autosegmentation software.

Previously reported comparison studies mostly report the degree of **overlap** between contours including concordance index or Jaccard index and Dice

similarity coefficient (DSC). The latter, used in the next two chapters, can be described as

$$DSC = \frac{2(X \cap Y)}{X + Y}$$

Where X and Y are the volumes of two contours being considered and (X∩Y) is the intersection or overlap between them. This is illustrated in Figure 1.5.

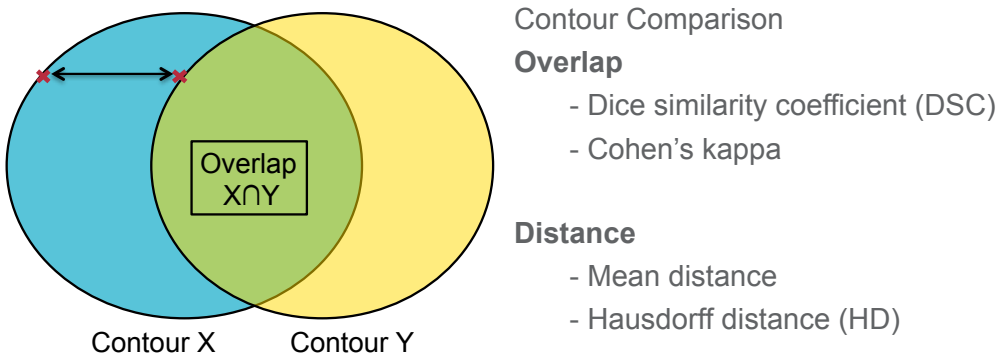

Figure 1.4- Summary of the contour comparison measurements used in Chapters 4-6, a combinations of overlap and distance measurements. The figure shows the comparison of two contours X and Y, where X∩Y is the overlap between contours and x depicts the corresponding point on the two contours.

In addition, I report the Cohen's kappa, a correlation co-efficient of agreement between contours. Rather than simply assessing the overlap, this is a statistical measure of inter-rater reliability [186] . Initially described by Jacob Cohen [187], the purpose of this statistic is to take into account the agreement between observers due to chance alone. For both these measurements, a value of 1 represents complete agreement and overlap between structures with the same

shape and volume, a value of 0 indicates no agreement at all between structures. As well as the difficulty in choosing which measure to use, how to interpret the calculated values remains challenging. Increasing concordance indicates a reduction in interobserver variability when comparing observers or increasing accuracy when comparing to a gold standard. However the level at which the overlap is acceptable is unknown and will vary depending on structure and the area of disagreement.

Distance or dimension measurements assess the difference between the corresponding point or vertex on the surface of two contours, depicted in Figure 1.5. This can be completed for multiple points to give a 'mean distance', which assesses the entire contour. The Hausdorff distance is the maximum distance, and will therefore indicate the greatest discrepancy. Although this may be helpful in the context of margins, outliers bias this value. For distance measurements, decreasing values, where the contours being compared are closer together, indicate a reduction in interobserver variability when comparing observers or increasing accuracy when comparing to a gold standard.

1.6.2 Addressing the 'weakest link'

Given the variation in delineation even amongst experts and the complexities of analysing any differences, measures can be taken to reduce the variation seen. This may be done with the use of training [174, 179, 188] and consensus guidelines [181, 188-190]. Contour consistency is particularly relevant in clinical trials where quality assurance measures are required to ensure that trial outcome data is robust [191, 192].

With CT imaging, although contouring can vary depending on the quality of imaging such as slice thickness or the use of kilovoltage imaging (ref), with MRI there are multiple sequences which may be used and affect the contouring accuracy. In the next two chapters, I assess the impact of MR sequence on clinician and radiographer interobserver variability, radiographer accuracy and autosegmentation accuracy.

Of more clinical relevance is the dosimetric impact of any contour differences [193, 194] and further to that, any effect on clinical outcome. Depending on the position of the discrepancy, the addition of a margin may minimise any influence. Alternatively the difference may be large enough to contribute to a geographical miss where the relevant contour is smaller or increased OAR dose when the contour is too large. This is addressed further in Chapter 6.

1.6.3 The T2*W sequence

At our institution, a set of three gold seeds is implanted in each patient prior to prostate radiotherapy planning. As discussed in Section 1.1.2, as well as improving the accuracy of daily set-up, the gold seeds provide a way of accurately fusing a planning CT and MRI. Specialised sequences for FM visualisation have been discussed in Section 1.2.3. Studies so far for these similar sequences, including the work in Chapter 2, have focussed on accuracy of fiducial detection [50-55].

The T2*W sequence is optimised for marker visualisation using the combination of several gradient-echoes with different echo-times which follow each excitation. This T2*W sequence maximises visualisation of the markers for radiotherapy planning fusion whilst also resulting in a more defined prostate capsule [195]. The use of this sequence for manual contouring and automatic contouring is considered in Chapters 4 and 5 respectively

1.7 Auto-contouring

1.7.1 Benefits of auto-contouring

Manual contouring of the radiotherapy target and OAR is time consuming, with significant intra- and interobserver variability even amongst expert clinicians. The time taken for contouring in prostate radiotherapy planning is considerable given the high proportion of the radiotherapy department workload. In addition, having a clinician re-contour a patient in real-time as part of an adaptive workflow is not feasible on a daily basis.

Auto-contouring (also called auto-segmentation) can reduce the time for contouring [163, 175, 196-198] and when used as a starting point reduces interobserver variability [182, 199]. For real-time ART, auto-contouring will allow rapid re-planning based on real-time images, ultimately without the need for a clinician to be present.

1.7.2 Auto-contouring methods

There are multiple approaches for auto-contouring available, with the most basic techniques using features of the imaging alone such as greyscale measures to create contours. This includes classification-based methods, which use imaging features to classify each voxel for segmentation [200]. In addition, there are statistical model-based methods where contour points are defined by algorithms, used to predict the shape of the organ to be contoured [201-203].

However the more sophisticated, rapidly evolving automated atlas-based segmentation (AABS) software use a pre-existing library of contoured reference atlases (see Figure 1.6) to automatically generate contours on a new set of images using rigid and/or deformable image registration (DIR). Multi-atlas segmentation (MAS) approaches use a number of atlases and are therefore more accurate than single-atlas methods due to the incorporation of anatomical variation. Multi-atlas methods can also be used to simultaneously create auto-contours and a pseudo-CT for MR-only planning (see MR-only planning, Section 1.8) [204, 205].

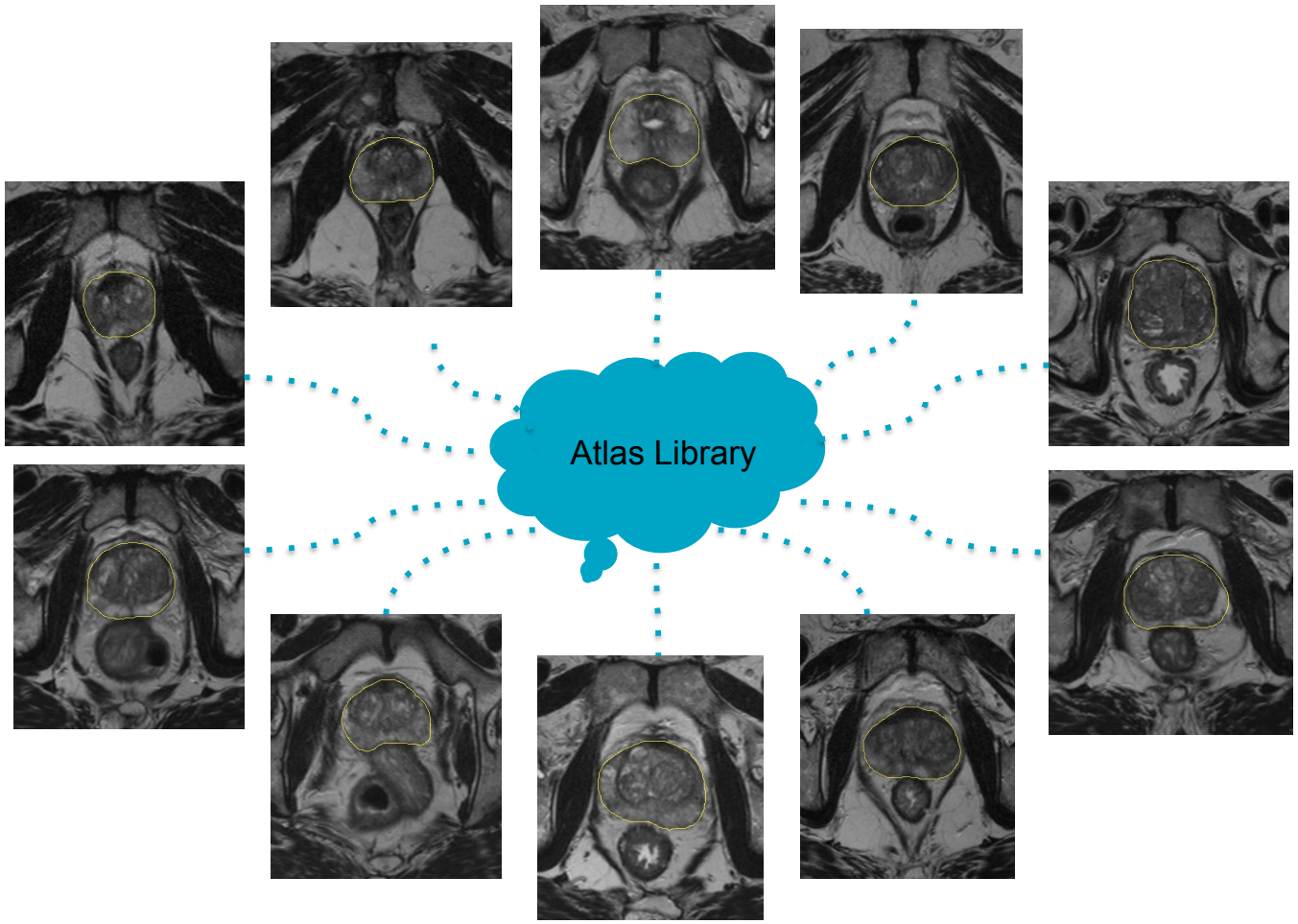

Figure 1.5- A visual representation of an atlas 'library'- T2W imaging for ten patients is shown here. The clinician gold standard STAPLE contour is shown in yellow. The auto-contouring software uses all atlases as directed, using further defined features to increase the influence of the most relevant atlases.

With MAS, summarised in Figure 1.7, the initial step is registration of each atlas to the new test case by rigid registration for alignment of the images, followed by DIR. For the second step, based on the deformation matrix of the image sets, contours are propagated from each atlas onto the test case giving a number of intermediate auto-contours. The final step of 'label fusion' uses methods such as simultaneous truth and performance level estimation (STAPLE) [180], majority vote or selective and iterative method for performance level estimation (SIMPLE) [206] to create the final auto-contour from a number of fused intermediates.

STAPLE contours have the disadvantage of using the segmentation information only, rather than the imaging data. The more discriminating 'patch fusion', the approach for label fusion used in Chapter 5, combines the individual atlas outputs using image intensity [207]. Each atlas is weighted based on the section of imaging or 'patch' surrounding a particular voxel. Each corresponding patch of imaging is used to assess the registration accuracy by comparing the test imaging to the atlas imaging.

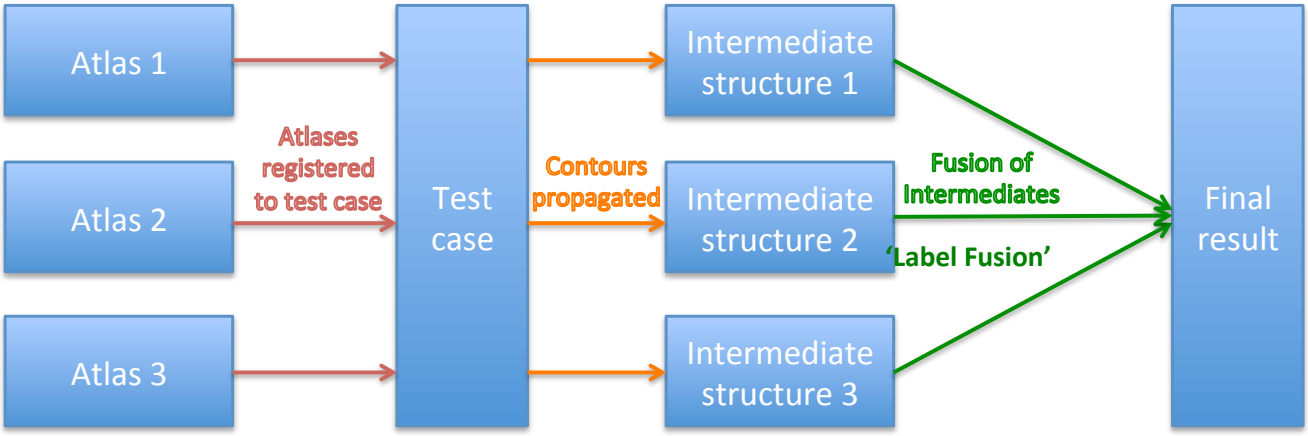

Figure 1.6- Summary of multi-atlas based auto-contouring, using three atlases as an example. The registration step is usually a combination of rigid registration followed by DIR. There are several methods for fusing the intermediate contours, detailed in the text.

MAS itself therefore encompasses a wide array of methods [208]. Improvements in the efficiency of auto-contouring can either be based on the registration stage or the 'label fusion' step. Given the time required to register each atlas to the test case, some research has focussed on identifying the best atlases to select first, prior to the registration step to reduce the computation time [209, 210]. These approaches could save time but also exclude the atlases where inclusion would make the final auto-contour less accurate.

More refined programmes use machine learning [211, 212], where in addition to the label fusion step further weighting can be given to the most relevant atlases, using features in addition to image intensity. Machine learning is also comprised of a large spectrum; the algorithm used in Chapter 5 is a random forest

classifier [208, 213, 214]. This is a type of supervised learning [208], which uses the atlases as training data to create a predictor function or classifier [215] for contouring structures (summarised in Figure 1.8). The features of the voxels in close proximity to the structure border are analysed as this is where the discrepancy will lie. Therefore this step focuses on the 'uncertain' or 'ambiguous' voxels, rather than on the voxels which are classified as definitely 'prostate' or definitely 'not prostate'. The output from the standard label fusion step is combined with the output created by this trained classifier to give the final result.

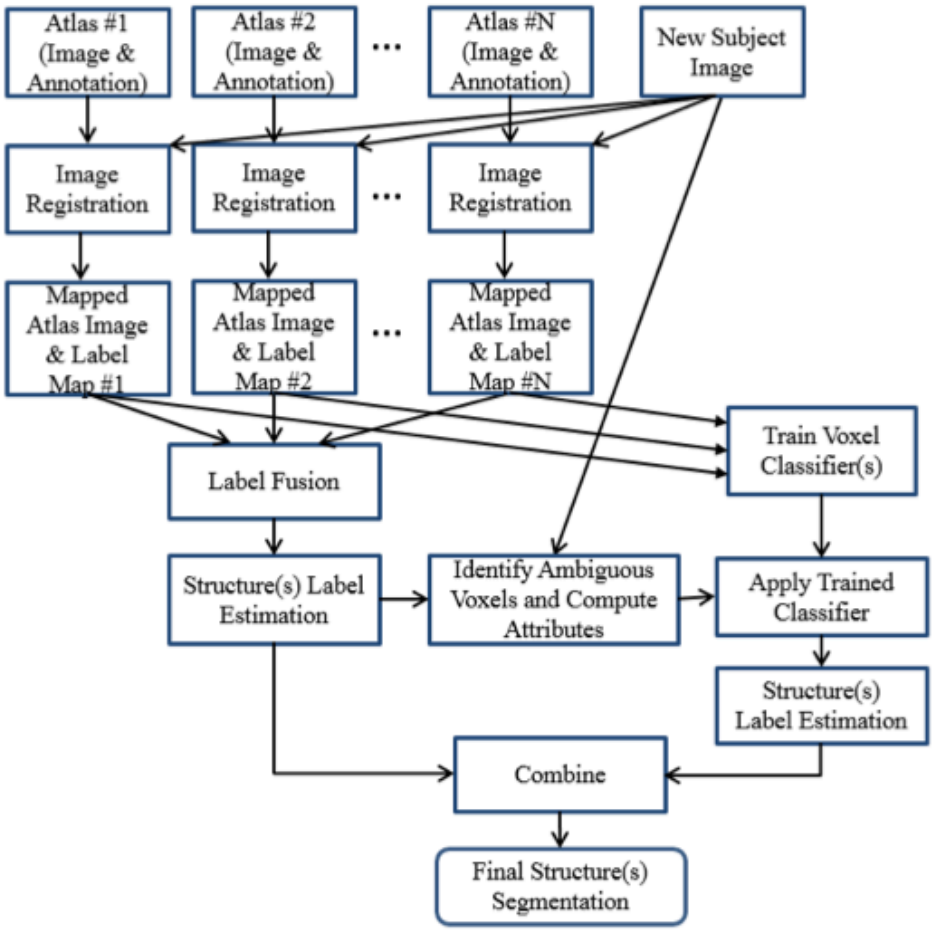

Figure 1.7- Flowchart of multi-atlas label fusion with online random forest model training. Taken from Elekta white paper '*Learning boosted multi-atlas label fusion for atlas-based auto-segmentation (ABAS)*' [215].

1.7.3 Accuracy of auto-contouring

Just as for manual contours, assessment of auto-contours is limited by the lack of ground truth. Accuracy will usually be reported by comparison to a gold standard clinician contour or consensus contour, as discussed in Section 1.6. The optimal number of atlases required for MAS will vary depending on a number of factors including software and the structure to be delineated. Although additional atlases provide more comprehensive anatomical data [216], this is with the computational cost of additional time and the accuracy of auto-contours plateau with increasing atlas numbers [217, 218].

The level of agreement between manually drawn and auto-contours is dependent on the target volume. For prostate radiotherapy planning, in general good concordance is seen for auto-contouring of structures such as the femoral heads and bladder [175, 217, 219-222] with variable results for the rectum [175, 216, 221, 223] and poor concordance is seen for seminal vesicles [224, 225] and penile bulb [216]. Variable results are seen for accuracy of prostate definition with CT, however, as expected, this is improved when MRI is used for auto-delineation [201, 225]. MR optimisation, such as sequences improving the visualisation of the prostate capsule, may further improve auto-contouring and is considered in Chapter 5.

The benefit of auto-contours is dependent on their accuracy, as time is required for clinicians to modify erroneous slices. Langmack et al [163] demonstrated that the time saving achieved for auto-contours correlated to the interobserver variability. Within their study, for structures where DSC is less than 0.65, such

as the SV where there low interobserver agreement, editing an auto-contour can take longer than delineating the structure de novo. This is compounded for structures such as the SV where there is huge anatomical variability between patients and less distinction on imaging.

Although there is potential for these programmes to improve efficiency, current limitations are due to the huge variability in pelvic anatomy and the poor soft tissue contrast previously seen with various CT modalities [175, 226]. In the first instance at least, review and editing of any auto-contours is required [175, 196, 227, 228].

1.7.4 Inter-patient and Intra-patient auto-contouring

In Chapter 5, I consider **inter-patient** auto-contouring, that is, creating contours on the image set of a new patient from scratch.

Issue regarding **intra-patient** contours are discussed in chapter 7. With real-time intrafractional segmentation based on a registration based method where the reference atlas is patient-specific; the DIR and the resultant intra-patient auto-contours are likely to be more accurate [216, 218, 229] and time efficient. Online replanning for the MR-Linac currently uses one prior set of imaging but the auto-segmentation software could also use a multi-atlas approach by combining several of the previous days [218, 229].

Specifically with Monaco ADMIRE (version 2.0, Elekta AB, Stockholm, Sweden), intra-patient contouring is optimised at several stages. Firstly, at

present for CT images only, there is a pre-processing step, which acts to improve registration accuracy in the presence of variable bladder and rectum filling. During the rigid registration step that follows for alignment, there is a 6-degree rigid registration for intrapatient contouring (translations and rotations only) compared to the 12-degree registration used in inter-patient contouring, which also takes into account scaling and shearing of imaging [230]. As a result, online intra-patient contouring is a quicker process.

1.7.5 Specific challenges for MRI

Although initial commercial solutions understandably focussed on CT imaging, with MR-guided radiotherapy the accuracy of auto-contours on MRI is more relevant. There are specific challenges associated with auto-contouring on MRI, most notably the diversity of sequences used. This is significant, as the propagation of contours described and summarised in Figure 1.7 is dependent on the accurate registration of images, which in turn is dependent on similarities between the atlas and novel image set. Using an atlas library consisting of a different sequence may give poor auto-segmentation results [231].

For prostate auto-segmentation, further obstacles related specifically to MRI include variation of the appearance of the prostate capsule and internal intensity, the zones within the prostate and the presence of imaging artefacts. These problems are compounded by differing anatomy and varying bladder and bowel filling.

Just as T2W MRI is the preferred sequence for prostate diagnostic imaging, due to the high signal to noise ratio and contrast within the prostate, this has been the focus for prostate auto-segmentation. However, even within a particular sequence such as T2W imaging, there can be a considerable variation in parameters [231, 232] based on the imaging protocol [43, 233], vendor and field strength. This also creates difficulties when attempting to compare the results from publications. This was addressed by the impartial Prostate MR Image Segmentation (PROMISE12) challenge [232] which evaluated a number of different prostate segmentation algorithms from 11 groups. The algorithms included MAS and active shape based methods, also encompassing fully automatic, semi-automatic and interactive methods. In this study, part of a series of 'Grand Challenges in Medical Imaging', 100 prostate T2W MRI datasets were acquired from four different centres; 50 were used for training, 30 as test cases and the last 20 within a live challenge. The accuracy of auto-contours from each group was assessed using a scoring system by comparison to a reference standard contour using the metrics DSC, the 95% percentile HD, the absolute relative volume difference and average boundary distance. Within this challenge, the automatic shape based models performed the best overall for accuracy and shortest time. Across all methods during the online and live challenge, the DSC ranged from 0.71 to 0.89 and the 95% HD from 5.54 to 11.08 mm. Interestingly within this study, despite the variety of imaging across the four centres providing the T2W images, the performance of the auto-segmentation algorithms was similar regardless of where the imaging was acquired. However, this may be related to the high volume of atlases used, fifty, which would incorporate the variation seen in the test cases.

Segmentation for target tracking must be both rapid and accurate but will depend on image contrast, MR field strength and the method of auto-segmentation used [234]. There continue to be uncertainties about the accuracy of auto-contours, the optimal number of atlases required in the MAS methods, the optimal sequence selection and the impact on the time taken to create a new auto-contour. These are addressed further in Chapter 5.

1.8 MRI-only workflow

1.8.1 Benefits of MR-only workflow

Radiotherapy planning currently uses CT imaging, which provides the relevant electron density required for dose calculations. A mixed CT-MRI workflow requires image co-registration, which incurs the risk of introducing inaccuracy as a result of there being discrepancies in patient positioning, imaging information and anatomical changes between scans. The latter is particularly relevant for prostate patients where bladder and rectal filling can vary between scans, although minimising the time between CT and MR acquisitions can reduce this problem.

The registration error has been estimated to be approximately 2 mm [235], and remains a problem even when using gold fiducial markers to co-register the CT and MRI [236] but the 'real truth' of image registration inaccuracy is unknown. However, the ultimate goal of the MRgRT would be to avoid the need for fiducial markers, which require extra resources for insertion and have associated risks for the patient.

Planning directly on an MRI scan removes the systematic error of co-registration [237] which may be large enough to counteract any advantage from the addition of the MRI into the process. MR-only workflow requires a synthetic CT or pseudo CT [78, 79] to give electron density information required for dose calculations. A major challenge when utilising MRI is geometric distortion, which may be as a result of either machine-related or patient-related factors. Geometric distortion is greater at a distance from the centre of the field, but for accurate dose calculation spatial integrity maintained to the skin surface is essential. This should be minimised using post-processing prior to use of images for planning [78]. Efforts have been made to characterize correction maps but further work is needed to quantify and develop methods for mitigating geometric distortion [238].

1.8.2 MR only workflow – obstacles and solutions

There are a number of methods to create a pseudo/synthetic CT;

1) Tissue segmentation

Following manual or automatic segmentation of an MR dataset, assigning separate densities to air, soft tissue and bone is more accurate than applying a single electron density equivalent to water to the whole body [80, 239] and gives comparable results to the standard method of a planning CT [80, 81]. However bone segmentation is time consuming on standard MR sequences and the value used for assigned densities must also be relevant [80, 82, 240].

2) Atlas mapping method

The first step of this approach [204, 220] involves the generation of MRI and pseudo-CT atlases from patient data. When MRI data from a new patient is acquired, the same deformations required to register the compiled MRI atlas to the new MR images are applied to the pseudo-CT atlas to map the electron density information to the new patient. Comparison of the standard planning CT to the pseudo-CT gives a dose difference of less than 2% [204, 241], in agreement with data from other MR planning studies [239, 242]. This method can also be used to propagate contours [204, 220], however there are limitations, with atypical patient anatomy and the initial step of atlas formation requiring DIR, with the potential errors described above.

3) Voxel method

Statistical models to differentiate the attenuation of tissue types have been investigated to allow the automatic conversion of the MR intensity in each voxel to a Hounsfield unit (HU) [243-245]. By using the information from all voxels, a greater spectrum of attenuation coefficients is obtained for more accurate dose calculation, rather than the limited number used with tissue segmentation [245, 246].

Ultimately, an automated approach for pseudo-CT generation, combining the described methods above, will be more clinically useful. The now commercially available Philips MRCAT (MR for Calculation ATtenuation) creates a pseudo-CT from an mDIXON sequence, acquired with two echo times. The initial step comprises of model-based automatic tissue segmentation into the five classes

of air, fat, water-rich tissue, spongy bone and compact bone. In the second step, each voxel is assigned a pseudo-HU value based on density values. There are a number of factors contributing to dose calculations in this process [247], however the workflow appears to be dosimetrically accurate when compared to CT-based planning [248] and has been implemented clinically in prostate radiotherapy [249].

MR-only workflow is now a realistic prospect in the near future and may improve the accuracy of radiotherapy planning.

1.9 This Thesis

The work presented here is comprised of the pre-clinical studies assessing the various components of online adaptive radiotherapy. In chapter 6, I discuss the treatment of the first patients with MRI-guided radiotherapy within the United Kingdom. Each chapter is relevant for the MRI-guided online workflow and an overview is summarised in Figure 1.9.

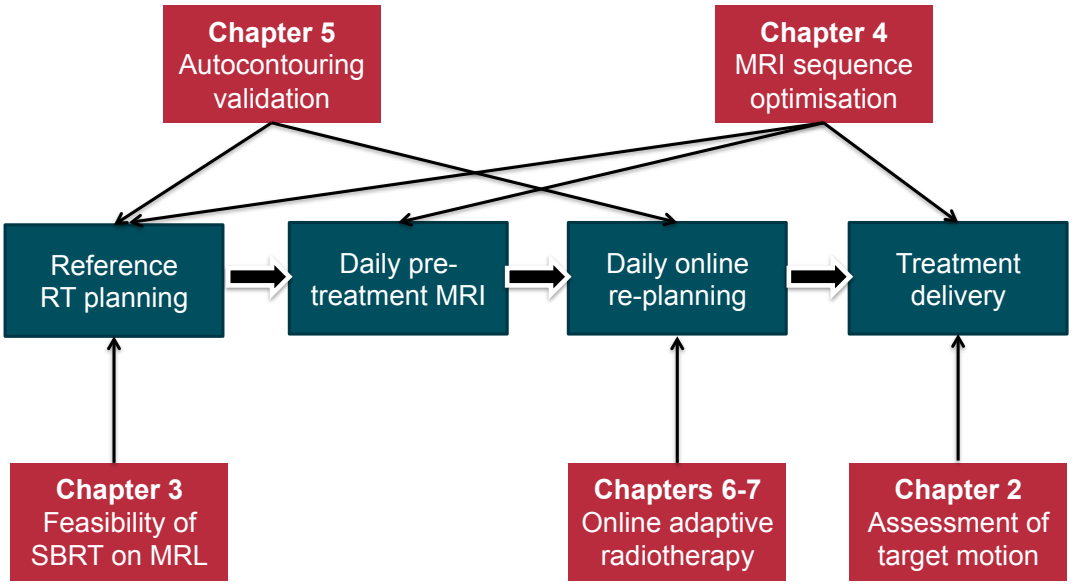

Figure 1.8- Summary of the work presented in this thesis (red boxes) and the relevance for the different stages (green boxes) of online adaptive radiotherapy.

Within the thesis, I have included figures of axial and sagittal planes of MR imaging. The orientation of these figures, with respect to anterior-posterior, left-right and superior-inferior, is as per standard imaging and is summarised below in Figures 1.10 and 1.11.

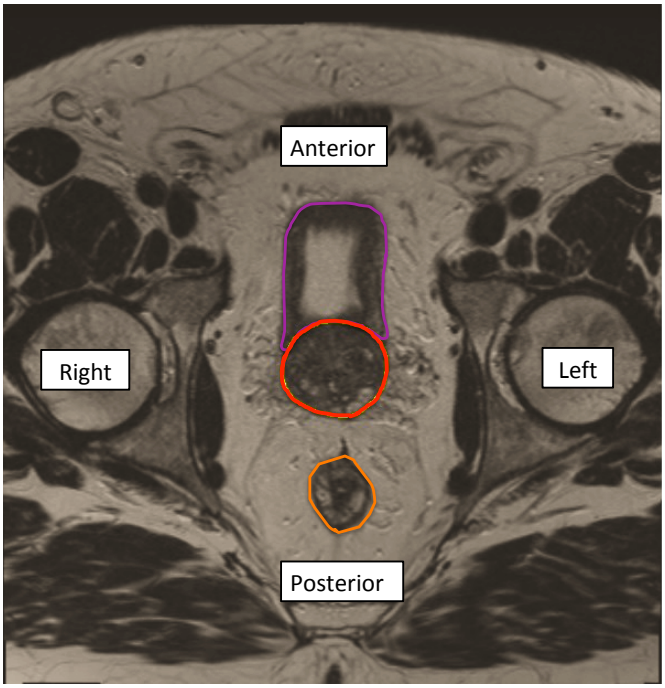

Figure 1.10- An axial plane image of T2-weighted MRI with labels to show the orientation and anatomy of images within the thesis. For this figure: red- prostate, purple- bladder, orange-rectum.

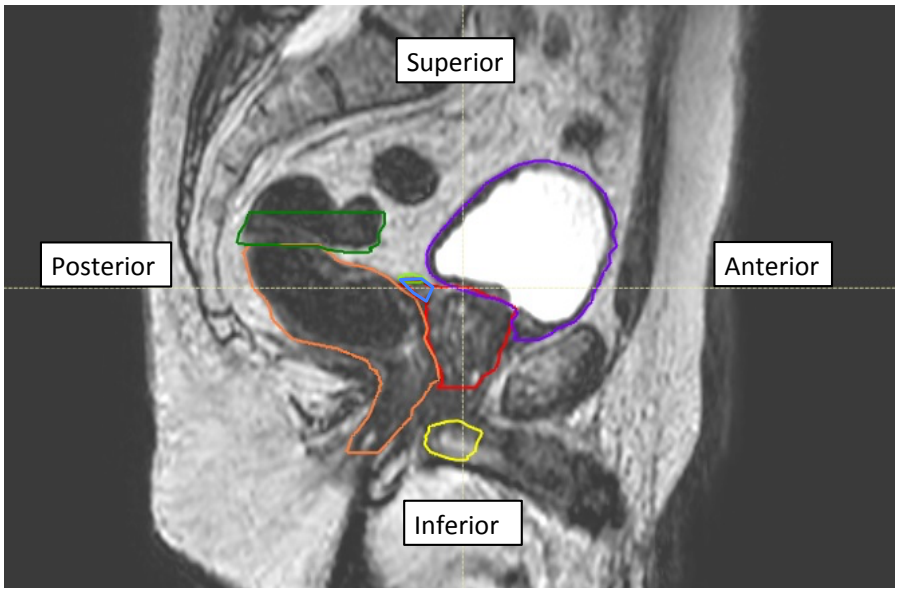

Figure 1.11- A sagittal plane image of T2-weighted MRI with labels to show the orientation and anatomy of images within the thesis. For this figure: red- prostate, purple- bladder, orange- rectum, green- small bowel, blue- seminal vesicles, yellow- penile bulb.

1.10 References

1) Cancer registration statistics, England: 2017. Office for National Statistics April 2019.
2) Hamdy FC, Donovan JL, Lane JA et al. 10-Year Outcomes after Monitoring, Surgery, or Radiotherapy for Localized Prostate Cancer. New England Journal Medicine 2016; 375: 1415-1424.
3) Dasu A, Toma-Dasu I. Prostate alpha/beta revisited -- an analysis of clinical results from 14 168 patients. Acta Oncology 2012; 51: 963-974.
4) Brenner DJ, Martinez AA, Edmundson GK et al. Direct evidence that prostate tumors show high sensitivity to fractionation (low α/β ratio), similar to late-responding normal tissue. International Journal of Radiation Oncology, Biology and Physics 2002; 52: 6-13.
5) Tree AC, Alexander EJ, Van As NJ et al. Biological Dose Escalation and Hypofractionation: What is There to be Gained and How Will it Best be Done? Clinical Oncology 2013; 25: 483-498.
6) Tree AC, Khoo VS, van As NJ, Partridge M. Is biochemical relapse-free survival after profoundly hypofractionated radiotherapy consistent with current radiobiological models? Clinical Oncology (R Coll Radiol) 2014; 26: 216-229.
7) Langen KM, Jones DTL. Organ motion and its management. International Journal of Radiation Oncology, Biology and Physics 2001; 50: 265-278.
8) Aubry J-F, Beaulieu L, Girouard L-M et al. Measurements of intrafraction motion and interfraction and intrafraction rotation of prostate by three-dimensional analysis of daily portal imaging with radiopaque markers. International Journal of Radiation Oncology, Biology and Physics 60: 30-39.
9) Willoughby TR, Kupelian PA, Pouliot J et al. Target localization and real-time tracking using the Calypso 4D localization system in patients with localized prostate cancer. International Journal of Radiation Oncology, Biology and Physics 2006; 65: 528-534.
10) McPartlin AJ, Li XA, Kershaw LE et al. MRI-guided prostate adaptive radiotherapy – A systematic review. Radiotherapy and Oncology 2016; 119: 371-380.
11) Ghilezan MJ, Jaffray DA, Siewerdsen JH et al. Prostate gland motion assessed with cine-magnetic resonance imaging (cine-MRI). International Journal of Radiation Oncology, Biology and Physics 2005; 62: 406-417.
12) Terashima K, Nakamura K, Shioyama Y et al. Can a belly board reduce respiratory-induced prostate motion in the prone position?--assessed by cine-magnetic resonance imaging. Technology in Cancer Research and Treatment 2013; 12: 447-453.
13) Ogino I, Kaneko T, Suzuki R et al. Rectal content and intrafractional prostate gland motion assessed by magnetic resonance imaging. Journal of Radiation Research 2011; 52: 199-207.
14) Nichol AM, Warde PR, Lockwood GA et al. A cinematic magnetic resonance imaging study of milk of magnesia laxative and an antiflatulent diet to reduce intrafraction prostate motion. International Journal of Radiation Oncology, Biology and Physics 2010; 77: 1072-1078.
15) Mah D, Freedman G, Milestone B et al. Measurement of intrafractional prostate motion using magnetic resonance imaging. International Journal of Radiation Oncology, Biology and Physics 2002; 54: 568-575.

16) Padhani AR, Khoo VS, Suckling J et al. Evaluating the effect of rectal distension and rectal movement on prostate gland position using cine MRI. International Journal of Radiation Oncology, Biology and Physics 1999; 44: 525-533.
17) Langen KM, Willoughby TR, Meeks SL et al. Observations on Real-Time Prostate Gland Motion Using Electromagnetic Tracking. International Journal of Radiation Oncology, Biology and Physics 2008; 71: 1084-1090.
18) Lovelock DM, Messineo AP, Cox BW et al. Continuous Monitoring and Intrafraction Target Position Correction During Treatment Improves Target Coverage for Patients Undergoing SBRT Prostate Therapy. International Journal of Radiation Oncology, Biology and Physics 2015; 91: 588-594.
19) Colvill E, Booth JT, O'Brien RT et al. Multileaf Collimator Tracking Improves Dose Delivery for Prostate Cancer Radiation Therapy: Results of the First Clinical Trial. International Journal of Radiation Oncology, Biology and Physics 2015; 92: 1141-1147.
20) Keall PJ, Ng JA, Juneja P et al. Real-Time 3D Image Guidance Using a Standard LINAC: Measured Motion, Accuracy, and Precision of the First Prospective Clinical Trial of Kilovoltage Intrafraction Monitoring–Guided Gating for Prostate Cancer Radiation Therapy. International Journal of Radiation Oncology, Biology and Physics 2016; 94: 1015-1021.
21) Wortel RC, Incrocci L, Pos FJ et al. Acute Toxicity After Image-Guided Intensity Modulated Radiation Therapy Compared to 3D Conformal Radiation Therapy in Prostate Cancer Patients. International Journal of Radiation Oncology, Biology and Physics 2015; 91: 737-744.
22) Singh J, Greer PB, White MA et al. Treatment-Related Morbidity in Prostate Cancer: A Comparison of 3-Dimensional Conformal Radiation Therapy With and Without Image Guidance Using Implanted Fiducial Markers. International Journal of Radiation Oncology, Biology and Physics 2013; 85: 1018-1023.
23) van der Heide UA, Kotte AN, Dehnad H et al. Analysis of fiducial marker-based position verification in the external beam radiotherapy of patients with prostate cancer. Radiotherapy and Oncology 2007; 82: 38-45.
24) Beltran C, Herman MG, Davis BJ. Planning target margin calculations for prostate radiotherapy based on intrafraction and interfraction motion using four localization methods. Int J Radiat Oncol Biol Phys 2008; 70: 289-295.
25) Litzenberg DW, Balter JM, Hadley SW et al. Influence of intrafraction motion on margins for prostate radiotherapy. International Journal of Radiation Oncology, Biology and Physics 2006; 65: 548-553.
26) Kontaxis C, Bol GH, Lagendijk JJW, Raaymakers BW. Towards adaptive IMRT sequencing for the MR-linac. Physics in Medicine and Biology 2015; 60: 2493.
27) Wang Y, Mazur TR, Park JC et al. Development of a fast Monte Carlo dose calculation system for online adaptive radiation therapy quality assurance. Physics in Medicine & Biology 2017; 62: 4970.
28) Fast MF, Kamerling CP, Ziegenhein P et al. Assessment of MLC tracking performance during hypofractionated prostate radiotherapy using real-time dose reconstruction. Physics in Medicine and Biology 2016; 61: 1546.
29) Kamerling C, Fast M, Ziegenhein P et al. TH-CD-202-12: Online Inter-Beam Replanning Based On Real-Time Dose Reconstruction. Medical Physics 2016; 43: 3879-3879.

30) Villeirs GM, Vaerenbergh K, Vakaet L et al. Interobserver Delineation Variation Using CT versus Combined CT + MRI in Intensity–Modulated Radiotherapy for Prostate Cancer. Strahlentherapie und Onkologie 2005; 181: 424-430.
31) Debois M, Oyen R, Maes F et al. The contribution of magnetic resonance imaging to the three-dimensional treatment planning of localized prostate cancer. International Journal of Radiation Oncology, Biology and Physics1999; 45: 857-865.
32) Steenbakkers RJHM, Deurloo KEI, Nowak PJCM et al. Reduction of dose delivered to the rectum and bulb of the penis using MRI delineation for radiotherapy of the prostate. International Journal of Radiation Oncology, Biology and Physics 2003; 57: 1269-1279.
33) Fütterer JJ, Heijmink SWTPJ, Scheenen TWJ et al. Prostate Cancer Localization with Dynamic Contrast-enhanced MR Imaging and Proton MR Spectroscopic Imaging. Radiology 2006; 241: 449-458.
34) Haider MA, van der Kwast TH, Tanguay J et al. Combined T2-Weighted and Diffusion-Weighted MRI for Localization of Prostate Cancer. American Journal of Roentgenology 2007; 189: 323-328.
35) Scheidler J, Hricak H, Vigneron DB et al. Prostate Cancer: Localization with Three-dimensional Proton MR Spectroscopic Imaging—Clinicopathologic Study. Radiology 1999; 213: 473-480.
36) Isebaert S, Van den Bergh L, Haustermans K et al. Multiparametric MRI for prostate cancer localization in correlation to whole-mount histopathology. Journal of Magnetic Resonance Imaging 2013; 37: 1392-1401.
37) Wu L-M, Xu J-R, Ye Y-Q et al. The Clinical Value of Diffusion-Weighted Imaging in Combination With T2-Weighted Imaging in Diagnosing Prostate Carcinoma: A Systematic Review and Meta-Analysis. American Journal of Roentgenology 2012; 199: 103-110.
38) Turkbey B, Pinto PA, Mani H et al. Prostate Cancer: Value of Multiparametric MR Imaging at 3 T for Detection—Histopathologifc Correlation. Radiology 2010; 255: 89-99.
39) deSouza NM, Riches SF, VanAs NJ et al. Diffusion-weighted magnetic resonance imaging: a potential non-invasive marker of tumour aggressiveness in localized prostate cancer. Clinical Radiology 2008; 63: 774-782.
40) Henderson DR, de Souza NM, Thomas K et al. Nine-year Follow-up for a Study of Diffusion-weighted Magnetic Resonance Imaging in a Prospective Prostate Cancer Active Surveillance Cohort. European Urology.
41) de Rooij M, Hamoen EHJ, Fütterer JJ et al. Accuracy of Multiparametric MRI for Prostate Cancer Detection: A Meta-Analysis. American Journal of Roentgenology 2014; 202: 343-351.
42) Riches SF, Payne GS, Morgan VA et al. MRI in the Detection of Prostate Cancer: Combined Apparent Diffusion Coefficient, Metabolite Ratio, and Vascular Parameters. American Journal of Roentgenology 2009; 193: 1583-1591.
43) Barentsz JO, Richenberg J, Clements R et al. ESUR prostate MR guidelines 2012. European Radiology 2012; 22: 746-757.
44) Fütterer JJ, Engelbrecht MR, Jager GJ et al. Prostate cancer: comparison of local staging accuracy of pelvic phased-array coil alone versus

integrated endorectal–pelvic phased-array coils. European Radiology 2006; 17: 1055-1065.
45) Coakley FV, Kurhanewicz J, Lu Y et al. Prostate Cancer Tumor Volume: Measurement with Endorectal MR and MR Spectroscopic Imaging. Radiology 2002; 223: 91-97.
46) Rosenkrantz AB, Mendrinos S, Babb JS, Taneja SS. Prostate Cancer Foci Detected on Multiparametric Magnetic Resonance Imaging are Histologically Distinct From Those Not Detected. The Journal of Urology 2012; 187: 2032-2038.
47) Langer DL, Kwast THvd, Evans AJ et al. Intermixed Normal Tissue within Prostate Cancer: Effect on MR Imaging Measurements of Apparent Diffusion Coefficient and T2—Sparse versus Dense Cancers. Radiology 2008; 249: 900-908.
48) Parker CC, Damyanovich A, Haycocks T et al. Magnetic resonance imaging in the radiation treatment planning of localized prostate cancer using intra-prostatic fiducial markers for computed tomography co-registration. Radiotherapy and Oncology 2003; 66: 217-224.
49) Meyer E, Raupach R, Lell M et al. Normalized metal artifact reduction (NMAR) in computed tomography. Medical Physics 2010; 37: 5482-5493.
50) Dinis Fernandes C, Dinh CV, Steggerda MJ et al. Prostate fiducial marker detection with the use of multi-parametric magnetic resonance imaging. Physics and Imaging in Radiation Oncology 2017; 1: 14-20.
51) Schieda N, Avruch L, Shabana WM, Malone SC. Multi-echo gradient recalled echo imaging of the pelvis for improved depiction of brachytherapy seeds and fiducial markers facilitating radiotherapy planning and treatment of prostatic carcinoma. Journal of Magnetic Resonance Imaging 2015; 41: 715-720.
52) Ghose S, Mitra J, Rivest-Henault D et al. MRI-alone radiation therapy planning for prostate cancer: Automatic fiducial marker detection. Medical Physics 2016; 43: 2218.
53) Gustafsson C, Korhonen J, Persson E et al. Registration free automatic identification of gold fiducial markers in MRI target delineation images for prostate radiotherapy. Medical Physics 2017; n/a-n/a.
54) Zijlstra F, Moerland MA, van der Voort van Zyp JRN et al. Challenges in MR-only seed localization for postimplant dosimetry in permanent prostate brachytherapy. Medical Physics 2017.
55) Maspero M, van den Berg CAT, Zijlstra F et al. Evaluation of an automatic MR-based gold fiducial marker localisation method for MR-only prostate radiotherapy. Physics in Medicine and Biology 2017; 62: 7981-8002.
56) Martin N, Malfair D, Zhao Y et al. Comparison of MERGE and axial T2-weighted fast spin-echo sequences for detection of multiple sclerosis lesions in the cervical spinal cord. AJR Am J Roentgenol 2012; 199: 157-162.
57) Held P, Dorenbeck U, Seitz J et al. MRI of the abnormal cervical spinal cord using 2D spoiled gradient echo multiecho sequence (MEDIC) with magnetization transfer saturation pulse. A T2* weighted feasibility study. J Neuroradiol 2003; 30: 83-90.
58) Pathmanathan A, Schmidt M, Brand D et al. Improving fiducial and prostate capsule visualisation for radiotherapy planning using MRI. Journal of Applied Clinical Medical Physics 2019 Mar; 20(3):27-36.

59) Schenck JF. The role of magnetic susceptibility in magnetic resonance imaging: MRI magnetic compatibility of the first and second kinds. Medical Physics 1996; 23: 815-850.
60) Jonsson JH, Garpebring A, Karlsson MG, Nyholm T. Internal fiducial markers and susceptibility effects in MRI-simulation and measurement of spatial accuracy. International Journal of Radiation Oncology, Biology and Physics 2012; 82: 1612-1618.
61) Zeng GG, McGowan TS, Larsen TM et al. Calcifications Are Potential Surrogates for Prostate Localization in Image-Guided Radiotherapy. International Journal of Radiation Oncology, Biology and Physics 2008; 72: 963-966.
62) Cellini N, Morganti AG, Mattiucci GC et al. Analysis of intraprostatic failures in patients treated with hormonal therapy and radiotherapy: implications for conformal therapy planning. Int J Radiat Oncol Biol Phys 2002; 53: 595-599.
63) Arrayeh E, Westphalen AC, Kurhanewicz J et al. Does local recurrence of prostate cancer after radiation therapy occur at the site of primary tumor? Results of a longitudinal MRI and MRSI study. International Journal of Radiation Oncology, Biology, Physics 2012; 82: e787-e793.
64) Kuban DA, Levy LB, Cheung MR et al. Long-Term Failure Patterns and Survival in a Randomized Dose-Escalation Trial for Prostate Cancer. Who Dies of Disease International Journal of Radiation Oncology, Biology and Physics 2011; 79: 1310-1317.
65) Nutting CM, Corbishley CM, Sanchez-Nieto B et al. Potential improvements in the therapeutic ratio of prostate cancer irradiation: dose escalation of pathologically identified tumour nodules using intensity modulated radiotherapy. The British Journal of Radiology 2002; 75: 151-161.
66) Viani GA, Stefano EJ, Afonso SL. Higher-Than-Conventional Radiation Doses in Localized Prostate Cancer Treatment: A Meta-analysis of Randomized, Controlled Trials. International Journal of Radiation Oncology, Biology and Physics 2009; 74: 1405-1418.
67) Zietman AL, DeSilvio ML, Slater JD, et al. Comparison of conventional-dose vs high-dose conformal radiation therapy in clinically localized adenocarcinoma of the prostate: A randomized controlled trial. JAMA 2005; 294: 1233-1239.
68) Groenendaal G, van Vulpen M, Pereboom SR et al. The effect of hormonal treatment on conspicuity of prostate cancer: Implications for focal boosting radiotherapy. Radiotherapy and Oncology 103: 233-238.
69) Pathmanathan AU, Alexander EJ, Huddart RA, Tree AC. The delineation of intraprostatic boost regions for radiotherapy using multimodality imaging. Future Oncology 2016; 12: 2495-2511.
70) Lips IM, van der Heide UA, Haustermans K et al. Single blind randomized Phase III trial to investigate the benefit of a focal lesion ablative microboost in prostate cancer (FLAME-trial): study protocol for a randomized controlled trial. Trials 2011; 12: 255-255.
71) Monninkhof EM, van Loon JWL, van Vulpen M et al. Standard whole prostate gland radiotherapy with and without lesion boost in prostate cancer: Toxicity in the FLAME randomized controlled trial. Radiotherapy and Oncology 2018; 127: 74-80.

72) Yang Y, Cao M, Sheng K et al. Longitudinal diffusion MRI for treatment response assessment: Preliminary experience using an MRI-guided tri-cobalt 60 radiotherapy system. Medical Physics 2016; 43: 1369-1373.
73) Ling CC, Humm J, Larson S et al. Towards multidimensional radiotherapy (MD-CRT): biological imaging and biological conformality. International Journal of Radiation Oncology, Biology and Physics 2000; 47: 551-560.
74) van As NJ, de Souza NM, Riches SF et al. A Study of Diffusion-Weighted Magnetic Resonance Imaging in Men with Untreated Localised Prostate Cancer on Active Surveillance. European Urology 2009; 56: 981-988.
75) Park SY, Kim CK, Park BK et al. Early Changes in Apparent Diffusion Coefficient From Diffusion-Weighted MR Imaging During Radiotherapy for Prostate Cancer. International Journal of Radiation Oncology, Biology and Physics 2012; 83: 749-755.
76) liu L, Wu N, Ouyang H et al. Diffusion-weighted MRI in early assessment of tumour response to radiotherapy in high-risk prostate cancer. The British Journal of Radiology 2014; 87: 20140359.
77) Decker G, Mürtz P, Gieseke J et al. Intensity-modulated radiotherapy of the prostate: Dynamic ADC monitoring by DWI at 3.0 T. Radiotherapy and Oncology 2014; 113: 115-120.
78) Schmidt AM, Payne SG. Radiotherapy planning using MRI. Physics in Medicine and Biology 2015; 60: R323.
79) Nyholm T, Jonsson J. Counterpoint: Opportunities and Challenges of a Magnetic Resonance Imaging–Only Radiotherapy Work Flow. Seminars in Radiation Oncology 2014; 24: 175-180.
80) Jonsson JH, Karlsson MG, Karlsson M, Nyholm T. Treatment planning using MRI data: an analysis of the dose calculation accuracy for different treatment regions. Radiation Oncology (London, England) 2010; 5: 62-62.
81) Korsholm ME, Waring LW, Edmund JM. A criterion for the reliable use of MRI-only radiotherapy. Radiation Oncology (London, England) 2014; 9: 16-16.
82) Kim J, Garbarino K, Schultz L et al. Dosimetric evaluation of synthetic CT relative to bulk density assignment-based magnetic resonance-only approaches for prostate radiotherapy. Radiation Oncology (London, England) 2015; 10: 239.
83) Dearnaley DP, Jovic G, Syndikus I et al. Escalated-dose versus control-dose conformal radiotherapy for prostate cancer: long-term results from the MRC RT01 randomised controlled trial. The Lancet Oncology 2014; 15: 464-473.
84) Dearnaley D, Syndikus I, Mossop H et al. Conventional versus hypofractionated high-dose intensity-modulated radiotherapy for prostate cancer: 5-year outcomes of the randomised, non-inferiority, phase 3 CHHiP trial. The Lancet Oncology 2016.
85) Fowler J, Chappell R, Ritter M. Is α/β for prostate tumors really low? International Journal of Radiation Oncology, Biology and Physics 2001; 50: 1021-1031.
86) Miralbell R, Roberts SA, Zubizarreta E, Hendry JH. Dose-Fractionation Sensitivity of Prostate Cancer Deduced From Radiotherapy Outcomes of 5,969 Patients in Seven International Institutional Datasets: α/β = 1.4 (0.9–2.2) Gy. International Journal of Radiation Oncology, Biology and Physics 2012; 82: e17-e24.

87) Catton CN, Lukka H, Gu C-S et al. Randomized Trial of a Hypofractionated Radiation Regimen for the Treatment of Localized Prostate Cancer. Journal of Clinical Oncology 2017; 35: 1884-1890.
88) Incrocci L, Wortel RC, Alemayehu WG et al. Hypofractionated versus conventionally fractionated radiotherapy for patients with localised prostate cancer (HYPRO): final efficacy results from a randomised, multicentre, open-label, phase 3 trial. The Lancet Oncology 2016.
89) Kothari G, Loblaw A, Tree AC et al. Stereotactic Body Radiotherapy for Primary Prostate Cancer. Technology in cancer research & treatment 2018; 17: 1533033818789633-1533033818789633.
90) Loblaw A, Cheung P, D'Alimonte L et al. Prostate stereotactic ablative body radiotherapy using a standard linear accelerator: Toxicity, biochemical, and pathological outcomes. Radiotherapy and Oncology 2013; 107: 153-158.
91) King CR, Brooks JD, Gill H, Presti Jr JC. Long-Term Outcomes From a Prospective Trial of Stereotactic Body Radiotherapy for Low-Risk Prostate Cancer. International Journal of Radiation Oncology, Biology and Physics 2012; 82: 877-882.
92) Boike TP, Lotan Y, Cho LC et al. Phase I Dose-Escalation Study of Stereotactic Body Radiation Therapy for Low- and Intermediate-Risk Prostate Cancer. Journal of Clinical Oncology 2011; 29: 2020-2026.
93) Hannan R, Tumati V, Xie XJ et al. Stereotactic body radiation therapy for low and intermediate risk prostate cancer-Results from a multi-institutional clinical trial. European Journal Cancer 2016; 59: 142-151.
94) Madsen BL, Hsi RA, Pham HT et al. Stereotactic hypofractionated accurate radiotherapy of the prostate (SHARP), 33.5 Gy in five fractions for localized disease: first clinical trial results. International Journal of Radiation Oncology, Biology and Physics 2007; 67: 1099-1105.
95) King CR, Freeman D, Kaplan I et al. Stereotactic body radiotherapy for localized prostate cancer: Pooled analysis from a multi-institutional consortium of prospective phase II trials. Radiotherapy and Oncology 2013; 109: 217-221.
96) Widmark A, Gunnlaugsson A, Beckman L et al. OC-0599: Ultrahypofractionation for prostate cancer: Outcome from the Scandinavian phase 3 HYPO-RT-PC trial. Radiotherapy and Oncology 2018; 127: S314.
97) Widmark A, Gunnlaugsson A, Beckman L et al. Extreme Hypofractionation versus Conventionally Fractionated Radiotherapy for Intermediate Risk Prostate Cancer: Early Toxicity Results from the Scandinavian Randomized Phase III Trial "HYPO-RT-PC International Journal of Radiation Oncology, Biology and Physics 2016; 96: 938-939.
98) Brand DH, Tree AC, Ostler P et al. Intensity-modulated fractionated radiotherapy versus stereotactic body radiotherapy for prostate cancer (PACE-B): acute toxicity findings from an international, randomised, open-label, phase 3, non-inferiority trial. Lancet Oncol 2019; 20: 1531-1543.
99) Hoskin P, Rojas A, Ostler P et al. High-dose-rate brachytherapy with two or three fractions as monotherapy in the treatment of locally advanced prostate cancer. Radiotherapy and Oncology 2014; 112: 63-67.
100) Hoskin P, Rojas A, Ostler P et al. Single-dose high-dose-rate brachytherapy compared to two and three fractions for locally advanced prostate cancer. Radiotherapy and Oncology 2017; 124: 56-60.

101) Hoskin P, Rojas A, Ostler P et al. High-dose-rate brachytherapy alone given as two or one fraction to patients for locally advanced prostate cancer: Acute toxicity. Radiotherapy and Oncology 2014; 110: 268-271.
102) Prada PJ, Jimenez I, González-Suárez H et al. High-dose-rate interstitial brachytherapy as monotherapy in one fraction and transperineal hyaluronic acid injection into the perirectal fat for the treatment of favorable stage prostate cancer: Treatment description and preliminary results. Brachytherapy 2012; 11: 105-110.
103) Krauss DJ, Ye H, Martinez AA et al. Favorable Preliminary Outcomes for Men With Low- and Intermediate-risk Prostate Cancer Treated With 19-Gy Single-fraction High-dose-rate Brachytherapy. International Journal of Radiation Oncology, Biology and Physics 2017; 97: 98-106.
104) Dankulchai P, Alonzi R, Lowe GJ et al. Optimal source distribution for focal boosts using high dose rate (HDR) brachytherapy alone in prostate cancer. Radiotherapy and Oncology 2014; 113: 121-125.
105) Siddiqui ZA, Gustafson GS, Ye H et al. Five-Year Outcomes of a Single-Institution Prospective Trial of 19-Gy Single-Fraction High-Dose-Rate Brachytherapy for Low- and Intermediate-Risk Prostate Cancer. International Journal of Radiation Oncology, Biology and Physics 2019; 104: 1038-1044.
106) Tharmalingam H, Tsang Y, Ostler P et al. Single dose high-dose rate (HDR) brachytherapy (BT) as monotherapy for localised prostate cancer: Early results of a UK national cohort study. Radiotherapy and Oncology 2020.
107) Morton G, McGuffin M, Chung HT et al. Prostate high dose-rate brachytherapy as monotherapy for low and intermediate risk prostate cancer: Efficacy results from a randomized phase II clinical trial of one fraction of 19 Gy or two fractions of 13.5 Gy. Radiotherapy and Oncology 2020; 146: 90-96.
108) Morris WJ, Keyes M, Spadinger I et al. Population-based 10-year oncologic outcomes after low-dose-rate brachytherapy for low-risk and intermediate-risk prostate cancer. Cancer 2013; 119: 1537-1546.
109) Zaorsky NG, Davis BJ, Nguyen PL et al. The evolution of brachytherapy for prostate cancer. Nat Rev Urol 2017; 14: 415-439.
110) Morris WJ, Tyldesley S, Rodda S et al. Androgen Suppression Combined with Elective Nodal and Dose Escalated Radiation Therapy (the ASCENDE-RT Trial): An Analysis of Survival Endpoints for a Randomized Trial Comparing a Low-Dose-Rate Brachytherapy Boost to a Dose-Escalated External Beam Boost for High- and Intermediate-risk Prostate Cancer. International Journal of Radiation Oncology, Biology and Physics 2017; 98: 275-285.
111) Rodda S, Tyldesley S, Morris WJ et al. ASCENDE-RT: An Analysis of Treatment-Related Morbidity for a Randomized Trial Comparing a Low-Dose-Rate Brachytherapy Boost with a Dose-Escalated External Beam Boost for High- and Intermediate-Risk Prostate Cancer. International Journal of Radiation Oncology, Biology and Physics 2017; 98: 286-295.
112) Henderson D, Tree A, van As N. Single Fraction External Beam Radiotherapy for Localised Prostate Cancer: a Planning Study. Clinical Oncology 2017; 29: e87.

113) Choudhury A, Budgell G, MacKay R et al. The Future of Image-guided Radiotherapy. Clinical Oncology 2017; 29: 662-666.
114) Raaymakers BW, Lagendijk JJW, Overweg J et al. Integrating a 1.5 T MRI scanner with a 6 MV accelerator: proof of concept. Physics in Medicine and Biology 2009; 54: N229.
115) Mutic S, Dempsey JF. The ViewRay System: Magnetic Resonance–Guided and Controlled Radiotherapy. Seminars in Radiation Oncology 2014; 24: 196-199.
116) Keall PJ, Barton M, Crozier S. The Australian Magnetic Resonance Imaging-Linac Program. Seminars in Radiation Oncology 2014; 24: 203-206.
117) Fallone BG, Murray B, Rathee S et al. First MR images obtained during megavoltage photon irradiation from a prototype integrated linac-MR system. Medical Physics 2009; 36: 2084-2088.
118) Noel CE, Parikh PJ, Spencer CR et al. Comparison of onboard low-field magnetic resonance imaging versus onboard computed tomography for anatomy visualization in radiotherapy. Acta Oncologica 2015; 54: 1474-1482.
119) Raaijmakers AJE, Raaymakers BW, Meer Svd, Lagendijk JJW. Integrating a MRI scanner with a 6 MV radiotherapy accelerator: impact of the surface orientation on the entrance and exit dose due to the transverse magnetic field. Physics in Medicine and Biology 2007; 52: 929.
120) Raaijmakers AJE, Raaymakers BW, Lagendijk JJW. Magnetic-field-induced dose effects in MR-guided radiotherapy systems: dependence on the magnetic field strength. Physics in Medicine and Biology 2008; 53: 909.
121) Wooten HO, Green O, Yang M et al. Quality of Intensity Modulated Radiation Therapy Treatment Plans Using a ^{60}Co Magnetic Resonance Image Guidance Radiation Therapy System. International Journal of Radiation Oncology, Biology and Physics 2015; 92: 771-778.
122) Pathmanathan A, Nill S, Oelfke U et al. Stereotactic Body Radiotherapy (SBRT) for Localised Prostate Cancer on the Magnetic Resonance Linac. Clinical Oncology 2017; 29: e88.
123) Lagendijk JJW, Raaymakers BW, Raaijmakers AJE et al. MRI/linac integration. Radiotherapy and Oncology 2008; 86: 25-29.
124) Kerkmeijer LGW, Fuller CD, Verkooijen HM et al. The MRI-Linear Accelerator Consortium: Evidence-Based Clinical Introduction of an Innovation in Radiation Oncology Connecting Researchers, Methodology, Data Collection, Quality Assurance, and Technical Development. Frontiers in oncology 2016; 6: 215-215.
125) Engels B, Soete G, Verellen D, Storme G. Conformal Arc Radiotherapy for Prostate Cancer: Increased Biochemical Failure in Patients With Distended Rectum on the Planning Computed Tomogram Despite Image Guidance by Implanted Markers. International Journal of Radiation Oncology, Biology and Physics 2009; 74: 388-391.
126) Mohan R, Zhang X, Wang H et al. Use of deformed intensity distributions for on-line modification of image-guided IMRT to account for interfractional anatomic changes. International Journal of Radiation Oncology, Biology and Physics 2005; 61: 1258-1266.
127) Acharya S, Fischer-Valuck BW, Kashani R et al. Online Magnetic Resonance Image Guided Adaptive Radiation Therapy: First Clinical

Applications. International Journal of Radiation Oncology, Biology and Physics 2016; 94: 394-403.
128) Bol GH, Lagendijk JJW, Raaymakers BW. Virtual couch shift (VCS): accounting for patient translation and rotation by online IMRT re-optimization. Physics in Medicine and Biology 2013; 58: 2989.
129) Shimizu S, Nishioka K, Suzuki R et al. Early results of urethral dose reduction and small safety margin in intensity-modulated radiation therapy (IMRT) for localized prostate cancer using a real-time tumor-tracking radiotherapy (RTRT) system. Radiation Oncology (London, England) 2014; 9: 118-118.
130) Bohoudi O, Bruynzeel AME, Senan S et al. Fast and robust online adaptive planning in stereotactic MR-guided adaptive radiation therapy (SMART) for pancreatic cancer. Radiotherapy and Oncology 2017.
131) Tetar SU, Bruynzeel AME, Lagerwaard FJ et al. Clinical implementation of magnetic resonance imaging guided adaptive radiotherapy for localized prostate cancer. Physics and Imaging in Radiation Oncology 2019; 9: 69-76.
132) King BL, Butler WM, Merrick GS et al. Electromagnetic Transponders Indicate Prostate Size Increase Followed by Decrease During the Course of External Beam Radiation Therapy. International Journal of Radiation Oncology, Biology and Physics 2011; 79: 1350-1357.
133) Nichol AM, Brock KK, Lockwood GA et al. A magnetic resonance imaging study of prostate deformation relative to implanted gold fiducial markers. International Journal of Radiation Oncology, Biology and Physics 2007; 67: 48-56.
134) Gunnlaugsson A, Kjellén E, Hagberg O et al. Change in prostate volume during extreme hypo-fractionation analysed with MRI. Radiation Oncology 2014; 9: 1-6.
135) Kerkhof EM, Put RWvd, Raaymakers BW et al. Variation in target and rectum dose due to prostate deformation: an assessment by repeated MR imaging and treatment planning. Physics in Medicine and Biology 2008; 53: 5623.
136) Peng C, Ahunbay E, Chen G et al. Characterizing Interfraction Variations and Their Dosimetric Effects in Prostate Cancer Radiotherapy. International Journal of Radiation Oncology, Biology and Physics 2011; 79: 909-914.
137) Kupelian P, Willoughby T, Mahadevan A et al. Multi-institutional clinical experience with the Calypso System in localization and continuous, real-time monitoring of the prostate gland during external radiotherapy. International Journal of Radiation Oncology, Biology and Physics 2007; 67: 1088-1098.
138) Nijkamp J, Pos FJ, Nuver TT et al. Adaptive Radiotherapy for Prostate Cancer Using Kilovoltage Cone-Beam Computed Tomography: First Clinical Results. International Journal of Radiation Oncology, Biology and Physics 2008; 70: 75-82.
139) Chen W, Gemmel A, Rietzel E. A patient-specific planning target volume used in ‘plan of the day’ adaptation for interfractional motion mitigation. Journal of Radiation Research 2013; 54: i82-i90.
140) Xia P, Qi P, Hwang A et al. Comparison of three strategies in management of independent movement of the prostate and pelvic lymph nodes. Medical Physics 2010; 37: 5006-5013.

141) Létourneau D, Martinez AA, Lockman D et al. Assessment of residual error for online cone-beam CT-guided treatment of prostate cancer patients. International Journal of Radiation Oncology, Biology and Physics 2005; 62: 1239-1246.
142) Rijkhorst E-J, Lakeman A, Nijkamp J et al. Strategies for Online Organ Motion Correction for Intensity-Modulated Radiotherapy of Prostate Cancer: Prostate, Rectum, and Bladder Dose Effects. International Journal of Radiation Oncology, Biology and Physics 2009; 75: 1254-1260.
143) O. Bohoudi AB, S. Senan, B. Slotman, M. Palacios, F. Lagerwaard. Using a MRI-guided radiation therapy system for prostate cancer patients. ESTRO 36 2017; SP-0494.
144) Seregni M, Paganelli C, Lee D et al. Motion prediction in MRI-guided radiotherapy based on interleaved orthogonal cine-MRI. Physics in Medicine and Biology 2016; 61: 872.
145) Marcel AvS, Peter S, Cuong Viet D et al. Repeatability of dose painting by numbers treatment planning in prostate cancer radiotherapy based on multiparametric magnetic resonance imaging. Physics in Medicine & Biology 2017; 62: 5575.
146) Wu QJ, Danthai T, Zhiheng W et al. On-line re-optimization of prostate IMRT plans for adaptive radiation therapy. Physics in Medicine and Biology 2008; 53: 673.
147) Feng Y, Castro-Pareja C, Shekhar R, Yu C. Direct aperture deformation: An interfraction image guidance strategy. Medical Physics 2006; 33: 4490-4498.
148) Ahunbay EE, Li XA. Gradient maintenance: A new algorithm for fast online replanning a). Medical Physics 2015; 42: 2863-2876.
149) Fu W, Yang Y, Yue NJ et al. A cone beam CT-guided online plan modification technique to correct interfractional anatomic changes for prostate cancer IMRT treatment. Physics in Medicine and Biology 2009; 54: 1691.
150) Ahunbay EE, Ates O, Li XA. An online replanning method using warm start optimization and aperture morphing for flattening-filter-free beams. Medical Physics 2016; 43: 4575-4584.
151) Ahunbay EE, Peng C, Chen G-P et al. An on-line replanning scheme for interfractional variationsa). Medical Physics 2008; 35: 3607-3615.
152) Ates O, Ahunbay EE, Moreau M, Li XA. Technical Note: A fast online adaptive replanning method for VMAT using flattening filter free beams. Medical Physics 2016; 43: 2756-2764.
153) Otto K. Real-time interactive treatment planning. Physics in Medicine and Biology 2014; 59: 4845.
154) Kamerling CP, Ziegenhein P, Sterzing F, Oelfke U. Interactive dose shaping part 2: proof of concept study for six prostate patients. Physics in Medicine and Biology 2016; 61: 2471.
155) Ziegenhein P, Kamerling CP, Oelfke U. Interactive dose shaping part 1: a new paradigm for IMRT treatment planning. Physics in Medicine and Biology 2016; 61: 2457.
156) Colvill E, Booth J, Nill S et al. A dosimetric comparison of real-time adaptive and non-adaptive radiotherapy: A multi-institutional study encompassing robotic, gimbaled, multileaf collimator and couch tracking. Radiotherapy and Oncology 2016; 119: 159-165.

157) Pathmanathan AU, van As NJ, Kerkmeijer LGW et al. Magnetic Resonance Imaging-Guided Adaptive Radiation Therapy: A “Game Changer” for Prostate Treatment? International Journal of Radiation Oncology, Biology and Physics 2018; 100: 361-373.
158) Njeh C. Tumor delineation: The weakest link in the search for accuracy in radiotherapy. Journal of Medical Physics 2008; 33: 136-140.
159) Lütgendorf-Caucig C, Fotina I, Stock M et al. Feasibility of CBCT-based target and normal structure delineation in prostate cancer radiotherapy: Multi-observer and image multi-modality study. Radiotherapy and Oncology 2011; 98: 154-161.
160) Alasti H, Cho Y-B, Catton C et al. Evaluation of high dose volumetric CT to reduce inter-observer delineation variability and PTV margins for prostate cancer radiotherapy. Radiotherapy and Oncology 2017; 125: 118-123.
161) Pasquier D, Boutaud de la Combe-Chossiere L, Carlier D et al. Harmonization of the Volume of Interest Delineation among All Eleven Radiotherapy Centers in the North of France. PLoS One 2016; 11: e0150917.
162) Shahedi M, Cool DW, Romagnoli C et al. Spatially varying accuracy and reproducibility of prostate segmentation in magnetic resonance images using manual and semiautomated methods. Medical Physics 2014; 41: 113503.
163) Langmack KA, Perry C, Sinstead C et al. The utility of atlas-assisted segmentation in the male pelvis is dependent on the interobserver agreement of the structures segmented. The British Journal of Radiology 2014; 87: 20140299.
164) Nyholm T, Jonsson J, Soderstrom K et al. Variability in prostate and seminal vesicle delineations defined on magnetic resonance images, a multi-observer, -center and -sequence study. Radiation Oncology 2013; 8: 126.
165) Simmat I, Georg P, Georg D et al. Assessment of accuracy and efficiency of atlas-based autosegmentation for prostate radiotherapy in a variety of clinical conditions. Strahlenther Onkol 2012; 188: 807-815.
166) Choi HJ, Kim YS, Lee SH et al. Inter- and intra-observer variability in contouring of the prostate gland on planning computed tomography and cone beam computed tomography. Acta Oncol 2011; 50: 539-546.
167) Rosewall T, Kong V, Vesprini D et al. Prostate delineation using CT and MRI for radiotherapy patients with bilateral hip prostheses. Radiotherapy and Oncology 2009; 90: 325-330.
168) White EA, Brock KK, Jaffray DA, Catton CN. Inter-observer variability of prostate delineation on cone beam computerised tomography images. Clinical Oncology (R Coll Radiol) 2009; 21: 32-38.
169) Gao Z, Wilkins D, Eapen L et al. A study of prostate delineation referenced against a gold standard created from the visible human data. Radiotherapy and Oncology 2007; 85: 239-246.
170) Song WY, Chiu B, Bauman GS et al. Prostate contouring uncertainty in megavoltage computed tomography images acquired with a helical tomotherapy unit during image-guided radiation therapy. International Journal of Radiation Oncology, Biology and Physics 2006; 65: 595-607.

171) Rasch C, Barillot I, Remeijer P et al. Definition of the prostate in CT and MRI: a multi-observer study. International Journal of Radiation Oncology, Biology and Physics 1999; 43: 57-66.
172) Fiorino C, Reni M, Bolognesi A et al. Intra- and inter-observer variability in contouring prostate and seminal vesicles: implications for conformal treatment planning. Radiotherapy and Oncology 1998; 47: 285-292.
173) Cazzaniga LF, Marinoni MA, Bossi A et al. Interphysician variability in defining the planning target volume in the irradiation of prostate and seminal vesicles. Radiotherapy and Oncology 1998; 47: 293-296.
174) Khoo EL, Schick K, Plank AW et al. Prostate contouring variation: can it be fixed? International Journal of Radiation Oncology, Biology and Physics 2012; 82: 1923-1929.
175) Simmat I, Georg P, Georg D et al. Assessment of accuracy and efficiency of atlas-based autosegmentation for prostate radiotherapy in a variety of clinical conditions. Strahlentherapie und Onkologie 2012; 188: 807-815.
176) Rischke HC, Nestle U, Fechter T et al. 3 Tesla multiparametric MRI for GTV-definition of Dominant Intraprostatic Lesions in patients with Prostate Cancer – an interobserver variability study. Radiation Oncology (London, England) 2013; 8: 183-183.
177) Lawton CAF, Michalski J, El-Naqa I et al. Variation in the Definition of Clinical Target Volumes for Pelvic Nodal Conformal Radiation Therapy for Prostate Cancer. International journal of radiation oncology, biology, physics 2009; 74: 377-382.
178) Ost P, De Meerleer G, Vercauteren T et al. Delineation of the postprostatectomy prostate bed using computed tomography: interobserver variability following the EORTC delineation guidelines. International Journal of Radiation Oncology, Biology and Physics 2011; 81: e143-149.
179) Szumacher E, Harnett N, Warner S et al. Effectiveness of educational intervention on the congruence of prostate and rectal contouring as compared with a gold standard in three-dimensional radiotherapy for prostate. International Journal of Radiation Oncology, Biology and Physics 2010; 76: 379-385.
180) Warfield SK, Zou KH, Wells WM. Simultaneous Truth and Performance Level Estimation (STAPLE): An Algorithm for the Validation of Image Segmentation. Ieee Transactions on Medical Imaging 2004; 23: 903-921.
181) Salembier C, Villeirs G, De Bari B et al. ESTRO ACROP consensus guideline on CT- and MRI-based target volume delineation for primary radiation therapy of localized prostate cancer. Radiotherapy and Oncology 2018; 127: 49-61.
182) Tao C-J, Yi J-L, Chen N-Y et al. Multi-subject atlas-based auto-segmentation reduces interobserver variation and improves dosimetric parameter consistency for organs at risk in nasopharyngeal carcinoma: A multi-institution clinical study. Radiotherapy and Oncology 2015; 115: 407-411.
183) Hanna GG, Hounsell AR, O'Sullivan JM. Geometrical analysis of radiotherapy target volume delineation: a systematic review of reported comparison methods. Clinical Oncology (R Coll Radiol) 2010; 22: 515-525.

184) Fotina I, Lutgendorf-Caucig C, Stock M et al. Critical discussion of evaluation parameters for inter-observer variability in target definition for radiation therapy. Strahlentherapie und Onkologie 2012; 188: 160-167.
185) Jameson MG, Holloway LC, Vial PJ et al. A review of methods of analysis in contouring studies for radiation oncology. Journal of Medical Imaging and Radiation Oncology 2010; 54: 401-410.
186) Bridge P, Fielding A, Rowntree P, Pullar A. Intraobserver Variability: Should We Worry? Journal of Medical Imaging and Radiation Sciences 2016; 47: 217-220.
187) Cohen J. A Coefficient of Agreement for Nominal Scales. Educational and Psychological Measurement 1960; 20: 37-46.
188) Vinod SK, Min M, Jameson MG, Holloway LC. A review of interventions to reduce inter-observer variability in volume delineation in radiation oncology. J Med Imaging Radiat Oncol 2016; 60: 393-406.
189) Harris VA, Staffurth J, Naismith O et al. Consensus Guidelines and Contouring Atlas for Pelvic Node Delineation in Prostate and Pelvic Node Intensity Modulated Radiation Therapy. International Journal of Radiation Oncology, Biology and Physics 2015; 92: 874-883.
190) Mitchell DM, Perry L, Smith S et al. Assessing the effect of a contouring protocol on postprostatectomy radiotherapy clinical target volumes and interphysician variation International Journal of Radiation Oncology, Biology and Physics 2009; 75: 990-993.
191) Chang ATY, Tan LT, Duke S, Ng W-T. Challenges for Quality Assurance of Target Volume Delineation in Clinical Trials. Frontiers in oncology 2017; 7: 221-221.
192) Ohri N, Shen X, Dicker AP et al. Radiotherapy protocol deviations and clinical outcomes: a meta-analysis of cooperative group clinical trials. Journal of the National Cancer Institute 2013; 105: 387-393.
193) Vinod SK, Jameson MG, Min M, Holloway LC. Uncertainties in volume delineation in radiation oncology: A systematic review and recommendations for future studies. Radiotherapy and Oncoogy 2016; 121: 169-179.
194) Livsey JE, Wylie JP, Swindell R et al. Do differences in target volume definition in prostate cancer lead to clinically relevant differences in normal tissue toxicity? International Journal of Radiation Oncology, Biology and Physics 2004; 60: 1076-1081.
195) Callaghan PT. Principles of Nuclear Magnetic Resonance Microscopy. . Clarendon Press, Oxford. 1991. p 208-217.
196) La Macchia M, Fellin F, Amichetti M et al. Systematic evaluation of three different commercial software solutions for automatic segmentation for adaptive therapy in head-and-neck, prostate and pleural cancer. Radiation Oncology 2012; 7: 160.
197) Martin S, Rodrigues G, Patil N et al. A multiphase validation of atlas-based automatic and semiautomatic segmentation strategies for prostate MRI. International Journal of Radiation Oncology, Biology and Physics 2013; 85: 95-100.
198) Sjoberg C, Lundmark M, Granberg C et al. Clinical evaluation of multi-atlas based segmentation of lymph node regions in head and neck and prostate cancer patients. Radiation Oncology 2013; 8: 229.

199) Young AV, Wortham A, Wernick I et al. Atlas-based segmentation improves consistency and decreases time required for contouring postoperative endometrial cancer nodal volumes. International Journal of Radiation Oncology, Biology and Physics 2011; 79: 943-947.
200) Li W, Liao S, Feng Q et al. Learning image context for segmentation of prostate in CT-guided radiotherapy. Med Image Comput Comput Assist Interv 2011; 14: 570-578.
201) Pasquier D, Lacornerie T, Vermandel M et al. Automatic Segmentation of Pelvic Structures From Magnetic Resonance Images for Prostate Cancer Radiotherapy. International Journal of Radiation Oncology, Biology and Physics 2007; 68: 592-600.
202) Tsai A, Yezzi A, Jr., Wells W et al. A shape-based approach to the segmentation of medical imagery using level sets. IEEE Trans Med Imaging 2003; 22: 137-154.
203) Korsager AS, Stephansen UL, Carl J, Ostergaard LR. The use of an active appearance model for automated prostate segmentation in magnetic resonance. Acta Oncol 2013; 52: 1374-1377.
204) Dowling JA, Lambert J, Parker J et al. An Atlas-Based Electron Density Mapping Method for Magnetic Resonance Imaging (MRI)-Alone Treatment Planning and Adaptive MRI-Based Prostate Radiation Therapy. International Journal of Radiation Oncology, Biology and Physics 2012; 83: e5-e11.
205) Burgos N, Guerreiro F, McClelland J et al. Iterative framework for the joint segmentation and CT synthesis of MR images: application to MRI-only radiotherapy treatment planning. Physics in Medicine and Biology 2017; 62: 4237-4253.
206) Langerak TR, Heide UAvd, Kotte ANTJ et al. Label Fusion in Atlas-Based Segmentation Using a Selective and Iterative Method for Performance Level Estimation (SIMPLE). IEEE Transactions on Medical Imaging 2010; 29: 2000-2008.
207) Intensity-weighted multi-atlas label fusion for ABAS. Elekta Inc. white paper.
208) Iglesias JE, Sabuncu MR. Multi-atlas segmentation of biomedical images: A survey. Medical image analysis 2015; 24: 205-219.
209) Xie Q, Ruan D. Low-complexity atlas-based prostate segmentation by combining global, regional, and local metrics. Medical Physics 2014; 41: 041909.
210) Langerak TR, Berendsen FF, Van der Heide UA et al. Multiatlas-based segmentation with preregistration atlas selection. Medical Physics 2013; 40: 091701.
211) Guo Y, Gao Y, Shen D. Deformable MR Prostate Segmentation via Deep Feature Learning and Sparse Patch Matching. IEEE Trans Med Imaging 2016; 35: 1077-1089.
212) Ma L, Guo R, Zhang G et al. Automatic segmentation of the prostate on CT images using deep learning and multi-atlas fusion. Proceedings of SPIE--the International Society for Optical Engineering 2017; 10133: 101332O.
213) Zikic D, Glocker B, Criminisi A. Encoding atlases by randomized classification forests for efficient multi-atlas label propagation. Medical Image Analysis 2014; 18: 1262-1273.

214) Konukoglu E, Glocker B, Zikic D, Criminisi A. Neighbourhood approximation using randomized forests. Medical Image Analysis 2013; 17: 790-804.
215) Learning-boosted Multi-Atlas Label Fusion for Atlas- based Auto-segmentation (ABAS). Elekta Inc. white paper.
216) Hwee J, Louie AV, Gaede S et al. Technology assessment of automated atlas based segmentation in prostate bed contouring. Radiation Oncology (London, England) 2011; 6: 110-110.
217) Wong WKH, Leung LHT, Kwong DLW. Evaluation and optimization of the parameters used in multiple-atlas-based segmentation of prostate cancers in radiation therapy. The British Journal of Radiology 2016; 89: 20140732.
218) Li W, Vassil A, Zhong Y, Xia P. Daily dose monitoring with atlas-based auto-segmentation on diagnostic quality CT for prostate cancer. Medical Physics 2013; 40: 111720.
219) Greenham S, Dean J, Fu CKK et al. Evaluation of atlas-based auto-segmentation software in prostate cancer patients. Journal of Medical Radiation Sciences 2014; 61: 151-158.
220) Burgos N, Guerreiro F, McClelland J et al. Iterative framework for the joint segmentation and CT synthesis of MR images: application to MRI-only radiotherapy treatment planning. Physics in Medicine and Biology 2017; 62: 4237-4253.
221) Delpon G, Escande A, Ruef T et al. Comparison of Automated Atlas-Based Segmentation Software for Postoperative Prostate Cancer Radiotherapy. Frontiers in oncology 2016; 6: 178-178.
222) Aluwini S, van Rooij P, Hoogeman M et al. Stereotactic body radiotherapy with a focal boost to the MRI-visible tumor as monotherapy for low- and intermediate-risk prostate cancer: early results. Radiation Oncology (London, England) 2013; 8: 84-84.
223) Huyskens DP, Maingon P, Vanuytsel L et al. A qualitative and a quantitative analysis of an auto-segmentation module for prostate cancer. Radiotherapy and Oncology 2009; 90: 337-345.
224) Wong WKH, Leung LHT, Kwong DLW. Evaluation and optimization of the parameters used in multiple-atlas-based segmentation of prostate cancers in radiation therapy. The British journal of radiology 2016; 89: 20140732-20140732.
225) Klein S, van der Heide UA, Lips IM et al. Automatic segmentation of the prostate in 3D MR images by atlas matching using localized mutual information. Medical Physics 2008; 35: 1407-1417.
226) Morrow NV, Lawton CA, Qi XS, Li XA. Impact of Computed Tomography Image Quality on Image-Guided Radiation Therapy Based on Soft Tissue Registration. International Journal of Radiation Oncology, Biology and Physics 2012; 82: e733-e738.
227) Altman MB, Kavanaugh JA, Wooten HO et al. A framework for automated contour quality assurance in radiation therapy including adaptive techniques. Physics in Medicine & Biology 2015; 60: 5199.
228) Beasley WM, Alan; Slevin, Nicholas; Mackay, Ranald; van Herk, Marcel. An automated workflow for patient-specific quality control of contour propagation. Physics in Medicine and Biology 2016; Article reference: PMB-104524.R1.

229) Godley A, Sheplan Olsen LJ, Stephans K, Zhao A. Combining prior day contours to improve automated prostate segmentation. Medical Physics 2013; 40: 021722.
230) ABAS: Intra-patient deformable image registration for adaptive radiotherapy- a white paper. Elekta Inc. white paper.
231) Padgett KR, Swallen A, Pirozzi S et al. Towards a universal MRI atlas of the prostate and prostate zones : Comparison of MRI vendor and image acquisition parameters. Strahlenther Onkol 2018.
232) Litjens G, Toth R, van de Ven W et al. Evaluation of prostate segmentation algorithms for MRI: the PROMISE12 challenge. Medical image analysis 2014; 18: 359-373.
233) Dickinson L, Ahmed HU, Allen C et al. Magnetic resonance imaging for the detection, localisation, and characterisation of prostate cancer: recommendations from a European consensus meeting. European Urology 2011; 59: 477-494.
234) Feng Y, Kawrakow I, Olsen J et al. A comparative study of automatic image segmentation algorithms for target tracking in MR-IGRT. Journal of Applied Clinical Medical Physics 2016; 17: 441-460.
235) Roberson PL, McLaughlin PW, Narayana V et al. Use and uncertainties of mutual information for computed tomography/magnetic resonance (CT/MR) registration post permanent implant of the prostate. Medical Physics 2005; 32: 473-482.
236) Huisman HJ, Fütterer JJ, Lin ENJTv et al. Prostate Cancer: Precision of Integrating Functional MR Imaging with Radiation Therapy Treatment by Using Fiducial Gold Markers. Radiology 2005; 236: 311-317.
237) Nyholm T, Nyberg M, Karlsson MG, Karlsson M. Systematisation of spatial uncertainties for comparison between a MR and a CT-based radiotherapy workflow for prostate treatments. Radiation Oncology (London, England) 2009; 4: 54-54.
238) Price RG, Kadbi M, Kim J et al. Technical Note: Characterization and correction of gradient nonlinearity induced distortion on a 1.0 T open bore MR-SIM. Medical Physics 2015; 42: 5955-5960.
239) Chen L, Price Jr RA, Wang L et al. MRI-based treatment planning for radiotherapy: Dosimetric verification for prostate IMRT International Journal of Radiation Oncology, Biology and Physics 2004; 60: 636-647.
240) Hu Y, Zhao W, Du D et al. Magnetic resonance imaging-based treatment planning for prostate cancer: Use of population average tissue densities within the irradiated volume to improve plan accuracy. Practical Radiation Oncology 2015; 5: 248-256.
241) Guerreiro F, Burgos N, Dunlop A et al. Evaluation of a multi-atlas CT synthesis approach for MRI-only radiotherapy treatment planning. Physica Medica 2017; 35: 7-17.
242) Uh J, Merchant TE, Li Y et al. MRI-based treatment planning with pseudo CT generated through atlas registration. Medical Physics 2014; 41: 051711.
243) Catana C, van der Kouwe A, Benner T et al. Towards Implementing an MR-based PET Attenuation Correction Method for Neurological Studies on the MR-PET Brain Prototype. Journal of nuclear medicine : official publication, Society of Nuclear Medicine 2010; 51: 1431-1438.
244) Berker Y, Franke J, Salomon A et al. MRI-Based Attenuation Correction for Hybrid PET/MRI Systems: A 4-Class Tissue Segmentation Technique

Using a Combined Ultrashort-Echo-Time/Dixon MRI Sequence. Journal of Nuclear Medicine 2012; 53: 796-804.
245) Johansson A, Karlsson M, Nyholm T. CT substitute derived from MRI sequences with ultrashort echo time. Medical Physics 2011; 38: 2708-2714.
246) Kapanen M, Tenhunen M. T1/T2*-weighted MRI provides clinically relevant pseudo-CT density data for the pelvic bones in MRI-only based radiotherapy treatment planning. Acta Oncol 2013; 52: 612-618.
247) Maspero M, Seevinck PR, Schubert G et al. Quantification of confounding factors in MRI-based dose calculations as applied to prostate IMRT. Physics in Medicine and Biology 2017; 62: 948-965.
248) Tyagi N, Fontenla S, Zhang J et al. Dosimetric and workflow evaluation of first commercial synthetic CT software for clinical use in pelvis. Physics in Medicine and Biology 2017; 62: 2961-2975.
249) Tyagi N, Fontenla S, Zelefsky M et al. Clinical workflow for MR-only simulation and planning in prostate. Radiation Oncology 2017; 12: 119.

Chapter 2- Assessment of prostate intrafraction motion using cine-MRI

2.1 Publications

The data from this chapter has been published in the following article;

Fiducial marker based intra-fraction motion assessment on cine-MR for MR-Linac treatment of prostate cancer

Daan M. de Muinck Keizer *, Angela U. Pathmanathan * (*joint first author), Anna Andreychenko, Linda G.W. Kerkmeijer, Jochem R.N. van der Voort van Zyp, Alison C. Tree, Nico C.A.T. van den Berg, Hans C.J. de Boer. Physics in Medicine and Biology 2019;64(7):07NT02

In addition, the data was presented in poster format at ESTRO 2018

Automatic fiducial tracking on 4D cine-MRI for MR-guided prostate radiotherapy. Pathmanathan A, Andreychenko A, de Muinck Keizer DM, Kerkmeijer LGW, Tree AC, van den Berg CAT, de Boer JCJ. Radiotherapy and Oncology 2018; 127: S548 - S549

2.2 Introduction

Fiducial markers (FM) have become the gold standard for position verification prior to prostate radiotherapy. As discussed in Section 1.2.3, dedicated magnetic resonance imaging (MRI) sequences are required to enhance the visualisation of FM, with more recent work focussing on automatic detection.

I undertook the work in this chapter as part of a collaboration between the Royal Marsden Hospital and the physics department at University Medical Centre, Utrecht. An extensive dataset of three dimensional (3D) balanced steady-state free precession sequence (bSSFP) cine-MR scans were used to assess the accuracy of an automatic fiducial detection method. In turn, prostate motion was assessed over the ten minute period of the cine-MR, reflecting the same duration of a radiotherapy fraction.

An FM template is a 3D representation of the marker positions relative to each other, which facilitates comparison to subsequent images. The overall aim was to establish the accuracy of a template method for automatic FM detection on bSSFP cine-MR and to further assess prostate motion.

2.3 Aims of Chapter 2

My hypothesis is that fiducial markers can be accurately detected using an automatic algorithm and therefore used with cine-MR frames to evaluate prostate motion and rotation

In order to test this hypothesis, I will;

1) Assess the accuracy of automatic FM detection on bSSFP cine-MR by comparison to manual identification
2) Quantify prostate motion in the left-right, anterior-posterior and caudal-cranial axis
3) Quantify prostate rotation
4) Assess the changes in motion and rotation over time

2.4 Materials and Methods

2.4.1 Patient Selection

Twenty-nine patients undergoing hypofractionated prostate SBRT within the HypoFLAME trial (NCT02853110) with four implanted cylindrical gold FMs (5 mm length, 1 mm diameter), had repeated MRI sessions at the University Medical Centre (UMC) Utrecht, in a multicentre Medical Ethics board approved study.

2.4.2 Image acquisition

The imaging sessions included several sequences including cine-MRI, T2-weighted and SPectral Attenuated Inversion Recovery (SPAIR) examinations prior to each of five weekly fractions. Patient positioning and immobilisation was similar to that during radiotherapy with drinking instructions for bladder filling as per institutional guidelines (400 ml of water prior to scanning or treatment). There was no rectal preparation specified.

Each cine-MR examination consisted of 55 sequentially obtained 3D datasets (dynamics) that were acquired with a 3D bSSFP sequence using fat suppression. The sequence was optimised for anatomical and FM contrast, imaging parameters included repetition time (TR) 4 ms, echo time (TE) 1.98 ms, flipangle 30°, B_0 1.5T. Each dynamic was acquired over a 11 second period, yielding a total acquisition time per examination of 10 minutes. Voxel size was 0.96 x 0.96 x 2 mm^3 and a 384 × 384 × 120 mm^3 field of view.

2.4.3 Manual FM identification

I manually located the locations of the FM on the axial images of the first dynamic of each cine-MR dataset using Research Volumetool version 2.5.1, dedicated software developed at UMC Utrecht for clinical contouring. I initiated the work for this chapter whilst resident in Utrecht for one week, the rest was completed using a virtual private network (VPN) connection. This provided remote secure access to the anonymised scans. The same software was used for all patients.

I reviewed the first dynamic image set, using axial, coronal and sagittal views to identify the voids consistent with FM. I identified the most superior and inferior aspect of each FM using a previously described method [1], from which the FM centre was obtained, without reference to the CT imaging. As many patients had calcifications mimicking the appearance of the markers, my final identification was based on imaging, in particular the prior knowledge that subjects had four FMs implanted, usually two in the upper prostate and two in the lower prostate, implanted using two tracks. The FMs created a linear void,

and due to the method of insertion was often seen in the same plane as the second FM inserted within the same track. This is depicted in Figure 2.1 in the SPAIR (shown for clarity) and cine-MR images.

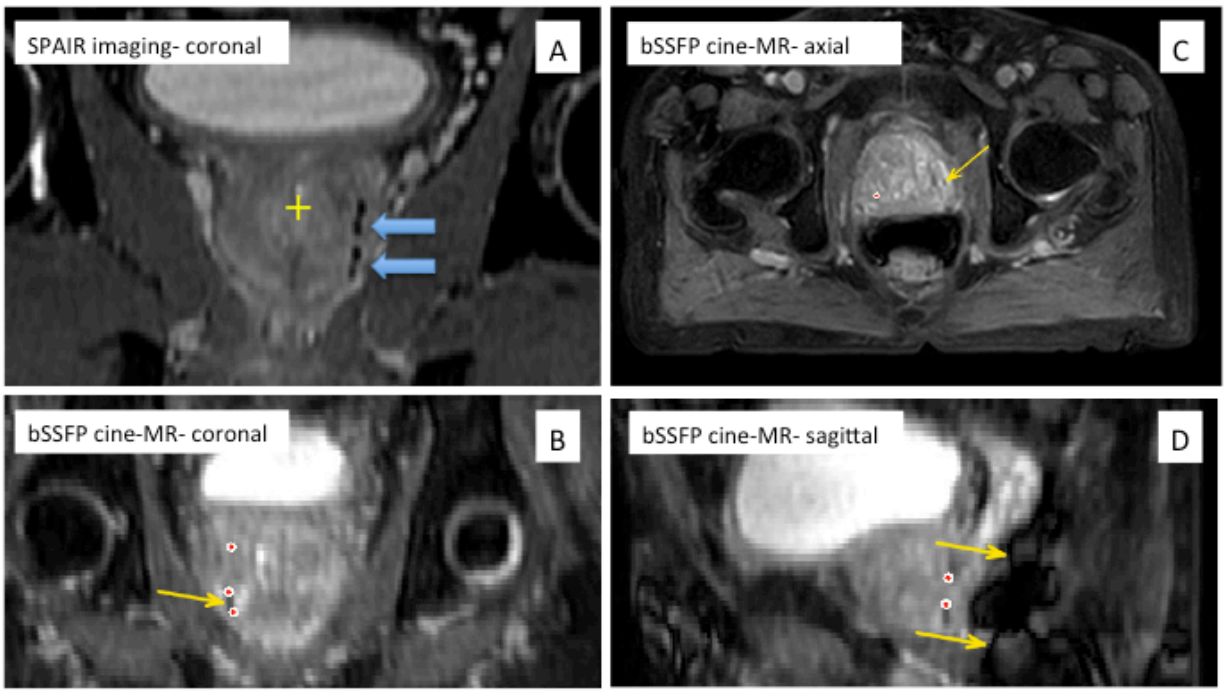

Figure 2.9- Overview of cine-MR images with manually segmented markers by myself. Image A is an example of SPAIR imaging to demonstrate the linear void created by FM, the blue block arrows show the two FM inserted within the same track. Images B, C and D show the sagittal, axial and sagittal slices respectively from the same patient (but different to that seen in Image A). Manually segmented marker top or bottom locations are visualized as the red dots. In (B) Only one red dot is visible for the superior FM as the lower point of this FM is out of plane in this image. The yellow arrows in image B and C show the effect of a signal void caused by a fiducial marker. The effect of the banding artifact caused by rectal gas is highlighted by the arrows in image D.

The FM template containing the 3D positions of all markers from the first dynamic was then stored. The FM template established from my identification of

the markers on cine-MR was compared by UMC Utrecht physicist Daan de Muinck Keizer (DdMK) with the available FM templates obtained from CT scans of the patients.

In addition to identifying the FM on the first dynamic to create the template necessary for the automatic labeling described in the next section, I used the same method to identify the FM on the middle dynamic (27^{th}) and end dynamic (55^{th}) of each cine-MR dataset to allow verification of the automatic FM detection.

2.4.4 Automatic FM identification

The steps from Section 2.4.3 and 2.4.4, required for the automatic determination of the FM, are summarised pictorially in Figure 2.2. The automatic FM identification was completed by DdMK. The FM centres in subsequent dynamics were determined automatically using an in-house Python code. FM patterns from the first dynamic were correlated by template matching with subsequent dynamics.

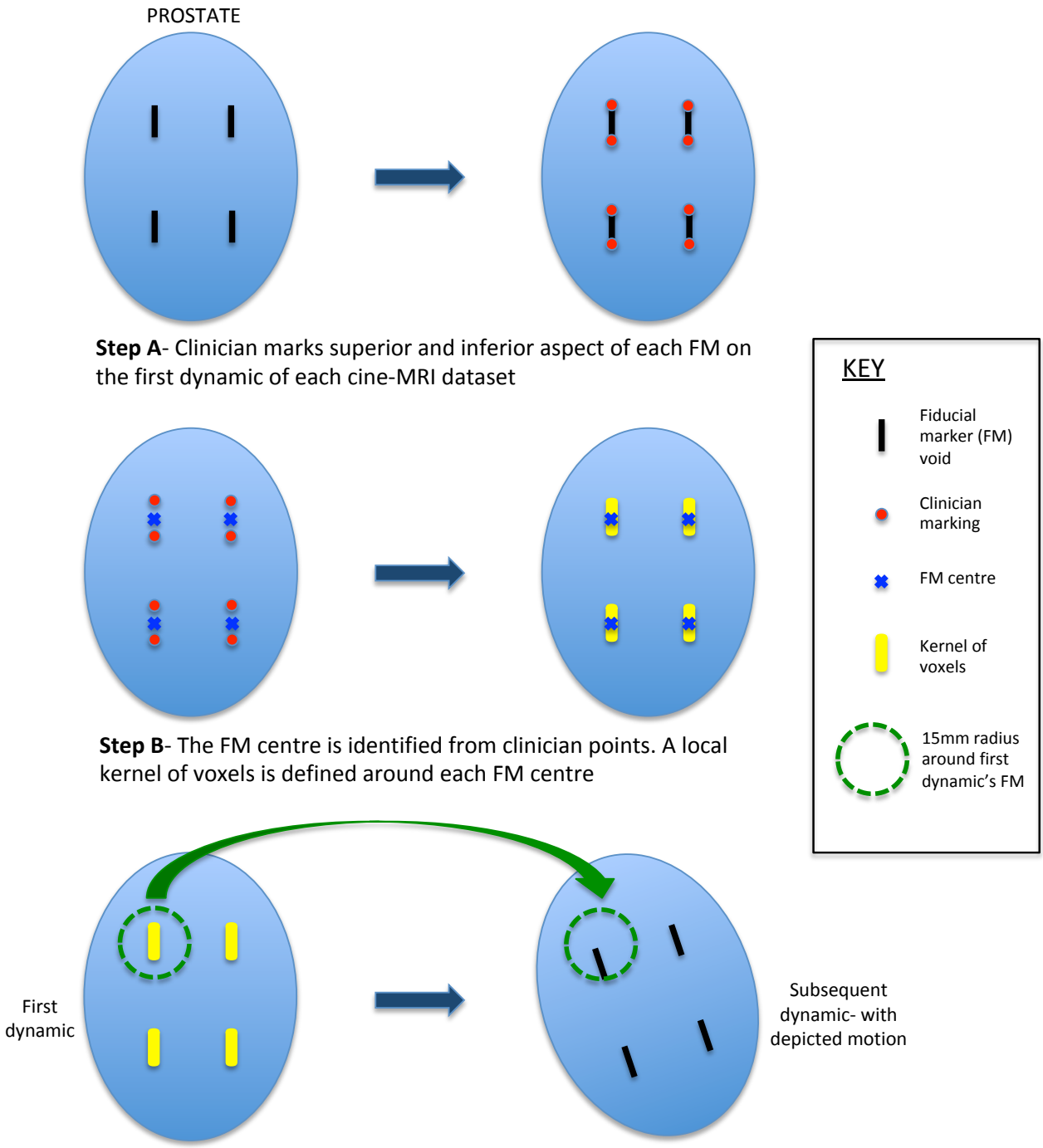

Figure 2.10- Summary of the steps to automatically determine the position of the fiducial markers in subsequent dynamics using template matching

All dynamics were resampled to a voxel spacing of 0.25 mm^3 to improve the accuracy and resolution of the automatic tracking results. Automatic determination of the FMs in subsequent frames was then performed by defining a local kernel of voxels with a diameter of 7 mm and height of 14 mm around each fiducial center in the first dynamic- this is based on the size of the void created by the FM on the MR images. The defined kernels were individually correlated to subsequent dynamics using the Pearson correlation to determine the current location of all FM, in a radius of 15 mm around the initial FM position of the first dynamic.

Due to the subjective review of imaging, there is potentially an error introduced when I manually identify the markers. To reduce the influence of outliers from incorrectly determined FM locations and increase robustness, the found FM locations of all subsequent dynamics were rigidly mapped to the marker template of the first dynamic using a 'leave-one-out strategy'. All four possible combinations of three markers from the current dynamic were used to calculate a rigid transformation to the marker template of the first dynamic. The transformation with the lowest intra-marker difference between the mapped and original FM points was used for the determination of the final Euler transformation. The calculated transformation was therefore based on three markers and describes the translation and rotation between the first and subsequent dynamics and these variables are stored as the centre of mass (COM) translation and rotation.

The results from the algorithm were verified by comparing the automatically found COM locations with the locations I manually identified at the halfway (27th) dynamic (after approximately 5 minutes) and end (55th) dynamic (after approximately 10 minutes). The grid system used in this chapter defines X as left-right (where positive denotes right), Y as anterior-posterior (where positive denotes posterior) and Z as the caudal-cranial axis (where positive denotes cranial).

2.4.5 Assessment of algorithm accuracy

The algorithm's success rate was determined by calculating the mean absolute intra-marker distance between the manually determined FMs found in the current dynamic and the FMs of the first dynamic, transformed to the current dynamic by the algorithm. The transformation of the FMs from the first to the current dynamic was performed by applying the inverse of the obtained transformation between the current and first dynamic. The intramarker distance was defined as the difference between the found position of a FM in the current dynamic and the transformed position of the same FM from the first to the current dynamic.

If the mean absolute intramarker distance was equal to or less than 0.25 mm (equal to the resampled voxel spacing), the identification of the individual FMs and the registration between the dynamics was considered a success.

2.4.6 Analysis of data

Different statistical analyses were used by DdMK to assess the results obtained from the COM locations. The analysed statistical metrics include the systematic error per patient per time point, the group mean displacement per time point, population systematical error per time point (**Σ**) and the population random error per time point (**σ**). The two latter values have been described in detail elsewhere [2].

The population systematical error can be seen as a measure for the mean displacement in all patients. The population random error can be denoted as the effective random displacement, as it provides a measure for the mean fluctuations in the found result of the population [3].

The Appendix, Section 2.9, summarises the equations used for these analyses.

2.5 Results

2.5.1 Manual FM identification

A total of 133 cine-MR scans from 29 patients were included. I manually identified the FM on the 1st, 27th and 55th dynamic for all 133 scans. In addition, I made written observations for the patients where the FM were particularly difficult to assess, for example due to large rectum or motion artefact.

2.5.2 Automatic FM identification

The algorithm was applied to all 7315 dynamics (55 per scan), full automatic analysis of a single dynamic took 10 seconds. Two scans were excluded from the analysis based on visual inspection of the cine-MR data and the performance of the marker tracking algorithm. This was due to excessive banding artifact, overlapping the prostate and distorting identification of the FM signal void. This is considered further in the Discussion section.

2.5.3 Assessment of algorithm accuracy

The mean 3D error in the COM position found by the algorithm compared with the clinician on dynamic 27 and 55 is 1.1±0.7 mm with the largest 3D error being 3.8 mm. The mean 3D error in the FM positions provided by the clinician based on MR images compared with the 3D positions obtained from CT scans is 1.6±1.2 mm. Linear regression analysis between the COM of the validation points by the clinician and the found COM positions by the algorithm returned a correlation value of 0.92. The success rate of the algorithm's tracking and registration was 97.7%.

2.5.4 Analysis of data

Patients spent an average of 2.4±0.7 minutes on the scanner table before the start of the cine-MR imaging sequence.

The calculated COM translations at 10 minutes were 0.0±0.8 mm (maximum 3.4 mm) for X, 1.0±1.9 mm (maximum 9.7 mm) for Y (posterior direction) and

0.9±2.0 mm (maximum 8.0 mm) for Z (caudal direction). The rotation results at 10 minutes were 0.1±3.9° (maximum 30.3°) for X (towards anterior), 0.0±1.3° (maximum 4.0°) for Y and 0.1±1.2° (maximum 3.8°) for Z.

Figure 2.3 shows the population mean translation results. Figure 2.4 displays the population mean rotation results

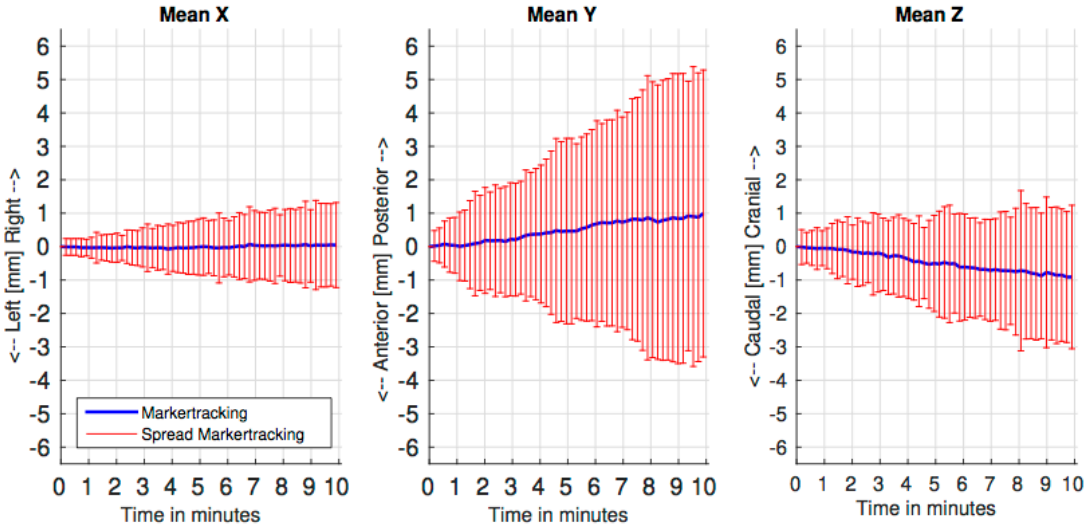

Figure 2.11- Summary of the population translation results for all patients and fractions, with the determined spread (95th percentile) at each time point, displayed as red error bars. Overall the translation trend is 1.0 mm posteriorly, 0.9 mm in the caudally with no translation trend was observed for the left-right direction. Figure courtesy of DdMK, taken from publication [4].

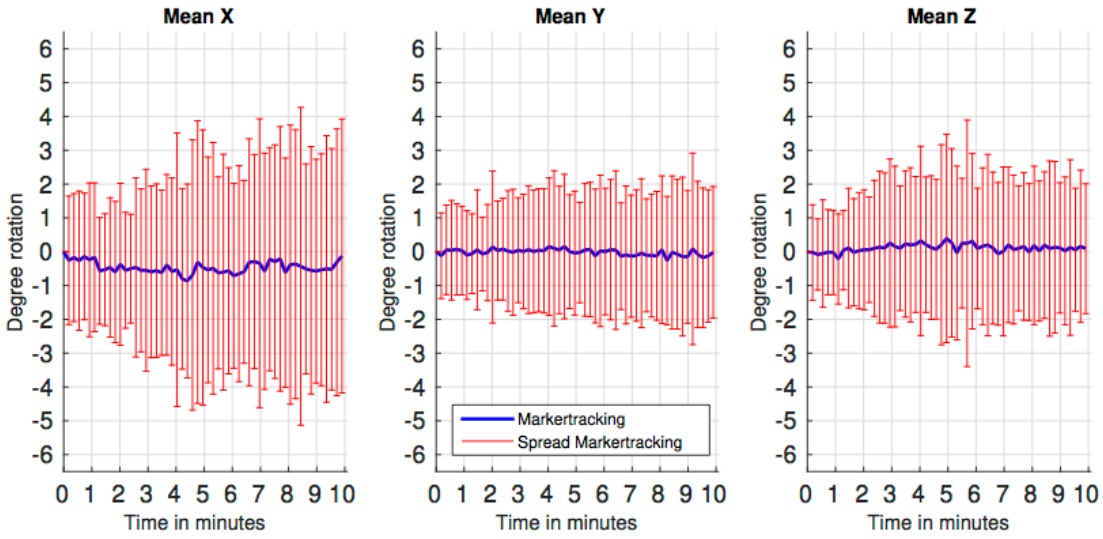

Figure 2.12- Summary of the population rotation results for all patients and fractions, with the determined spread (95th percentile) at each time point, displayed as red error bars. The left graph displays the mean overall anterior-posterior rotation trend (about the X-axis) of 0.5^{o} in the anterior direction. No rotational trend was observed for the Y and Z axis. Figure courtesy of DdMK, taken from publication [4].

The cumulative incidence of 3D translation in the COM of at least 2, 4 and 5 mm are provided in Figure 2.5. These results indicate the cumulative fraction of scans in which the 3D COM translation was larger than the thresholds from the start of the imaging sequence up to the time intervals of 1, 3, 5, 7, 9 and 10 minutes. Results on the cumulative occurrences of COM rotations of at least 2, 4 and 5 degrees in the X direction, where the significant rotations were observed, are presented in Figure 2.6.

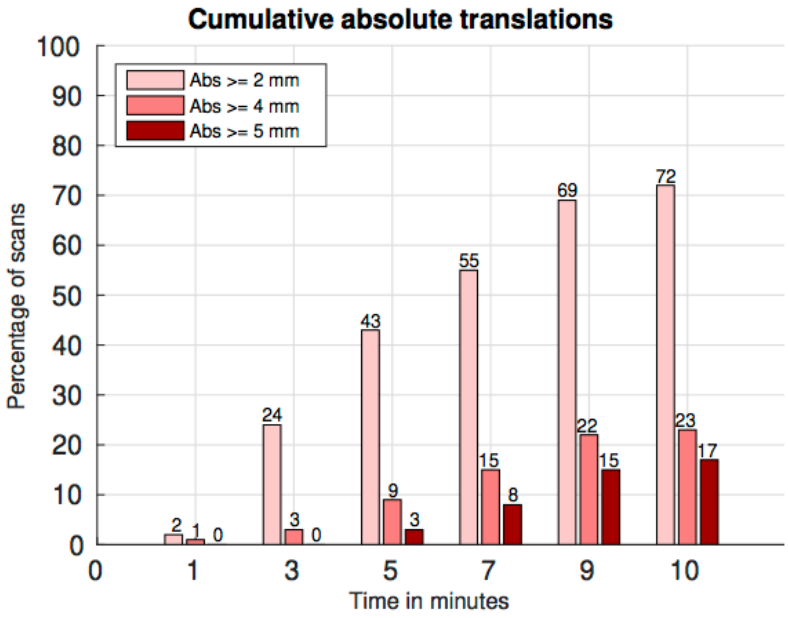

Figure 2.13- Bar chart summarising the cumulative percentage of scans over time in which the centre of mass translation was greater than 2, 4 or 5 mm. Figure courtesy of DdMK, taken from publication [4].

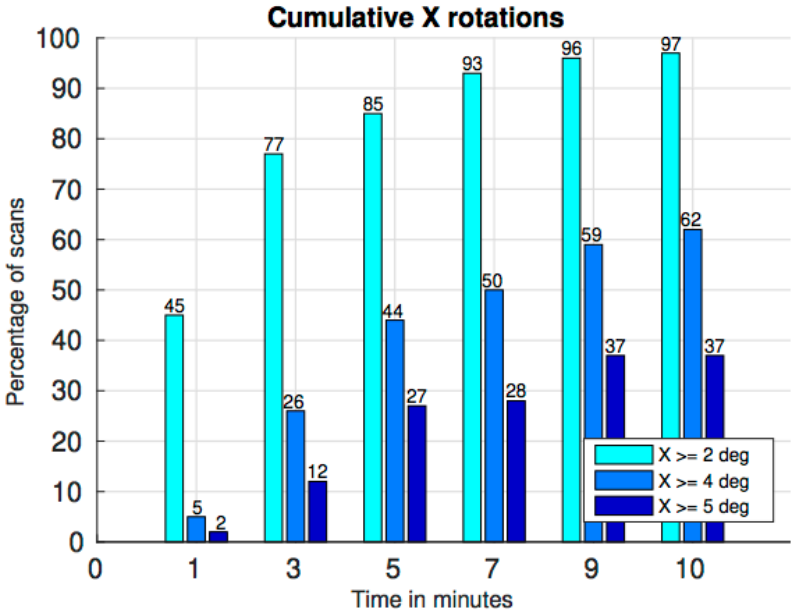

Figure 2.14- Bar chart summarising the cumulative percentage of scans over time in which the rotation about the X-axis was greater than 2, 4 or 5 degrees. Figure courtesy of DdMK, taken from publication [4]..

Figure 2.7 provides an overview of the population systematic translation error. The population random translation error is given in Figure 2.8.

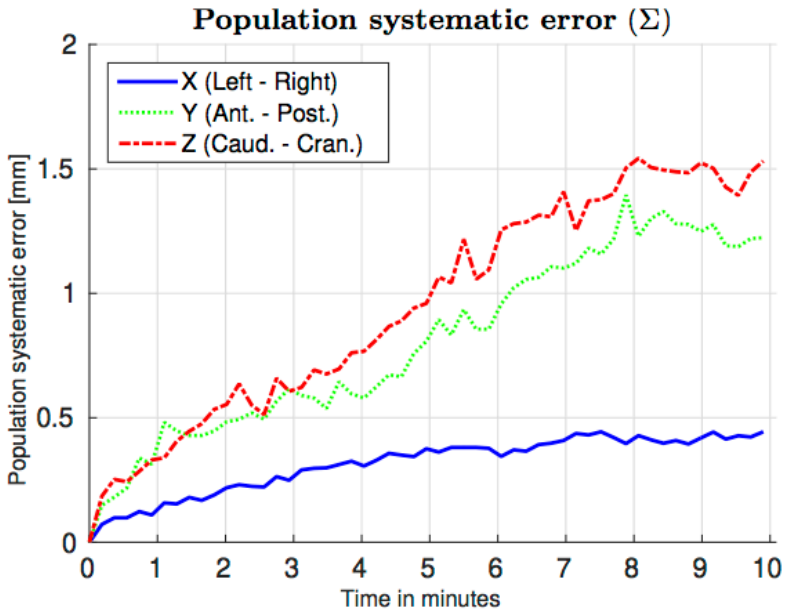

Figure 2.15- The development of the systematic translation errors (Σ) over time, for the three main directions. Figure courtesy of DdMK, taken from publication [4].

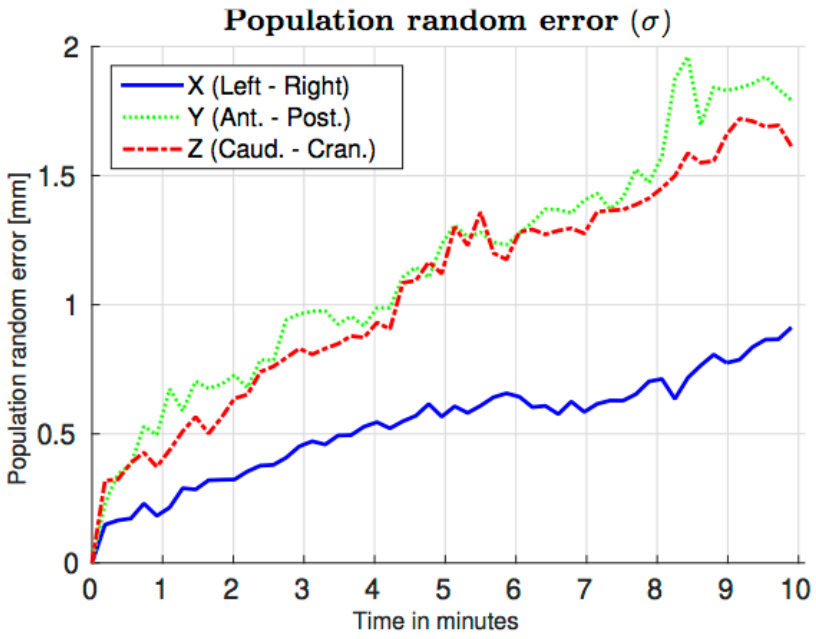

Figure 2.16- The development of the random translation errors (σ) over time, for the three main directions. Figure courtesy of DdMK, taken from publication [4].

2.6 Discussion

This data has shown that fast and accurate FM tracking on 3D cine-MR is feasible. Automatic analysis of a single dynamic took 10 seconds, which would be sufficiently fast enough to analyse a real-time cine-MR data stream without time delay.

Linear regression analysis indicated a good agreement between the COM of the clinician validation points (on dynamics 27 and 55) and the COM positions established by the algorithm. The success rate of the tracking method described here was 97.7% based on an independent conservative measure as described in the methods section. To our knowledge, this is the first 3D cine-MR analysis of prostate intrafraction motion. As a result, comparison to literature is

challenging with comparison only possible to algorithms optimised for automatic FM detection in non cine-MR sequences. An example of automatic fiducial detection is described by Ghose et al who reported a mean centroid difference of 0.5±0.5 mm using a voxel spacing of 0.6x0.6x2 mm with non cine-MR sequences specifically optimised for FM detection on a 3T scanner [5].

A maximum 3D error of 3.8 mm in the COM position found by the algorithm compared with the clinician was found. In this particular case, two markers were identified relatively close together in the prostate. Review of the imaging revealed that the signal void of both markers seemed to partially overlap in the cranial-caudal direction. The error of 3.8 mm was therefore due to deviations in the manual segmentations in the first dynamic, from which the template for the marker tracking is extracted, compared to dynamics 27 and 55. An investigation with multiple observers could specify if this is the case, or that the difference originates from an error in the algorithm.

Two scans were excluded due to an excessive banding artifact caused by local B0 distortions due to rectal gas and are typical for bSSFP sequences. The banding artifact overlapped on large portions of the prostate, which made it nearly impossible to find marker locations in the prostate with confidence. The effect of the banding artifact is shown in Figure 2.1, image D. Fernandes et al [6] had previously reported the impact on fiducial detection of gas within the rectum causing a signal drop-off. Use of a different MR sequence (e.g. spoiled gradient echo) can help to eliminate the influence of banding artifacts.

Although we did not contour the organs at risk or measure rectal size, larger excursions of the prostate were seen in individuals with a larger rectal diameter. A clinical example is seen in Figure 2.9. Previous cine-MR studies have demonstrated rectal distension as a predictor for prostate displacement [7-10], which can impact on clinical outcome and can be reduced with the use of bowel preparation [10], not used in this study.

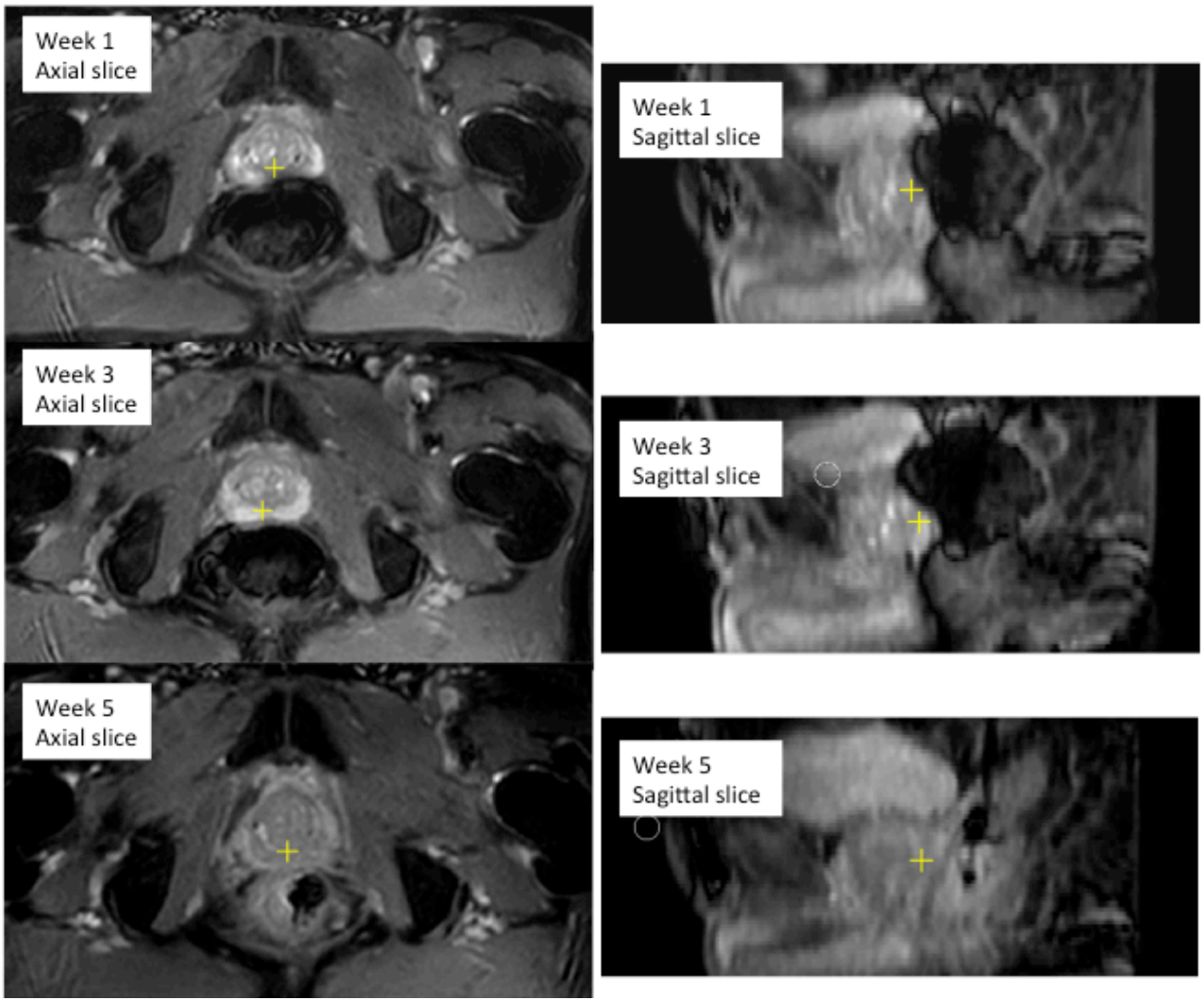

Figure 2.17- Clinical example displaying the axial (left) and sagittal (right) slices for the same patient during weeks 1, 3 and 5. The magnitude of prostate motion is higher for weeks 1 and 3 where a large rectum and accompanying prostate deformation is seen, compared to week 5 with a smaller rectal size.

For analysis of prostate motion, the population results in Figure 2.3 and Figure 2.4 show the small overall trends, with the magnitude of intrafraction displacements increasing continuously over the 10 minute interval. The data suggests that the prostate will continue to move after 10 minutes, consistent with the random walk model of Ballhausen et al [11]. A COM translation of at least 2 mm and 5 mm was seen in 72% and 17% respectively of the cine-MR scans at 10 minutes.

When assessing prostate rotation, more than one-third of the scans (37%) showed a X rotation of at least 5 degrees during the 10 minutes (Figure 2.6), with Z and Y rotations being less common. The maximum X rotation of 30.3^{o} was found in a case where the passage of gas caused severe intrafraction motion in the period of a single dynamic.

Our data is consistent with published results. We have shown that the largest rotation occurs about the left-right axis, while the translation motions are predominantly in the anterior-posterior and cranial-caudal direction [8, 10, 12, 13]. The population average trends can be described as a group mean displacement of 1.0 mm posteriorly, 0.9 mm caudally with an 0.5 degree rotational trend in the anterior direction over the X axis over the 10 minute time period. These changes will be due to a combination of bladder filling, rectal changes and muscle relaxation.

When considering prostate displacements, both the magnitude and duration are relevant. Our findings of increased movement over time are consistent with

tracking data from electromagnetic markers [14, 15], cine-MR studies [7] and transperineal ultrasound imaging [13]. Our findings indicate increasing displacement and variance over time, consistent with findings reported in literature [11]. Similar results obtained with the Calypso localization system over an 8 minute time period are reported by Olsen et al [16], with prostate displacement trends in the Y (0.64±0.5 mm) and Z (0.96±0.6 mm) direction and rotation over the X axis (5.7±5.0^{o}). Huang et al [17] also reported a X-axis rotation of at least 5 degrees in 35% of all scans at 8 minutes time interval, in agreement with our findings. Comparable motion characteristics within the same order of magnitude have been reported by other groups [18-20].

With a shorter treatment time resulting in less prostate motion, the emphasis should be on reducing the time between patient positioning and start of treatment where no strategies for countering intrafraction motion are available. This claim is supported by Ballhausen et al [21] who found that the 3D prostate displacement significantly reduced from 1.31±1.28 mm for intensity modulated radiotherapy (IMRT) at 6 minutes to 0.96±1.04 mm for volumetric arc therapy (VMAT) of under 3 minutes. Cramer et al [15] advised patient repositioning for treatment durations over 4-6 minutes, when no correction protocol for intrafraction motion is used.

The work presented here has not included consideration of the adequate margins for treatment. This extension to the work is being conducted by the UMC Utrecht team, margins can be calculated based on the population systematical error (**Σ**) and the population random error per time point (**σ**) [2].

Valid margins are important for any radiotherapy delivery but particularly in the case of hypofractionation and where image guidance can permit margin reduction.

Our work is particularly relevant for the MR-Linac for several reasons. In terms of the motion data we have acquired, even with short treatment times, we have demonstrated a trend for prostate motion and rotation. Each time point in Figures 2.3 and 2.4 represents the collated data for all 39 patients and all 133 cine-MR scans, there are therefore some scans showing significantly higher levels of motion, as demonstrated by Figure 2.9. The data we have presented here remains highly relevant, as the evaluation of prostate motion and margins during the MR-guided workflow is paramount, particularly with the aim of real-time adaptive radiotherapy during treatment delivery in the future [22]. Even without target tracking, we must ensure that the PTV margins are sufficient to cover prostate motion.

In terms of the automatic FM algorithm itself, FM tracking is just the first step in this process. The full potential of 3D cine-MR data for soft-tissue tracking and hence optimal dose adaptation, can further be exploited. Fiducial markers, at present, form part of the CT-MR workflow. The aim in the future will be to avoid the need for FM. The data acquired here has been used in further work by the UMC Utrecht team to validate soft tissue motion monitoring of the prostate [23], using the same cine-MR image sets, without the use of FM. This work is therefore a stepping stone for the development of a FM-free tracking method of the prostate, relevant for MR-guided radiotherapy.

2.7 Conclusion

We have assessed a robust, fast and accurate FM tracking algorithm on volumetric cine-MR data, allowing continuous monitoring of intrafraction motion and validation of FM-free soft-tissue tracking methods in MR-guided radiotherapy.

The data has displayed a group mean displacement of 1.0 mm posteriorly, 0.9 mm caudally with an 0.5 degree rotational trend in the anterior direction over the X axis over a 10 minute time period. There is a continuous increase with time in intrafraction motion magnitude (translations and rotations) over a ten minute period. The amplitude and temporal behavior of the intrafraction motion stresses the importance of real-time MR-guidance by fast imaging and dose re-optimisation for prostate SBRT.

2.8 References

1) Maspero M, Seevinck PR, Willems NJW et al. Evaluation of gold fiducial marker manual localisation for magnetic resonance-only prostate radiotherapy. Radiation oncology (London, England) 2018; 13: 105-105.
2) van Herk M. Errors and margins in radiotherapy. Seminars in Radiation Oncology 2004; 14: 52-64.
3) de Boer HCJ, Heijmen BJM. eNAL: An Extension of the NAL Setup Correction Protocol for Effective Use of Weekly Follow-up Measurements. International Journal of Radiation Oncology, Biology and Physics 2007; 67: 1586-1595.
4) de Muinck Keizer DM, Pathmanathan AU, Andreychenko A et al. Fiducial marker based intra-fraction motion assessment on cine-MR for MR-linac treatment of prostate cancer. Physics in Medicine and Biology 2019; 64: 07nt02.
5) Ghose S, Mitra J, Rivest-Henault D et al. MRI-alone radiation therapy planning for prostate cancer: Automatic fiducial marker detection. Medical Physics 2016; 43: 2218.
6) Dinis Fernandes C, Dinh CV, Steggerda MJ et al. Prostate fiducial marker detection with the use of multi-parametric magnetic resonance imaging. Physics and Imaging in Radiation Oncology 2017; 1: 14-20.
7) Ghilezan MJ, Jaffray DA, Siewerdsen JH et al. Prostate gland motion assessed with cine-magnetic resonance imaging (cine-MRI). International Journal of Radiation Oncology, Biology and Physics 2005; 62: 406-417.
8) Mah D, Freedman G, Milestone B et al. Measurement of intrafractional prostate motion using magnetic resonance imaging. International Journal of Radiation Oncology, Biology and Physics 2002; 54: 568-575.
9) Nichol AM, Warde PR, Lockwood GA et al. A cinematic magnetic resonance imaging study of milk of magnesia laxative and an antiflatulent diet to reduce intrafraction prostate motion. International Journal of Radiation Oncology, Biology and Physics 2010; 77: 1072-1078.
10) Padhani AR, Khoo VS, Suckling J et al. Evaluating the effect of rectal distension and rectal movement on prostate gland position using cine MRI. International Journal of Radiation Oncology, Biology and Physics 1999; 44: 525-533.
11) Ballhausen H, Li M, Hegemann NS et al. Intra-fraction motion of the prostate is a random walk. Physics in Medicine & Biology 2015; 60: 549.
12) Huang E, Dong L, Chandra A et al. Intrafraction prostate motion during IMRT for prostate cancer. International Journal of Radiation Oncology, Biology and Physics 2002; 53: 261-268.
13) Sihono DSK, Ehmann M, Heitmann S et al. Determination of Intrafraction Prostate Motion During External Beam Radiation Therapy With a Transperineal 4-Dimensional Ultrasound Real-Time Tracking System. International Journal of Radiation Oncology, Biology and Physics 2018; 101: 136-143.
14) Langen KM, Willoughby TR, Meeks SL et al. Observations on Real-Time Prostate Gland Motion Using Electromagnetic Tracking International Journal of Radiation Oncology, Biology and Physics 2008; 71: 1084-1090.

15) Cramer AK, Haile AG, Ognjenovic S et al. Real-time prostate motion assessment: image-guidance and the temporal dependence of intra-fraction motion. BMC medical physics 2013; 13: 4-4.
16) Olsen JR, Noel CE, Baker K et al. Practical method of adaptive radiotherapy for prostate cancer using real-time electromagnetic tracking. International Journal of Radiation Oncology, Biology and Physics 2012; 82: 1903-1911.
17) Huang C-Y, Tehrani JN, Ng JA et al. Six Degrees-of-Freedom Prostate and Lung Tumor Motion Measurements Using Kilovoltage Intrafraction Monitoring. International Journal of Radiation Oncology, Biology and Physics 2015; 91: 368-375.
18) Tehrani JN, O'Brien RT, Poulsen PR, Keall P. Real-time estimation of prostate tumor rotation and translation with a kV imaging system based on an iterative closest point algorithm. Physics in Medicine and Biology 2013; 58: 8517-8533.
19) Willoughby TR, Kupelian PA, Pouliot J et al. Target localization and real-time tracking using the Calypso 4D localization system in patients with localized prostate cancer. International Journal of Radiation Oncology, Biology and Physics 2006; 65: 528-534.
20) Li JS, Jin L, Pollack A et al. Gains From Real-Time Tracking of Prostate Motion During External Beam Radiation Therapy. International Journal of Radiation Oncology, Biology and Physics 2009; 75: 1613-1620.
21) Ballhausen H, Li M, Ganswindt U, Belka C. Shorter treatment times reduce the impact of intra-fractional motion. Strahlentherapie und Onkologie 2018; 194: 664-674.
22) Kontaxis C, Bol GH, Lagendijk JJW, Raaymakers BW. Towards adaptive IMRT sequencing for the MR-linac. Physics in Medicine and Biology 2015; 60: 2493.
23) de Muinck Keizer DM, Kerkmeijer LGW, Maspero M et al. Soft-tissue prostate intrafraction motion tracking in 3D cine-MR for MR-guided radiotherapy. Physics in Medicine & Biology 2019; 64: 235008.

2.9 Chapter 2 Appendix

2.9.1 Statistical analysis for prostate motion and rotation from automatic fiducial tracking

Courtesy of UMC Utrecht physicist Daan de Muinck Keizer (DdMK)

See Section 2.4.6. Different statistical analyses were used by DdMK to assess the results obtained from the COM locations. The analysed statistical metrics include the systematic error per patient per time point, the group mean displacement per time point, population systematical error per time point (**Σ**) and the population random error per time point (**σ**).

The **systematical error per patient (S_p)** can be seen as the mean error over the patient's treatment, and is calculated on time point t_i by:

$$Sp\ (ti) = \frac{1}{Nc(p)} \sum_{c=1}^{Nc(p)} \Delta p, c(ti)$$

With $N_{c(p)}$ as the number of total cine-MR scans per patient (p), c as the cine-MR scan number and Δ as the translation per direction in X, Y or Z.

The **group mean displacement (M)** on time point t_i can then be calculated with:

$$M(t_i) = \frac{1}{N_p} \sum_{p=1}^{N_p} S_p(t_i)$$

With N_p as the total number of included patients. Using equation 1 and 2, the **population systematical error** can be seen as a measure for the mean displacement in all patients and is calculated by:

$$\Sigma(t_i) = \left(\frac{1}{N_p - 1} \sum_{p=1}^{N_p} \left(S_p(t_i) - M(t_i) \right)^2 \right)^{1/2}$$

The **population random error** is calculated by using:

$$\sigma(t_i) = \left(\frac{1}{N_p} \sum_{p=1}^{N_p} \frac{1}{N_c(p) - 1} \sum_{c=1}^{N_c(p)} \left(\Delta_{p,c}(t_i) - S_p(t_i) \right)^2 \right)^{1/2}$$

The population random error can be denoted as the effective random displacement, as it provides a measure for the mean fluctuations in the found result of the population [28].

Chapter 3- Stereotactic body radiotherapy (SBRT) for localised prostate cancer on the MR-Linac

3.1 Publications

Data from this chapter has been published in abstract form following poster presentation at the following conferences;

British uro-oncology group (BUG) conference, September 2016

Stereotactic Body Radiotherapy (SBRT) for Localised Prostate Cancer on the Magnetic Resonance Linac

Angela Pathmanathan, Simeon Nill, Uwe Oelfke, Robert Huddart, Alison Tree

Clinical Oncology. 2017; 29(3):e88

ESTRO 36, April 2017;

Stereotactic Body Radiotherapy (SBRT) for Localised Prostate Cancer on the Magnetic Resonance Linac PO-0828

Angela Pathmanathan, Adam Mitchell, Karen Thomas, Dan Henderson, Simeon Nill, Uwe Oelfke, Robert Huddart, Nicholas van As, Alison Tree

Radiotherapy and Oncology. 2017;123(1):S445

3.2 Introduction

With a low estimated alpha-beta ratio for prostate cancer (3), moderate hypofractionation has been shown to be isoeffective (2). Prospective Phase II trials of extreme hypofractionation schedules, employing a dose of >7.0Gy per fraction, report acceptable toxicity (9, 21) with favourable outcomes confirmed by a pooled multi-institutional analysis (14).

With larger doses per fraction, optimal image-guided radiotherapy (IGRT) is imperative. With the use of online replanning on the MR-Linac, the potential for more accurate stereotactic body radiotherapy (SBRT) is available. However, for the MR-Linac, dose deposition may be affected due to the influence of the magnetic field on the trajectory of secondary electrons (22, 23), the Lorentz force, and can be modelled using Monte Carlo simulations (24). The MR-Linac currently delivers step-and-shoot intensity modulated radiotherapy (IMRT), a technique not often used for SBRT. During IMRT optimisation for standard dose fractionation, increasing the number of fields can increase dose homogeneity and conformity (25-27). Using a beam energy of 6MV, the benefit of additional fields declines with a field number higher than 7-9 (25, 27).

This chapter assesses whether adequate dose distributions for MR-Linac based prostate SBRT are possible with evaluation of the optimal number of fields for planning. Further comparison is made to non MR-Linac based planning techniques: standard linac IMRT, standard linac volumetric modulated arc therapy (VMAT) and CyberKnife.

3.3 Aims of Chapter 3

In this chapter, I will aim to assess the feasibility of clinically acceptable prostate SBRT plans using Monaco treatment planning system (TPS) for the MR-Linac.

My hypothesis is that clinically acceptable prostate SBRT plans can be created by Monaco TPS for the MR-Linac and give dose distributions similar to other treatment platforms.

To test this hypothesis I will

1) Assess the proportion of plans for MR-Linac treatment that meet the dose specifications for hypofractionated radiotherapy, as specified in the PACE trial
2) Assess the optimal beam arrangement for planning prostate SBRT using Monaco TPS for the MR-Linac
3) Compare the dose to the target and organs at risk compared with other RT delivery platforms

3.4 Materials and Methods

3.4.1 Patient population

This comparative treatment planning study was approved prospectively as a service evaluation by the clinical research and development department at the Royal Marsden Hospital (RMH) NHS Foundation Trust. Ten patients with low or intermediate risk National Comprehensive Cancer Network (NCCN) group prostate cancer treated consecutively off-trial using Cyberknife radiotherapy between November 2012 and April 2013 were selected.

3.4.2 Volume definition

Using the planning CT scans co-registered to planning MRI, the contours created by the Fulham road RMH clinical team for prostate radiotherapy planning were utilised. The clinical target volume (CTV) was defined as prostate plus proximal 1cm of seminal vesicles. The planning target volume (PTV) was created by addition of a 5mm isotropic margin, except 3mm posteriorly. The organs at risk (OAR), including rectum, bladder, left and right femoral heads and urethral bulb, were delineated by the clinical team, according to institutional guidelines.

The ten CT planning image sets, along with the associated structure sets as defined above, were transferred by myself and clinical research fellow Daniel Henderson from the Accuray TPS to research Monaco TPS using the secure internal data transfer network.

3.4.3 Planning technique

The planned dose to the PTV was 36.25Gy in 5 fractions with an integrated dose of 40Gy in 5 fractions to the CTV. Plans were created to achieve the dose constraints, as per the PACE trial and detailed in Table 3.1.

TARGET VOLUMES	
PTV (Planning Target Volume)	V36.25 Gy≥ 95% D98% ≥ 34.4Gy Dmax < 48Gy D2% ≤ 42.8Gy (where possible)
CTV (Clinical Target Volume)	V40 Gy≥ 95%
OAR	
Rectum	V18.1Gy < 50% (i.e. less than 50% rectum<18.1Gy) V29Gy < 20% V36Gy < 1cc
Bladder	V18.1Gy < 40% V37Gy < 10cc (optimal V37Gy < 5cc)
Femoral head	V14.5Gy < 5%
Penile bulb	V29.5Gy < 50%
Bowel	V18.1Gy < 5cc V30Gy < 1cc

Table 3.1- Summary of the dose constraints for the fractionation schedule 36.25 Gy in 5 fractions as per the PACE trial.

3.4.4 Radiotherapy delivery techniques

Figure 3.1 summarises the six treatment plans generated for each patient.

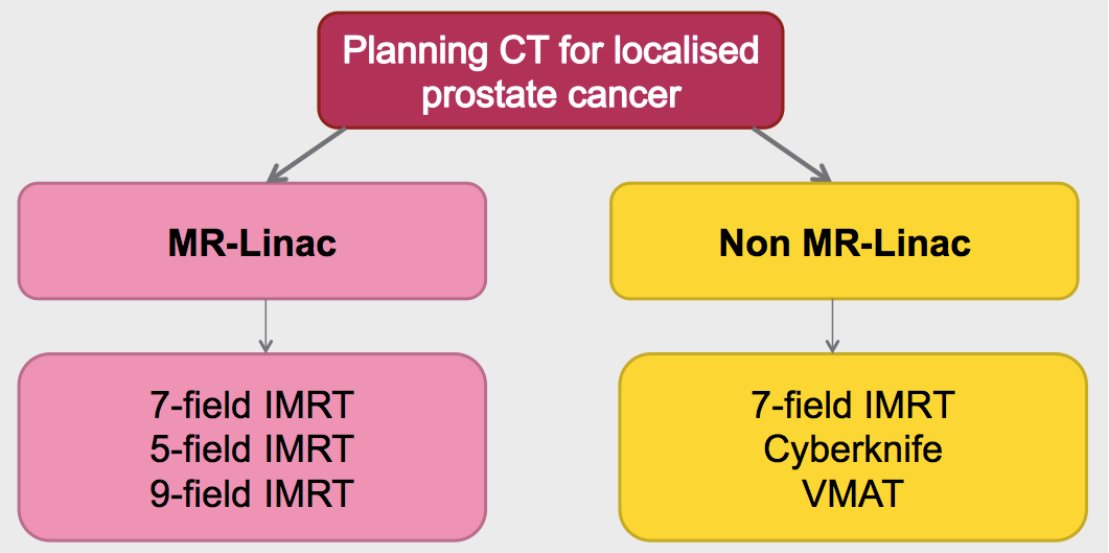

Figure 3.18- Summary of the prostate SBRT planning techniques used for comparison in Chapter 3.

For the MR-Linac, I used Research Monaco 5.19 (research version, Elekta AB, Stockholm, Sweden) to create 5, 7 and 9-field step-and-shoot IMRT plans with equispaced, co-planar, non-opposing 7MV flattening-filter free (FFF) beams. These plans created with Monaco TPS account for the presence of the 1.5T magnetic field and subsequent impact on dosimetry.

The calculation parameters I used for the plans created using Monaco TPS are summarised in Table 3.2. For the IMRT constraints, the dose to the CTV was prioritised using the 'underdose dose volume histogram (DVH)' cost function and I used the 'overdose DVH' cost function to constrain the dose to the OAR with order of priority given to the rectum, bladder, femoral heads and finally the penile bulb.

Calculation Properties	MR-Linac plans	Non MR-Linac plans
Calculation parameter	GPU Monte Carlo calculation	GPU Monte Carlo calculation
Magnetic field	Included at 1.5 Tesla	Not included
MRI housing	Included in calculations	Not included
Minimum segment area	3 cm^2	2 cm^2
Minimum segment width	1.0 cm	0.5 cm
Fluence smoothing	Medium	Medium
Minimum MU per segment	16	16
Maximum number of segments per plan	50	50

Table 3.2 - Summary of the calculation properties and parameters used for the MR-Linac and standard linac Agility plans created with Monaco TPS. GPU-Graphics processing unit.

In addition, the three non MR-Linac comparison plans included:

1) 7-field 6MV IMRT for a conventional Elekta Agility using Research Monaco 5.19 (Elekta AB, Stockholm, Sweden) planned by myself (see Table 3.2 for parameters).
2) 6MV FFF single 360° arc VMAT using Pinnacle 9.10 (Philips Radiation Oncology Systems, Fitchburg, WI) planned by physicist Adam Mitchell for a standard linear accelerator
3) CyberKnife treatment using Multiplan (Accuray inc, Sunnyvale, CA), the original clinical plan used for treatment, derived by physics team at the Fulham Road RMH.

3.4.5 Dose evaluation

I reviewed each plan on the respective TPS to assess the overall dose distribution, dose to the target and dose to OAR; the MR-Linac and Elekta Versa HD plans were reviewed on research Monaco, the VMAT plans on Pinnacle and Cyberknife plans on Multiplan. I recorded the number of constraints missed and radiotherapy plans were deemed clinically acceptable if there was no major variation to the protocol, as outlined in Table 3.3.

VOLUME	Minor Variation	Major Variation
Rectum	V36Gy≥1cc but <2cc	V36Gy≥2cc
Bladder	V37Gy≥10cc but <20cc	V37Gy≥20cc
CTV	V40 90-94.9%	V40<90%
PTV	V36.25 90-94.9%	V36.25<90%

Table 3.3- Summary of the target and OAR dose variations for prostate SBRT as defined within the PACE trial.

In addition, I calculated a number of indices to aid plan comparison by assessing conformity, homogeneity and the dose gradient.

I calculated the conformity index (CI) as defined by the Radiation Therapy Oncology Group (RTOG) and defined below (28). In theory a value of 1.0 would indicate a perfect match between the prescription isodose volume (36.25Gy in this case) and the target volume (CTV in this case). The CI does not indicate the intersection of these volumes and a value of 1.0 can in theory be achieved if these values are identical even with no overlap (28), this value therefore needs to be assessed in conjunction with the relevant plan images to ensure the coverage is adequate. In addition, although there may be excellent conformity with the prescription isodose, this does not indicate the dose fall off further away from the target volume, essential to ensure normal tissue sparing. I have therefore calculated the CI for both the 100% reference isodose (36.25Gy) and the 50% isodose (18.125Gy).

$$\boldsymbol{Conformity\ index} = \frac{\boldsymbol{Volume\ of\ reference\ isodose}}{\boldsymbol{Target\ volume}}$$

I have included the RTOG homogeneity index as defined below (28).

$$\boldsymbol{Homogeneity\ index} = \frac{\boldsymbol{Maximum\ isodose}}{\boldsymbol{Reference\ isodose}}$$

Finally, the gradient index is calculated as the ratio of the volume covered by a reference isodose to the volume covered by the prescription isodose. In this study, I considered the 50% (18.125Gy) isodose.

$$\boldsymbol{Gradient\ index} = \frac{\boldsymbol{Volume\ of\ reference\ isodose}}{\boldsymbol{Volume\ of\ prescription\ isodose}}$$

3.4.6 Statistical analysis

Given the small patient group, a limited number of exploratory ANOVA analyses were undertaken by statistician Karen Thomas to explore differences in dose metric between plan types. ANOVA models were fitted using plan type and patient ID as factors to account for the paired nature of the data. Standardised residuals were examined visually using histograms to check for normality.

The 8 dose metrics investigated were rectum V36Gy, bladder V37Gy, number of constraints missed, rectum D50%, rectum D1cc, conformity index (36.25), homogeneity index and conformity index (18.125). These are indicated in the red boxes in Table 3.4. The testing was limited to avoid 'data dredging', especially as individually testing the constraints in Table 1 would not be informative as they are dependent on the method of optimisation. The metrics for statistical analysis were chosen to assess conformity of the plan, the overall meeting of constraints and the two most challenging constraints to achieve- rectum V36Gy and bladder V37Gy. For models where the dose metric differed by plan type with $p<0.05$, post hoc tests were done to tests for differences between the 7-field IMRT MR-Linac plans compared to each of the other 5 plan

types. With 5 comparisons, a threshold of $p<0.01$ was used to define significance.

The 7-field MR-Linac plan was used as the reference plan for this study as preliminary work by the RMH physics team had determined that 7-field IMRT would be suitable for standard fractionation within the PRISM trial (see Chapter 6), therefore this would be the starting point for SBRT. Using this as the reference plan allows comparison between the field numbers, as well as assessment of variation with the non-MRL plans.

3.5 Results

3.5.1 Patient population

Median age for the ten patients was 72.5 years (range 60 to 78), median presenting PSA was 9.5 ug/L (range 5.2 to 19.4). All patients had T2N0 staged disease with Gleason scoring of Gleason 3+3 (three patients) or Gleason 3+4 (7 patients). None of the patients received androgen deprivation therapy prior to, or during radiotherapy. The median CTV volume for the ten patients included was 56.0cm^3 (range 32.3 to 143.6cm^3).

3.5.2 Dose evaluation

Examples of a 5-, 7- and 9-field MR-Linac IMRT plans for the same patient are shown in Figure 3.2.

Table 3A in the Appendix summarises the full dataset for the number of exceeded constraints and mean metrics (standard deviation in brackets) for each plan type. The constraints used for statistical analysis, as detailed in the Methods, are summarised in Table 3.4.

Clinically acceptable 7-field IMRT MR-Linac plans (see Table 3.4) were achieved in all ten patients. Clinically acceptable plans were also achieved for all ten patients using 9-field IMRT, non MR-Linac 7-field IMRT, non MR-Linac VMAT and CyberKnife treatment. Clinically acceptable 5-field IMRT MR-Linac plans were only possible in seven of the ten patients- for one patient, Monaco TPS was unable to complete the optimisation step, for two patients there was a major variation for the rectal V36Gy.

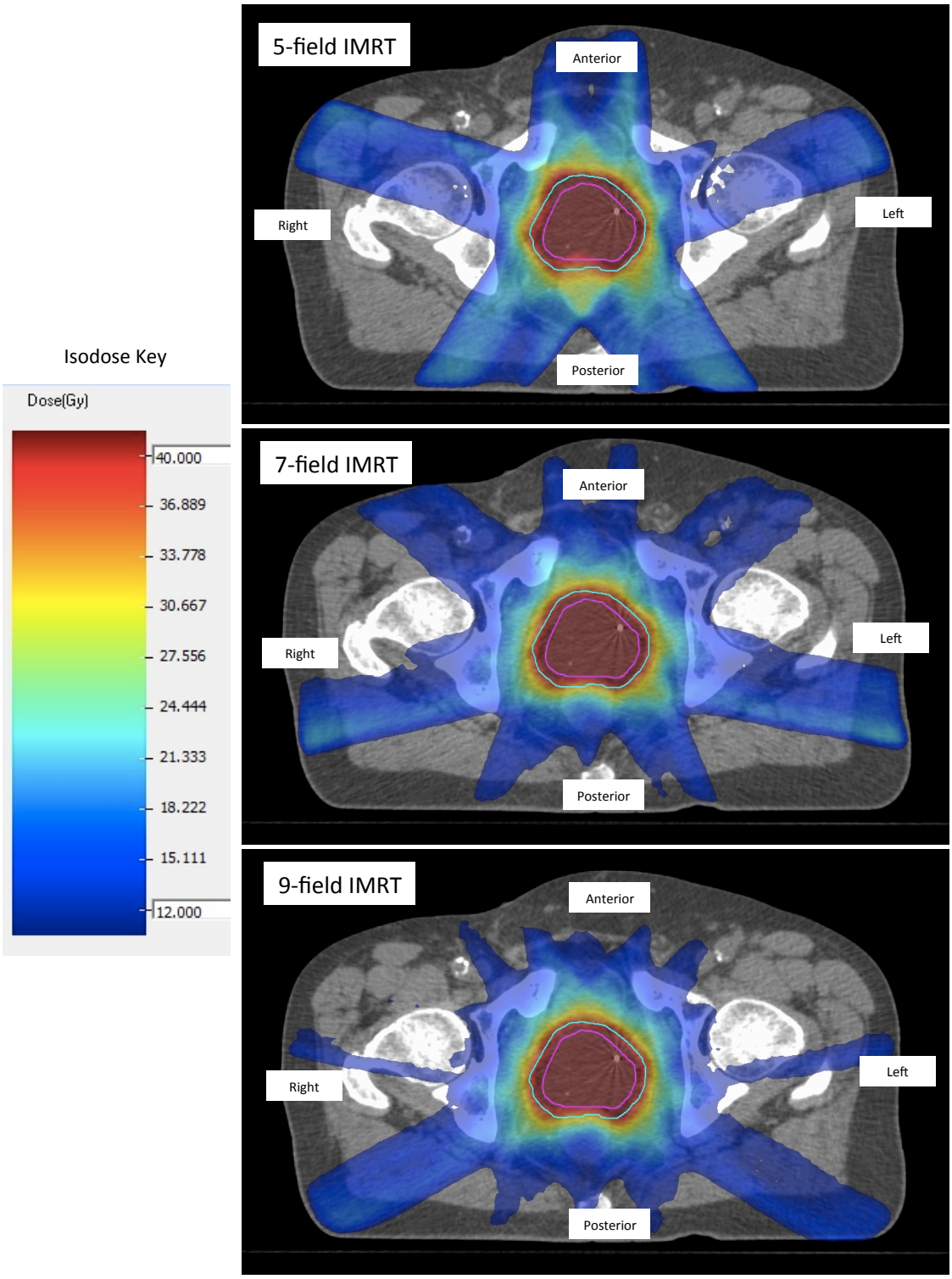

Figure 3.19- Examples of a 5-field, 7-field and 9-field prostate SBRT plan for the MR-Linac. Axial slices are shown here at the corresponding level of each plan for the same patient. Pink outline- prostate, blue outline- PTV. There is improved dose conformity to the target seen with 7 and 9-field treatment compared to the 5-field plan. In addition, the distant dose reduces with increasing beam numbers.

PLAN TYPE	5-field IMRT MRL	7-field IMRT MRL	9-field IMRT MRL	7-field IMRT Elekta Agility (non-MRL)	Cyber-Knife	VMAT (non-MRL)
Number of plans optimised	9§	10	10	10	10	10
Number of clinically acceptable plans	7	10	10	10	10	10
Constraints exceeded (16 per plan)	37/144§*	23/160	21/160	19/160	32/160	22/160
Rectum						
V36Gy (%) (Constraint <1cc)	1.5* (0.8)	0.9 (0.5)	0.8 (0.5)	1.3 (0.5)	1.5* (0.3)	0.9 (0.4)
D50% (Gy) (no trial defined constraint)	14.9 (4.8)	14.3 (3.2)	14.1 (3.7)	14.3 (3.4)	11.7* (4.5)	9.5* (4.0)
D1cc (Gy) (no trial defined constraint)	36.4* (1.0)	35.6 (1.0)	35.4 (1.2)	36.5* (1.0)	36.9* (0.5)	35.8 (0.5)
Bladder						
V37Gy (cc) (constraint < 10cc)	8.5* (2.8)	6.5 (2.4)	6.4 (2.4)	7.4* (2.2)	5.9 (2.4)	6.0 (2.3)
Conformity measures						
Conformity index 36.25Gy	1.1 (0.1)	1.1 (0.1)	1.1 (0.1)	1.2* (0.0)	1.0 (0.0)	1.0 (0.1)
Conformity index 18.125Gy	6.6* (1.1)	4.6 (0.5)	4.1 (0.4)	5.3* (0.7)	3.8* (0.3)	4.0* (0.2)
Homogeneity index	1.3* (0.0)	1.3 (0.0)	1.3 (0.0)	1.3 (0.0)	1.3 (0.0)	1.2* (0.0)

Table 3.4- Comparison of planning techniques for prostate SBRT- summary of the number of constraints exceeded and the mean (standard deviation) values for each plan type used for statistical analysis. Values are reported to 1 decimal place. The reference plan for comparison, the 7-field MR-Linac plan, is highlighted in red. * denotes statistically significant compared to the 7-field IMRT MR-Linac plan using $p<0.01$.

Key: §2 of which included a major variation to the PACE protocol constraints.
V(X)Gy- volume of target/organ receiving at least XGy.
D(X)%- minimum dose received by X% of the target/organ.
Dmax- maximum dose (Gy) received by target/organ.

To demonstrate the difference with increasing field numbers, the mean rectum V36Gy and V37Gy for the MR-linac plans are further summarised in graph format in Figures 3.3 and 3.4.

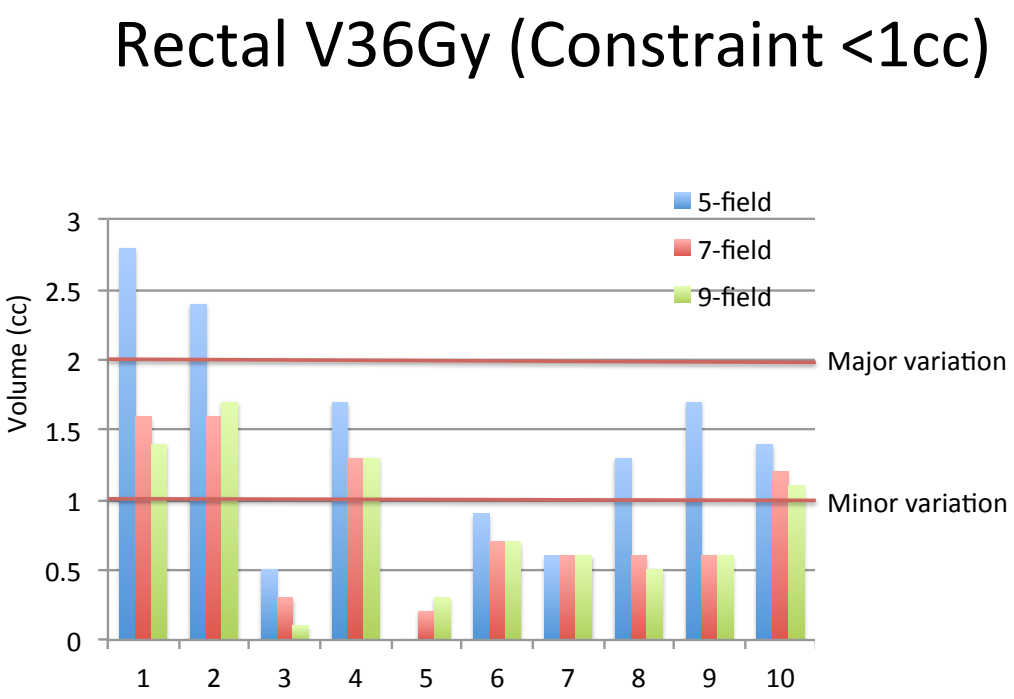

Figure 20.3- Bar chart summarising the rectal V36Gy (volume of rectum in cc receiving 36Gy or more) for each patient with the 5, 7 and 9-field MR-Linac IMRT plan. The constraint for optimisation is V36Gy <1cc. Major variations are seen for 5-field IMRT in patients 1 and 2, a plan could not be optimised for patient 5.

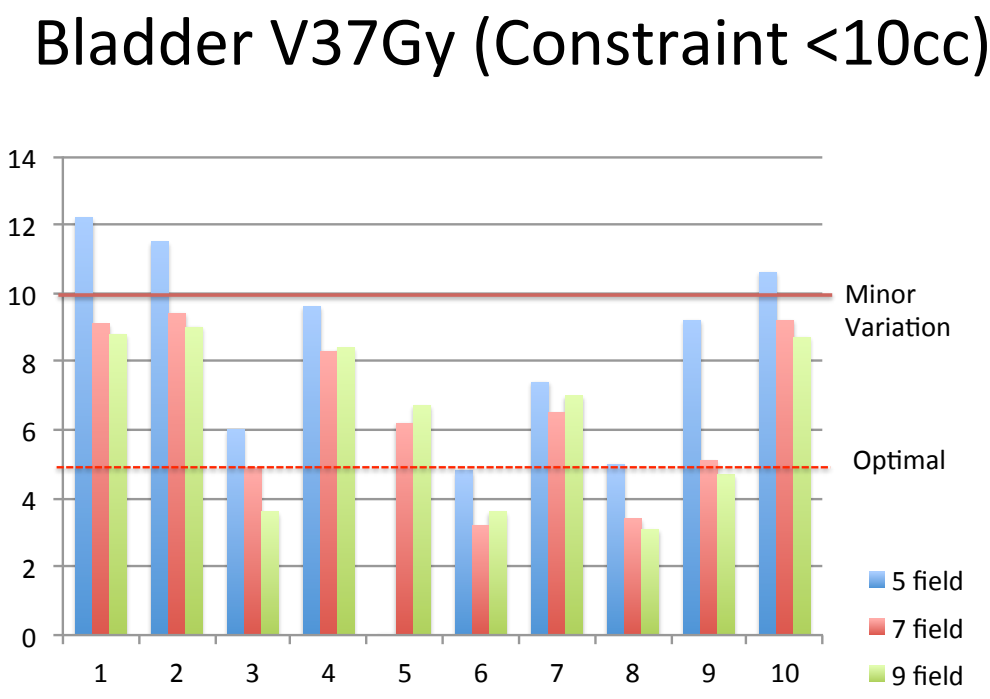

Figure 3.21- Bar chart summarising the bladder V37Gy (volume of bladder in cc receiving 37Gy or more) for each patient with the 5, 7 and 9-field MR-Linac IMRT plan. The constraint for optimisation is V37Gy <10cc.

3.5.3 Statistical analysis

The exploratory ANOVA analyses, as detailed in the Methods (Section 3.4.6) are summarised in Table 3.4. For the MR-Linac, 5-field IMRT MR-Linac plans performed significantly worse in six of out the eight metrics tested compared to 7-field IMRT. No statistically significant differences were seen between 9-field and 7-field IMRT MR-Linac plans.

7-field IMRT MR-Linac plans had significantly lower rectal doses compared to CyberKnife plans. No significant differences were seen between 9-field IMRT MR-Linac plans and non MR-Linac VMAT plans compared to 7-field IMRT.

3.6 Discussion

Our results demonstrate that it is feasible to create clinically acceptable plans for prostate SBRT on the MR-Linac. In addition, these plans are comparable dosimetrically to other methods of RT delivery. A number of metrics have been used here which take into account target coverage as well as the sparing of normal tissues. Target coverage, although not assessed statistically, was comparable with all six plan types (Table 3A, Appendix). A higher PTV D_{max} was seen across all the MR-Linac plans (Table 3A, Appendix), which appears to be a feature of the Monaco TPS. It must be considered that clinically achievable plans do not equate to feasible delivery, which can only be assessed once treatment for the MR-Linac is well established.

Clinical planning for the MR-Linac exploring the impact of the magnetic field has been examined for other tumour sites (29).The influence of the magnetic field due to the Lorentz force on secondary electrons, can create hot spots at air-tissue interfaces due to the electron return effect, more significant for lung cancer (23, 29) and increase the skin dose (29-31) particularly relevant for lung, breast and head and neck cancer. Given these previous findings, the skin D_{max} was assessed here, however the 7- and 9-field MR-Linac plans did not show an increased skin dose compared to other treatment techniques (see Table 3A, Appendix). None of the imaging used in this study had an air filled rectum, further datasets would therefore be required to ascertain whether hot spots are seen between a prostate and rectum distended with gas.

Reviewing the three MR-Linac beam arrangements, the 5-field IMRT appears inferior, as displayed in Table 3.4 despite only nine plans being optimised, a significantly higher number of constraints were missed. Dose to the rectum, bladder and femoral heads was higher which was significant for the rectal V36Gy, rectal D1cc, bladder V37Gy. As expected given the lower number of beams, the 50% isodose conformity index, homogeneity index and gradient index were inferior for this beam arrangement. This is visually represented in Figure 3.2, where the high isodose coverage is not as conformal to the target and dose fall off is inferior compared to the 7- and 9-field IMRT plan.

Monaco TPS was unable to complete the optimisation for a particular patient's 5-field MR-Linac IMRT plan; this was unexpected as the optimiser should produce a final plan, even if this does not meet planning constraints. On further investigation and discussion with Elekta, it transpired that this was a software bug, where the limited number of segments for an SBRT plan was not taken into account during the first step of optimisation, therefore the TPS enters multiple loops, unable to generate a plan. Although this has been corrected in subsequent software upgrades, the new plan for this patient has not been included as changes in the software during the upgrade would invalidate the other plans optimised and comparison between software versions is not appropriate.

It is anticipated that an increasing number of beam directions, and therefore modulations, will increase the plan quality (25-27). However we would expect there to be a point at which the benefit plateaus (25, 27), depending on the

optimal modulation required for a patient. This is relevant when choosing beam arrangement as increasing beam numbers equates to increased delivery time. There was no statistical difference between the 7- and 9-field IMRT plans for the MR-Linac, this is also demonstrated in Figures 3.3 and 3.4, where similar values are seen for the rectal V26Gy and bladder V37Gy. Visual assessment of the 7- and 9-field plans showed no discernible differences and clinically, the 9-field MR-Linac would have no additional benefit.

SBRT requires a highly conformal dose profile. When considering the non MR-Linac treatment platforms, the CyberKnife machine uses multiple non-isocentric, non-coplanar treatment beams, we would therefore expect high conformity with a steep drop off beyond the target, as seen in Table 3.4, particularly with the conformity index 18.125Gy and Gradient index. However the conformity measures for Cyberknife are very similar to the 9-field MRL plan and standard linear accelerator plan. Although VMAT could also give a better dose coverage as treatment is delivered from all angles, there are advantages to delivering increased modulation from particular beam orientation, for example to allow OAR sparing. We found no consistent improvement with the VMAT plans compared to 7-field MR-Linac IMRT, however, the rectal D50% was lower and the conformity index was similar to that for CyberKnife and 9-field IMRT on the MR-Linac.

There are previously reported direct comparisons of CyberKnife and standard linear accelerator plans. Although initial studies reported a higher conformal dose with CyberKnife (32) with hypofractionated schedules, other dosimetric

comparisons have shown similar conformity index to VMAT and IMRT (33). Seppala et al (33) reported a dosimetric comparison describing similar dosimetric parameters for CyberKnife, non coplanar IMRT, RapidArc and VMAT, although as expected, the CyberKnife treatment time would be significantly longer.

The data presented here is important for guiding treatment planning for prostate SBRT, particularly the three beam arrangements assessed for the MR-Linac. For each of the plan types, the same imaging sets and contours are used which eliminates the effect of delineation variability. However, meaningful comparisons between the treatment modalities are limited for a number of reasons. In particular when comparing delivery technique, the plan quality will vary as a result of the differences in the TPS, optimisation techniques, dose constraint priorities and planner experience. The comparison made in this study was between my relatively inexperienced planning, to those created by planning physicists. If anything, we would expect this to bias the comparison against the MR-Linac plans.

I have not assessed the treatment delivery time here, but this is pertinent for any comparison- the 'beam on' time, in addition to the total time the patient is on the treatment couch. This takes into account any re-planning required and is of clinical significance due to the effect on intrafraction prostate motion. From a practical point of view, time is relevant for patient comfort, patient throughput and target motion, as demonstrated in Chapter 2.

The plans created here have also not been assessed in the context of the actual dose delivery on the day, which is dependent on the accuracy of image guidance. For example a standard linear accelerator plan will involve fiducial matching followed by treatment with the same reference treatment plan each day, without any intrafractional imaging. MR-Linac treatment, using the current workflow would be delivered using a new online plan each day (see Chapter 6), whilst CyberKnife utilises orthogonal x-ray tracking of fiducial markers prior to each beam. Although most published series for prostate SBRT describe the use of CyberKnife, several groups have reported similar toxicity and biochemical outcomes with SBRT delivered on a standard linear accelerator (9, 34). At our institution, the 36.25Gy in 5 fraction schedule has been delivered on the Cyberknife machine and a standard linear accelerator as part of the PACE trial. Treatment on the MR-Linac has so far included the standard fractionation schedule 60 Gy in 20 fractions (Chapter 6), with the intention of using extreme hypofractionated schedules in the future, where the benefits of the MR-Linac can be fully realised.

3.7 Conclusions

MR-Linac IMRT plans for prostate SBRT achieved the PACE trial constraints in all patients with 9-field appearing similar to 7-field IMRT. 5-field IMRT in this set-up appears inferior for the MRL. All platforms considered here produced clinically acceptable plans. Further work is needed for the dosimetric validation and feasibility of MR-Linac delivery.

3.8 References

1) Fowler J, Chappell R, Ritter M. Is α/β for prostate tumors really low? International Journal of Radiation Oncology, Biology and Physics. 2001;50(4):1021-31.
2) Tree AC, Alexander EJ, Van As NJ, Dearnaley DP, Khoo V. Biological Dose Escalation and Hypofractionation: What is There to be Gained and How Will it Best be Done? Clinical Oncology. 2013;25(8):483-98.
3) Dearnaley D, Syndikus I, Mossop H, Khoo V, Birtle A, Bloomfield D, et al. Conventional versus hypofractionated high-dose intensity-modulated radiotherapy for prostate cancer: 5-year outcomes of the randomised, non-inferiority, phase 3 CHHiP trial. The Lancet Oncology. 2016.
4) Miralbell R, Roberts SA, Zubizarreta E, Hendry JH. Dose-Fractionation Sensitivity of Prostate Cancer Deduced From Radiotherapy Outcomes of 5,969 Patients in Seven International Institutional Datasets: α/β = 1.4 (0.9–2.2) Gy. International Journal of Radiation Oncology, Biology and Physics. 2012;82(1):e17-e24.
5) Aluwini S, Pos F, Schimmel E, Krol S, van der Toorn PP, de Jager H, et al. Hypofractionated versus conventionally fractionated radiotherapy for patients with prostate cancer (HYPRO): late toxicity results from a randomised, non-inferiority, phase 3 trial. The Lancet Oncology. 2016;17(4):464-74.
6) Incrocci L, Wortel RC, Alemayehu WG, Aluwini S, Schimmel E, Krol S, et al. Hypofractionated versus conventionally fractionated radiotherapy for patients with localised prostate cancer (HYPRO): final efficacy results from a randomised, multicentre, open-label, phase 3 trial. The Lancet Oncology. 2016.
7) Aluwini S, Pos F, Schimmel E, van Lin E, Krol S, van der Toorn PP, et al. Hypofractionated versus conventionally fractionated radiotherapy for patients with prostate cancer (HYPRO): acute toxicity results from a randomised non-inferiority phase 3 trial. The Lancet Oncology. 2015;16(3):274-83.
8) Kothari G, Loblaw A, Tree AC, van As NJ, Moghanaki D, Lo SS, et al. Stereotactic Body Radiotherapy for Primary Prostate Cancer. Technology in cancer research & treatment. 2018;17:1533033818789633-.
9) Loblaw A, Cheung P, D'Alimonte L, Deabreu A, Mamedov A, Zhang L, et al. Prostate stereotactic ablative body radiotherapy using a standard linear accelerator: Toxicity, biochemical, and pathological outcomes. Radiotherapy and Oncology. 2013;107(2):153-8.
10) King CR, Brooks JD, Gill H, Presti Jr JC. Long-Term Outcomes From a Prospective Trial of Stereotactic Body Radiotherapy for Low-Risk Prostate Cancer. International Journal of Radiation Oncology, Biology and Physics. 2012;82(2):877-82.
11) Boike TP, Lotan Y, Cho LC, Brindle J, DeRose P, Xie X-J, et al. Phase I Dose-Escalation Study of Stereotactic Body Radiation Therapy for Low- and Intermediate-Risk Prostate Cancer. Journal of Clinical Oncology. 2011;29(15):2020-6.
12) Hannan R, Tumati V, Xie XJ, Cho LC, Kavanagh BD, Brindle J, et al. Stereotactic body radiation therapy for low and intermediate risk prostate

cancer-Results from a multi-institutional clinical trial. European journal of cancer (Oxford, England : 1990). 2016;59:142-51.
13) Madsen BL, Hsi RA, Pham HT, Fowler JF, Esagui L, Corman J. Stereotactic hypofractionated accurate radiotherapy of the prostate (SHARP), 33.5 Gy in five fractions for localized disease: first clinical trial results. International Journal of Radiation Oncology, Biology and Physics 2007;67(4):1099-105.
14) King CR, Freeman D, Kaplan I, Fuller D, Bolzicco G, Collins S, et al. Stereotactic body radiotherapy for localized prostate cancer: Pooled analysis from a multi-institutional consortium of prospective phase II trials. Radiotherapy and Oncology. 2013;109(2):217-21.
15) Widmark A, Gunnlaugsson A, Beckman L, Thellenberg-Karlsson C, Hoyer M, Lagerlund M, et al. OC-0599: Ultrahypofractionation for prostate cancer: Outcome from the Scandinavian phase 3 HYPO-RT-PC trial. Radiotherapy and Oncology. 2018;127:S314.
16) Widmark A, Gunnlaugsson A, Beckman L, Thellenberg-Karlsson C, Hoyer M, Lagerlund M, et al. Extreme Hypofractionation versus Conventionally Fractionated Radiotherapy for Intermediate Risk Prostate Cancer: Early Toxicity Results from the Scandinavian Randomized Phase III Trial “HYPO-RT-PC”. International Journal of Radiation Oncology, Biology and Physics. 2016;96(5):938-9.
17) Hoskin P, Rojas A, Ostler P, Hughes R, Alonzi R, Lowe G, et al. High-dose-rate brachytherapy with two or three fractions as monotherapy in the treatment of locally advanced prostate cancer. Radiotherapy and Oncology. 2014;112(1):63-7.
18) Hoskin P, Rojas A, Ostler P, Hughes R, Alonzi R, Lowe G, et al. High-dose-rate brachytherapy alone given as two or one fraction to patients for locally advanced prostate cancer: Acute toxicity. Radiotherapy and Oncology. 2014;110(2):268-71.
19) Prada PJ, Jimenez I, González-Suárez H, Fernández J, Cuervo-Arango C, Mendez L. High-dose-rate interstitial brachytherapy as monotherapy in one fraction and transperineal hyaluronic acid injection into the perirectal fat for the treatment of favorable stage prostate cancer: Treatment description and preliminary results. Brachytherapy. 2012;11(2):105-10.
20) Dankulchai P, Alonzi R, Lowe GJ, Burnley J, Padhani AR, Hoskin PJ. Optimal source distribution for focal boosts using high dose rate (HDR) brachytherapy alone in prostate cancer. Radiotherapy and Oncology. 2014;113(1):121-5.
21) King CR, Brooks JD, Gill H, Pawlicki T, Presti JC, Cotruz C. Stereotactic Body Radiotherapy for Localized Prostate Cancer: Interim Results of a Prospective Phase II Clinical Trial. International Journal of Radiation Oncology, Biology and Physics. 2009;73.
22) Raaijmakers AJE, Raaymakers BW, Meer Svd, Lagendijk JJW. Integrating a MRI scanner with a 6 MV radiotherapy accelerator: impact of the surface orientation on the entrance and exit dose due to the transverse magnetic field. Physics in Medicine and Biology. 2007;52(4):929.
23) Raaymakers BW, Raaijmakers AJE, Kotte ANTJ, Jette D, Lagendijk JJW. Integrating a MRI scanner with a 6 MV radiotherapy accelerator: dose deposition in a transverse magnetic field. Physics in Medicine and Biology. 2004;49(17):4109.

24) Jette D. Magnetic fields with photon beams: Monte Carlo calculations for a model magnetic field. Medical Physics. 2000;27(12):2726-38.
25) Pirzkall A, Carol MP, Pickett B, Xia P, Roach M, 3rd, Verhey LJ. The effect of beam energy and number of fields on photon-based IMRT for deep-seated targets. Int J Radiat Oncol Biol Phys. 2002;53(2):434-42.
26) Cahlon O, Hunt M, Zelefsky MJ. Intensity-Modulated Radiation Therapy: Supportive Data for Prostate Cancer. Seminars in Radiation Oncology. 2008;18(1):48-57.
27) Derbyshire SJ, Morgan AM, Thompson RCA, Henry AM, Thwaites DI. Optimal planning parameters for simultaneous boost IMRT treatment of prostate cancer using a Beam Modulator™. Reports of Practical Oncology & Radiotherapy. 2009;14(6):205-13.
28) Feuvret L, Noel G, Mazeron JJ, Bey P. Conformity index: a review. International Journal of Radiation Oncology, Biology and Physics. 2006;64(2):333-42.
29) Bainbridge HE, Menten MJ, Fast MF, Nill S, Oelfke U, McDonald F. Treating locally advanced lung cancer with a 1.5 T MR-Linac – Effects of the magnetic field and irradiation geometry on conventionally fractionated and isotoxic dose-escalated radiotherapy. Radiotherapy and Oncology. 2017;125(2):280-5.
30) Menten MJ, Fast MF, Nill S, Kamerling CP, McDonald F, Oelfke U. Lung stereotactic body radiotherapy with an MR-linac - Quantifying the impact of the magnetic field and real-time tumor tracking. Radiotherapy and Oncology. 2016;119(3):461-6.
31) van Heijst TC, den Hartogh MD, Lagendijk JJ, van den Bongard HJ, van Asselen B. MR-guided breast radiotherapy: feasibility and magnetic-field impact on skin dose. Physics in Medicine and Biology. 2013;58(17):5917-30.
32) Hossain S, Xia P, Huang K, Descovich M, Chuang C, Gottschalk AR, et al. Dose Gradient Near Target–Normal Structure Interface for Nonisocentric CyberKnife and Isocentric Intensity-Modulated Body Radiotherapy for Prostate Cancer. International Journal of Radiation Oncology, Biology and Physics. 2010;78(1):58-63.
33) Seppälä J, Suilamo S, Tenhunen M, Sailas L, Virsunen H, Kaleva E, et al. Dosimetric Comparison and Evaluation of 4 Stereotactic Body Radiotherapy Techniques for the Treatment of Prostate Cancer. Technology in cancer research & treatment. 2017;16(2):238-45.
34) D'Agostino G, Franzese C, De Rose F, Franceschini D, Comito T, Villa E, et al. High-quality Linac-based Stereotactic Body Radiation Therapy with Flattening Filter Free Beams and Volumetric Modulated Arc Therapy for Low–Intermediate Risk Prostate Cancer. A Mono-institutional Experience with 90 Patients. Clinical Oncology. 2016;28(12):e173-e8.

3.9 Chapter 3 Appendix

Table 3A summarises the number of exceeded constraints and mean metrics (standard deviation in brackets) for each plan type.

PLAN TYPE	5-field IMRT MRL	7-field IMRT MRL	9-field IMRT MRL	7-field IMRT Elekta Agility (non-MRL)	Cyber-Knife	VMAT (non-MRL)
Number of plans optimised	9§	10	10	10	10	10
Number of clinically acceptable plans	7	10	10	10	10	10
Constraints exceeded (16 per plan)	37/144§*	23/160	21/160	19/160	32/160	22/160
PTV						
V36.25Gy (%) (constraint ≥ 95%)	96.3 (1.4)	96.0 (1.0)	96.2 (1.0)	98.1 (1.1)	95.9 (0.8)	96.1 (1.6)
D98% (Gy) (constraint ≥ 34.4Gy)	35.6 (0.6)	35.3 (0.5)	35.7 (1.3)	36.4 (0.8)	35.5 (0.4)	35.5 (0.6)
Dmax (Gy) (constraint <48Gy)	48.4 (1.6)	46.6 (0.9)	46.5 (1.0)	45.7 (0.8)	45.5 (0.9)	45.2 (1.1)
D2% (Gy) (constraint <42.8Gy)	46.7 (1.3)	44.8 (0.8)	44.6 (0.9)	43.7 (0.5)	44.7 (1.0)	44.3 (1.3)
Mean dose (Gy) (no trial defined constraint)	41.6 (0.5)	41.4 (1.6)	40.8 (0.5)	40.6 (0.3)	Not recorded	41.1 (0.5)
CTV						
V40Gy (%) (constraint ≥ 95%)	95.4 (1.0)	95.3 (0.7)	95.2 (0.4)	95.0 (0.0)	91.6 (8.6)	95.7 (1.4)
Mean dose (Gy) (no trial defined constraint)	43.3 (0.6)	42.3 (0.5)	42.2 (0.7)	41.5 (0.3)	Not recorded	42.8 (0.9)
Rectum						
V36Gy (%) (Constraint <1cc)	1.5* (0.8)	0.9 (0.5)	0.8 (0.5)	1.3 (0.5)	1.5* (0.3)	0.9 (0.4)
V18.1Gy (%) (constraint <50%)	44.9 (9.0)	37.5 (7.1)	36.8 (8.1)	38.8 (7.6)	33.2 (9.6)	32.2 (5.8)
V29Gy (%) (constraint <20%)	13.9 (3.4)	9.3 (2.0)	9.4 (2.5)	9.3 (1.9)	11.8 (3.1)	11.8 (3.7)
D50% (Gy) (no trial defined constraint)	14.9 (4.8)	14.3 (3.2)	14.1 (3.7)	14.3 (3.4)	11.7* (4.5)	9.5* (4.0)
D1cc (Gy)	36.4*	35.6	35.4	36.5*	36.9*	35.8

(no trial defined constraint)	(1.0)	(1.0)	(1.2)	(1.0)	(0.5)	(0.5)
Bladder						
V18.1Gy (%) (constraint < 40%)	27.8 (10.4)	23.0 (7.9)	22.2 (7.4)	24.5 (8.2)	25.9 (9.3)	20.2 (7.0)
V37Gy (cc) (constraint < 10cc)	8.5* (2.8)	6.5 (2.4)	6.4 (2.4)	7.4* (2.2)	5.9 (2.4)	6.0 (2.3)
Femoral head						
Left V14.5Gy (%) (constraint < 5%)	4.3 (2.0)	0.5 (0.6)	0.4 (0.7)	0.5 (0.7)	3.6 (11.2)	0.3 (0.4)
Right V14.5Gy (%) (constraint < 5%)	4.8 (1.7)	0.7 (0.8)	0.3 (0.4)	0.4 (0.4)	5.2 (9.4)	0.2 (0.3)
Penile bulb						
V29.5Gy (%) (constraint < 50%)	10.2 (6.6)	10.9 (6.2)	11.2 (6.5)	14.9 (7.9)	13.9 (7.3)	9.7 (6.1)
Bowel						
V18.1Gy (cc) (constraint < 5cc)	0.2 (0.5)	0.2 (0.6)	0.2 (0.6)	0.4 (1.1)	0.5 (1.2)	0.1 (0.2)
V30Gy (cc) (constraint <1cc)	0.0 (0.1)	0.0 (0.1)	0.0 (0.1)	0.1 (0.2)	0.1 (0.2)	0.0 (0.0)
Skin						
Dmax (Gy) (no trial defined constraint)	14.4 (2.5)	11.4 (1.7)	12.0 (3.4)	11.4 (2.4)	17.0 (1.6)	10.8 (1.8)
Conformity measures						
Conformity index 36.25Gy	1.1 (0.1)	1.1 (0.1)	1.1 (0.1)	1.2* (0.0)	1.0 (0.0)	1.0 (0.1)
Conformity index 18.125Gy	6.6* (1.1)	4.6 (0.5)	4.1 (0.4)	5.3* (0.7)	3.8* (0.3)	4.0* (0.2)
Homogeneity index	1.3* (0.0)	1.3 (0.0)	1.3 (0.0)	1.3 (0.0)	1.3 (0.0)	1.2* (0.0)
Gradient Index V18.125Gy/ V36.25Gy	6.2 (0.8)	4.3 (0.3)	3.8 (0.3)	4.4 (0.5)	3.8 (0.2)	3.9 (0.2)

Table 3A- Comparison of planning techniques for prostate SBRT- summary of the number of constraints exceeded and the mean (standard deviation) values for each plan type. Values are reported to 1 decimal place. The metrics used for statistical analysis are indicated in the red boxes, where * denotes statistically significant compared to the 7-field IMRT MR-Linac plan using $p<0.01$.

Key:

§2 of which included a major variation to the PACE protocol constraints. V(X)Gy- volume of target/organ receiving at least XGy.
D(X)%- minimum dose received by X% of the target/organ.
Dmax- maximum dose (Gy) received by target/organ.

Chapter 4- Sequence optimisation for prostate delineation

4.1 Publications

The data from this chapter has been published in the following articles;

Improving fiducial and prostate capsule visualisation for radiotherapy planning using MRI
Angela Pathmanathan, Maria Schmidt, Douglas Brand, Evanthia Kousi, Nicholas van As, Alison Tree. Journal of Applied Clinical Medical Physics 2019 Mar; 20(3):27-36

Comparison of prostate delineation on multi-modality imaging for MR-guided radiotherapy
Angela Pathmanathan, Helen McNair, Maria Schmidt, Douglas Brand, Louise Delacroix, Cynthia Eccles, Alexandra Gordon, Trina Herbert, Nicholas van As, Robert Huddart, Alison Tree. British Journal of Radiology 2019 Mar; 92(1095):20180948

In addition data was accepted as a poster at ESTRO 37, April 2018;

Comparison of prostate delineation on multi-modality imaging for MR-guided radiotherapy EP-1613
Angela Pathmanathan, Maria Schmidt, Douglas Brand, Louise Delacroix, Cynthia Eccles, Alexandra Gordon, Trina Herbert, Helen McNair, Nicholas van As, Robert Huddart, Alison Tree. Radiotherapy and Oncology 2018; 127: S868-S869.

4.2 Introduction

As discussed in Section 1.2, MRI provides several advantages during the planning process but there are a number of available sequences, each providing differing benefits. The T2*W sequence allows not only visualisation of the fiducial markers but also improved contrast for the prostate. In this chapter I examine the T2*W sequence and investigate whether it is possible to use this sequence alone in prostate studies with respect to the ability to locate marker positions and the ability to provide enough contrast for prostate volume outlining.

With relative unfamiliarity of MRI compared to CT, MRI must be introduced carefully into the RT planning process, involving all members of the inter-professional team, together with appropriate training [1]. Treatment radiographers are experienced in reviewing the prostate position on cone-beam CT (CBCT) for image guidance prior to treatment delivery. Radiotherapy services benefit from the expanded role of treatment radiographers including radiographer led delineation of the target or organs at risk which can shorten the treatment planning process [2]. At our institution, following a training programme specialised treatment radiographers outline the prostate and SV on RT planning CT prior to clinician review and sign off.

With the installation and use of the Elekta MR-Linac [3], we wish to extend this role for MR-guided RT. There are three additional radiographer responsibilities required for adaptive replanning- contouring during the planning stage, online recontouring and intrafraction target motion monitoring.

Here I will assess the accuracy of radiographer contours and interobserver variability of therapeutic radiographers using three imaging types; CT, T2-weighted (T2W) and T2*W MRI.

4.3 Aims of Chapter 4

In this chapter I will aim to assess clinician and radiographer prostate contours on CT, T2W and T2*W imaging.

My hypothesis is that the use of MR imaging, particularly T2*W MRI, will improve the consistency of clinician and radiographer prostate contours and improve the accuracy of radiographer contours.

To test this hypothesis I will:

1) Assess the interobserver variability of clinician contours on CT, T2W MRI and T2*W MRI
2) Assess the interobserver variability of radiographer contours on CT, T2W MRI and T2*W MRI
3) Assess the accuracy of radiographer contours compared to a gold standard clinician combination STAPLE contour
4) Establish any difference in the time taken for radiographer contouring and confidence in contouring for CT, T2W MRI and T2*W MRI

4.4 Materials and Methods

4.4.1 Patient population

Ten patients with localised prostate cancer treated with SBRT at the Royal Marsden Hospital, Sutton from January 2015 to December 2016 were selected. These patients received treatment consecutively within the Prostate Advances in Comparative Evidence (PACE) trial (NCT01584258). PACE A randomises patients between prostatectomy and stereotactic body radiotherapy (SBRT) to a dose of 36.25 Gy in 5 fractions, and PACE B randomised patients between SBRT and conventionally fractionated RT, either 62 Gy in 20 fractions or 78 Gy in 39 fractions. Patients did not receive androgen deprivation therapy.

Each patient had three imaging datasets- RT planning CT, T2W and T2*W MRI sequences as described below. Examples are seen in Figure 4.1. A minimum of one week prior to planning imaging, three 1.0 x 3.0 mm knurled gold markers were inserted using an 18 gauge, 20 cm needle. Fiducial positions were used to fuse the CT and MR scans and for position verification prior to each treatment.

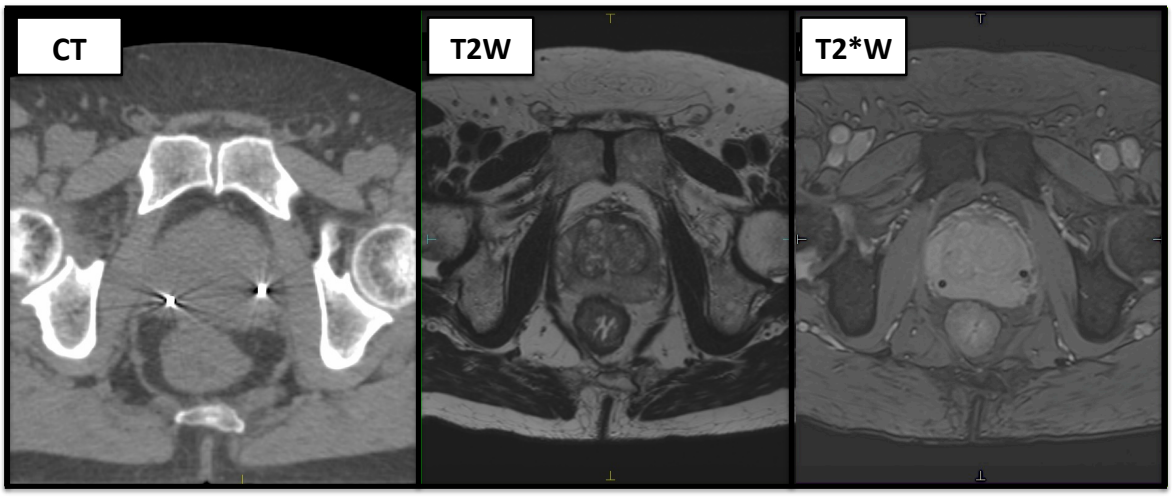

Figure 4.22- The three imaging sequences used for prostate contours showing the corresponding levels for the same patient. From left to right (i) CT imaging- fiducials seen as bright markers with surrounding artifact (ii) T2W MRI sequence- fiducials not visible (iii) T2*W MRI sequence- fiducials seen as dark void areas.

4.4.2 Planning CT acquisition

At the Royal Marsden Hospital, all patients receiving RT in PACE have a RT planning CT followed, on the same day, by a planning MRI scan. Patients are scanned with bladder filling and rectal preparation as per institutional guidelines and no intravenous contrast is used. Patients receive two days of rectal preparation with enemas prior to planning, and an enema just before their planning CT scan. The CT scan incorporates axial slices of 1.5 mm from mid lumbar spine to below the obturator foramen.

4.4.3 Planning MRI acquisition

Prostate MRI examinations were acquired using a 1.5T MR scanner (Siemens Aera, Erlangen, Germany), with two 2-dimensional (2D) sequences, covering the prostate volume in 28 adjacent slices (2.5 mm thickness). The two sequences used here, discussed further in Sections 1.2.2 and 1.2.3, were;

a. A standard T2W pulse sequence used in diagnostic MRI of the prostate.
b. The T2*W or “medic” sequence which is gradient-echo-based, thereby maximising the signal loss surrounding the fiducial markers.

Both sequences covered the same volume, centred on the prostate and including at least part of the pelvic bones. Both sequences use the same shimming volume to optimise the magnetic field homogeneity and the manufacturer’s own distortion correction software (in 2D). Parameters of both sequences are provided in Table 4.1.

	T2W Acquisition (2D T2W FSE)	T2*W Acquisition (2D "medic")
FOV readout (phase)	240mm (100%)	240mm (100%)
PE oversampling	60%	60%
Number of Slices	28	28
Slice thickness/gap	2.5mm/ 0	2.5mm/ 0
Acquisition Matrix (phase)	320 (75 %)	256 (75 %)
TE/ TR	110 ms /7210 ms	24 ms /550 ms
Averages	3	2
Orientation	Transaxial	Transaxial
PE direction	Left/Right	Left/Right
Reconstruction Matrix	320 x 32	512 x 512
Receiver Bandwidth	200 Hz/pixel fat-water shift = 0.84mm	230 Hz/pixel fat-water shift = 0.92mm
Pixel size	0.75 mm x 0.75mm	0.47 mm x 0.47 mm
Other	Echo-train length 25, echo spacing 9.98 ms, echo-trains per slice 16.	Combined echoes 5, Flip Angle 28 degrees.
Filters	PrescanNormalise/ DistCorrection 2D	PrescanNormalise/ DistCorrection 2D
Coil Arrangement	Spine coil & Body array	Spine coil & Body array
Total Acquisition Time	2min 46s parallel imaging = 2 (GRAPPA)	6min 4s parallel imaging = 2 (GRAPPA)

Table 4.1- Parameters of MRI Sequences for prostate RT Planning. Abbreviations: FSE- fast spin echo; FOV- field of view; TE- echo time; TR- relaxation time; GRAPPA- GeneRalised Autocalibrating Partial Parallel Acquisition.

4.4.4 Image review and clinician contouring

Visibility of fiducials: Without reference to the CT images, T2W and T2*W images were reviewed by myself to assess the number of fiducial markers visible.

Volume definition: Using Research Monaco 5.19.02 (Elekta AB, Stockholm, Sweden), the prostate contour was delineated on each of the three sequences for all ten patients by three clinicians from the same institution- myself, Dr Douglas Brand and Dr Alison Tree. All three are from the Royal Marsden NHS Foundation trust and experienced with prostate contouring on both CT and MRI. The clinicians were instructed to contour the prostate alone; i.e. excluding the seminal vesicles (SV). Contouring was completed on each dataset independently, without reference to the other two types of imaging. In addition, each observer was blinded to the other clinicians' contours. I created a timetable for each observer (Table 4.2) so that the three sequences for each patient were contoured during three separate sessions, with at least two weeks between each session to minimise recall bias. In addition during each session, there was a mixture of T2W, T2*W and CT image sets contoured.

Patient	Session 1	Session 2	Session 3
1	MR1	MR2	CT
2	MR1	MR2	CT
3	MR1	MR2	CT
4	MR2	CT	MR1
5	MR2	CT	MR1
6	MR2	CT	MR1
7	CT	MR1	MR2
8	CT	MR1	MR2
9	CT	MR1	MR2
10	CT	MR1	MR2

Table 4.2- Table of contouring to ensure a mix of imaging sets during each session and a minimum of two weeks between contours for the same patient

4.4.5 Radiographer contouring

Five therapeutic radiographers from the Royal Marsden NHS Foundation Trust participated in this part of the study. All five were experienced in registration of the prostate using CT during prostate radiotherapy delivery. In addition, two of the observers had experience with prostate delineation on CT imaging. Prior to contouring, I conducted a single training session which included a Powerpoint presentation reviewing the anatomy on each of the three imaging types and access to a printed version of CT, T2W and T2*W 'atlases' with axial contours to refer to. Each reference atlas was created by myself contouring the prostate on the three imaging types for one patient, not included in the study. Contours were additionally checked by consultant Alison Tree. The training session also included instructions for delineation using Research Monaco.

The radiographers delineated the prostate on CT, T2W and T2*W MRI for the same ten patients using the same instructions and timetable as detailed above. In addition, the time taken for delineation was recorded and images were scored from 0-10 for 'image quality' and 'confidence in contouring', where a higher score indicates an improvement.

4.4.6 Assessment of clinician interobserver variability

Creation of the clinician STAPLE contour: I created a simultaneous truth and performance level estimation (STAPLE) contour (see Section 1.6) from the three clinician contours using the command-line available with Monaco ADMIRE software version 2.0 (Elekta AB, Stockholm, Sweden). This was for assessment of inter-observer variability as detailed below and this STAPLE contour was also used as the 'gold standard' clinician contour for the assessment of the radiographer contours in Section 4.4.7. I reviewed all STAPLE contours to ensure they were clinically appropriate.

Clinician contour variability: Clinician inter-observer variability, as a measure of consistency, was assessed for each sequence by comparing each individual clinician contour to the clinician STAPLE contour. I used Monaco ADMIRE to generate a combination of contour comparison indices [4, 5] to analyse the difference between the clinician contours for the same imaging dataset. These are discussed in further detail in the Introduction, Section 1.6.1.

Distance measurements analysed were the Hausdorff distance (HD) and mean distance between contours. Overlap measures analysed were Dice similarity co-efficient (DSC) and Cohen's Kappa. As discussed in Section 1.6.1, a shorter

distance between contours or higher overlap index indicates higher agreement, reduced inter-observer variability, between observers.

Statistical analysis: Using SPSS Statistics version 23, I examined the data using Q-plots. I also carried out the Shapiro-Wilk test, confirming non-normality of the data. I therefore performed a separate Freidman's test for all four delineation metrics, examining for differences across the three imaging modalities. Where significant, I undertook pair-wise group comparison using Wilcoxon's signed rank testing with Bonferroni correction for the three comparisons. A comparison was therefore significant if $p<0.017$.

4.4.7 Assessment of radiographer interobserver variability

Creation of the radiographer STAPLE contour: Using the same method as described above, I created the radiographer STAPLE contour from the five radiographer contours.

Radiographer contour variability: Interobserver variability for the radiographer group was assessed by comparing individual radiographer contours to the radiographer STAPLE contour. As detailed above, Monaco ADMIRE v2.0 was used to generate the comparison measures of HD, mean distance, DSC and Cohen's kappa.

A**ccuracy of radiographer contours**: Accuracy was assessed by comparing each of the individual radiographer contours to the 'gold standard' clinician

STAPLE. Once again, Monaco ADMIRE v2.0 was used to generate the HD, mean distance, DSC and Cohen's kappa.

Statistical analysis: Using GraphPad Prism v7.0d, I performed non-parametric Friedman testing (as for the clinician comparison) with Dunn's test for multiple comparisons. The three imaging comparisons- CT versus T2W, CT versus T2*W and T2W versus T2*W were pre-planned. Values were defined as statistically different if the adjusted p-value was <0.05.

4.5 Results

4.5.1 Image review and clinician contouring

Visibility of fiducials: I reviewed the T2W imaging alone of all patients and found only 3 out of 30 fiducials were correctly identified. Figure 4.2 is an example of the fiducial appearance on T2W MRI when visible. On T2*W imaging, all 30 fiducial markers were visible. However, when I reviewed the CT imaging, it revealed that 1 out of 30 markers was incorrectly identified due to the presence of calcifications creating a similar signal loss. Such calcifications were variable in number and size but were seen in 8 out of the 10 patients. An example is seen in Figure 4.3. In addition, although the appearance of the FM was mostly uniform, some were variable. Review of the CT imaging revealed this to be due to the marker being in a different orientation (example seen in Figure 4.4).

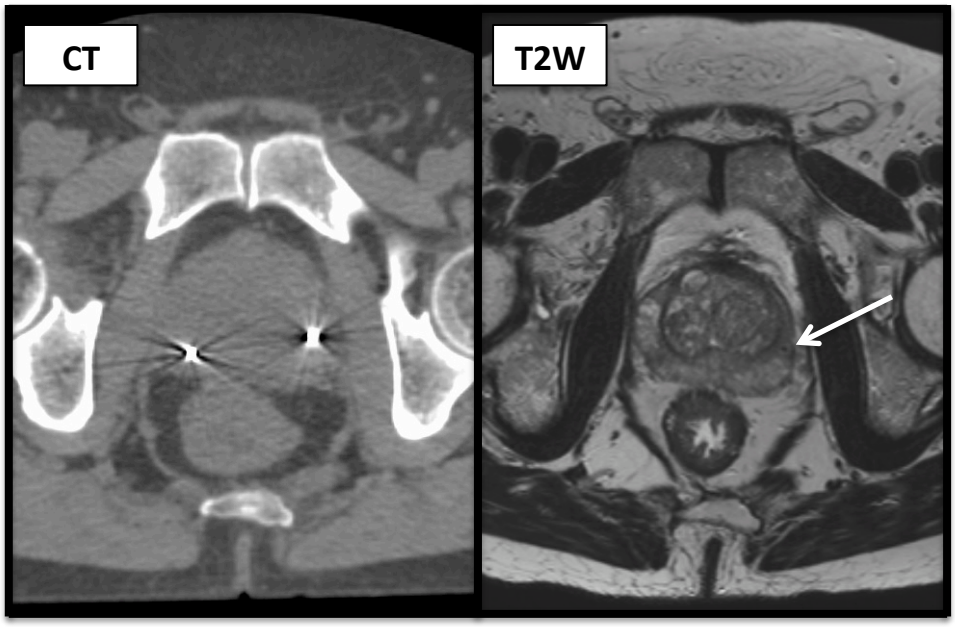

Figure 4.23- Corresponding CT axial slice (left) and T2W axial (right) images for a patient showing the appearance of a fiducial marker on standard T2W imaging, as indicated by the arrow. The second fiducial marker visible on CT imaging could not be identified on T2W images here.

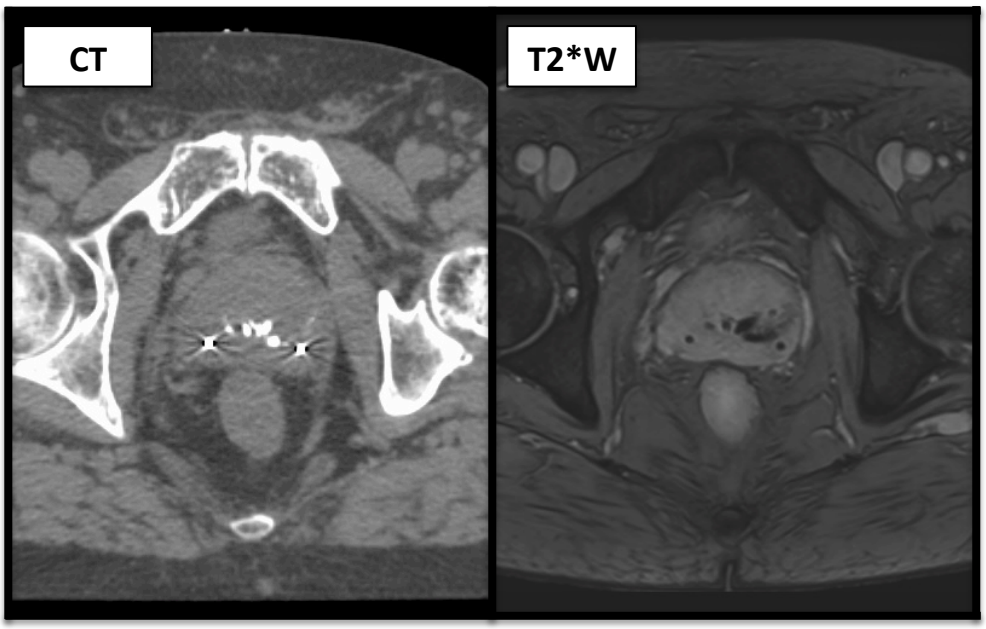

Figure 4.24- Corresponding CT (left) and T2*W (right) images for a patients showing two fiducials with surrounding artifact on CT images and central calcifications, all showing as signal loss on T2*W imaging.

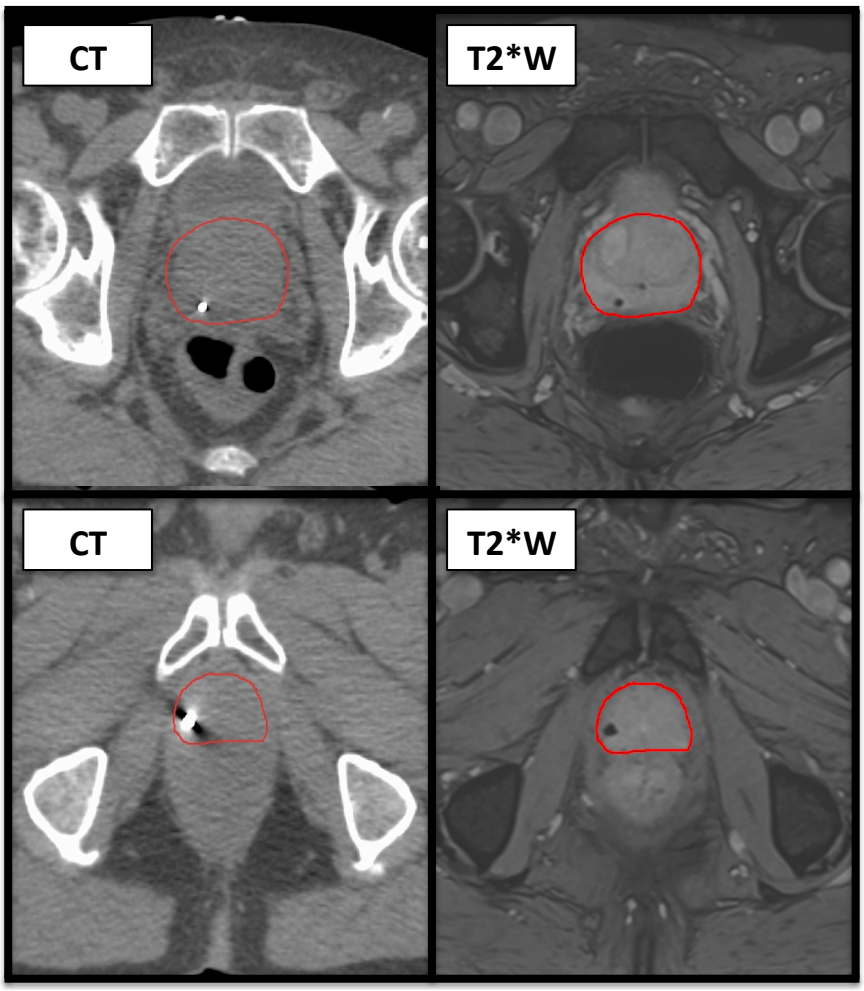

Figure 25.4- Clinical example of the variation in signal loss. Top line- CT (left) and T2*W (right) imaging displaying the usual signal loss associated with a fiducial marker in the cranio-caudal position. Bottom line- CT (left) and T2*W (right) imaging for the same patient showing the altered signal loss seen with the inferior fiducial marker which in this case is angled more in the transverse plane.

4.5.2 Clinician interobserver variability

Summary of the comparison metrics for all ten patients for each imaging modality is seen in Table 4.3.

	CT	T2W MRI	T2*W MRI
DSC	0.95* (0.94-0.96)	0.97 (0.96-0.97)	0.97 (0.96-0.97)
Cohen Kappa	0.92* (0.89-0.93)	0.94 (0.93-0.96)	0.95 (0.94-0.96)
HD (mm)	5.0* (4.7-5.7)	4.1 (3.6-4.9)	3.6 (3.2-3.7)
Mean d (mm)	0.8* (0.7-0.9)	0.5 (0.5-0.6)	0.5 (0.4-0.5)

Table 4.3- Summary of the median (interquartile range) comparison metrics for the three clinician observers for each imaging type (with interquartile range in brackets). Values are reported to one decimal place apart from overlap measures reported to two decimal places. * Denotes a statistically significant difference when compared to T2*W. Abbreviations: d-distance.

There is good agreement between the three observers for all imaging modalities. Distance measurements between contours were greater and overlap indices lower for CT compared to both MR sequences, indicating a poorer interobserver variability for CT imaging compared to MRI. This was statistically significant when comparing CT with T2*W, as indicated in Table 4.3. There was no statistically significant difference between CT and T2W for the clinician contouring.

4.5.3 Radiographer interobserver variability

Examples of radiographer contours are shown in Figure 4.5.

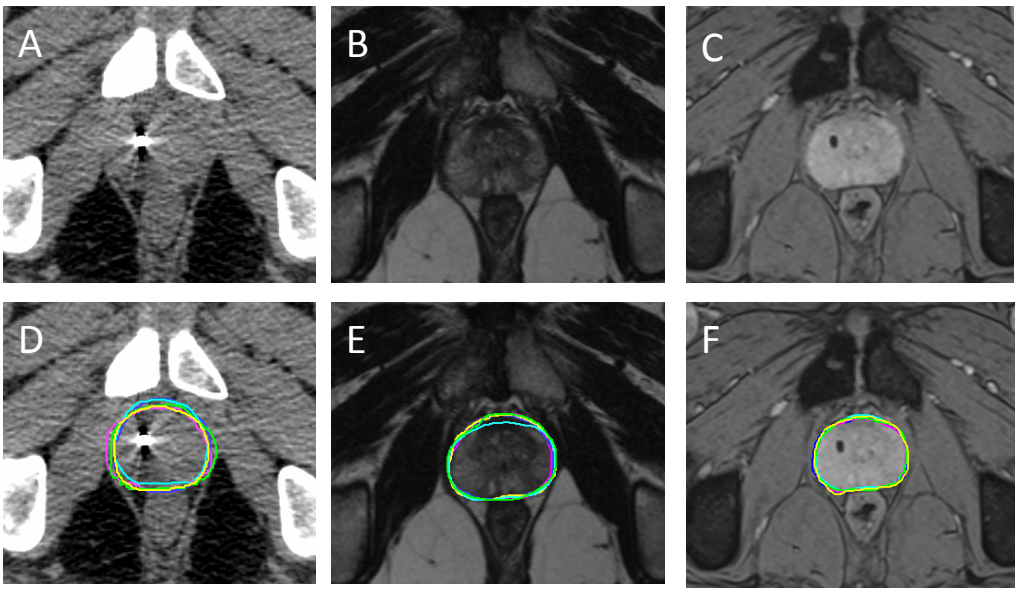

Figure 4.26- A-C are examples of CT, T2W and T2*W imaging at corresponding levels for the same patient, without contours. D-F demonstrate the same imaging with superimposed radiographer contours.

Median (interquartile range) comparisons for each imaging type, delineation times and imaging scores are summarised in Table 4.4.

		CT	T2W MRI	T2*W MRI
Inter-observer variability	DSC	0.93 (0.91-0.95)	0.94 (0.93-0.95)	0.96 (0.95-0.96)
	Cohen Kappa	0.90 (0.87-0.91)	0.91 (0.89-0.92)	0.93 (0.92-0.94)
	HD (mm)	6.5 (5.7-7.9)	4.8 (4.2-5.8)	4.7 (3.9-5.4)
	Mean d (mm)	0.9 (0.8-1.1)	0.8 (0.7-1.0)	0.7 (0.6-0.7)
Comparison to gold standard	DSC	0.91 (0.89-0.92)	0.93 (0.91-0.94)	0.94 (0.93-0.95)
	Cohen Kappa	0.85 (0.83-0.88)	0.89 (0.86-0.90)	0.91 (0.89-0.93)
	HD (mm)	7.6 (6.6-9.1)	5.2 (4.4-6.2)	4.6 (4.0-5.5)
	Mean d (mm)	1.2 (1.2-1.4)	1.0 (0.9-1.2)	0.9 (0.7-1.0)
Assessment of contouring efficiency	Time taken to contour (min)	15.4 (12.0-16.3)	9.6 (8.3-12.6)	9.8 (8.9-10.9)
	Image quality (0-10)	5.3 (5.2-5.8)	7.8 (7.4-8.1)	8.5 (8.2-8.8)
	Confidence in contour (0-10)	5.5 (5.2-5.6)	6.8 (6.7-7.3)	7.8 (7.5-7.9)

Table 4.4- Summary of median (interquartile range) comparison values for the five radiographer observers for each imaging type. Values are reported to one decimal place, apart from overlap measures reported to two decimal places. Abbreviations: d-distance.

The high scores of agreement (all ≥0.85) illustrate a good agreement between radiographers and between radiographers and the gold standard across all imaging types.

Results of statistical testing are summarised in Figure 4.6.

A) Interobserver variability

	T2W DSC 0.94	T2W Cohen 0.91	T2W HD 4.8	T2W meand 0.8
CT DSC 0.93	>0.99			
CT Cohen 0.90		0.79		
CT HD 6.5			0.04	
CT meand 0.9				>0.99

CT and T2W comparison

	T2*W DSC 0.96	T2*W Cohen 0.93	T2*W HD 4.7	T2*W meand 0.7
CT DSC 0.93	<0.01			
CT Cohen 0.90		<0.01		
CT HD 6.5			0.01	
CT meand 0.9				<0.01

CT and T2*W comparison

	T2*W DSC 0.96	T2*W Cohen 0.93	T2*W HD 4.7	T2*W mean 0.7
T2W DSC 0.94	0.02			
T2W Cohen 0.91		0.04		
T2W HD 4.8			>0.99	
T2W meand 0.8				0.02

T2Wand T2*W comparison

B) Comparison to gold standard

	T2W DSC 0.93	T2W Cohen 0.89	T2W HD 5.2	T2W meand 1.0
CT DSC 0.91	0.35			
CT Cohen 0.85		0.22		
CT HD 7.6			0.02	
CT meand 1.2				0.22

CT and T2W comparison

	T2*W DSC 0.94	T2*W Cohen 0.91	T2*W HD 4.6	T2*W meand 0.9
CT DSC 0.91	<0.01			
CT Cohen 0.85		<0.01		
CT HD 7.6			<0.01	
CT meand 1.2				<0.01

CT and T2*W comparison

	T2*W DSC 0.94	T2*W Cohen 0.91	T2*W HD 4.6	T2*W meand 0.9
T2W DSC 0.93	0.03			
T2W Cohen 0.89		0.04		
T2W HD 5.2			0.53	
T2W meand 1.0				0.22

T2Wand T2*W comparison

C) Time and image scores

	T2W time 9.6	T2W image 7.8	T2W confid 6.8
CT time 15.4	0.07		
CT image 5.3		0.03	
CT confid 5.5			0.04

CT and T2W comparison

	T2*W time 9.8	T2*W Image 8.5	T2*W confid 7.8
CT time 15.4	0.04		
CT image 5.3		<0.01	
CT confid 5.5			<0.01

CT and T2*W comparison

	T2*W time 9.8	T2*W image 8.5	T2*W confid 7.8
T2W Time 9.6	>0.99		
T2W image 7.8		0.35	
T2W confid 6.8			0.22

T2Wand T2*W comparison

p-value	Statistically significant p<0.05
p-value	Not statistically significant p≥0.05

Figure 4.27- Summary of p-values (reported to 2 decimal places) from statistical testing for comparison between imaging modalities. Values are adjusted for multiple comparisons and statistically significant if p <0.05. Abbreviations: Cohen- Cohen's kappa, meand- mean distance between contours, confid.- confidence in contouring score, image- image quality score.

On comparison of MRI to CT, radiographer contours on T2W MRI show higher accuracy when compared to the gold standard contour. T2*W contours show significantly reduced interobserver variability and significantly higher agreement with the gold standard compared to CT, for all comparison metrics.

In addition, comparison of the two MRI sequences reveals that prostate contours delineated using T2*W show significantly decreased interobserver variability for significantly improved accuracy compared to T2W MRI for all measurements excluding HD when comparing to gold standard (Table 4.4). Greater quality images and confidence in contouring were reported for both MRI types but especially T2*W MRI, reflected in the shorter time (mean reduction by 5.3 minutes) to complete contours.

4.6 Discussion

I found a high level of agreement for clinician prostate contouring on all image sets with a DSC $\geq$ 0.95 and Cohen's kappa of $\geq$ 0.92, likely to reflect the high level of experience of all clinicians, from the same institution and familiar with using MRI for contouring. To put this into context, a small study was performed with seven international expert clinicians from the MR-Linac consortium sites (unpublished data, see Appendix Figure 4A and Table 4A), the overall DSC for the prostate was 0.69 on a single test T2W MRI case. However, following the creation of consortium contouring guidelines, this improved to 0.89, confirming the importance of guidelines for consistency.

The higher agreement for contours on MRI compared to CT is consistent with previous studies as a result of the improved soft tissue contrast with MRI [6, 7]. Despite the visual appearance of a more defined prostate capsule on the T2*W sequence, there was no significant difference in interobserver variability when compared to T2W imaging, which again may reflect the users' experience with MR sequences. For this group of observers, the T2*W sequence is similar to standard T2W imaging, but with the added benefit of fiducial identification.

The more recent development of MR-guided RT allows the use of continuous MRI during treatment for motion monitoring and gating [8]. Ultimately the aim would be for an MRI only workflow [9] without the need for markers, using soft tissue visualisation alone (see Section 1.8). In this context the T2*W sequence may be advantageous in comparison to the standard diagnostic T2W sequence as the prostate is hyperintense and fewer internal structures are clearly depicted. However, at present, MR-guided delivery relies on a mixed MR-CT workflow with fiducials allowing more accurate fusion of images [10]. The sequences used for fiducial detection are discussed in detail in Section 1.2.3 and Chapter 2.

With progressively more targeted treatment delivery, the accuracy of delineation becomes even more essential [11]. For the prostate, this requires adequate tissue contrast of the capsule to improve confidence in contouring and reduce inter-observer variability. With the development of prostate motion monitoring in MR-guided RT, the prostate contour can be used for gated treatment [12]. This requires easy and accurate identification of the target either visually or using

automated algorithms. The latter may either rely on registration of images and propagation of contours or de novo auto-delineation of the prostate on new images [13-15]. The sequence described here would therefore be an attractive solution for detailing seeds and the prostate capsule.

Given the importance of prostate delineation during MR-guided RT, the second part of this chapter has focussed on the role of our therapeutic radiographers. We have demonstrated that despite the unfamiliarity of MRI, interobserver variability and accuracy of treatment radiographer prostate contours improved with both MR sequences, in particular T2*W MRI.

In particular here I have considered both consistency and accuracy of radiographer contours (see Section 1.4.7). The reduced radiographer interobserver variability on MRI is in keeping with our clinician results as well as previous studies of clinician contouring [6, 16, 17] as a result of improved soft tissue contrast, reflected in the higher scores for image quality and confidence in contouring. However, this was only statistically significant for T2*W versus CT.

For accuracy of radiographer contouring, as discussed above in Section 4.5.3, a gold standard for RT planning is difficult to define; here I have used the STAPLE of three experienced clinicians to reduce any bias and the effect of interobserver variability for the gold standard contour. Both groups of observers, clinicians and radiographers, are from the same institution, which will influence

both consistency and accuracy, as assessed by the overlap and distance measurements here.

With regards to time taken for radiographer contouring, the prostate was delineated on both MR sequences more quickly compared to CT. Although this is mirrored in the higher confidence in contouring and image quality of MRI compared to CT, note must be made of the differing slice thickness of the images- 1.5mm for CT and 2.5mm for MRI. As a result, there were a greater number of slices over the length of the prostate for contouring. Although observers were allowed to use interpolation of contours if desired on any of the image sets, the time taken must be interpreted with caution for this reason. Studies so far have not assessed timing which is of less relevance in the pre-treatment setting where speed is less pertinent but highly relevant in the online/ real time setting where increasing time will correlate with increased organ motion and patient discomfort.

There is no consensus on the best method for contour comparison [4, 5], I have therefore used a combination of comparison values here to encompass the overlap and distance between contours. Although there is no predefined threshold for clinically acceptable contour comparison (see Section 1.6.1), overlap values here are $\geq$0.9 for DSC and $\geq$0.85 for Cohen's kappa (Table 4.4) when comparing radiographer contours to the gold standard, indicating a good agreement. These values are approaching those for the clinician interobserver comparison (Table 4.3) and higher than those reported by previous studies [18-20] (see Tables 1.2 and Table 1.3).

Although I have carried out statistical testing here, I have not assessed the clinical impact of a significant difference in these comparisons. For example the clinical implication of a DSC of 0.93 versus 0.95 may be negligible although this will also be dependent on where the discrepancy lies and the margins added during planning. The resulting dosimetric effect, not assessed here, would be more relevant [21].

Our findings are particularly important, as we have commenced MR-guided radiotherapy at our institution with online replanning, which requires new contours on daily imaging. This could be contouring from scratch or by amending propagated contours produced by registering new images to reference imaging (addressed further in Chapter 6 and 7). Accurate target identification is also required for motion monitoring of the target prostate. To begin with, this would be clinician led with the aim of expanding the role of our radiographers to encompass this step. This is an essential progression of the extended role which has developed from evaluating treatment portal images [22], evaluating verification images for hypofractionated treatments [23], and to more recently, choosing the 'plan of the day' [24].

In addition, although T2W imaging is the standard sequence for contouring, additional sequences may provide additional information. The T2*W sequence allows visualisation of the fiducials and prostate contour, particularly important for a mixed CT-MR workflow. MRI for delineation is not used routinely outside of a trial setting in our institution but implanted fiducial markers are standardly used for image guidance prior to each fraction. Our study shows that

sequences such as T2*W allowing improved prostate capsule visualisation and contour accuracy can continue to be useful even if fiducials are not longer required, such as with the clinical use of MR only workflow. Any advantage will need to be weighed up against the acquisition time of the sequence, the 6 minute T2*W imaging used here is three times as long as the current 2 minute sequence used for re-contouring on the MR-Linac (Chapter 6) and would therefore contribute to a longer couch time.

The performance of automated contouring software based on autosegmentation techniques is investigated for these same imaging sequences, including T2*W in Chapter 5. This work with radiographer contours and automated contours will be expanded further to assess the dosimetric impact of any differences in contours in Chapter 7. A formal training programme will also be designed for treatment radiographer training as the role of MR-guided RT develops.

4.7 Conclusions

I have considered here a single T2*W MR sequence suitable for fiducial depiction and prostate contouring. Clinician prostate contours on MR are more consistent than CT-based contours with good agreement between prostate RT clinicians.

Despite unfamiliarity with MRI for treatment verification, therapeutic radiographer prostate contours are more accurate, show less interobserver variability and are more confidently and quickly outlined on MRI compared to CT. In addition, this improvement is consistently statistically significant for the T2*W MRI sequence. This is particularly relevant for MRI sequence choice and development of the roles of the inter-professional team in the advancement of MRI-guided radiotherapy.

4.8 References

1) Potter R, Eriksen JG, Beavis AW et al. Competencies in radiation oncology: a new approach for education and training of professionals for Radiotherapy and Oncology in Europe. Radiotherapy and Oncology 2012; 103: 1-4.
2) Boston S, Scrase C, Hardy V. 140 Implementation of radiographer led planning target delineation for prostate cancer. Radiotherapy and Oncology 2005; 76: S73.
3) Raaymakers BW, Lagendijk JJW, Overweg J et al. Integrating a 1.5 T MRI scanner with a 6 MV accelerator: proof of concept. Physics in Medicine and Biology 2009; 54: N229.
4) Hanna GG, Hounsell AR, O'Sullivan JM. Geometrical analysis of radiotherapy target volume delineation: a systematic review of reported comparison methods. Clinical Oncology (R Coll Radiol) 2010; 22: 515-525.
5) Fotina I, Lutgendorf-Caucig C, Stock M et al. Critical discussion of evaluation parameters for inter-observer variability in target definition for radiation therapy. Strahlentherapie und Onkologie 2012; 188: 160-167.
6) Villeirs GM, Vaerenbergh K, Vakaet L et al. Interobserver Delineation Variation Using CT versus Combined CT + MRI in Intensity–Modulated Radiotherapy for Prostate Cancer. Strahlentherapie und Onkologie 2005; 181: 424-430.
7) Debois M, Oyen R, Maes F et al. The contribution of magnetic resonance imaging to the three-dimensional treatment planning of localized prostate cancer. International Journal of Radiation Oncology, Biology and Physics 1999; 45: 857-865.
8) Pathmanathan AU, van As NJ, Kerkmeijer LGW et al. Magnetic Resonance Imaging-Guided Adaptive Radiation Therapy: A “Game Changer” for Prostate Treatment? International Journal of Radiation Oncology, Biology and Physics 2018; 100: 361-373.
9) Nyholm T, Jonsson J. Counterpoint: Opportunities and Challenges of a Magnetic Resonance Imaging–Only Radiotherapy Work Flow. Seminars in Radiation Oncology 2014; 24: 175-180.
10) Parker CC, Damyanovich A, Haycocks T et al. Magnetic resonance imaging in the radiation treatment planning of localized prostate cancer using intra-prostatic fiducial markers for computed tomography co-registration. Radiotherapy and Oncology 2003; 66: 217-224.
11) Njeh C. Tumor delineation: The weakest link in the search for accuracy in radiotherapy. Journal of Medical Physics 2008; 33: 136-140.
12) O. Bohoudi AB, S. Senan, B. Slotman, M. Palacios, F. Lagerwaard. Using a MRI-guided radiation therapy system for prostate cancer patients. ESTRO 36 2017; SP-0494.
13) Greenham S, Dean J, Fu CKK et al. Evaluation of atlas-based auto-segmentation software in prostate cancer patients. Journal of Medical Radiation Sciences 2014; 61: 151-158.
14) Klein S, van der Heide UA, Lips IM et al. Automatic segmentation of the prostate in 3D MR images by atlas matching using localized mutual information. Medical Physics 2008; 35: 1407-1417.
15) Pasquier D, Lacornerie T, Vermandel M et al. Automatic Segmentation of Pelvic Structures From Magnetic Resonance Images for Prostate Cancer

Radiotherapy. International Journal of Radiation Oncology, Biology and Physics 2007; 68: 592-600.
16) Khoo VS, Padhani AR, Tanner SF et al. Comparison of MRI with CT for the radiotherapy planning of prostate cancer: a feasibility study. The British Journal of Radiology 1999; 72: 590-597.
17) Rasch C, Barillot I, Remeijer P et al. Definition of the prostate in CT and MRI: a multi-observer study. International Journal of Radiation Oncology, Biology and Physics 1999; 43: 57-66.
18) Pasquier D, Boutaud de la Combe-Chossiere L, Carlier D et al. Harmonization of the Volume of Interest Delineation among All Eleven Radiotherapy Centers in the North of France. PLoS One 2016; 11: e0150917.
19) Langmack KA, Perry C, Sinstead C et al. The utility of atlas-assisted segmentation in the male pelvis is dependent on the interobserver agreement of the structures segmented. The British Journal of Radiology 2014; 87: 20140299.
20) Simmat I, Georg P, Georg D et al. Assessment of accuracy and efficiency of atlas-based autosegmentation for prostate radiotherapy in a variety of clinical conditions. Strahlentherapie und Onkologie 2012; 188: 807-815.
21) Vinod SK, Jameson MG, Min M, Holloway LC. Uncertainties in volume delineation in radiation oncology: A systematic review and recommendations for future studies. Radiotherapy and Oncology 2016; 121: 169-179.
22) Suter B, Shoulders B, Maclean M, Balyckyi J. Machine verification radiographs: an opportunity for role extension? Radiography 2000; 6: 245-251.
23) Hudson J, Doolan C, McDonald F et al. Are therapeutic radiographers able to achieve clinically acceptable verification for stereotactic lung radiotherapy treatment (SBRT)? Journal of Radiotherapy in Practice 2015; 14: 10-17.
24) McNair HA, Hafeez S, Taylor H et al. Radiographer-led plan selection for bladder cancer radiotherapy: initiating a training programme and maintaining competency. The British Journal of Radiology 2015; 88: 20140690.

4.9 Chapter 4 Appendix

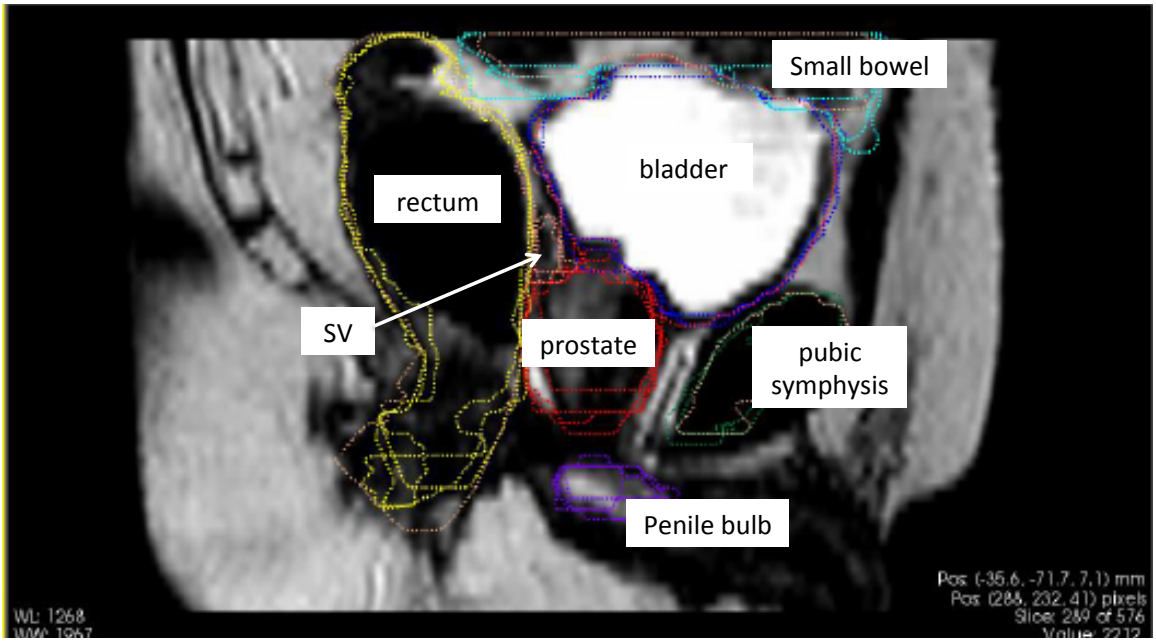

Figure 4A- Sagittal section from a T2W MRI showing contours from seven consultants across the different consortium sites. The contours showed here were completed prior to discussion and creation of the Prostate TSG consortium contouring guidelines. Figure courtesy of John Christodouleas and prostate TSG members.

Target/ Organ at risk	Cohen's Kappa (measure of agreement)	
	Before guidelines	After guidelines
Prostate	0.69	0.89
SV	0.55	0.73
Rectum	0.80	0.81

Table 4A- Summary of the interobserver variability for the prostate, seminal vesicles (SV) and rectum contours, as assessed with Cohen's kappa, for the seven consortium members. Values are reported for two separate T2W MRI scans prior to, and following, the creation of the Prostate TSG consortium contouring guidelines. Data courtesy of John Christodouleas and prostate TSG members.

Chapter 5- Auto-contouring on MRI for prostate radiotherapy

5.1 Publications

The data from this chapter was submitted as an abstract and accepted as an oral presentation for the “Helen Patterson Award for Registrar Research” at the British Uro-oncology Group Annual meeting, September 2018.

Varying atlas numbers and imaging modality for auto-contouring in prostate radiotherapy

Angela Pathmanathan, Jennifer Kieselmann, Douglas Brand, John Christodouleas, Nicholas van As, Simeon Nill, Robert Huddart, Alison Tree. Clinical Oncology 2019; 31(2):e24

5.2 Introduction

As outlined in Chapter 1 (Section 1.7.1) auto-contouring, or auto-segmentation, reduces clinician delineation time and improves interobserver variability [1] which is particularly relevant in adaptive radiotherapy [2]. There are a number of factors that may improve the accuracy of auto-contours but can also impact the time taken to create auto-contours.

Chapter 4 evaluated the impact of imaging modality on the accuracy of radiographer contouring using computed tomography (CT), T2-weighted (T2W) magnetic resonance imaging (MRI) and T2*-weighted (T2*W) MRI.

Here I assess the impact of atlas number and imaging modality (CT, T2W and T2*W MRI) on the accuracy and speed of an auto-contouring research tool (Monaco ADMIRE, v2.0, Elekta AB, Stockholm, Sweden). This algorithm includes several potential approaches for the type of auto-segmentation, as discussed in the introduction, Section 1.7.2. Here I utilise multi-atlas segmentation (MAS) with the 'random forest label fusion' method, where 'random forest' refers to the type of machine learning employed, the use of multiple decision trees using twenty features of the imaging, independent of the image intensity.

5.3 Aims of Chapter 5

In this chapter, I will aim to assess the impact of varying atlas number and imaging modality on the accuracy of prostate auto-contours create by Monaco ADMIRE.

My hypothesis is that MRI imaging, particularly T2*W MRI, will improve the accuracy of auto-contours when compared to CT. Increasing the number of atlases when creating an auto-contour increases the accuracy but also increases the time taken to generate the auto-contour.

To test this hypothesis, I will;

1) Assess the accuracy of ADMIRE prostate auto-contours compared to a gold standard clinician combination Simultaneous Truth and Performance Level Estimation (STAPLE) contour
2) Assess any difference in the accuracy of ADMIRE prostate auto-contours on CT, T2W MRI and T2*W MRI
3) Establish the impact of increasing atlas number on auto-contour accuracy and the time taken

Materials and Methods

The methods for this chapter are divided into two sections. Following review of the results from Section A, I extended the work to assess prostate auto-contouring using single institution imaging.

5.4 Methods Section A- MR-Linac prostate TSG

5.4.1 Patient population and imaging acquisition

In total, fourteen T2W MRI datasets for prostate radiotherapy planning were acquired by Elekta, from a combination of the seven MR-Linac consortium sites.

5.4.2 Creation of gold standard contour for atlases

The steps for this section are summarised in Figure 5.1 and 5.2. Four clinicians, representing 3 different institutions from the MR-Linac consortium prostate Tumour Site Group (TSG) (AT, JC, CL and myself) contoured the prostate, seminal vesicles (SV) and rectum on ten T2W MRI datasets, using MR-Linac consortium prostate TSG consensus guidelines (Chapter 5 Appendix, Section 5.11). I used the command line from Monaco ADMIRE (research version 2.0, Elekta AB) to create a STAPLE contour from all clinicians for each MR dataset. I reviewed all STAPLE contours to ensure they remained clinically and anatomically accurate. These were edited if appropriate, for example when there was overlapping of structures. These ten image sets with corresponding STAPLE contours formed the atlases for the auto-contouring library.

5.4.3 Creation of gold standard contour for test cases

Six clinicians from the MR-Linac consortium prostate TSG, representing 6 institutions (AT, AC, DV, FP, JC, WH) contoured the prostate, SV and rectum on six T2W MRI datasets, different to those used for the atlases, using MR-Linac consortium prostate TSG consensus guidelines. As above, I used the command line from Monaco ADMIRE to create a STAPLE ‘gold standard’

contour from all clinicians for each MR dataset. These six image sets with corresponding STAPLE contours formed the test cases.

5.4.4 Creation of ADMIRE auto-contours

I imported the ten atlases into Monaco ADMIRE generated prostate, SV and rectum auto-contours using random forest label fusion for each of the six test cases using four, seven then ten atlases. To avoid selection bias, I selected the atlases in order of image set, which had identification numbers assigned by Elekta when data was anonymised centrally.

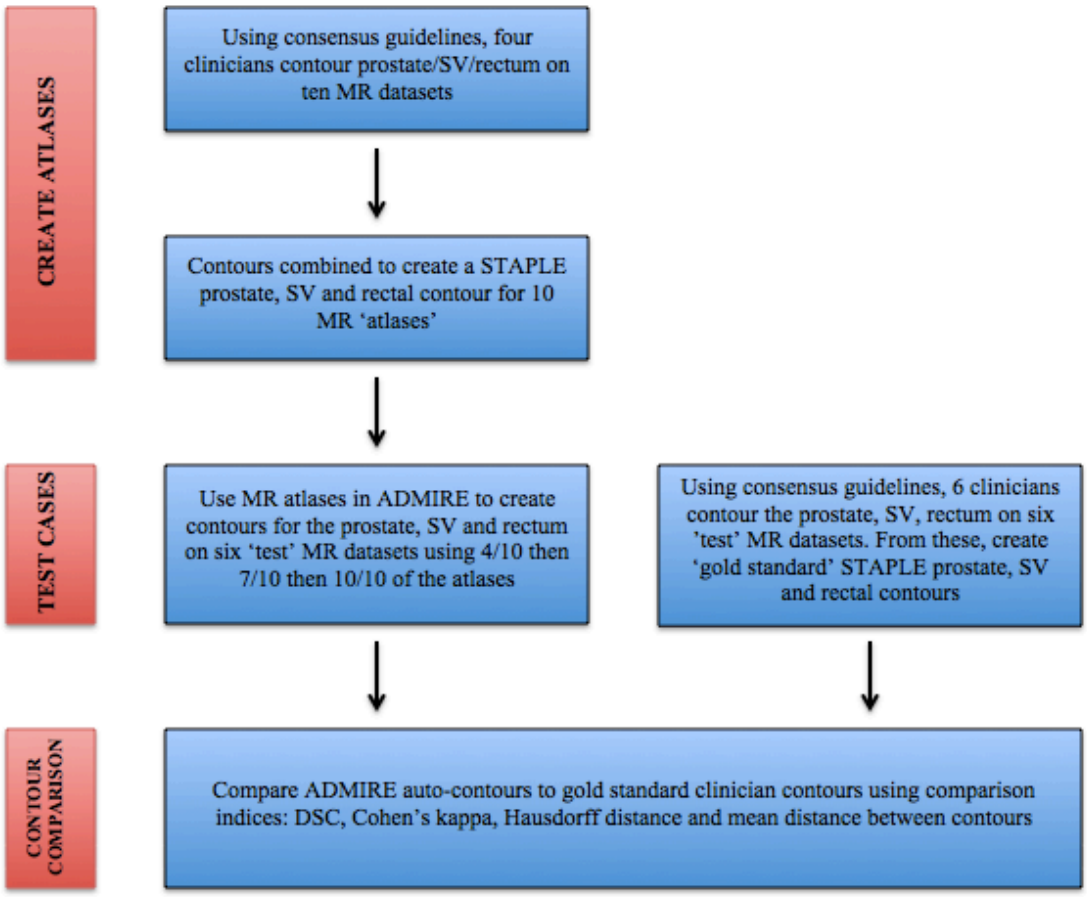

Figure 5.28- Flowchart summary of the steps (described in Methods-Section A) for creating atlases and test cases for Monaco ADMIRE testing followed by comparison for assessment of accuracy.

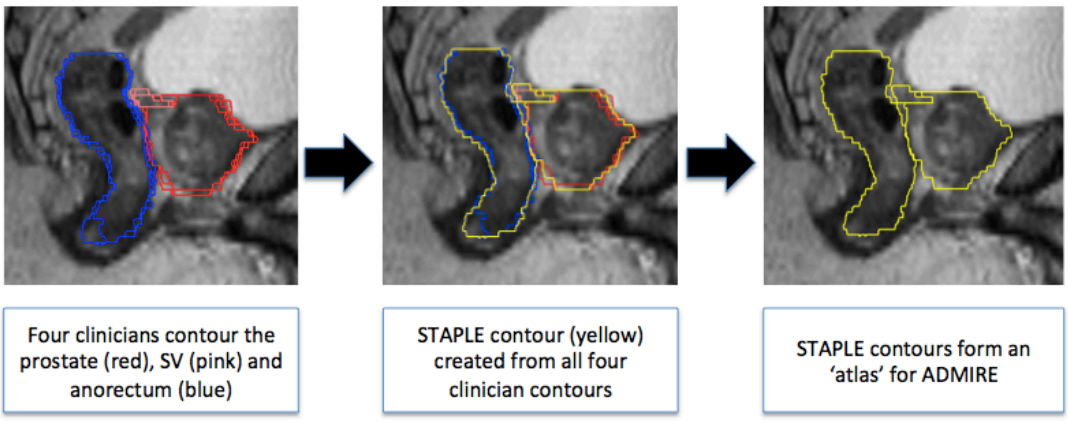

Figure 5.29- Imaging summary of the steps (described in Methods-Section A) for creating the atlases for Monaco ADMIRE testing. The imaging used was T2W MRI with sagittal images shown here.

5.4.5 Assessment of auto-contour accuracy

As previously described in Section 4.4.7, I used Monaco ADMIRE to assess auto-contour accuracy by comparison to the STAPLE gold standard with Dice similarity coefficient (DSC), Cohen's kappa, Hausdorff distance (HD) and mean distance between contours, thereby testing auto-contours versus the gold standard contour, derived by multiple clinicians.

5.5 Methods Section B- Single institution testing

The work from Section A was extended for the prostate alone by testing within our institution. This was to allow specific testing of auto-contours using different sequences. As discussed in the Results, Section A used imaging from different institutions, and I wanted to investigate whether the impact of varying the atlas number would be different when using single institution, and therefore equivalent, imaging.

5.5.1 Patient population and imaging acquisition

The ten CT, T2W and T2*W imaging sets used to test ADMIRE are the same as described in Chapter 4 (Section 4.4.2 and 4.4.3).

5.5.2 Creation of gold standard contour

The clinician gold standard STAPLE contours for each imaging set, used to assess accuracy, are the same as described in Section 4.4.6 and summarised in Figure 5.3. I used the same image sets for the atlases and test cases and

reviewed all STAPLE contours to ensure that they were clinically acceptable and remained appropriate for the imaging.

5.5.3 Creation of ADMIRE prostate auto-contours

For each of the three imaging modalities, I imported the ten patient datasets with the corresponding gold standard STAPLE contour to generate the ADMIRE atlas library for auto-contouring (as illustrated in Figure 5.3). I used the same ten imaging sets to test ADMIRE using the leave-one-out cross validation method. In this method, I used Monaco ADMIRE to create a prostate auto-contour on each imaging dataset without using the atlas from the same patient i.e. the remaining nine datasets for the other patients were used to create the auto-contour. Using the random forest label fusion function, I used Monaco ADMIRE to create prostate auto-contours using 3, 6 then 9 atlases. To minimise bias, I chose atlases consecutively by using the scan acquisition date.

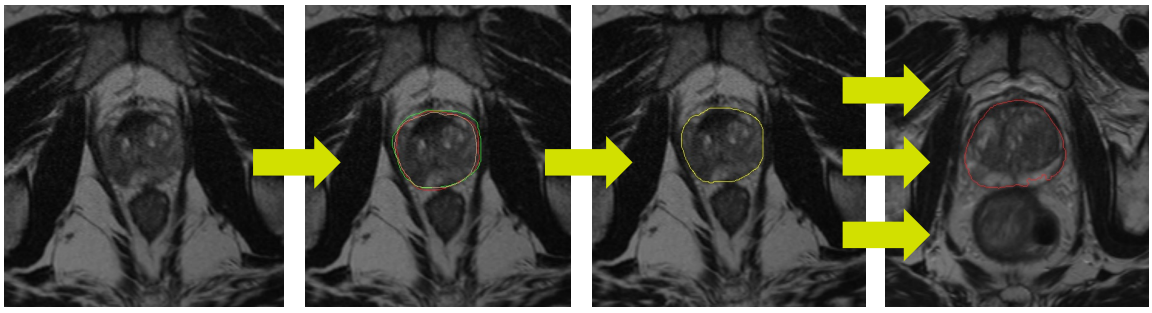

Figure 5.30 - Imaging summary of the steps (described in Methods-Section B) for creating the atlases and test cases for Monaco ADMIRE testing. T2W imaging is shown here. Each atlas, ten for each imaging type, is created using the gold standard clinician STAPLE contour.

5.5.4 Assessment of auto-contour accuracy

Accuracy of auto-contours: As previously described in Section 4.4.6, I used Monaco ADMIRE to assess auto-contour accuracy by comparison to the gold standard with DSC, Cohen's kappa, HD and mean distance between contours.

Statistical analysis: Using GraphPad Prism v7.0d, I performed non-parametric Friedman testing with Dunn's test for multiple comparisons. The three imaging comparisons- CT versus T2W, CT versus T2*W and T2W versus T2*W were pre-planned. Values were defined as statistically different if the adjusted p-value was <0.05.

Results

5.6 Results Section A- MR-Linac prostate TSG

5.6.1 Assessment of interobserver variability

The interobserver variability of the clinicians for the six test cases is summarised in Table 5.1.

Clinician Interobserver Variability	Dice similarity coefficient	Cohen's kappa coefficient	Hausdorff distance (mm)	Mean distance (mm)
Prostate	0.93 (0.92-0.93)	0.89 (0.87-0.89)	6.4 (5.2-7.3)	1.0 (1.0-1.2)
Seminal Vesicles	0.77 (0.73-0.78)	0.73 (0.68-0.75)	8.4 (7.5-9.2)	1.7 (1.3-2.0)
Anorectum	0.86 (0.82-0.90)	0.81 (0.79-0.87)	16.6 (12.3-20.1)	2.3 (1.7-2.7)

Table 5.1- Summary of the median (interquartile range) comparison values for interobserver variability of the six clinicians contouring the test cases for the prostate, SV and anorectum.

5.6.2 Assessment of auto-contour accuracy

Auto-contours were created for the prostate and anorectum for all six MR datasets with 4, 7 and 10 atlases (18 auto-contours in total), an example is seen in Figure 5.4 and 5.5. Only ten SV auto-contours could be created (4/6 cases with 4 atlases, 2/6 with 7 atlases and 4/6 with 10 atlases). For those cases where an SV auto-contour was not produced, Monaco ADMIRE returned an error message stating '*SV slicing resulted in 0 contours, structure is likely small and fell between slice locations or mapped entirely outside the image volume*'.

Using a greater number of atlases increased the time taken to create the auto-contours. The mean time to create all three auto-contours (prostate, SV and anorectum) was 1.3, 2.2 and 3.1 minutes using 4, 7 and 10 atlases respectively.

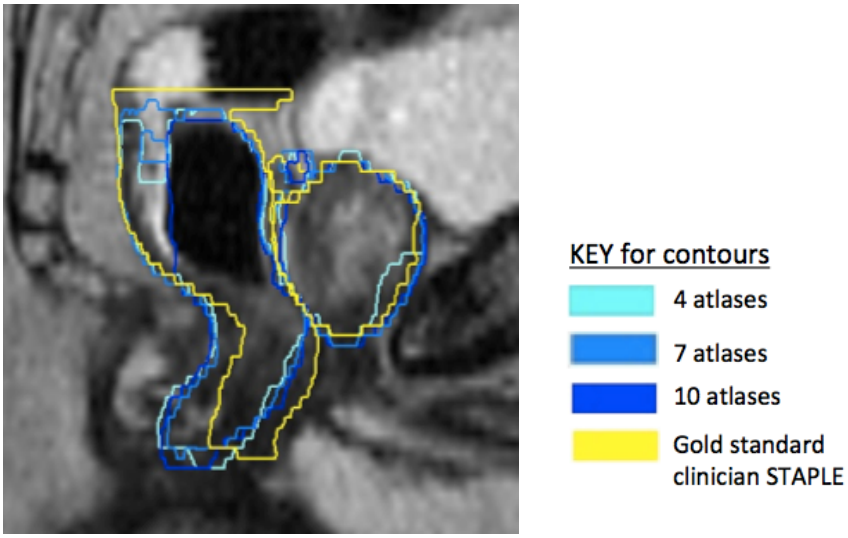

Figure 5.31- An example of Monaco ADMIRE prostate, SV and anorectum auto-contours created with 4, 7 and 10 multi-institutional atlases, as described in Methods, Section B. A sagittal slice of a T2W MRI scan is shown here with key depicting the auto-contours and gold standard STAPLE contour.

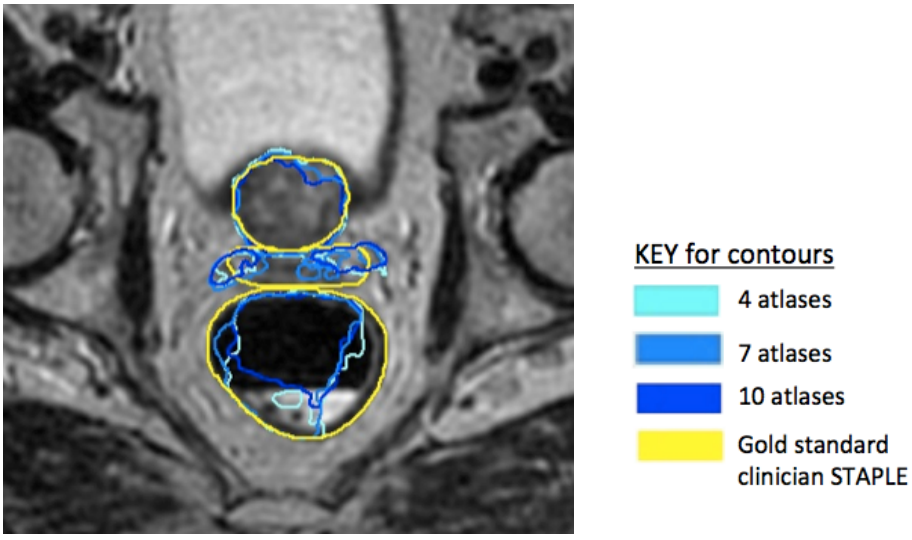

Figure 32.5- An example of Monaco ADMIRE prostate, SV and anorectum auto-contours created with 4, 7 and 10 multi-institutional atlases, as described in Methods, Section B. An axial slice of a T2W MRI scan is shown here, with key depicting the auto-contours and gold standard STAPLE contour.

The comparison of the generated auto-contours to the gold standard contours is summarised in Table 5.2. Overall there is poor concordance between the auto-contours and the gold standard, particularly for the SV and anorectum. With the limited number of atlases used in this study (4 to 10), improved accuracy of prostate autosegmentation is seen with 10 atlases, as demonstrated by the higher DSC/ Cohen's kappa and reduced distance values. Otherwise, there does not appear to be an improvement in the accuracy of auto-contours with increasing atlas numbers.

Some unexpected results were obtained: there is a detriment to the accuracy indicated by some of the comparison metrics in Table 5.2 when increasing the number of atlases. For example for the anorectum contours, the DSC was 0.66 and 0.62, with mean distance 4.9 and 7.0 mm for 4 and 10 atlases respectively, whereas I had expected these values to improve with a greater number of inputted atlases.

Review of the anorectum auto-contours showed particular cases (as illustrated in Figures 5.4 and 5.5) where inaccurate auto-contours appear to be due to gas within the rectum.

		Dice similarity coefficient	Cohen's kappa coefficient	Hausdorff distance (mm)	Mean distance (mm)
Prostate auto-contour accuracy	4 atlases	0.80 (0.74-0.83)	0.71 (0.63-0.75)	9.3 (8.4-11.3)	2.8 (2.3-3.7)
	7 atlases	0.70 (0.64-0.75)	0.60 (0.51-0.65)	12.4 (10.7-13.1)	4.0 (3.3-4.8)
	10 atlases	0.86 (0.84-0.89)	0.79 (0.77-0.83)	9.3 (7.0-14.7)	1.8 (1.6-2.2)
Seminal Vesicles auto-contour accuracy	4 atlases	0.20 (0.11-0.35)	0.13 (0.07-0.29)	17.0 (16.0-31.2)	5.6 (4.8-13.3)
	7 atlases	0.29 (0.16-0.41)	0.24 (0.13-0.34)	26.1 (19.9-32.4)	10.0 (6.4-13.6)
	10 atlases	0.19 (0.03-0.35)	0.16 (0.03-0.28)	34.6 (28.2-36.4)	13.4 (9.8-14.7)
Anorectum auto-contour accuracy	4 atlases	0.66 (0.60-0.73)	0.56 (0.51-0.65)	22.2 (19.5-24.7)	4.9 (3.9-6.1)
	7 atlases	0.60 (0.51-0.72)	0.50 (0.42-0.65)	22.3 (17.9-27.1)	5.8 (4.2-7.5)
	10 atlases	0.62 (0.60-0.69)	0.54 (0.50-0.63)	25.1 (17.1-26.5)	7.0 (4.4-8.0)

Table 5.2- Accuracy of Monaco ADMIRE prostate, seminal vesicles (SV) and anorectum auto-contours- summary of the median (interquartile range) comparison values for each structure with increasing number of atlases. The values for the SV were calculated with the reduced number of contours as described in the text.

5.6.3 Review of imaging datasets

Individual review of the imaging sets showed that there is great variation in the datasets (submitted by the different institutions) used for the atlas and test cases, with varying slice thickness, field of view and image quality. In addition, as imaging was from different institutions, we would expect the specific sequence parameters of the T2W imaging to differ.

5.7 Results Section B- Single institution testing

5.7.1 Assessment of auto-contour accuracy

Table 5.3 summarises the median comparison metrics and time taken for each imaging type according to the number of atlases used. Statistical testing for assessing the effect of increasing atlas number is also displayed in this table.

		Time (min/sec)	Dice similarity coefficient	Cohen's kappa	Hausdorff distance (mm)	Mean distance (mm)
CT Imaging	3 atlases	1m 40s	0.85 (0.77-0.90)	0.77 (0.67-0.84)	11.6 (7.2-14.2)	2.1 (1.6-4.1)
	6 atlases	3m 22s[3]	0.89 (0.85-0.90)	0.83 (0.77-0.84)	9.2 (7.6-11.2)	1.8 (1.5-2.1)
	9 atlases	5m 04s[3,6]	0.90 (0.86-0.91)	0.83 (0.77-0.85)	8.4 (7.2-9.9)	1.7 (1.5-2.1)
T2W MRI	3 atlases	0m 24s	0.85 (0.82-0.88)	0.78 (0.74-0.83)	8.8 (7.1-10.0)	2.1 (1.7-2.8)
	6 atlases	0m 46s[3]	0.89 (0.87-0.90)	0.83 (0.81-0.84)	8.5 (6.8-10.0)	1.6 (1.4-2.1)
	9 atlases	1m 09s[3,6]	0.90[3] (0.88-0.91)	0.84[3] (0.82-0.87)	6.9[6] (5.9-8.8)	1.5[3] (1.3-1.8)
T2*W MRI	3 atlases	0m 43s	0.87 (0.80-0.90)	0.80 (0.70-0.85)	10.2 (7.6-12.6)	1.9 (1.3-3.3)
	6 atlases	1m 24s[3]	0.90 (0.86-0.91)	0.84 (0.80-0.85)	9.4 (7.3-13.5)	1.5 (1.3-1.9)
	9 atlases	2m 05s[3,6]	0.91[3] (0.87-0.92)	0.86 (0.79-0.87)	9.8 (8.6-11.1)	1.2[3] (1.2-2.1)

Table 5.3- Comparison of Monaco ADMIRE prostate auto-contours with gold standard clinician STAPLE: Summary of median (interquartile range) comparison values for each imaging type and atlas number. Values are reported to one decimal place, apart from overlap measures reported to two decimal places. 3- statistically significant compared to 3 atlases; 6- statistically significant compared to 6 atlases.

Auto-contours were possible for all imaging sets and overall showed good concordance with the clinician gold standard, regardless of atlas number or imaging type, as seen by the DSC 0.85-0.91 and Cohen's kappa 0.77-0.86. Visual review of the auto-contours showed that greatest agreement was at the mid-prostate with more variability at the apex and base. This is illustrated in a example in Figure 5.6.

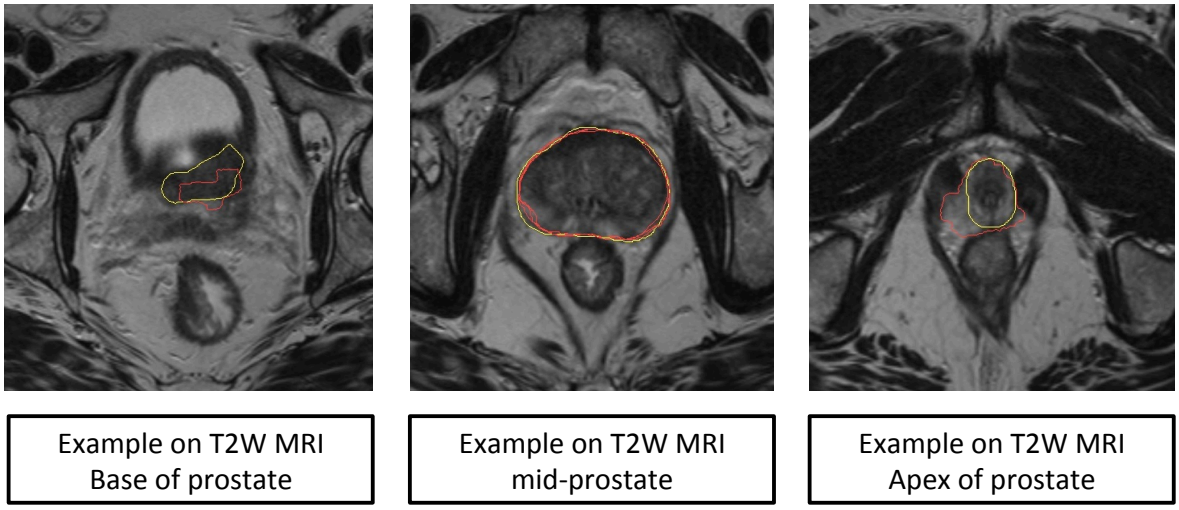

Figure 5.33- Example of ADMIRE prostate auto-contours compared to gold standard at different axial levels of the prostate. Images seen here are for T2W imaging from the same patient. The base and apex slices show auto-contours using 3 atlases alone. The mid-prostate slice shows the three overlapping auto-contours for 3,6 and 9 atlases.

Increasing the number of atlases significantly increases the time taken to create a prostate auto-contour. In addition, there is a significant difference between imaging modalities in auto-contouring time, with CT imaging requiring the longest and standard T2W imaging requiring the shortest time.

There is a trend for improving accuracy of auto-contours when increasing the number of atlases, as seen by the increase in overlap indices (DSC and Cohen's kappa) and reduction in distance values (HD and mean distance). However, as seen in Table 5.3, this is only statistically significant for certain parameters when 9 atlases are used.

When comparing the imaging types using the same number of atlases, there is no significant difference between imaging modalities.

5.8 Discussion

5.8.1 Multi-institutional imaging for MAS

The results obtained in Section A, using imaging from multiple institutions suggest that there is no consistent improvement in prostate, rectal and SV auto-contours when increasing the number of atlases for auto-contouring. Overall the prostate auto-contours were more accurate compared to rectal auto-contours, with SV auto-segmentation performing the worst, consistent with previous studies [3-8] as summarised in Section 1.7.3. The failure to create SV auto-contours here by Monaco ADMIRE would be due to a combination of the variation between image sets, compounded by the small size of this structure. This has implications for online recontouring for adaptive radiotherapy where there is great intrafraction variation in the SV position for a given patient.

The use of ten atlases does appear to give the better results for prostate auto-contours. This is not the case for SV and rectum, where some of the

comparisons indicate paradoxical diminished accuracy with an increase in atlases. For example for rectal auto-contours, DSC reduced from 0.66 to 0.62 and mean distance between contours increased from 4.9 to 7.0 mm with an increase in the atlases from 4 to 10, reflecting reduced accuracy when compared to the gold standard STAPLE contour.

As discussed in the introduction, Section 1.7.5, even when a specific sequence is specified, T2W MRI in this instance, there will be variability due to the parameters used [9-12] therefore impacting the registration of images, exacerbated here by the small number of atlas and test cases. This may also explain the deterioration in metrics seen when increasing the number of atlases from 4 to 10, due to the inclusion of an atlas irrelevant for a particular test case.

Due to this variability encountered with the imaging from different institutions, further discussion will focus on the results outlined from Section B, which are more robust for further evaluation.

5.8.2 Assessment of atlas numbers with single institution imaging

The prostate auto-contours created by ADMIRE using single institution imaging show a good agreement with clinician contours, regardless of imaging type, even with a limited number of atlases. There is an overall trend indicating improvement in accuracy of auto-contours with increasing atlas number. However this was only statistically significant for a limited number of results,

with 9 atlases better than 3 for some parameters, and was not as marked as expected.

I have considered a set of ten patients here, it may be that larger number of test cases would demonstrate a significant difference when increasing the number of atlases. However, there are other arguments for why improvement in auto-contours with increasing atlas number was not more pronounced. Firstly, even with only three atlases, ADMIRE auto-contours here showed good concordance with the gold standard clinician contour with DSC of 0.85, 0.85 and 0.87 for CT, T2W and T2*W imaging respectively. As there appears to be a plateau for atlas number, above which no further improvement is seen, this may have already been reached by three atlases, particularly as the type of auto-segmentation tested here uses deep learning methods rather than atlas based segmentation alone.

Secondly, I used here a specific imaging library to test the same imaging modality i.e. the single institution T2W library was used for the T2W test case etc. This is particularly relevant, as discussed earlier, as MAS requires identification of similarities between the atlases and test cases. However variation in sequence and therefore contrast compromises this as seen with the results in Section A. With such a specific library, we would expect the registration between each atlas and the test case to be more accurate.

Padgett et al reported an inferior performance when atlases from a different vendor were used [13]. As a result, multi-atlas contours performed similarly to auto-contours created from matching contrast and vendor of the test case to the

atlas. This may further explain why increasing the number of atlases in our study did not show significant differences between groups, because by using the same imaging for the test cases and atlases, our atlas library was already very specific i.e. with the same sequence, institution, vendor. In addition, the mean prostate volume here was higher than for standard prostate patients as ADT was not used in the patients included here. Prostate size is also important when comparing atlases to test cases [14], Korsager et al reported larger errors for test cases with a prostate volume of >100cm^3 as few large volumes were present in the atlas image sets. As a result of this highly specific atlas to test case propagation, even with just three atlases, accurate auto-contours were achieved.

As atlas-based segmentation methods are dependent on similarities between anatomies, we would expect the optimal number of atlases to vary depending on the organ to be delineated- with more being required for a target such as the SV where there is great variation between patients.

In this study, due to the multiple combinations available for choosing 3 or 6 atlases out of the nine available, these were chosen in order of image acquisition in order to prevent bias. If an automated way of testing auto-contouring were possible, ideally all possible combinations would be tested to give the best results. This would be dependent on the software being fast enough to choose the most relevant atlases within an acceptable timeframe. However, the results reported here remain relevant and allow interpretation. Even if by chance the earlier image sets are particularly good as atlases,

therefore giving unusually high accuracy values, we would not expect this to be true for all the test cases.

5.8.3 Other factors affecting the accuracy of prostate auto-segmentation

In this study, MRI atlas based auto-contours on MRI are not more accurate compared to CT auto-contours derived from CT atlases. The specific nature of the atlases, as discussed above, may also be the reason for this. Although there have publications looking at auto-contours on either MRI or CT, there have been no direct comparisons.

It was hypothesised that the T2*W set may be more accurate than T2W due to the improved clarity of the capsule. In Chapter 4, I considered the difference in radiographer contours on these sequences demonstrating that contours on T2*W imaging were more accurate and showed less interobserver variability compared to T2W MRI for some metrics, and T2*W was better than CT for all comparison metrics [15]. For any given atlas number, the auto-contouring results show a very slight improvement in the accuracy metrics for T2*W MRI compared to T2W, although this was not as marked as expected and not statistically significant. The effect of MRI sequence and contrast on auto-segmentation has recently been described, assessing the performance of MAS using fat saturated MRI images, where the contrast of the prostate is enhanced [13]. Similar to our results, this study reported a slightly improved DSC 0.83 and HD 2.4 mm compared to DSC 0.81 and HD of 2.7 mm for the fat saturated sequence and standard T2W sequence respectively, however statistical

analysis was not performed. To our knowledge, there has been no other direct comparison of MRI sequences for auto-segmentation although this question continues to be pertinent for MR-guided RT.

Just as manual contours vary the most at the apex and base of the prostate [16], this work is in keeping with previous studies reporting that auto-contours are less accurate in these regions where the contrast to the surrounding tissue is less [8, 9, 13, 14, 17-19]. This is relevant, as in a time pressured environment such as online adaptive treatment, editing of auto-contours can be focused on these areas.

5.8.4 Speed of prostate auto-segmentation

As expected, increasing the number of atlases selected for an auto-contour increases the time taken, this was statistically significant across all imaging types when increasing the atlas number by three, as used here. This is due to the time taken to register each atlas image set to the new test set. Although here I have considered the time taken for creation of the prostate contour only, auto-contouring of OAR and SV would only give a small incremental increase in the time, as most of the time recorded here is for image registration.

Any improvement in accuracy must also be weighed up against the increasing length of time to create the auto-contour. The time recorded consists of the time taken for registration of each of the atlases to the test case, the label fusion step to merge these intermediate segmentations and finally the application of the deep learning features. This is less relevant in the offline setting, where

even a small incremental improvement can justify the extra time required. However the speed of autosegmentation is particularly significant in an online adaptive replanning setting.

We have found a significant difference between imaging modalities in auto-contouring time. It is logical that the CT auto-contours would take longer, due to a combination of the increased number of slices and the larger field of view. However, an unexpected finding was that the T2*W MRI set took twice as long compared to the T2W imaging to create an auto-contour using the same number of atlases. Review of the registration step shows that the DIR stage was longer for this imaging. When the image set is split into smaller components during the DIR step, these are subsequently re-joined using multi-resolution features of the imaging. It may be that the uniform bright contrast appearance of the prostate delays 'convergence' of these components (personal correspondence, Elekta) therefore giving an increased time for auto-contouring.

5.8.5 Accuracy of ADMIRE prostate auto-segmentation

Given the huge variation in the methods of auto-segmentation available, direct comparison between our results and other publications is challenging. Even amongst atlas-based methods with deep learning, the features and atlases used varies considerably [17, 20]. Considering these studies alone, Guo et al reported auto-segmentation accuracy on T2W MRI with DSC of 87.1±4.2% and HD 8.12±2.89 mm using deep feature learning [20], however this group reported a computational time of 45 minutes using their methods. Ma et al

reported a DSC of 86.8% for the whole prostate using a combination of deep learning with convolutional neural networks and MAS on CT imaging [17].

The PROMISE12 challenge considered in Section 1.7.5 reported DSC 0.65 to 0.84 and modified 95% HD 5.89 to 8.59 mm for the MAS algorithms [9]. Even using just three atlases our results are comparable, taking into account the HD we have reported will be higher than the 95th percentile HD presented by the challenge. However the MAS algorithms used within PROMISE12 did not incorporate machine learning and used atlas selection from the 50 'training' atlases with reported average times of 22 to 40 minutes per case.

5.8.6 Relevance of results for online replanning

With the onset of MR-guided radiotherapy on the MR-Linac (see Chapter 6), it is relevant to extrapolate the results obtained here for intra-patient contouring in the online setting. As discussed in the introduction, Section 1.7.4, the propagation of intra-patient contours, from the same patient's imaging from one day to the next, is different despite the overlapping steps with inter-patient contouring. In terms of the optimal number of atlases, the intra-patient atlas is specific, previous studies report that a combination of atlases (for example from several fractions) is better than use of a single atlas, however, we have seen here that may be dependent on imaging quality and how sophisticated the auto-contouring components are. The priority again will have to be the balance between producing an accurate auto-contour that needs minimal editing in the time-precious online environment and any time required to combine several days of atlases [21, 22].

5.8.7 Summary of findings for MAS

Overall, these results have shown that when using the same imaging modality and parameters, a prostate auto-contour with good agreement when compared to a gold standard can be created with just a few atlases, regardless of imaging type. The results have implications, quality appears to be more important than quantity for MAS. It is important to consider the type of atlases in the library and the similarity to the target case, rather than the number of atlases available. This is necessary for both accuracy and to minimise computational time. A specific atlas library would be feasible within a particular institution where imaging will be acquired using a limited number of scanners.

Table 5.4 summarises the results here along with those from Chapter 4 on T2W MRI, the image type most relevant for the MR-Linac at present.

		Dice similarity coefficient	Cohen's kappa coefficient	Hausdorff distance (mm)	Mean distance (mm)
Prostate clinician manual contours	RMH IOV	0.97	0.94	4.1	0.5
	MRL TSG IOV	0.93	0.89	6.4	4.0
Prostate radiographer manual contours	IOV	0.94	0.91	4.8	0.8
	Accuracy	0.93	0.89	5.2	1.0
Prostate ADMIRE auto-contour accuracy (variable image sets)	4 atlases	0.80	0.71	9.3	2.8
	7 atlases	0.70	0.60	12.4	4.0
	10 atlases	0.86	0.79	9.3	1.8
Prostate ADMIRE auto-contour accuracy (single institution MRI)	3 atlases	0.85	0.78	8.8	2.1
	6 atlases	0.89	0.83	8.5	1.6
	9 atlases	0.90	0.84	6.9	1.5

Table 5.4- Summary of the median comparison contour metrics for prostate contours on T2W MRI. Results are shown for RMH clinician interobserver variability (IOV) (Full results Table 4.3), MR-Linac tumour site group (MRL TSG) clinician IOV (Table 5.1), RMH radiographer IOV and accuracy (Table 4.4), Monaco ADMIRE auto-contours on multi-institutional imaging (Table 5.2) and Monaco ADMIRE auto-contours on single institution imaging (Table 5.3).

The auto-contour results on T2W MRI are favourable, but as expected, are not as accurate as the manual contours, especially when considering the distance measurements. However, the DSC for auto-contours with 9 atlases on single institutional imaging (0.90) is approaching the values seen with the MR-Linac TSG clinical interobserver variability and radiographer contour accuracy (0.93). It must also be noted that the auto-contours were not amended at all, which

would not be realistic in a clinical setting at present. As discussed earlier, even limiting amendments to the apex and base would reduce most discrepancies.

For further optimisation of MAS software, further work should focus on improving auto-contours without incurring a time penalty. Finally, just as in Chapter 4, I discussed that the metrics used here do not reflect the significance of contour variation on the dose delivered. This work is extended further in Chapter 6 where I assess the clinical impact of any differences when using auto-contours for prostate radiotherapy.

5.9 Conclusions

ADMIRE auto-contours showed good agreement with clinician gold standard. Both increasing atlas numbers and differing modality impact auto-contouring time, with some evidence that increasing atlas numbers improves accuracy. An atlas library specific to the test cases for auto-contouring, that is, acquired using the same sequence and imaging parameters, will give accurate auto-contours, even with a few atlases. Significant variation in the atlases and test cases used can have a negative impact on the accuracy of any auto-contours created. Future research needs to assess clinical significance of such differences and identify ways to improve accuracy without time penalty.

5.10 References

1) Tao C-J, Yi J-L, Chen N-Y et al. Multi-subject atlas-based auto-segmentation reduces interobserver variation and improves dosimetric parameter consistency for organs at risk in nasopharyngeal carcinoma: A multi-institution clinical study. Radiotherapy and Oncology 2015; 115: 407-411.
2) Pathmanathan AU, van As NJ, Kerkmeijer LGW et al. Magnetic Resonance Imaging-Guided Adaptive Radiation Therapy: A “Game Changer” for Prostate Treatment? International Journal of Radiation Oncology, Biology and Physics 2018; 100: 361-373.
3) Simmat I, Georg P, Georg D et al. Assessment of accuracy and efficiency of atlas-based autosegmentation for prostate radiotherapy in a variety of clinical conditions. Strahlentherapie und Onkologie 2012; 188: 807-815.
4) Hwee J, Louie AV, Gaede S et al. Technology assessment of automated atlas based segmentation in prostate bed contouring. Radiation Oncology (London, England) 2011; 6: 110-110.
5) Delpon G, Escande A, Ruef T et al. Comparison of Automated Atlas-Based Segmentation Software for Postoperative Prostate Cancer Radiotherapy. Frontiers in oncology 2016; 6: 178-178.
6) Huyskens DP, Maingon P, Vanuytsel L et al. A qualitative and a quantitative analysis of an auto-segmentation module for prostate cancer. Radiotherapy and Oncology 2009; 90: 337-345.
7) Wong WKH, Leung LHT, Kwong DLW. Evaluation and optimization of the parameters used in multiple-atlas-based segmentation of prostate cancers in radiation therapy. The British Journal of Radiology 2016; 89: 20140732-20140732.
8) Klein S, van der Heide UA, Lips IM et al. Automatic segmentation of the prostate in 3D MR images by atlas matching using localized mutual information. Medical Physics 2008; 35: 1407-1417.
9) Litjens G, Toth R, van de Ven W et al. Evaluation of prostate segmentation algorithms for MRI: the PROMISE12 challenge. Medical image analysis 2014; 18: 359-373.
10) Feng Y, Kawrakow I, Olsen J et al. A comparative study of automatic image segmentation algorithms for target tracking in MR-IGRT. Journal of Applied Clinical Medical Physics 2016; 17: 441-460.
11) Dickinson L, Ahmed HU, Allen C et al. Magnetic resonance imaging for the detection, localisation, and characterisation of prostate cancer: recommendations from a European consensus meeting. European Urology 2011; 59: 477-494.
12) Barentsz JO, Richenberg J, Clements R et al. ESUR prostate MR guidelines 2012. European Radiology 2012; 22: 746-757.
13) Padgett KR, Swallen A, Pirozzi S et al. Towards a universal MRI atlas of the prostate and prostate zones : Comparison of MRI vendor and image acquisition parameters. Strahlentherapie und Onkologie 2018.
14) Korsager AS, Fortunati V, van der Lijn F et al. The use of atlas registration and graph cuts for prostate segmentation in magnetic resonance images. Medical Physics 2015; 42: 1614-1624.

15) Pathmanathan AU, McNair HA, Schmidt MA et al. Comparison of prostate delineation on multimodality imaging for MR-guided radiotherapy. The British Journal Radiology 2019; 92: 20180948.
16) Rasch C, Barillot I, Remeijer P et al. Definition of the prostate in CT and MRI: a multi-observer study. International Journal of Radiation Oncology, Biology and Physics 1999; 43: 57-66.
17) Ma L, Guo R, Zhang G et al. Automatic segmentation of the prostate on CT images using deep learning and multi-atlas fusion. Proceedings of SPIE--the International Society for Optical Engineering 2017; 10133: 101332O.
18) Martin S, Troccaz J, Daanenc V. Automated segmentation of the prostate in 3D MR images using a probabilistic atlas and a spatially constrained deformable model. Medical Physics 2010; 37: 1579-1590.
19) La Macchia M, Fellin F, Amichetti M et al. Systematic evaluation of three different commercial software solutions for automatic segmentation for adaptive therapy in head-and-neck, prostate and pleural cancer. Radiation Oncology (London, England) 2012; 7: 160.
20) Guo Y, Gao Y, Shen D. Deformable MR Prostate Segmentation via Deep Feature Learning and Sparse Patch Matching. IEEE Trans Med Imaging 2016; 35: 1077-1089.
21) Li W, Vassil A, Zhong Y, Xia P. Daily dose monitoring with atlas-based auto-segmentation on diagnostic quality CT for prostate cancer. Medical Physics 2013; 40: 111720.
22) Godley A, Sheplan Olsen LJ, Stephans K, Zhao A. Combining prior day contours to improve automated prostate segmentation. Medical Physics 2013; 40: 021722.

5.11 Chapter 5 Appendix

Table 5A summarises the Prostate TSG consensus guidelines for the delineation of structures for prostate radiotherapy.

Structure		Description
Penile Bulb	Comments	N/A
	Superior	Superior edge of the bulbous spongiosum
	Anterior	Extends to the shaft portion of the bulbous spongiosum
	Posterior	Posterior edge of the bulbous spongiosum
	Lateral	Lateral edge of the bulbous spongiosum
	Inferior	Inferior edge of the bulbous spongiosum
Anal Canal	Comments	Should be contoured as a solid structure including the muscle wall and lumen.
	Superior	At the anorectal junction which on axial imaging corresponds to the point where the puborectalis muscle no longer completely surrounds the alimentary lumen. At this point, the rectal ampulla narrows abruptly into a narrow slip.
	Anterior	Extends to anterior aspect of the muscle wall
	Posterior	Extends to posterior aspect of the muscle wall
	Lateral	Extends to lateral aspect of the muscle wall
	Inferior	Extends to anal verge or the most the most inferior aspect of the ischial tuberosities (right or left)
Rectum	Comments	Should be contoured as a solid structure including the muscle wall and lumen.
	Superior	At the recto-sigmoid junction which is defined by the most inferior of the following three landmarks: a) the point where the rectum loses its round shape in the axial plane and turns anteriorly into the sigmoid; b) the bifurcation of the inferior mesenteric artery into the sigmoid and superior rectal arteries; c) the S2/S3 junction.
	Anterior	Extends to anterior aspect of the muscle wall
	Posterior	Extends to posterior aspect of the muscle wall
	Lateral	Extends to lateral aspect of the muscle wall
	Inferior	Extends to the anorectal junction which on axial imaging corresponds to the point where the puborectalis muscle no longer completely surrounds and abuts the alimentary lumen. At this point, the rectal ampulla narrows abruptly into a narrow slip.
Anorectum	Comments	Is the union of anal canal and rectum structures. Not identified by TG 263.
Prostate	Comments	N/A
	Superior	Extends to superior aspect of the gland and abuts the seminal vesicle.
	Anterior	Extends to anterior aspect of gland including the anterior fibromuscular stroma.
	Posterior	Extends to posterior aspect of the gland and abuts the anorectum. The neurovascular bundles should not be included.
	Lateral	Extends to lateral aspect of the gland.
	Inferior	At the prostate apex, the point above the hourglass or slit shape that results from the in-bowing of the levator ani. The apex is approximately 1cm above the penile bulb or at the start of the high signal prostate visible on T2-weighted MRI. If the capsule is visible, the muscles and soft tissues abutting the capsule are not included as “prostate”.

Seminal Vesicles	Comments	Contour the visible seminal vesicles as a single structure. The seminal vesicles are paired grape-like pouches filled with high signal-intensity fluid on T2 weighted MR.
	Superior	Extends to superior aspect of the gland.
	Anterior	Extends to anterior aspect of the gland.
	Posterior	Extends to posterior aspect of the gland.
	Lateral	Extends to lateral aspect of the gland.
	Inferior	Abuts the prostate.
Bladder	Comments	Contoured as a solid structure including the bladder wall and lumen.
	Superior	Extends to superior aspect of the muscle of the dome.
	Anterior	Extends to anterior aspect of the muscle.
	Posterior	Extends to posterior aspect of the muscle.
	Lateral	Extends to lateral aspect of the muscle.
	Inferior	Defined where urine (white on T2 MRI) is no longer visible.
Bowel Loops Low	Comments	Includes individual loops of large bowel and small bowel THAT ARE WITHIN 3cm of the most superior aspect of the SVs in sup-inf direction. Not identified by TG 263. Used for localized prostate.
Femur Whole Right	Comments	Includes both femoral head and neck and visible shaft of the bone.
	Superior	Extend to superior aspect of femoral head
	Anterior	Extend to anterior aspect of bone
	Posterior	Extend to posterior aspect of bone
	Lateral	Extend to lateral aspect of bone
	Inferior	Include all visible shaft in simulation scan
	Comments	Includes the ipsilateral ilium, ischium, pubic bone.
Femur Whole Left	Comments	Includes both femoral head and neck and visible shaft of the bone.
	Superior	Extend to superior aspect of femoral head
	Anterior	Extend to anterior aspect of bone
	Posterior	Extend to posterior aspect of bone
	Lateral	Extend to lateral aspect of bone
	Inferior	Include all visible shaft in simulation scan
	Comments	Includes the ipsilateral ilium, ischium, pubic bone.
Pubic Bones	Comments	Union of Pubic Bone Left and Right
	Superior	Extent superiorly to the junction of the ischium.
	Anterior	Extend to anterior aspect of bone
	Posterior	Extend to posterior aspect of bone
	Lateral	Extend to lateral aspect of bone
	Inferior	Extend to inferiorly to the junction of the ischium.
Bony Pelvis Left	Comment	Does not include sacrum
Bony Pelvis Right	Comments	Does not include sacrum

Table 5A- Summary of the MR-Linac consortium consensus guidelines, for the delineation of structures for prostate radiotherapy planning. Courtesy of John Christodouleas and prostate TSG members

Chapter 6- Prostate Radiotherapy Integrated with Simultaneous MRI- the PRISM trial

6.1 Publications

Data from this chapter has been published in abstract form following poster presentation at ESTRO 38, Milan 2019;

MR-guided online adaptive radiotherapy: First experience in the UK (EP-1566)

Angela Pathmanathan, Lorna Bower, Helen Creasey, Alex Dunlop, Emma Hall, Ian Hanson, Trina Herbert, Rebekah Lawes, Dualta McQuaid, Helen McNair, Adam Mitchell, Gillian Smith, Robert Huddart, Uwe Oelfke, Simeon Nill, Alison Tree. Radiotherapy and Oncology 2019; 133:S845

In addition, data from this chapter has been published in abstract form, following selection for poster presentation at ASTRO 2019;

The PRISM trial- First UK experience of MR-guided adaptive radiotherapy

Angela Pathmanathan, Lorna Bower, Helen Creasey, Alex Dunlop, Emma Hall, Ian Hanson, Trina Herbert, Rebekah Lawes, Dualta McQuaid, Helen McNair, Adam Mitchell, Julia Murray, Mercy Ofuya, Chris Parker, Jordan Rossan, Gillian Smith, Robert Huddart, Uwe Oelfke, Simeon Nill, Alison Tree. International Journal of Radiation Oncology, Biology and Physics 2019; 105(1): E301

I am co-author on the following publications, which have resulted from work presented in this chapter;

Automatic reconstruction of the delivered dose of the day using MR-linac treatment log files and online MR imaging. Menten M, Mohajer J, Nilawar R, Bertholet J, Dunlop A, Pathmanathan AU, Moreau M, Marshall S, Wetscherek A, Nill S, Tree AC, Oelfke U. Radiotherapy and Oncology 2020; 145: 88-94.

Daily adaptive radiotherapy for patients with prostate cancer using a high field MR-linac: initial clinical experiences and assessment of delivered doses compared to a C-arm linac. Dunlop A, Mitchell A, Tree A, Barnes H, Bower L, Chick J, Goodwin E, Herbert T, Lawes R, McNair H, McQuaid D, Mohajer J, Nilawar R, Pathmanathan A, Smith G, Hanson I, Nill S, Oelfke U. Submitted October 2019 to Clinical and Translational Radiation Oncology.

6.2 Introduction

The *Prostate Radiotherapy (RT) Integrated with Simultaneous MRI* (PRISM) trial (NCT03658525) is a single centre, non-randomised R-IDEAL phase I/IIa study [2]. Patients treated within the study have daily magnetic resonance imaging (MRI) guided adaptive radiotherapy.

The categories of adaptive radiotherapy are summarised in Section 1.5. For treatment on the MR-Linac, as patient repositioning is not possible, the equivalent is shifting the plan to the patient, a simple dose shift or the 'adapt to position' (ATP) workflow. To adjust for any change in set-up, the reference and new daily image set are rigidly registered to establish an isocentre shift for the reference plan.

However as all structure and OAR contours remain the same, this does not account for any variation in the shape of the daily anatomy treatment. The PRISM study involves online adaptive replanning, that is, the delivery of a new plan based on the daily anatomy. For the MR-Linac, this is described as the 'adapt to shape' (ATS) workflow, where the clinical target volumes (CTV) and/or the organs at risk (OAR) are amended to reflect the current imaging and a new plan is created.

There are several optimisation modes available in the online setting. The segments from the initial reference plan can be modified, called 'segment shape optimisation' (SSO). On account of this 'head start' for planning, this is named 'warm start optimisation'. The shape and weights of the segments from the

reference plan are adjusted using five SSO loops, essentially meaning that five changes to the configuration of the segments are allowed in the online setting. The number of loops was chosen following initial work on the template used for online replanning [3]. Alternatively, re-optimisation from fluence amends the intensity profile of each beam angle, prior to further optimisation with five SSO loops. This 'cold start optimisation' is therefore a longer process with this approach being particularly useful for patients with more variable anatomy.

6.3 Aims of Chapter 6

The aim of the PRISM trial is to assess the feasibility, safety and tolerability of radical prostate radiotherapy, using standard fractionation dose of 60 Gray (Gy) in 20 fractions, by recording the method of re-optimisation used, the time taken for each stage of treatment, clinician reported toxicity and patient reported outcomes.

As such, it will test the hypothesis that MR-Linac guided adaptive prostate radiotherapy is clinically feasible and well tolerated.

To test this hypothesis, I will;

1) Assess if MR-guided adaptive radiotherapy can be delivered within a clinically feasible time frame
2) Assess the number of fractions requiring real time adaptation
3) Assess the time taken to re-plan a fraction of treatment using the Elekta Unity
4) Assess acute and late gastrointestinal (GI) and genitourinary (GU) toxicities and patient reported outcomes

5) Assess patient acceptability of treatment on the Elekta Unity

Subsequently, prostate specific antigen (PSA) outcomes will be assessed as part of the trial but as this data is not mature I will not included this endpoint here.

The predefined Primary endpoint is the proportion of patients who complete >90% of fractions in 60 minutes or less.

6.4 Materials and Methods

6.4.1 Patient population

This chapter includes the initial feasibility cohort of five patients completing treatment within the PRISM study between August to December 2018 at the Royal Marsden Hospital NHS Foundation Trust. These patients had localised prostate cancer due planned to be treated with radical radiotherapy to the prostate and seminal vesicles (SV), who met the. Inclusion and exclusion criteria for the study as listed in Table 6.1.

Inclusion Criteria
Histologically confirmed adenocarcinoma prostate- grade group 3 or less (Gleason 4+3=7 or less)
Staging T2-T3a, N0, M0
PSA < 25 ug/l
6 months short course androgen deprivation therapy (ADT) allowed, not mandated
Maximum prostate volume 70cc
International prostate symptom (IPSS) score <12 at baseline
WHO performance status 0 or 1
Written informed consent
Exclusion criteria
Other invasive malignancy within the last two years- excluding basal cell carcinoma and squamous cell carcinoma of the skin
Patients who require long course (> 6 months) ADT
Contraindications to MRI - Including pacemaker, implanted devices, any non-MR compatible metallic implants - Severe claustrophobia
Contraindications to gold fiducial marker implantation - Clotting disorders, very high risk of bleeding - Clinically unacceptable risk of temporarily stopping anticoagulation or antiplatelet medications
Contraindications to prostate radiotherapy, - Previous pelvic radiotherapy - Clinically significant inflammatory bowel disease
Bilateral or single hip replacements

Table 6.1- Summary of the inclusion and exclusion criteria for the PRISM trial

6.4.2 Reference imaging acquisition

At least one week prior to acquisition of the reference imaging, three gold fiducial markers are inserted under transrectal ultrasound guidance.

Prior to imaging, bladder filling and bowel preparation instructions are as per institutional guidelines. Patients are advised to drink 300ml of water 30 minutes prior to imaging. Microlette microenemas are used in the two days prior to and

on the day of imaging and restarted two days prior to the start of treatment for the first two weeks.

The protocol for computed tomography (CT) and magnetic resonance imaging (MRI), acquired on the same day, has previously been described in Chapter 4 Methods, Section 4.4. Using the MR-Linac overlay for the bed, the CT scan incorporates axial slices of 1.5 mm from mid lumbar spine to below the obturator foramen. Following the CT, the patient empties their bladder and repeats the bladder filling instructions for the MRI. Patients are scanned at 1.5T, on the diagnostic scanner with two-dimensional T2-weighted (T2W) and T2*-weighted (T2*W) sequences at 2.5 mm slice thickness to cover the prostate. Parameters are summarised in Table 4.1; as previously discussed in Chapter 4, the T2*W sequence allows visualisation of the fiducial markers for image registration.

6.4.3 Target volume and organs at risk (OAR) delineation

CT and MRI reference plans are fused by the physics team, using the fiducial markers for co-registration. Prior to contouring each patient, I reviewed the image fusion, adjusting the rigid registration where required. Using RayStation treatment planning system (TPS), I contoured the target volumes of prostate and SV using the fused images. For the OAR I contoured the rectum, bladder, penile bulb, urethra, femoral heads, small bowel and pubic bone. All contouring was completed as per the PRISM trial protocol, congruous with the MR-Linac prostate tumour site group (TSG) contouring guidelines. In addition, the external body and bones are automatically contoured using thresholding of the imaging.

All contours were reviewed by Dr Alison Tree prior to planning, as per usual clinical practice.

Clinical target volume 1 (CTV1) was created from the prostate plus the proximal 1 cm of SV, defined by the SV encompassed by expanding the prostate uniformly by 1 cm (see Figure 6.1). CTV2 was created from the prostate plus the proximal 2 cm of SV, defined by the SV encompassed by expanding the prostate uniformly by 2 cm.

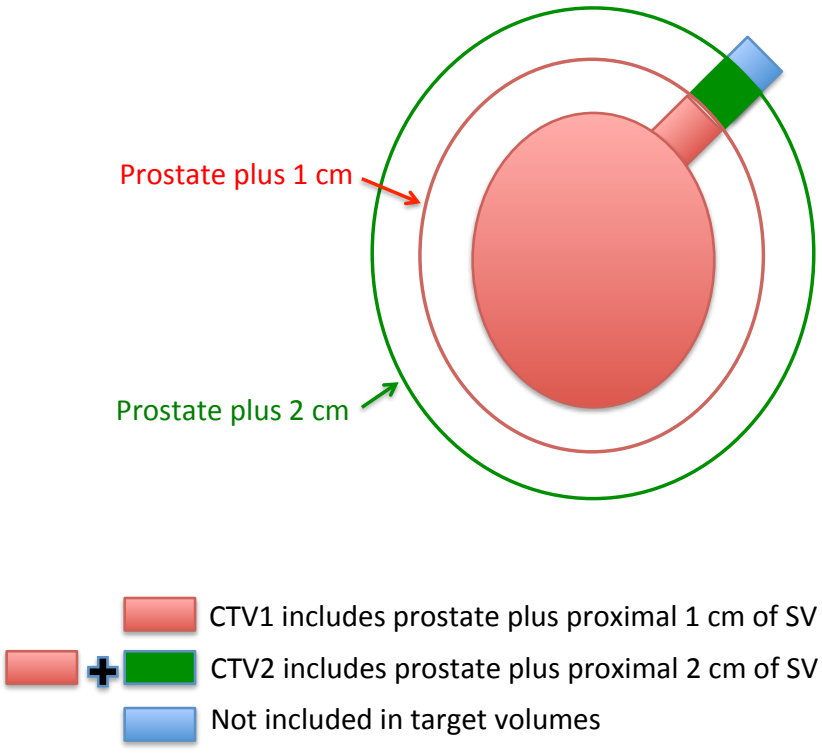

Figure 6.34- Figure depicting the clinical target volumes (CTV) for the PRISM trial and inclusion of the seminal vesicles. Adapted from figure in the PRISM protocol.

6.4.4 Reference plan creation

Planning target volume 1 (PTV1) or PTV_6000 is created from CTV1 by the addition of a 5 mm isotropic margin, except 3 mm posteriorly. PTV2 (PTV_4860) is generated by expanding CTV2 with a 5 mm isotropic margin.

The electron density of the bones, CTV2 (prostate and proximal 2 cm of SV) and all other tissue within the external contour is determined from the CT imaging and used to override the densities on MRI during the planning process.

The reference CT plan for standard dose fractionation, 60Gy in 20 fractions, is generated by the physics team using Monaco clinical version 5.4 (Elekta AB, Stockholm, Sweden). The total dose to PTV1 and PTV2 is 60Gy and 48.6Gy respectively with dose constraints summarised in Table 6.2. Organ at risk constraints are summarised in Table 6.3.

PTV	Volume (%)	Minimum/ maximum dose (Gy)	
		Optimal	Mandatory
PTV_6000	98	> 57.0	> 55.8
	50	-	> 59.4
	50	-	< 60.6
	5	-	< 63.0
	0.1cm^3	< 64.2	< 66.0
PTV_4860	98	> 46.17	> 45.2
	50	-	> 48.6

Table 6.2- Summary of the target dose constraints for the PRISM trial

OAR	Dose (Gy)	Maximum volume (% or cc)	
		Optimal	Mandatory
Rectum	24.4	80%	-
	32.4	65%	-
	40.5	50%	60%
	48.6	35%	50%
	52.7	-	30%
	56.8	-	15%
	60.8	3%	5%
Bladder	40.5	50%	-
	48.7	25%	-
	52.7	-	50%
	56.76	5%	35%
	60.8	3%	25%
Femoral heads	40.5	-	50%
Bowel	36.5	78cc	158cc
	40.5	17cc	110cc
	44.6	14cc	28cc
	48.7	0.5cc	6cc
	52.7	-	<0.01cc
Penile bulb	40.5	-	50%
Pubic symphysis	56	25%	-

Table 6.3- Summary of the OAR dose constraints for the PRISM trial

Treatment for the MR-Linac is planned using inverse planned step and shoot IMRT technique with 7 equally spaced, co-planar non-opposing beams. As previously discussed in Chapter 3, Monaco TPS incorporates the effect of the magnetic field on dosimetry.

In addition to the plan for the MR-Linac, all patients had a ‘back-up’ plan created with RayStation TPS using single arc volumetric modulated arc therapy (VMAT) for a standard linear accelerator, in case of machine breakdown.

6.4.5 Daily treatment planning and delivery

An overview of the clinical workflow is summarised in Figure 6.2.

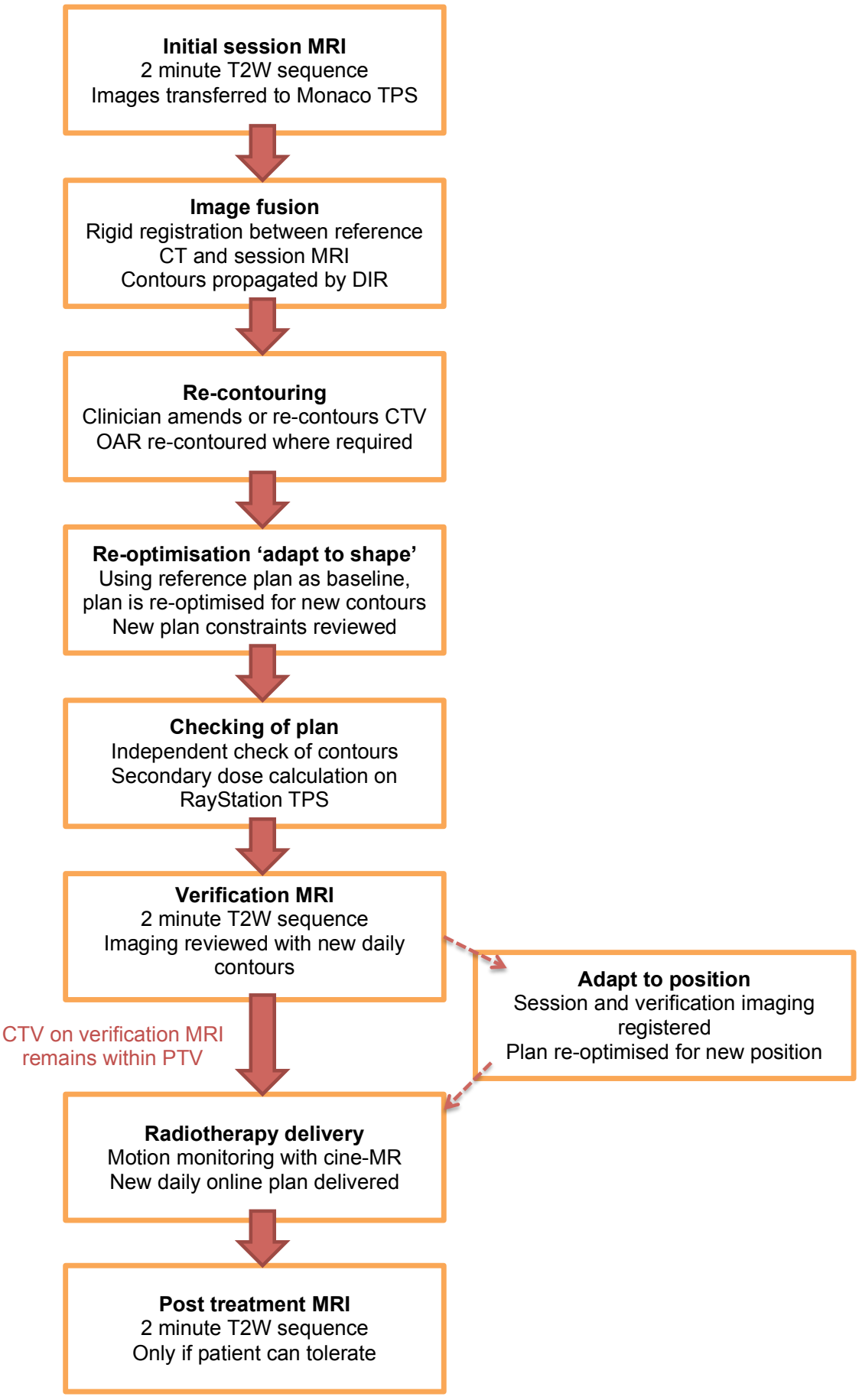

Figure 6.35- Summary of the clinical workflow used for daily MR-guided adaptive radiotherapy within the PRISM trial

Team members

At each fraction, there are two treatment radiographers, two physicists and one clinician present. One of the radiographers is responsible for image acquisition, the other for image review and fusion. The physicists create and check the new daily plan. The clinician is responsible for re-contouring, evaluation and acceptance of the new plan

For the first three patients, the clinician present was either Dr Alison Tree or myself for all twenty fractions. For the fourth and fifth patients, the clinicians involved included myself, Dr Alison Tree, Dr Julia Murray or Dr Chris Parker. Overall, I was the supervising clinician present for 50 to 60 out of the 100 fractions considered here.

Test cases

Prior to online re-contouring on the MR-Linac, test cases of diagnostic T2W MRI were completed on Research Monaco to allow familiarisation of the contouring tools and to assess interobserver variability to ensure contour consistency. The latter was calculated using the same methods as described in Chapter 4 Methods, Section 4.4.6.

MR Imaging

All MRI scans in this workflow are acquired with a 2 minute T2W sequence, from an Elekta approved pre-defined exam card. Parameters for this sequence are summarised in Table 6.4. This sequence had already been assessed as

being appropriate for prostate and SV visualisation during the PRIMER study (discussed in Section 1.4.2).

Parameter	Value
Scan mode	3D turbo spin echo
Acquisition time	1 minute 57 seconds
Patient position	head first, supine
Field of view (AP x RL x FH mm)	400 x 400 x 300
Acquired voxel size (AP x RL x FH mm)	1.5 x 1.5 x 2.0
Reconstructed voxel size (AP x RL x FH mm)	0.83 x 0.83 x 1.0
Number of slices	300
Slice thickness (mm)	1.0
Slice orientation	transverse

Table 6.4- Summary of the parameters for the 2 minute T2W sequence used during the online adaptive radiotherapy workflow for PRISM. 3D- three dimensional, AP-anterior/posterior, RL- right/left, FH- foot/head.

Workflow

This description relates to the workflow for the first five patients being discussed here. This workflow has been constantly iterated over the following months, and is still in evolution.

Each patient is set up in the same position as their initial imaging, the documented couch index indicates the visual alignment for the tattoo (lasers are not used) with a further reference for the index bar used for the immobilisation device.

The steps as detailed in Figure 6.2 are as follows;

1) **Initial session MRI**- after patient set-up, the initial 'session' MRI is acquired by one of the radiographers, reconstructed then automatically transferred to the Monaco TPS.

2) **Image fusion**- the second radiographer reviews the new daily session MRI with the reference CT imaging. Although Monaco TPS provides an automatic fusion of these image sets, this is not accurate. Therefore the radiographer manually selects a region of interest encompassing the prostate and repeats the fusion step. The registration of the image sets at this step is rigid i.e. includes translation of the new image set only, without any deformation of the images. Once the rigid registration step is completed, the images are reviewed to ensure the fusion is accurate with a manual adjustment used to align the image sets is required. Finally, the contours are propagated from the reference CT to the new daily session MRI using deformable image registration (DIR)

3) **Re-contouring**- the clinician reviews the propagated contours CTV1 and CTV2 and at this point makes a decision as to whether they are reasonable enough to require editing only, or whether the structure requires re-contouring 'from scratch', by deleting the propagated structure. Starting with CTV1, the contouring tools are used to either edit or create the contour once every few axial slices, given the 1 mm slice thickness, deleting the contours in between where relevant The interpolation function is used to construct the whole CTV1 volume which

is reviewed and edited where necessary. For the first five patients, as the 'boolean' or expansion function could not be used in an online setting, the proximal one cm of SV was contoured 'by eye' using knowledge of the pre-existing contours on the reference imaging.

The remaining volume required for CTV2 i.e. the SV 1 to 2 cm from the prostate is contoured next, again estimated either by editing the propagated contour or creating completely new contours.

Finally the clinician reviews the OAR, particularly the rectum and bowel, these are amended where the propagated contours deviate significantly from the anatomy and would otherwise be inaccurate for replanning, with the exception of the bladder which fills significantly during the workflow hence recontouring at the start of the session is also not representative of the anatomy at beam-on. Re-contouring of the OAR is restricted to the slices most relevant for planning, usually those adjacent to CTV1/2 and within 2 cm from the superior aspect of CTV2

4) **Re-optimisation 'adapt to shape'**- re-optimisation of the reference plan is completed by one of the physics team. This is achieved on the new session MRI, using patient specific densities for the bones, external contour and CTV2, derived from the reference CT plan. All other densities for plan calculation are set to 1.0. As discussed in the Introduction of this chapter, re-optimisation can be by adjusting the segment shapes alone, or from fluence for more variable anatomy. This decision was taken daily depending on the consistency of the anatomy and is discussed further in the Results section.

Finally, the prescription is rescaled to ensure that 60 Gy covers 50% of PTV_6000, a separate constraints tab summarises the plan indicating whether the constraints summarised in Table 6.2 and 6.3 have been achieved. The clinician reviews the dose coverage, and the new daily online plan is transferred to RayStation.

5) **Checking of plan**- RayStation provides a secondary dose calculation with the new plan approved if RayStation recalculation is within -1% to 5% of the Monaco dose.

6) **Verification MRI**- the second MRI of the day, using the same 2 minute T2W sequence, is acquired and transferred to Monaco. The radiographer reviews the two image sets- the session and verification MRI with the new CTV and PTV contours created by Step (3). The decision to proceed with the daily online plan is dependent on CTV1 still remaining within PTV1, as illustrated in Figure 6.3.

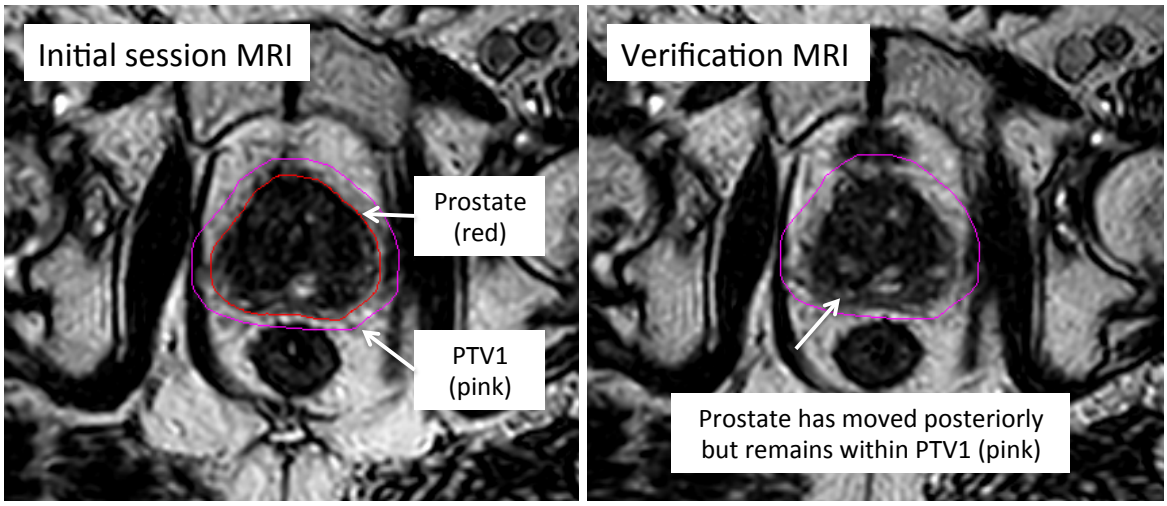

Figure 6.36a)- An example of a MR-Linac treatment fraction for Patient 3 where ATP is <u>not</u> required when the initial session MRI (left) is compared to the verification MRI (right). Corresponding axial slices are shown for the two MRI scans of the same fraction. The prostate (red) has moved posteriorly but remains within the PTV (pink).

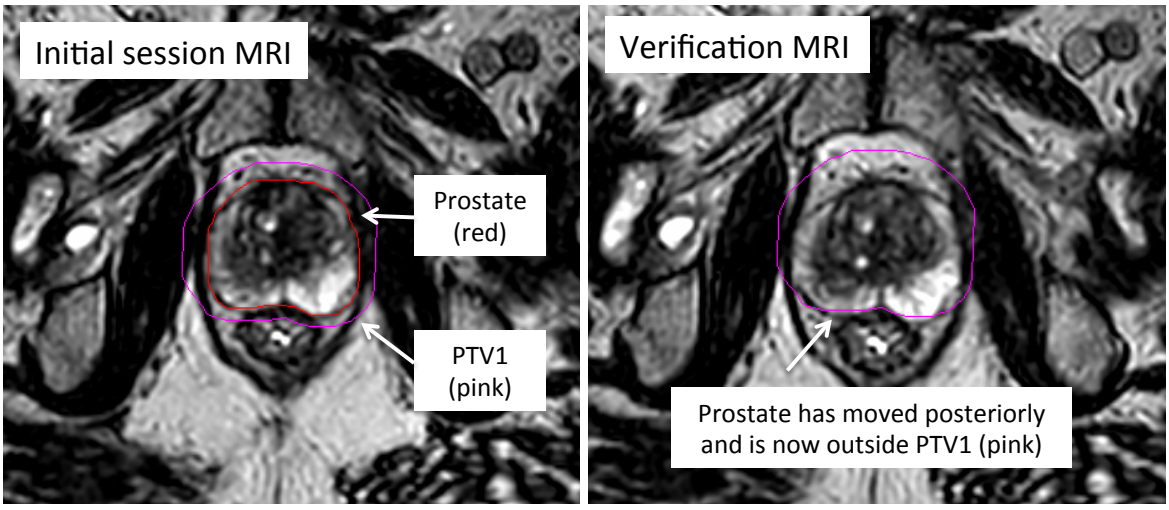

Figure 6.3b)- An example of a different MR-Linac treatment fraction for Patient 3 where ATP <u>is</u> required when the initial session MRI (left) is compared to the verification MRI (right). Corresponding axial slices are shown for the two MRI scans of the same fraction. The prostate (red) has moved posteriorly and is now outside the PTV (pink).

7) **‘Adapt to position’ workflow**- if the CTV falls outside the PTV, as illustrated in Figure 6.3b, then an ATP of the newly generated ATS plan is performed. The radiographer fuses the verification and session imaging either using the automatic fusion operation, or by manually shifting the image set. The ATP is based on this registration and recalculates the plan based on the shifted isocentre. This is therefore a quicker process than re-optimisation, taking approximately 2 minutes. The new plan is re-assessed in terms of constraints and dose coverage with brief review of the contours and plan, without a full secondary dose calculation.

8) **Radiotherapy delivery**- once checking of the daily plan to be delivered is complete, the physicist instructs the radiographer to commence the cine-MR motion monitoring (MM). This provides real-time axial, sagittal and coronal views taken through the isocentre, with PTV2 superimposed on imaging. An example is seen in Figure 6.4. After the final check to ensure the data transfer is correct, treatment is approved followed by delivery of the new daily plan. During treatment delivery, the MM images are viewed, without interruption to treatment, with the instruction to consider pausing treatment should there be a gross, persistent displacement of the prostate.

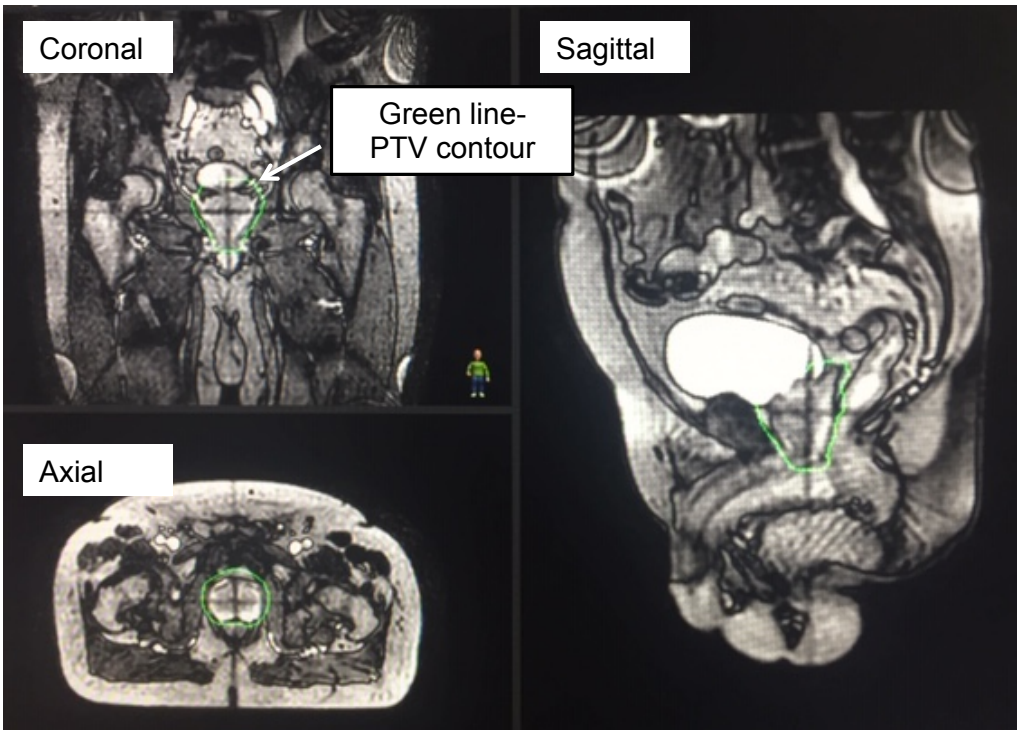

Figure 6.37- An example of cine-MR motion monitoring during MR-Linac treatment delivery. Three fields of view are shown- coronal (top left), axial (bottom right) and sagittal (right). PTV2 (prostate plus proximal 2cm SV with 5mm isotropic margin) is shown in green.

9) **Post-treatment MRI**- once the fraction has been delivered, the radiographer confirms with the patient that they can tolerate the additional time on the treatment couch, and if agreed, the same 2 minute T2W is acquired.

6.4.6 Patient tolerability

Patients were asked to complete a 'Patient Experience Questionnaire' following the end of treatment to check their tolerability of treatment, including the

treatment position, claustrophobia, comfort and symptoms such as tingling or dizziness. The full questionnaire is in the Appendix.

6.4.7 Toxicity assessment and follow-up

The schedule of assessments is followed as per PRISM trial protocol.

Standard investigations

This includes PSA, multiparametric MRI and histopathological confirmation of prostate cancer at baseline. PSA is measured at 12 weeks and six months following completion of treatment and six monthly thereafter.

Toxicity assessment

Common terminology criteria for adverse event reporting (CTCAE) version 4.03 GU and GI domains and Radiation therapy oncology group (RTOG) bladder and bowel toxicity are used at baseline. Further toxicity assessment is completed during weeks 2 and 4 of radiotherapy then at 2, 4, 8, 12 weeks and six months following completion of treatment. Further evaluation is then every three months for the first 2 years then six monthly until 5 years post treatment.

Patient reported outcome measures (PROMs)

The International prostate symptom score (IPSS), EuroQuol five-dimensional (EQ-5D) questionnaire and the expanded prostate index composite-26 (EPIC-26) short form questionnaire are utilised. PROMs data is collected at baseline, during week 4 of radiotherapy, then 4, 12 weeks and six months following completion of treatment then annually thereafter.

6.5 Results

6.5.1 Patient population

The patient characteristics for the first five patients, in order of recruitment to the PRISM trial, are summarised in Table 6.5.

Patient	Age	Staging	Histopathology	Presenting PSA	ADT
1	66	T2N0	Gleason 3+4	6.8	Yes
2	74	T2N0	Gleason 3+4	8.8	Yes
3	71	T2N0	Gleason 3+4	4.7	No
4	72	T2N0	Gleason 3+3	5.8	Yes
5	65	T2N0	Gleason 3+4	18.0	Yes

Table 6.5- Summary of the characteristics of the first five patients recruited to and treated within the PRISM trial.

6.5.2 Reference plan creation

A clinically acceptable reference plan, meeting all mandatory constraints, was achieved in four out of the five patients. Further details are summarised in Table 6.6.

Patient	CTV2 volume (cm^3)	Constraints missed on reference plan	Contouring	Re-optimisation	Number of fractions with ATP of ATS	Number of fractions longer than 60 minutes
1	58.3	None	CTVs	ATS 20/20 fractions Warm start optimisation	None	None
2	50.4	Three in total Two optimal; Bladder V56.76Gy 8.28%, PTV_6000 D98% 48.5Gy One mandatory; PTV_6000 D98% 48.5Gy	CTVs Bowel/ rectum when required (most fractions)	ATS 20/20 fractions Optimisation from fluence Bowel PRV used	7	None
3	67.3	One optimal (bladder V56.76Gy 5.8%)	CTVs Bowel/ rectum when required	ATS 20/20 fractions Warm start optimisation	8	One- delayed to the following day due to software issues
4	69.1	One optimal (bladder V56.76Gy 5.9%)	CTVs Bowel/ rectum when required	ATS 19/20 fractions, One ATP alone Warm start optimisation	None	None
5	31.3	None	CTVs Bowel/ rectum when required	ATS 20/20 fractions Warm start optimisation	3	Two- one delayed to following day. Second delayed to later the same day, both due to software issues

Table 6.6- Summary of the reference planning and workflow used for each of the first five patients treated within the PRISM trial.

For patient 2, due to the presence of small bowel adjacent to the prostate and SV (Figure 6.5) the target coverage was compromised giving a PTV_6000 D98% of 48.51Gy (mandatory constraint D98% >55.8 Gy) in order to meet the bowel dose constraints. This patient proceeded with radiotherapy within the trial, with changes to the workflow described in the next section.

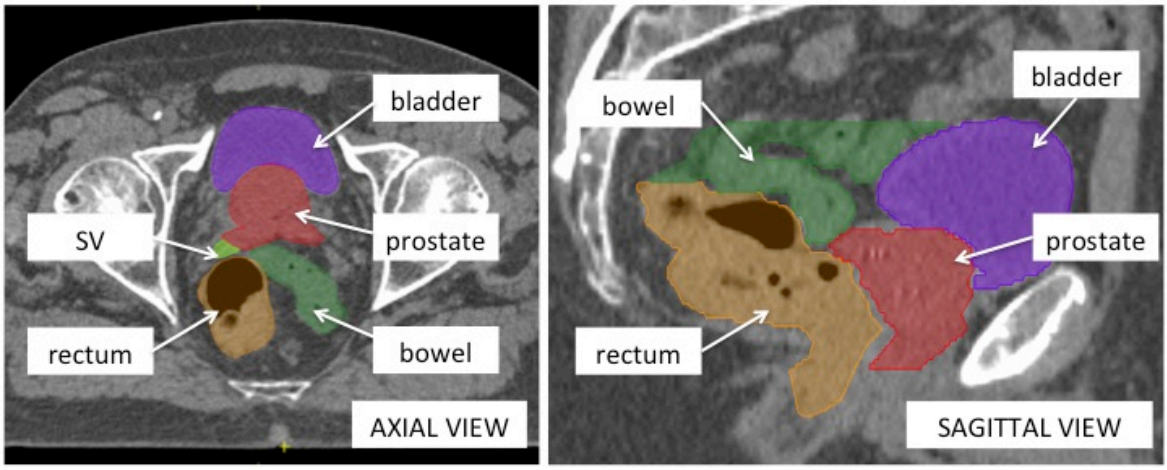

Figure 6.38- Reference CT axial and sagittal views for patient 2 of the PRISM trial showing the proximity of the bowel to the prostate and SV. Red- prostate, purple- bladder, dark green- bowel, orange- rectum, light green (seen on axial image only)- SV.

6.5.3 Daily treatment planning and delivery

All 100 fractions were delivered using the MR-Linac. The mean times for individual steps are summarised in Table 6.7. The total time reported is from the start of acquisition of the session MRI to the end of treatment delivery and therefore excludes patient set up time.

Using the five diagnostic T2W imaging test cases completed prior to online recontouring, assessment was made of the interobserver variability for the four clinicians involved in re-contouring the prostate during the online workflow. Median contour comparison values (interquartile range) for the prostate alone were calculated with a Dice similarity co-efficient of 0.95 (0.95-0.95), Cohen's kappa 0.92 (0.91-0.92), Hausdorff distance 4.5 mm (4.47-5.05) and mean distance 0.78 mm (0.75-0.79) with results reported to 2 decimal places.

A clinician re-contoured the CTVs each day. For patient 2 onwards, the bowel and rectum were amended when gross errors in the propagated contours and current anatomy were seen. The latter was seen most frequently for patient 2 where there was great variability from day to day with the position of the bowel (see Figure 6.6) as seen for the higher contouring times for this patient.

Patient Number	Patient set-up	Session MRI and fusion	Contouring	Optimisation	Checking	Verification MRI and fusion	Treatment delivery	Total time
1	4.9 (0.8)	6.2 (1.1)	8.7 (0.8)	5.6 (0.6)	4.8 (0.8)	5.3 (0.8) No ATP for all	5.2 (0.7)	43.2 (4.1)
2	5.0 (0.9)	5.1 (0.5)	11.1 (1.6)	6.0 (1.7)	4.5 (0.8)	7.0 (2.6) No ATP 5.1 (0.9) ATP 10.2 (0.6)	4.7 (0.6)	46.0 (4.2)
3	5.0 (1.0)	5.4 (0.4)	6.9 (1.0)	5.7 (0.4)	4.2 (0.5)	7.4 (3.1) No ATP 5.0 (0.5) ATP 11.0 (0.7)	5.2 (0.6)	42.2 (3.4)
4	4.0 (1.0)	5.2 (0.6)	10.3 (2.7)	4.0 (0.4)	3.5 (0.4)	4.6 (0.7) No ATP for all	4.3 (0.4)	40.0 (3.7)
5	4.2 (1.3)	5.0 (0.9)	8.5 (2.4)	4.9 (0.6)	4.2 (0.8)	4.9 (1.8) No ATP 4.5 (0.5) ATP 11.7 (0)§	4.1 (0.5)	39.4 (3.5)
Overall	**4.6 (1.1)**	**5.4 (0.9)**	**9.1 (2.3)**	**5.2 (1.1)**	**4.2 (0.8)**	**5.9 (2.3) No ATP 4.9 (0.7) ATP 10.7 (0.8)**	**4.7 (0.7)**	**42.2 (4.4)**

Table 6.7- Summary of the mean (standard deviation in brackets) times taken for each step within the PRISM trial. Values are reported to 1 decimal place. Where relevant, the time taken for the verification step, has been subdivided into fractions with and without ATP. §- due to missing recorded values, although this patient had three fractions with ATP, only one value for this step is available

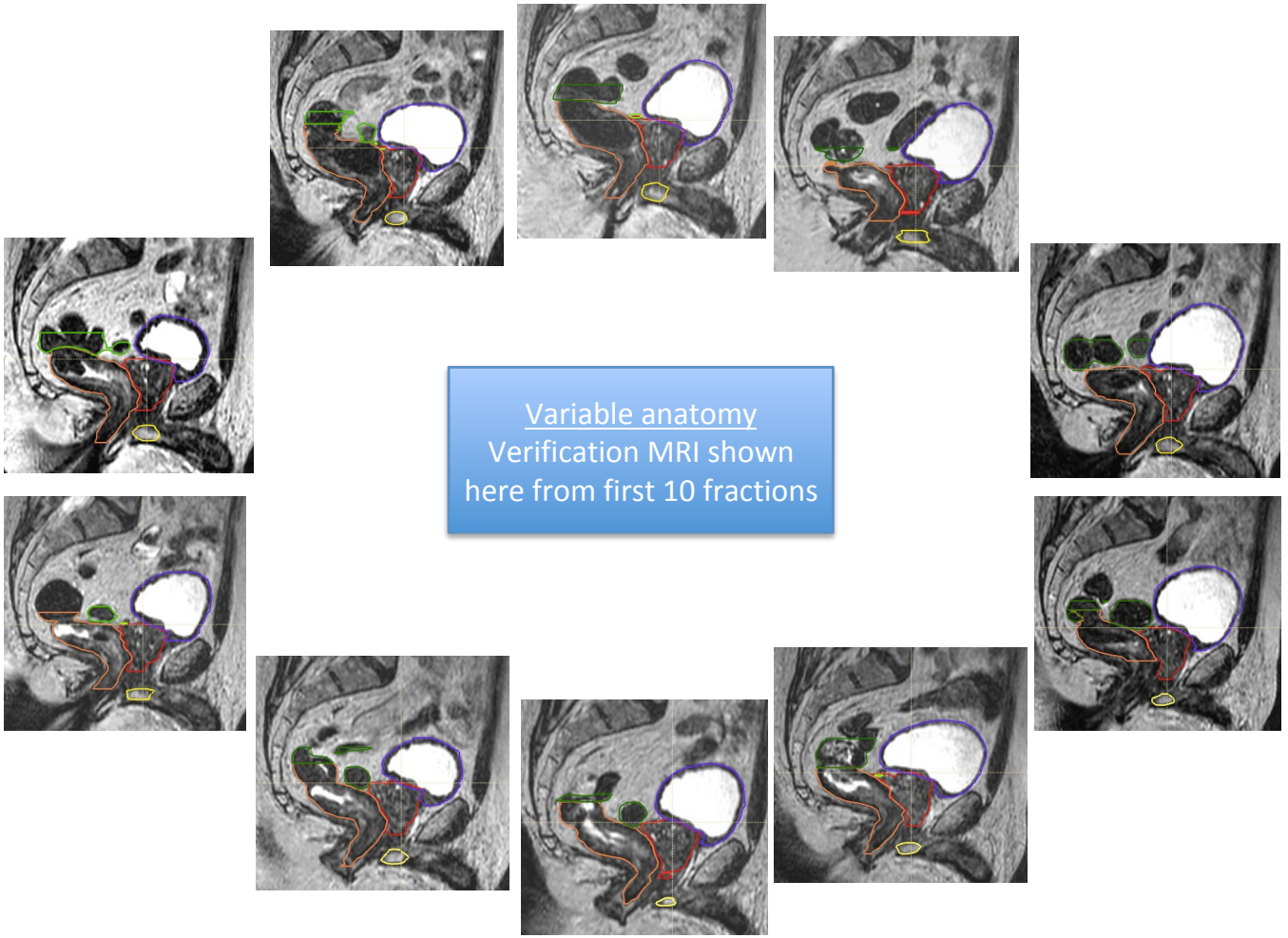

Figure 39.6- Sagittal slices from the verification scans of the first ten fractions of treatment for patient 2 showing the interfractional anatomical variation. Red- prostate, light green- SV, dark green- bowel, orange- rectum, purple- bladder

99 out of 100 fractions proceeded with the ATS workflow as described. For one fraction, due to software failure, despite several attempts, re-optimisation for ATS was not possible. Therefore that fraction proceeded with the ATP workflow alone. For patient 2, plan optimisation proceeded from fluence due to the variability in anatomy and applied the bowel planning organ at risk volume (PRV) in place of the bowel alone, created from the bowel contour plus a 5 mm margin, to take into account uncertainty in the bowel volume.

For all fractions, a clinically acceptable plan was achieved for treatment each day; for patient 2, the daily plan was deemed to be acceptable if the PTV coverage was at least as good as the reference plan. For some fractions for patient 2, the PTV coverage was improved significantly compared to the reference plan due to a more favourable bowel position. This is considered further in the Discussion.

The number of fractions requiring ATP following the verification scan is summarised in Table 6.6.

6.5.4 Patient tolerability

The patient questionnaire was completed from patient 2 onwards. All patients felt ‘very’ calm during treatment (rated 3) and did not feel claustrophobic at any time. All patients found the treatment position ‘moderately’ or ‘very’ comfortable. All patients reported it as being ‘moderately’ or ‘very’ easy to stay still.

One patient felt slightly hot during treatment, otherwise there were no other reported symptoms of feeling hot, dizzy or having tingling. All patients found the noise, smell and lighting very easy to endure.

6.5.5 Toxicity assessment and follow-up

There was no Grade 3 toxicity. RTOG lower GI and GU toxicity and the most common CTCAE toxicities, diarrhoea and urinary frequency, are summarised in Figure 6.7.

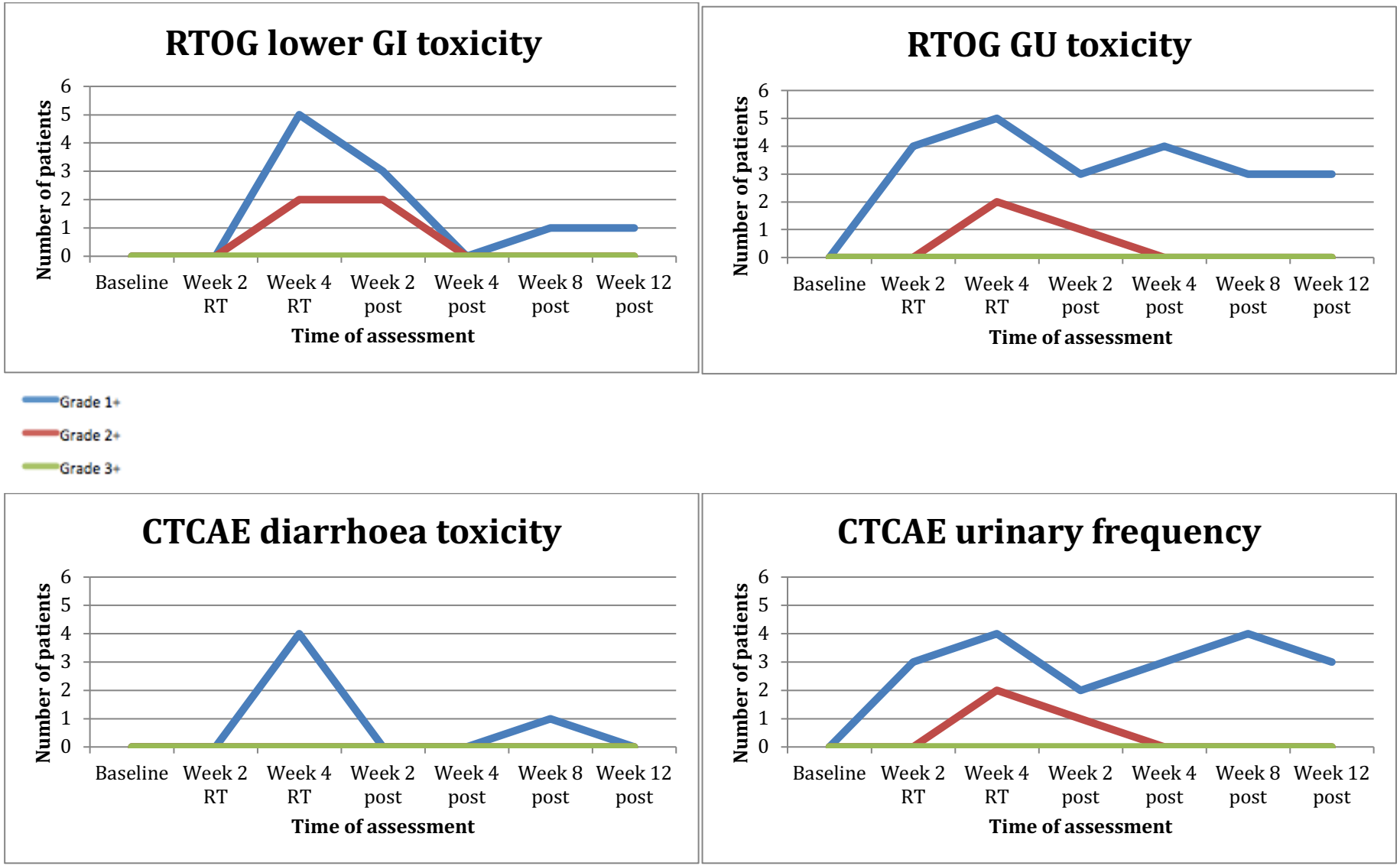

Figure 6.40- Line graphs summarising the genitourinary and gastrointestinal toxicity at baseline, during radiotherapy and during the first 12 weeks following completion of radiotherapy within the PRISM trial. RTOG- Radiation Therapy Oncology Group, CTCAE- Common terminology criteria for adverse event reporting, GI- gastrointestinal, GU- genitourinary

6.6 Discussion

This summary of the first patients treated within the PRISM study demonstrates that MR-guided radiotherapy is feasible and well tolerated. The workflow summarised in Figure 6.2 is considerably more complicated than treatment on a standard linear accelerator with the creation of a new plan each day based on new anatomy. Despite this more complex pathway, ATS was possible in 99 of the 100 fractions considered here. All fractions were delivered on the MR-Linac.

As discussed in the Chapter 1, patients have been treated with MR-guided radiotherapy with online plan adaptation using the MRIdian system since 2016 with some comparisons made here [4]. Most of the data is reported using the Cobalt system, although all machines have now been replaced with a linear accelerator, only a few patients have been treated in the context of a trial [4].

Other groups have reported their first-in-man experiences with treatment on the Elekta MR-Linac [5-7]. However, our centre is the only one to date to have used the more comprehensive ATS workflow for every fraction of prostate radiotherapy. UMC Utrecht have described the ATS workflow for palliative lumbar spine metastases [5] and pelvic node oligometastases [6], others have used a mixture of ATP and ATS [7] with occasional software issues reported by all groups [6, 7].

We found that a clinically acceptable plan was possible for every fraction. To enable the online adaptation, there was development of the template by the

physics team prior to treating the first patient, to determine parameters including the optimal number of SSO loops [3].

Despite the average time of 42.2 minutes being approximately four times the length of couch time for standard linac treatment, this was well tolerated by patients without any interruption to the workflow. This was a particular concern with this type of treatment requiring a full bladder, especially with the onset of toxicity making bladder filling more challenging. Of note, all patients treated in our department have review and optimisation of lower urinary tract symptoms prior to commencing radiotherapy. In addition, an inclusion criterion of the study is IPSS <12 and all patients are counselled, prior to recruitment within the trial, on the extended treatment time. The bladder filling protocol for the MR-Linac patients differs to instructions used for our patients receiving standard radiotherapy, where a comfortably full bladder is required at the time of treatment. Due to the longer treatment session, there is a shorter time duration between drinking the required fluid and setting the patient up. Tetar et al understandably found that a full bladder at the start of the MR-guided radiotherapy session led to treatment interruptions [4]. The volume of fluid required and time for bladder filling for each PRISM patient is reviewed on a day-to-day basis by our team with instructions reflecting the bladder volume seen during online imaging.

The primary endpoint of the study is assessing the proportion of patients who complete > 90% of fractions in 60 minutes or less. For 97 out of 100 fractions, treatment was delivered during the scheduled treatment slot of 60 minutes. For

the remaining fractions, due to software problems preventing reoptimisation, the treatment was delivered with a delay, therefore exceeding the specified 60 minutes. For these three fractions, treatment was delivered in a separate session later the same day or the following day.

Our treatment times here are in keeping with other centres reporting first outcomes. Bertelsen et al [7] reported a median session time of 42 minutes with median contouring time of 12 minutes and, as expected, a considerably reduced time of 26 minutes with the ATP workflow alone. Werensteijn-Honingh et al [6] reported an average of 32 minutes on couch time using the 2 minute MRI scan for the pelvic nodal oligometastases, lower than the values reported here. Although the time taken for individual steps by this group is not reported, we would expect any recontouring of a small node to be significantly faster compared to recontouring the prostate. Our recorded times for each individual step are also comparable to those reported by Tetar et al for the MRIdian system with a total time of 44.7 minutes (including patient set-up) and delineation time of 10.7 minutes. The greatest difference in timings is seen for treatment delivery, compared to our mean delivery time of 4.7 minutes, this was 15.9 minutes for the MRIdian system, which uses gated delivery, pausing treatment when 7% of the CTV lies outside the PTV [4].

Although the first five patients tolerated the extended treatment times, the impetus remains to reduce the on-couch time. This would have a number of benefits for patient comfort and convenience, to minimise intrafractional motion and increase patient throughput when appropriate. Since these first patients

were treated, there has been a reduction in the time taken for certain steps including image transfer and plan checking. As seen in Table 6.7, re-contouring comprises a significant portion of the total session time, although the length of this step is variable depending on patient anatomy- both target and OAR, the accuracy of contour propagation and clinician experience. Patient 2 required the longest time for re-contouring at 11.1 minutes due to the additional time for amending the adjacent bowel. Patient 3 however, was the quickest to re-contour at 6.9 minutes due to the particularly well defined prostate capsule. When the OAR are reviewed, amendments are kept to the proximity of target most relevant for dose optimisation, in particular within the prostate plus 2 cm expansion used to create CTV2 (illustrated in Figure 6.1), which is comparable to the limited re-contouring described for the MRIdian system [4, 8]

A further iteration in the current workflow includes the propagation of contours from reference MRI to daily MRI, rather than CT to MRI. Although this is yet to be assessed formally, using the same imaging modality should improve the accuracy of the registration step required for contour propagation with the resulting contours requiring less editing.

The work in Chapter 7 looks at initiating changes to both reduce the length of time for each treatment session, by considering the use of propagated contours without amendments, and also eliminate the need for a clinician being present for each hour long session with adequate radiographer training.

The second patient recruited to the trial was particularly challenging (Figure 6.5) due to proximity of the bowel giving compromised target coverage. For this patient, daily re-planning was adjusted to optimise ‘from fluence’, improving the target dose. Further work carried out by our group has recalculated the clinically delivered MR-Linac plans on the verification images in order to compare the estimated delivered dose on the MR-Linac to the dose that would have been received on a standard linac [1]. This work has shown that for patient 2, the creation of a new plan each day enabled target dose constraints to be achieved on the days when the bowel was in a more favourable position (see Figure 6.8). This allowed an average estimated improvement of 4.6 Gy to the prostate CTV D98, from 49.9 Gy to 54.5 Gy, with the ATS workflow compared to standard treatment.

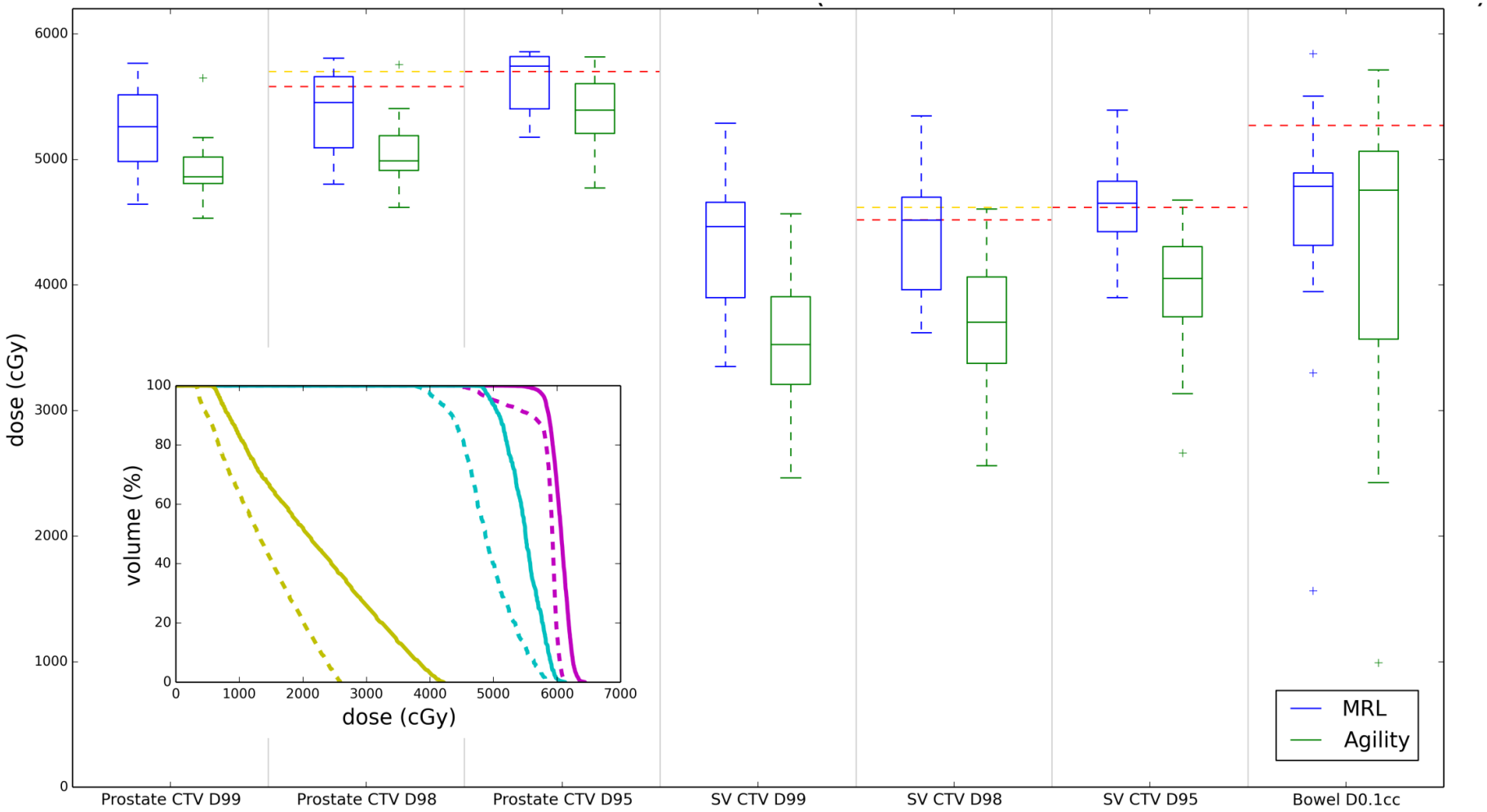

Figure 6.8: Estimates of delivered dose from patient 2. Main figure: boxplots comparing the target coverage dose-volume metrics and critical bowel D0.01cc mandatory clinical goal for the estimates of the clinical MR-linac and standard linac (Agility) fractional delivered dose estimates. Mandatory and optimal clinical goal levels are shown as red and gold lines, respectively. Inset: an example fractional delivered dose DVH estimate with prostate CTV, SV CTV, and bowel shown as purple, cyan, and yellow, respectively. Clinical MR-linac and standard linac estimates are shown as solid and dashed lines. For both the boxplots and DVHs, all estimates of fractional delivered dose were scaled to 20 fractions. Figure courtesy of Dr Alex Dunlop, data submitted for publication [1].

Table 6.6 shows the variation in the frequency of the 'ATP of ATS' step in this limited group of patients, ranging from zero to 8 times out of the twenty fraction schedule. Two patients did not have ATP performed at all during the treatment course. For the first patient this was partly due to the novelty of the entire workflow and unfamiliarity of reviewing the images at this step but also due to the absence of gross shifts in this patient anatomy between scans (Figure 6.3). However for patient 4, once the team had more experience, the absence of ATP following the verification imaging was due to stable anatomy in this patient.

Finally, the toxicity described here, although for a limited group of patients, is in keeping with toxicity seen with a standard linear accelerator with the CHHiP trial [9] reporting 38% grade 2 or more acute RTOG bowel toxicity (reported in 2 out of 5 of our patients) and 49% grade 2 or worse acute RTOG bladder toxicity (2 out of 5 of our patients) in the 60 Gy group. No grade 3 toxicity was reported for these patients treated on the MR-Linac.

PRISM remains open to recruitment with a number of changes to the workflow used for the first five patients. Some changes have been discussed already including the use of a reference MRI that allows MR to MR image registration and in future will hopefully eliminate the need for a planning CT, reverting to an MR only workflow. In terms of staffing, one physicist now completes the re-optimisation and checking steps. For the re-contouring step, the estimation of the proximal 1 cm of SV has been replaced with an automatic step using Boolean function to incorporate the required volumes for CTV1 and CTV2, enabling a more accurate and consistent set of contours from day to day.

Finally, the optimisation is now calculated from fluence, as utilised for patient 2, for all patients independent of anatomy.

The PRISM trial at RMH, together with the use of this protocol at other consortium sites, will allow further assessment of the feasibility, toxicity and outcomes of patients treated with our standard fractionation schedule of 60 Gy in 20 fractions. However, the greatest gains are likely to be with the use of margin reduction, treating patients with unfavourable or variable anatomy, adopting extreme hypofractionated schedules, assessment of treatment response and the use of dose escalation to an intraprostatic lesion. This is considered further in the Discussions chapter.

6.7 Conclusion

Daily prostate MRI guided radiotherapy with online replanning is feasible and delivered within a reasonable time. Acute toxicity is comparable to treatment delivered with a standard linear accelerator. Certain patients with unfavourable anatomy may particularly benefit from the re-optimisation of a new treatment plan on daily anatomy. PRISM recruitment is ongoing with a total recruitment of 30 patients planned.

6.8 References

1) Alex Dunlop AM, Alison Tree, Helen Barnes, Lorna Bower, Joan Chick, Edmund Goodwin, Trina Herbert, Rebekah Laws, Helen McNair, Dualta McQuaid, Jonathan Mohajer, Rahul Nilawar, Angela Pathmanathan, Gillian Smith, Ian Hanson, Simeon Nill, Uwe Oelfke. Daily adaptive radiotherapy for patients with prostate cancer using the Elekta MR-linac: initial clinical experiences and assessment of delivered doses compared to a C-arm linac. Submitted for publication August 2019 2019.
2) Verkooijen HM, Kerkmeijer LGW, Fuller CD et al. R-IDEAL: A Framework for Systematic Clinical Evaluation of Technical Innovations in Radiation Oncology. Frontiers in Oncology 2017; 7: 59.
3) Adam Mitchell AD, Angela Pathmanathan, Simeon Nill, Alison Tree, Uwe Oelfke. Prostate treatment planning for the MR-linac: effect of online performance on template development. Radiotherapy and Oncology 2019; ESTRO 38 conference: EP-2002
4) Tetar SU, Bruynzeel AME, Lagerwaard FJ et al. Clinical implementation of magnetic resonance imaging guided adaptive radiotherapy for localized prostate cancer. Physics and Imaging in Radiation Oncology 2019; 9: 69-76.
5) Raaymakers BW, Jurgenliemk-Schulz IM, Bol GH et al. First patients treated with a 1.5 T MRI-Linac: clinical proof of concept of a high-precision, high-field MRI guided radiotherapy treatment. Physics in Medicine and Biology 2017; 62: L41-l50.
6) Werensteijn-Honingh AM, Kroon PS, Winkel D et al. Feasibility of stereotactic radiotherapy using a 1.5 T MR-linac: Multi-fraction treatment of pelvic lymph node oligometastases. Radiotherapy and Oncology 2019; 134: 50-54.
7) Bertelsen AS, Schytte T, Møller PK et al. First clinical experiences with a high field 1.5 T MR linac. Acta Oncologica 2019; 1-6.
8) Bohoudi O, Bruynzeel AME, Senan S et al. Fast and robust online adaptive planning in stereotactic MR-guided adaptive radiation therapy (SMART) for pancreatic cancer. Radiotherapy and Oncology 2017.
9) Dearnaley D, Syndikus I, Mossop H et al. Conventional versus hypofractionated high-dose intensity-modulated radiotherapy for prostate cancer: 5-year outcomes of the randomised, non-inferiority, phase 3 CHHiP trial. The Lancet Oncology 2016.

6.9 Chapter 6 Appendix

	0 Not at all	1 Slightly	2 Moderately	3 Very
I found the treatment position comfortable				
I found it easy to stay still				
I wanted to come out of the machine during my treatment				
I felt calm during my treatment				
I found the noise in the room was easy to endure				
I felt the smell in the room was easy to endure				
I found the lighting in the room was easy to endure				
I felt dizzy during my treatment				
I felt hot during my treatment				
I felt tingling sensations during my treatment				

Table 6A- Patient Experience Questionnaire given to patients following the end of treatment within the PRISM trial, to check their tolerability of treatment

Chapter 7- Dosimetric comparison of propagated and radiographer contours for the MR-Linac

7.1 Introduction

This chapter brings together the outcomes from previous chapters. Chapter 6 outlines the treatment of the first five patients within the PRISM trial, with the average treatment time of 42.2 minutes and the requirement for the presence of a clinician for re-contouring. Amending the target and/or organs at risk (OAR) online is unique to the MR-Linac workflow but is time consuming, as the clinician is present for the entire session to ensure streamlined workflow.

Furthermore, it had been observed that the propagated contours generated online, from registering the reference imaging to the new daily session imaging, were more accurate when using a reference MRI, compared to reference computed tomography (CT), and in some instances needed minimal adjustment to be clinically accurate.

In Chapter 4, I demonstrated that even with limited training, therapeutic radiographers achieved accurate and consistent contours on MRI with a Dice similarity co-efficient (DSC) of 0.94 on T2-weighted (T2W) magnetic resonance imaging (MRI), relevant when considering extending the role of radiographers to

lead this step during the MR-Linac workflow [1]. As reviewed in the Discussion of Chapter 4, with regards to radiographer contouring, and Chapter 5, in relation to auto-contours, the agreement of contours with a gold standard does not reflect whether these would be dosimetrically adequate.

This chapter takes this work a step further, using un-edited propagated contours and propagated contours edited by therapeutic radiographers on MR-Linac image sets, acquired from patients within the PRISM trial. I look at whether the target, as delineated by a clinician, would have received an adequate dose if an online plan created from the propagated or radiographer contours, was delivered.

7.2 Aims of Chapter 7

In this chapter, I will aim to assess whether there is a clinically significant difference in the plans created from propagated or radiographer contours, compared to plans created using a gold standard clinician contour, using the MR-Linac online workflow.

My hypothesis is that prostate radiotherapy plans optimised using contours propagated by image registration, or contours created by therapeutic radiographers can meet the mandatory constraints for the ‘gold standard’ clinician delineated target.

To test this hypothesis I will:

1) Assess whether un-edited propagated contours are sufficient for use in the online workflow for the MR-Linac
2) Assess whether radiographer edited contours are sufficient for use in the online workflow for the MR-Linac
3) Assess whether contour comparison metrics such as DSC and mean distance can be used to predict whether contours will be accurate enough for online planning
4) Assess the proportion of plans optimised from propagated or radiographer contours that meet the online planning constraints for the gold standard contour.

7.3 Materials and Methods

The Methods used here have followed the online workflow, using the same planning techniques as far as possible. As a result, all contouring and planning was completed on Monaco treatment planning system (TPS) version 5.40.01 (Elekta AB, Stockholm, Sweden).

7.3.1 Radiographer training for contouring

Five therapeutic radiographers, all involved in delivering treatment on the MR-Linac attended an initial training session led by myself. During this session, I reviewed the anatomy of the prostate, seminal vesicles (SV) and OAR especially the rectum. In particular I explained the prostate tumour site group (TSG) contouring guidelines and reviewed the prostate contour on consecutive

axial slices of T2W imaging. The radiographers were given a copy of this T2W ‘atlas’ to refer to during contouring.

The radiographers then completed prostate, SV and rectum contours on five sets of T2W diagnostic MRI, from the same set used in the Chapter 4, Section 4.4. The radiographers were asked to complete a sheet where they could comment on any particular difficulties they encountered during the contouring.

Following this, I conducted a further teaching session, where I reviewed the contours with all radiographers present, in particular discussing the more common discrepancies for contouring, and where possible relating this to the anatomy of the prostate. The axial contours were reviewed in relation to a ‘gold standard’ clinician contour I had previously created from the STAPLE of three clinician contours as in Chapter 4, Section 4.4.6, and subsequently reviewed by Dr Alison Tree to ensure these STAPLE contours were clinically correct.

An example of inaccuracies in initial radiographer contouring is seen in Figure 7.1.

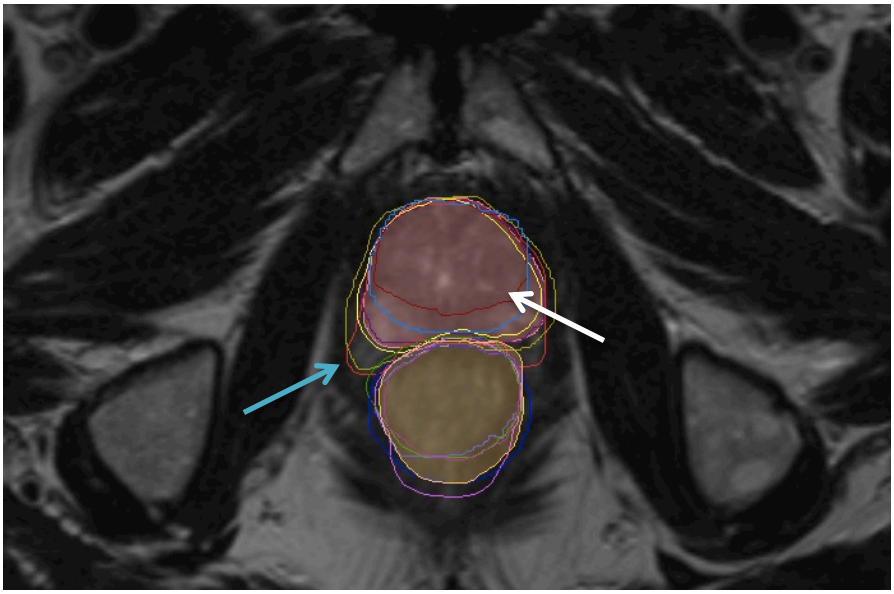

Figure 7.41- Overlay of five therapeutic radiographer practice contours on diagnostic T2W imaging. Red shading- 'gold standard' clinician prostate; yellow shading- 'gold standard' clinician rectum; contour lines from radiographer contours. White arrow indicates incorrect exclusion of the peripheral zone by the red contour. Blue arrow indicates incorrect posterior extension of prostate contour by the red and yellow contours.

7.3.2 Imaging sets for dosimetric comparison study

Dr Alex Dunlop, physicist from the Royal Marsden Hospital imported all images sets required for this study into clinical Monaco TPS for five patients from the PRISM trial- patient 1 and patients 3-6. As detailed in the Results section, Chapter 6, patient 2 had an unfavourable bowel distribution leading to missed mandatory constraints, and was therefore not appropriate for inclusion in this study.

For each patient, four image sets were required

1) Reference CT (RefCT) imaging

2) One MR-Linac verification image set to be used as the reference MRI (RefMR)
3) Two MR-Linac session image sets to be used for contouring (MR1-7 and MR8-14).

The RefCT imaging was already available and imported for all five patients. In addition a RefMR was required to create a reference MRI plan for contour propagation and online replanning. This had to be created for the patients included here, as at the time of their treatment, the reference CT was used as reference imaging during online replanning. However, since patient 8, a reference MRI has been used routinely in the workflow. For each patient, the reference MRI was chosen to be the verification MRI (the MRI taken just before treatment delivery) with bladder volume closest to the reference CT to ensure an accurate RefMR plan was generated. Finally, for consistency and to avoid bias when selecting image sets for contouring, the two image sets used for each patient for contouring were the session MRI datasets from fraction 1 and fraction 11 of treatment. The same image sets were imported seven times each for contouring and planning- one for the clinician 'gold standard' contour, one for the propagated contour, five for each of the radiographer contours. This was to ensure that each image set would only have one set of contours and one plan. A summary of the image sets for each patient is seen in Table 7.1.

Source of image set	MRI dataset	Contouring
Reference (pre-treatment) CT	RefCT	Reference clinician contours
One verification MRI from fractions 1 to 5	RefMR	Reference clinician contours
Fraction 1	MR1	Clinician
	MR2	Propagated
	MR3	Radiographer 1
	MR4	Radiographer 2
	MR5	Radiographer 3
	MR6	Radiographer 4
	MR7	Radiographer 5
Fraction 11	MR8	Clinician
	MR9	Propagated
	MR10	Radiographer 1
	MR11	Radiographer 2
	MR12	Radiographer 3
	MR13	Radiographer 4
	MR14	Radiographer 5

Table 7.1- Summary of the image data sets required for each of the five patients included in the study.

7.3.3 Creating reference MRI plan

I generated the RefMR plan from the RefCT plan in the same way that daily online plans are created. The RefCT already had contours completed by myself and reviewed by consultant Dr Tree, as per usual clinical practice. I propagated the contours from RefCT to RefMR using the 'adapt anatomy' tool on Monaco TPS, which produces the new contours on the RefMR using the deformable

registration between these two image sets. I then amended the prostate, SV and OAR contours as appropriate. All contouring including clinical target volume (CTV) and planning target volume (PTV) definitions are summarised in Section 6.4.3, Methods of Chapter 6.

The different optimisation techniques are discussed in Chapter 6 Introduction, Section 6.2. To create the RefMR plan, I selected the 'optimise shapes from fluence' method, as per current online MR-Linac workflow. All parameters are pre-programmed for the online workflow following the work from the physicists prior to commencing treatment on the MR-Linac [2, 3]. Optimisation parameters include a statistical uncertainty of 1%, maximum 60 segments, minimum segment area of 4 cm^2, and minimum of 3 monitor units per segment. In addition I selected 10 segment shape optimisation (SSO) loops, as is standard practice for reference plans. Once the optimisation was complete, I rescaled the prescription for 60.0 Gy to cover 50% of PTV_6000, reviewed the constraints to ensure these were achieved and approved the plan on Monaco TPS. The constraints have previously been summarised in Chapter 6, Table 6.2 (target constraints) and 6.3 (OAR constraints).

7.3.4 Contouring for dosimetric comparison study

As described above, there were ten datasets for contouring- two for each of the five patients included. Reflecting the online workflow, I propagated the contours from RefMR to each of the MRI datasets (MR1-14) for each patient, again using the 'adapt anatomy' tool.

For the purposes of this study, I created the 'gold standard' contour for each of the ten image sets. This is considered further in the Discussion, but this was considered to be appropriate as I am one of the clinicians re-contouring for the online plans, hence this reflects the current 'best practice' online workflow. I created the clinician 'gold standard' contour on MR1 and MR8 (see Table 7.1) by amending the prostate and SV propagated contours. I reviewed the OAR contours to ensure that these were clinically appropriate but these were not amended.

The propagated contours remained un-edited on datasets MR2 and MR9 for each patient.

Identical written instructions were given to all five radiographers, who were asked to amend the prostate and SV contours on their allocated image sets, as summarised in Table 7.1. The radiographers were given the choice to either amend or completely replace 'from scratch' the target volumes and had a timing sheet to record the method used and the length of time required to re-contour.

7.3.5 Creation of plan for each contour

I created a new plan for each set of contours, again using the 'optimise shapes from fluence' option with parameters as summarised above but optimising plans using 5 SSO loops, as per the online workflow. As above, I rescaled the prescription for 60.0 Gy to cover 50% of PTV_6000 and approved the plans on Monaco TPS. I reviewed the constraints of all plans to assess if they were clinically acceptable, based on the contours of that image set. These

radiotherapy plans represent the treatment that would have been delivered on that day based on the clinician/ propagated/ radiographer contours used for optimisation.

7.3.6 Assessment of dose to 'gold standard' delineated target

The 'gold standard' clinician contours act as a surrogate here for the 'true' target volumes. In order to assess the dose the 'gold standard' targets would have received, I copied over each plan created above, with the exact original segments, onto the image set with the gold standard contours.

Using the clinical constraints tab, I then recorded the dose to the 'gold standard' target contours and the gold standard OAR, which were unaltered on all image sets, including whether the mandatory or optimal constraints were met. This simulated the effect of the radiographer contours being used to create the daily online plan.

7.3.7 Contour comparison metrics

In order to correlate the dose to the 'gold standard' target to the accuracy of each of the radiographer and propagated contours, I used ADMIRE software version 2.0 (Elekta AB, Stockholm, Sweden) to calculate the DSC, Cohen's kappa co-efficient, mean distance and Hausdorff distance between each propagated or radiographer contour and my gold standard contour. For this I used the CTV1, that is, the contour combining the prostate plus proximal 1cm of SV, as this is the high dose target and therefore differences in accuracy will have the greatest clinical impact.

7.4 Results

7.4.1 Reference MRI plans

A clinically acceptable reference plan was achievable for all ten image sets, that is, a radiotherapy plan meeting at least all mandatory constraints.

7.4.2 Contouring for dosimetric comparison study

For my re-contouring, I amended the propagated contours for all sets excluding the SV for one patient, where I deleted the contours and re-contoured from the beginning. The mean time for my re-contouring was 7.4 minutes (min) with a standard deviation (sd) 1.5 min. The five therapeutic radiographers used a mixture of amending the propagated contours provided and deleting the provided contours, before contouring 'from scratch'. The mean time for contouring was 10.1 min (sd 1.5 min).

7.4.3 Creation of plan for each contour

For each of the ten imported image sets, there was one clinician plan, one propagated contour plan and five radiographer contour plans. Overall therefore, there were ten clinician plans, ten propagated contour plans and 50 radiographer contour plans. A clinically acceptable online plan was obtainable for all 70 plans.

7.4.4 Assessment of dose to the 'gold standard' delineated target

Table 7.2 summarises each target and OAR and the number of times either the mandatory or optimal constraint was missed.

Target/ OAR	Constraint (mandatory in brackets)	Clinician			Propagated			Radiographer		
		None missed	Optimal Missed	Mandatory missed	None missed	Optimal Missed	Mandatory missed	None missed	Optimal missed	Mandatory missed
PTV_6000	D0.1cm3 < 64.2Gy (+1.8Gy)	10/10	0	0	10/10	0	0	50/50	0	0
	D5% < 63Gy	10/10	0	0	10/10	0	0	50/50	0	0
	D50% > 59.4Gy	10/10	0	0	10/10	0	0	50/50	0	0
	D50% < 60.6Gy	10/10	0	0	10/10	0	0	50/50	0	0
	D98% > 57Gy (-1.2Gy)	10/10	0	0	7/10	3/10	0	14/50	21/50	15/50
PTV_4860	D50% > 48.6 Gy	10/10	0	0	10/10	0	0	50/50	0	0
	D98% > 46.17 Gy (-0.97Gy)	10/10	0	0	10/10	0	0	45/50	3/50	2/50
Bowel	V52.7Gy < 0.01cm3	9/10	0	1/10	10/10	0	0	50/50	0	0
	V48.7Gy < 0.5 cm3 (+5.5cm3)	10/10	0	0	10/10	0	0	50/50	0	0
	V44.6Gy < 14cm3 (+14cm3)	10/10	0	0	10/10	0	0	50/50	0	0
	V40.5Gy < 17cm3 (+93cm3)	10/10	0	0	10/10	0	0	50/50	0	0
	V36.5Gy < 78cm3 (+80cm3)	10/10	0	0	10/10	0	0	50/50	0	0
Penile bulb	V40.5Gy < 50%	10/10	0	0	10/10	0	0	50/50	0	0

Bladder	V60.8Gy < 3% (+22%)	10/10	0	0	10/10	0	0	50/50	0	0
	V56.76Gy < 5% (+30%)	3/10	7/10	0	4/10	6/10	0	21/50	29/50	0
	V52.7Gy < 50%	10/10	0	0	10/10	0	0	50/50	0	0
	V48.7Gy < 25%	10/10	0	0	10/10	0	0	50/50	0	0
	V40.5Gy < 50%	10/10	0	0	10/10	0	0	50/50	0	0
L fem head	V40.5Gy < 50%	10/10	0	0	10/10	0	0	50/50	0	0
R fem head	V40.5Gy < 50%	10/10	0	0	10/10	0	0	50/50	0	0
Pubic symphysis	V56Gy < 25%	10/10	0	0	10/10	0	0	50/50	0	0
Rectum	V60.8Gy < 3% (+2%)	10/10	0	0	10/10	0	0	50/50	0	0
	V56.8Gy < 15%	10/10	0	0	10/10	0	0	50/50	0	0
	V52.7Gy < 30%	10/10	0	0	10/10	0	0	50/50	0	0
	V48.6Gy < 35% (+15%)	10/10	0	0	10/10	0	0	50/50	0	0
	V40.5Gy < 50% (+10%)	10/10	0	0	10/10	0	0	50/50	0	0
	V32.4Gy < 65%	10/10	0	0	10/10	0	0	50/50	0	0
	V24.4Gy < 80%	10/10	0	0	10/10	0	0	50/50	0	0

Table 7.2- Summary of the number of plans not meeting optimal and/or mandatory constraints for each target and OAR. These are displayed for each contour type- clinician, propagated and radiographer. Abbreviations: fem- femoral; Gy- Gray; L- left; R-right.

This is further outlined below in Table 7.3 summarising the overall number of clinically acceptable plans.

Contour	All constraints achieved	Mandatory constraint(s) achieved	Mandatory constraint(s) missed	Clinically acceptable plans
Clinician	3/10	6/10	1/10§	10/10
Propagated	2/10	8/10	0/10	10/10
Radiographer	6/10	29/50	16/50±	35/50

Table 7.3- Summary of the number of plans achieving all constraints, missing optimal constraints only and missing mandatory constraints for each contour type. § mandatory bowel constraint narrowly missed but plan still clinically acceptable. ± PTV_4860 D98% mandatory constraint narrowly missed for one plan but still clinically acceptable.

7.4.5 Target constraints

Firstly considering the target constraints, all plans based on the un-edited propagated contours met at least the optimal dose constraints for the low and high dose PTV. However, 15 out of 50 plans based on radiographer contours failed to meet the mandatory constraint for PTV_6000 D98%, one of these plans also failed to meet the PTV_4860 D98%. All 15 plans failing to meet the PTV_6000 would be deemed unacceptable for delivery. A further 16th plan failed to meet the PTV_4860 D98% (but did meet the optimal constraint for PTV_6000) however the PTV_4860 D98% value was 45.19 Gy, with mandatory

constraint of 45.2 Gy, therefore this plan would have been clinically acceptable online.

7.4.6 OAR constraints

Secondly considering the OAR constraints, the majority of these were achieved by all three types of contours. The main exception is the bladder V56.76 Gy, which is often missed in the online setting and in this study was missed by 7/10 clinician, 6/10 propagated and 29/50 radiographer plans. The only other unachievable OAR goal was seen with one of the clinician plans, which did not meet the mandatory constraint of $<0.01cm^3$ for bowel V52.7Gy. For this particular plan, the V52.7Gy was $0.011cm^3$ and was therefore categorised as being clinically acceptable, as during the online setting, this plan would be accepted for treatment delivery.

I examined the failure to meet the PTV_6000 D98% further, as this was the cause of the plans being clinically unacceptable. The range and median values for each contour type are summarised in Table 7.4, the lowest PTV_6000 D98% was 50.8 Gy, considerably lower than the mandatory constraint of 55.8 Gy. In addition, there was variation between radiographers in the accuracy of contours, with 8/15 of the rejected plans as a result of one observer (Rad2), this is displayed further in Figure 7.2. Two out of the five radiographers only had 1/10 plans miss this constraint with the PTV_6000 D98% still over 55.2 Gy.

Contour type	Median PTV_6000 D98% (Gy)	Range for PTV_6000 D98% (Gy)
Clinician	57.7	57.3 - 57.9
Propagated	57.2	56.0 - 57.9
Radiographer	56.5	50.8 - 57.7

Table 7.4- Summary of the range and median PTV_6000 D98% values for each contour type (values reported in in Gray to 1 decimal place). The PTV_6000 D98% optimal value is 57Gy and mandatory value is 55.8 Gy.

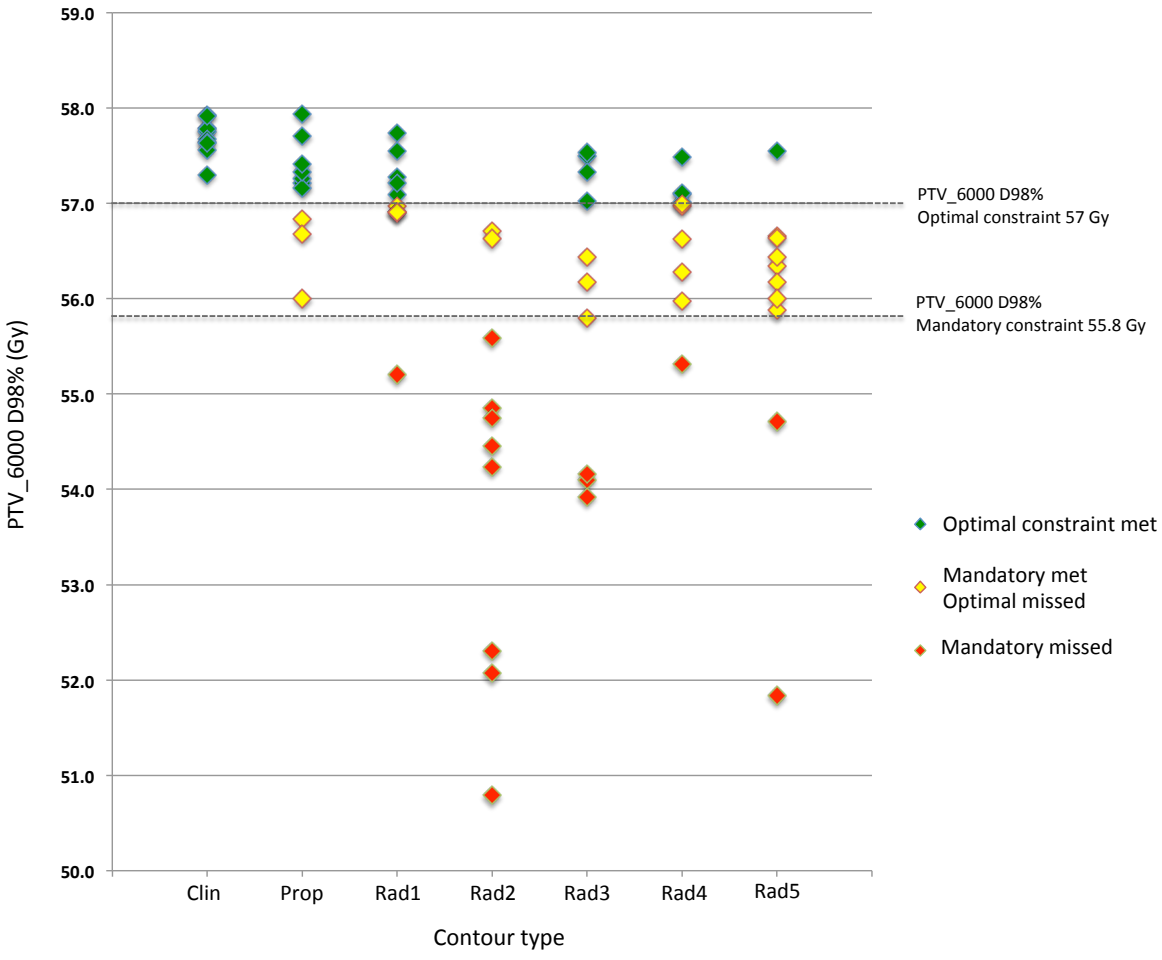

Figure 7.42- Graph summarising the PTV_6000 D98% (in Gray) for the ten plans for the clinician, propagated and each of the radiographer contours. The dotted lines represent the mandatory constraint PTV_6000 D98% > 55.8Gy and optimal constraint PTV_6000 D98% > 57 Gy.

7.4.7 Contour comparison metrics

Table 7.5 summarises the contour comparison metrics, when comparing the CTV1 for each propagated or radiographer contour to the corresponding 'gold standard' contour.

Contour type	DSC	Cohen's kappa	Hausdorff distance (mm)	Mean distance (mm)
Propagated	0.96 (0.94-0.96)	0.94 (0.91-0.95)	4.1 (3.3-4.3)	0.5 (0.4-0.6)
Rad1	0.94 (0.91-0.95)	0.91 (0.86-0.93)	5.0 (4.4-5.7)	0.8 (0.6-1.0)
Rad2	0.83 (0.80-0.87)	0.76 (0.73-0.83)	7.7 (6.5-9.3)	2.0 (1.4-2.3)
Rad3	0.88 (0.85-0.94)	0.83 (0.79-0.92)	6.4 (5.2-7.3)	1.3 (0.7-1.7)
Rad4	0.93 (0.87-0.96)	0.90 (0.82-0.94)	6.5 (5.7-7.6)	0.91 (0.81-0.94)
Rad5	0.89 (0.86-0.92)	0.85 (0.81-0.89)	6.4 5(.6-7.6)	0.8 (0.8-0.9)

Table 7.5- Summary of the median (interquartile range) comparison values for each observer, calculated by comparing each contour to the 'gold standard' clinician contour. Overlap comparisons (DSC, Cohen's kappa) are reported to 2 decimal places, distance measurements (Hausdorff distance, mean distance) are reported to 1 decimal place.

Finally, as detailed in the Introduction Section 1.6 with consideration to the relevance of contour comparison metrics or optimal values, I plotted the DSC when comparing each contour to the gold standard clinician contour, against the

PTV_6000 D98% achieved by that contour when assessing the dose to the 'gold standard' PTV. This is seen in Figure 7.3.

This graph indicates that if the DSC between a contour and the gold standard is at least 0.90, the plan will be clinically acceptable. If the DSC is <0.85 then the plan is not clinically acceptable. A DSC of 0.85-0.90 gives variable outcomes when assessing the plans, this is discussed further below.

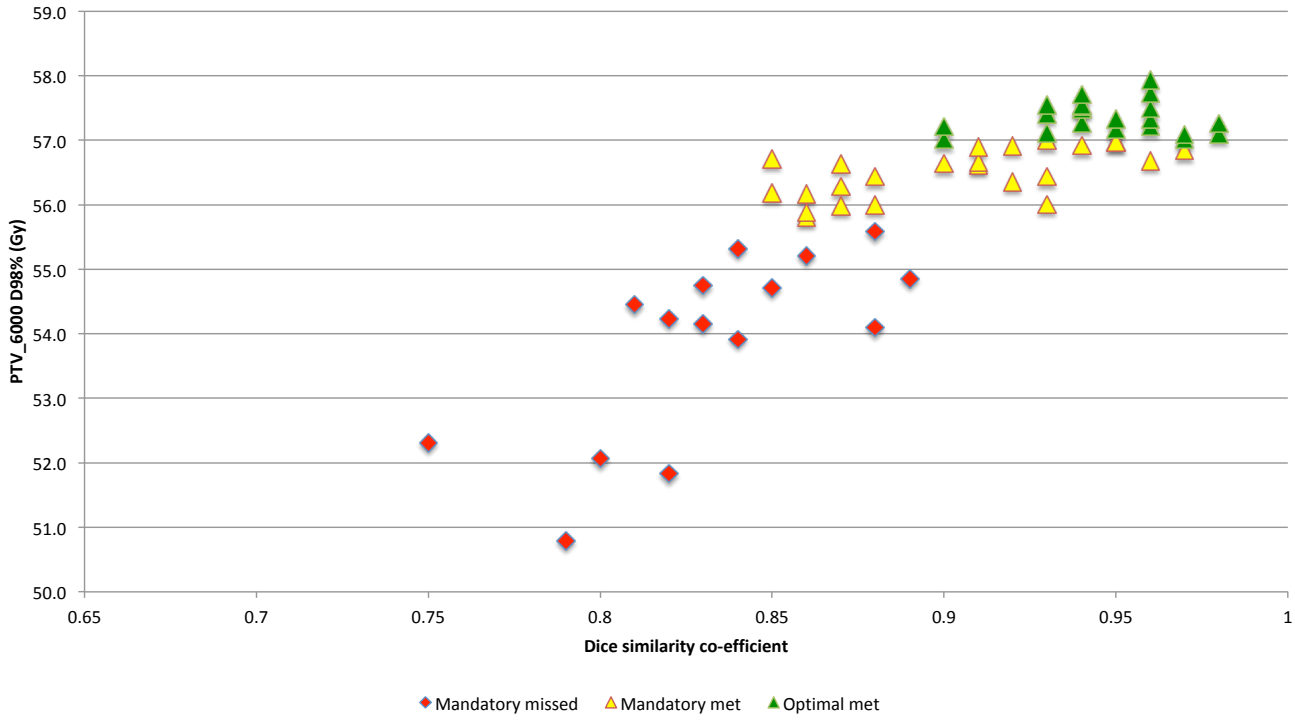

Figure 7.43- Scatter plot showing the relationship between the PTV_6000 D98% and the accuracy of a contour, as assessed by Dice similarity co-efficient, when comparing each contour to the gold standard clinician contour

7.5 Discussion

This final chapter brings together the work from previous chapters, in relation to contour interobserver variability, accuracy and MR-Linac online workflow, with some unexpected results.

Firstly, although it had been observed that propagated contours could be accurate, especially when using deformable registration from reference MRI, it was unexpected that these would do so well when assessing dosimetrically and in particular surprising that all ten plans based on un-edited propagated contours would give a clinically acceptable dose to the high dose PTV.

The results are promising but there are are caveats. The propagated contours have been observed to be variable, especially the SV which can fluctuate significantly in position. The results here are for a limited number of cases, with just five patients, and will need to be corroborated with much higher numbers.

The use of the un-edited contours alone could potentially have a huge impact on the current workflow, not only meaning that a clinician would not need to be present, but also removing, or at least reducing the current online re-contouring time of 9.1 minutes, as reported in Chapter 6. Propagated contours will always need to be reviewed, however the results here demonstrate that even if editing is required, this could be much more limited.

It is important to distinguish the propagated contours used here, generated using deformable registration from the RefMR to the daily online MRI, from the

auto-contours described in Chapter 5, produced on a completely new patient's imaging. Auto-contours are produced de-novo, without the benefit of the patient anatomy, however as discussed in Chapter 5, the inclusion of more sophisticated software can also take into account voxel to voxel changes. Ultimately the best option for the most accurate contours, without editing, would be to use a combination of both the patient's reference imaging as well as software incorporating image intensity, focussed on the targets.

There are variable results from the radiographer contours, with 30% of the plans failing to meet the mandatory constraint for the high dose PTV D98%. The variability between radiographers is demonstrated in Figure 7.2 and further in Table 7.5 when assessing the DSC. However, the results indicate that two radiographers (Rad1 and Rad4) had a higher concordance with the gold standard contour, as seen with the DSC of 0.94 and 0.93 respectively (Table 7.5). In addition, when the plans from their contours were transferred to assess the dose to the gold standard, only one out of ten plans showed a missed PTV_6000 D98%, but this value remained above 55 Gy (Figure 7.2) giving a higher dose to the PTV compared to the other failed plans. This introduces the possibility of there being a phased introduction of radiographer contouring, with observers starting when appropriate, this could be further assessed by a minimum DSC, such as 0.90.

Consistent contouring is critical for quality assurance of trials, in particular multi-centre studies. All clinicians contouring on the MR-Linac have prior experience of prostate contouring. In advance of online re-contouring, the same T2W test

cases used here are completed, followed by consultant review of contours and further practice if required. Within a centre, there will be a training programme, followed by assessment.

Here we have evaluated the dose to the ‘gold standard’ target, however this is a time consuming method of validating contours, and we have shown here that the DSC appears to be a good indicator of the contour accuracy and relevant to target dose. Extrapolation from these results could use a threshold DSC required for a new trained observer, prior to online contouring on the MR-Linac.

McNair et al [4] demonstrated with bladder radiotherapy plan of the day training, that there was increased concordance between trained observers and an independent observer following a second round of training. It is anticipated that following further training and feedback on the contours completed here, there would be improved concordance with the ‘gold standard’. In addition, the radiographers here were assessed as individual observers. Concordance with two observers, consistent with treatment delivery in clinical practice, can be higher [4]. However, although this is appropriate for steps such as plan of the day selection, or image registration, this may be less practical when contouring and also risks increasing the time for this step.

The time taken for the re-contouring step is of significance. The radiographer time will improve with more experience, but given the accuracy of the propagated contours, any additional time for this step- by clinicians or

radiographers, needs to have enough benefit to justify the additional couch time.

In addition to the restricted numbers used here, a major limitation is the use of a single clinician's contour as the 'gold standard'. The difficulty of this has been debated in the Introduction, Section 1.6. For this work, my contours were used as the gold standard as my re-contouring is used in the online setting for daily plans. In addition, the previous work in Chapter 4 showed a DSC of 0.97 with other clinicians from the same institution. Other options considered included using a clinician STAPLE, as utilised in Chapter 4, or by using my contour further reviewed and amended if required by a second clinician. However both of these options are not reflective of the online process.

Further work will focus on using other clinicians, also involved in the MR-Linac workflow, to contour the same sets of imaging. The plans created by their contours can similarly be 'copied over' onto my 'gold standard' contour to ascertain if, due to interobserver variability alone, there would be missed constraints.

Finally, to allow a fair comparison, OAR were not amended here, as any changes would have an impact on the optimisation steps. This does not appear to have impacted the study, firstly as optimisation is based on the target, excluding any overlap with the OAR i.e. 'CTV minus bladder' and 'CTV minus rectum'. Secondly, all OAR were reviewed and deemed to be clinically appropriate. Finally, as seen in Table 7.2, there was no impact on the OAR

constraints, although the optimisation is configured to spare the OAR, we would expect there to have been some impact on at least the optimal constraints.

When reviewing the DSC of each of the observers, it must be considered that the propagated contours will have a falsely high concordance, as the clinician contours were created by amending these contours where required, rather than 'from scratch', therefore some of the propagated contour will not have altered at all.

The results presented here, although applicable for prostate radiotherapy in general, have been collected using our current online radiotherapy planning and fractionation. The indications for the 'ideal' DSC are therefore only relevant for a margin of 5 mm for the prostate with 3 mm posteriorly. I have observed that some plans even with a high DSC only achieve optimal constraints- this will be dependent on where discrepancy is. For example, if there is a difference posteriorly, then a prostate contour 'under'-volumed at this site is less likely to be compensated for with a reduced margin of 3 mm versus 5 mm elsewhere. Other locations less likely to be compensated for, include parts of the contour at more conformal areas with a steeper dose gradient, for example at the prostate base adjacent to the bladder, where there can be dose fall off due to optimisation settings.

I have presented the data here assuming that one contour is used for a whole treatment course, in reality, there are a number of clinicians responsible for re-contouring during the treatment course for an MR-Linac patient. Given the lack

of ground truth or true gold standard, several competent contourers could grant the advantage of a more accurate cumulative prostate target due to interobserver variability for each patient. We would expect the dose discrepancy in contours to be more significant with SBRT.

As always, training forms a vital role in the implementation of new technology. The work here with the limited group can also be extended to future radiographers working with the MR-Linac and provides a good starting point for a formal training process, for prostate radiotherapy and other tumour sites. Also to be considered will be the appropriate maintenance of competency, for example by attending ‘refresher’ teaching or contouring a certain number of cases over the course of a year [5].

In practical terms, these results have implications for potential changes in the workflow. We would expect the therapeutic radiographer role to be extended, as previously discussed in Chapter 4, for either re-contouring, or assessing the propagated contour with limited changes, to ensure this is clinically appropriate. This could have the benefit of not requiring a clinician at each fraction, as well as a potential to reduce the total treatment time.

7.6 Conclusion

Un-edited propagated contours show promising results when assessing the target coverage during the online workflow for the MR-Linac. Radiographer contours show variable results depending on the observer but would be expected to improve with further training. The DSC between an observer contour and a defined gold standard can be useful to predict whether a contour will be accurate enough for online planning.

The work presented here will be validated on an independent larger data set and following further training of radiographer practitioners. Verification of this data has important implications for the number of team members, especially clinicians, required during a fraction and the duration of couch time for a patient.

7.7 References

1) Pathmanathan AU, McNair HA, Schmidt MA et al. Comparison of prostate delineation on multimodality imaging for MR-guided radiotherapy. The British Journal Radiology 2019; 92: 20180948.
2) Adam Mitchell AD, Angela Pathmanathan, Simeon Nill, Alison Tree, Uwe Oelfke. Prostate treatment planning for the MR-linac: effect of online performance on template development. Radiotherapy and Oncology 2019; ESTRO 38 conference: EP-2002
3) Alex Dunlop AM, Alison Tree, Helen Barnes, Lorna Bower, Joan Chick, Edmund Goodwin, Trina Herbert, Rebekah Laws, Helen McNair, Dualta McQuaid, Jonathan Mohajer, Rahul Nilawar, Angela Pathmanathan, Gillian Smith, Ian Hanson, Simeon Nill, Uwe Oelfke. Daily adaptive radiotherapy for patients with prostate cancer using the Elekta MR-linac: initial clinical experiences and assessment of delivered doses compared to a C-arm linac. Submitted for publication August 2019 2019.
4) McNair HA, Hafeez S, Taylor H et al. Radiographer-led plan selection for bladder cancer radiotherapy: initiating a training programme and maintaining competency. The British Journal Radiology 2015; 88: 20140690.
5) McNair HA, Hafeez S, Taylor H et al. Radiographer-led plan selection for bladder cancer radiotherapy: initiating a training programme and maintaining competency. The British Journal of Radiology 2015; 88: 20140690.

Conclusions

8.1 MR-guided workflow: The ever-changing pathway

Magnetic resonance imaging (MRI) guided radiotherapy is a rapidly evolving field. When I begun the work for my thesis, the MR-Linac was being installed in the early adopter sites, including our centre, with the MR-Linac consortium (Section 1.4.2) making plans for pre-clinical and first-in-man studies. The first MRI-guided treatment in the UK was delivered at our centre in September 2018 [1] and our experience in this complex technique has been exponentially growing. As summarised in Figure 1.9, there are a number of steps involved in this complex pathway of online adaptive radiotherapy, all under constant revision.

8.1.1 Initial 'baby' steps

As summarised in the Chapter 6 Discussion, there have been a number of changes in the workflow since inception, with ongoing modifications. Research MRI sequences are now acquired during the time used for re-contouring and re-optimisation. T2-weighted (T2W) MRI is by far the most familiar sequence for prostate radiotherapy, however, given the more distinct appearance of the capsule on other types of imaging, as demonstrated with the T2*-weighted sequence in Chapter 4, work is required to elucidate the most appropriate sequence for this workflow, which may differ between stages of treatment.

One of the biggest challenges is related to the length of each fraction. Changes have been made to optimise the time available, including overlapping components of the workflow summarised in Figure 6.2. For example, the verification MRI is now started before plan checking is complete. Consistently, the longest step within the workflow remains the re-contouring with a mean time of 9.1 minutes (Table 6.5). My work in Chapter 7 has indicated this may be significantly reduced if the propagated contour is clinically adequate for treatment, or adjustments could be limited, rather than amending the entire contour.

There are many advantages to the re-contouring step becoming fully automated, although all contours will need review and there may be limited corrections required. As seen in Chapters 4 and 7, with a careful training programme, this step can be managed by the treatment radiographers. The data in Chapter 7 suggests that to avoid the time consuming process of assessing contours by comparing dose coverage, the DSC could be used as an indicator as to whether these contours would be clinically adequate.

One of the biggest changes has been the use of the first fraction's imaging as the reference MRI for further fractions of treatment. This has the advantage of enabling MRI to MRI propagation of contours, which are more accurate. The next step would be to dispense with a CT planning scan, allowing an MRI only workflow (Section 1.8), which may be instituted in stages. Ideally imaging on the MR-Linac itself would act as the reference imaging, as the processing of the images and creation of propagated contours online is more accurate with 'like to

like' imaging. In future, with the use of plan templates, we would hope that the pre-treatment planning stage would be eliminated, with the first treatment plan created on the day of the first fraction.

8.1.2 Contouring- back to the 'weakest link'

I have discussed how more accurate treatment delivery places contour accuracy and variability in the spotlight. As well as the implications of time and clinician involvement, as discussed in Chapter 7 with the accuracy of radiographer contouring, there is the rapidly progressing field of automated contours.

In Chapter 7, I have shown that for a limited number of cases, the propagated 'intrapatient' contour from one specific patient image-set to another, appears to give clinically adequate target coverage. In Chapter 5, I demonstrated that the use of atlas-based autosegmentation with machine learning, utilising imaging with the same sequence parameters, gives a DSC of 0.85 to 0.90 (depending on atlas number) on T2W MRI.

The ideal setting would incorporate a combination of these techniques to create reliable target and OAR contours, using all available fraction imaging. The initial step would be the creation of the propagated contour from the registration of images, as currently in practice. This would be followed by 'fine-tuning' of the contours using the multi-atlas approach reviewed in Chapter 5, where the patient specific atlas library would be comprised of the patient's image sets from the previous days. This could initially be tested using similar methods to

Chapter 5. Using the 20 re-contoured image sets for each PRISM patient, these would be added to the atlas library one by one. The resulting intrapatient auto-contours would be tested to see if there was any improvement. For example, to assess whether a contour for the 4th fraction of treatment is more accurate when created from the previous three fraction image sets, compared to the contour we would normally use i.e. the contour propagated from reference imaging alone. Over the course of treatment, there would be an increasing number of image sets from each fraction in the atlas library. With the increase in time taken for an auto-contour with increased number of atlases (Table 5.3), a varying number of atlases could be selected to determine the most effective number of atlases required and which fractions they are taken from.

Finally, again integrated into atlas-based autosegmentation software such as ADMIRE, machine learning would be incorporated to utilise the voxel intensities. Accurate contours are required not just for the treatment plan, but also for target tracking with intrafractional imaging. The latter is achieved by continuous registration of images from each cine-MR image frame to the next.

8.1.3 Real-time imaging and tracking

In Chapter 2, the automated fiducial tracking mirrored previous studies showing increasing prostate motion over time (Figure 2.3). The mean treatment delivery time for the first five patients within the PRISM trial was 4.7 minutes (Table 6.5), however with the verification step, there is over 8 minutes between the end of the verification scan and the completion of treatment delivery. This is even

longer in the patients requiring a further ATP of the initial plan and it could be argued that these may be the patients with more prostate motion.

At present, treatment is delivered on the MR-Linac with intensity modulated radiotherapy (IMRT). The speed of delivery would be improved with the use of volumetric modulated arc therapy (VMAT). Beyond this change however, we would not expect substantial improvements in delivery time. Further advancement in treatment delivery would therefore include prostate tracking. Following on from the work in Chapter 2, soft tissue tracking of the prostate using cine-MR has been validated [2], a vital part of intrafractional target tracking. Adjusting treatment delivery according to this motion monitoring would be paramount, especially with longer fractions in extreme fractionation schedules.

Exception gating (Section 1.5.4) is the simpler solution for adjusting treatment delivery, currently achieved by the ViewRay system, where radiation is automatically paused if more than a specified proportion of the CTV lies outside the PTV during intrafraction monitoring [3]. Additional work can utilise the cine-MRI data from patients within the PRISM trial to determine the threshold beyond which we would expect a significant deterioration in dose, if treatment were not paused.

Ultimately however, the goal would be to adjust the shape of treatment delivery in real-time [4], as discussed in further detail in Section 1.5.6, for example with the use of multi leaf collimator (MLC) tracking [5] to allow continuous intrafractional adjustments. This incorporates a number of steps, beginning with

pre-existing goals of the dose to be delivered and organ constraints. The contours of the day would be propagated from one cine frame to the next during treatment delivery, with continuous recalculation of the dose being delivered to the targets and OAR. The dose delivered at any one point is subtracted from the initial ideal dose distribution [4] with re-optimisation of the ensuing beams, with MLC adjusted to the new shape and position of the target, for the real-time anatomy. The remaining excess or deficiency in dose is then compensated for, by adjusting the dose calculations in the remaining fractions.

8.2 Future directions

Developments in radiotherapy have allowed more complex planning and delivery techniques, enabling more conformal treatments and improvements in the therapeutic ratio. In Chapter 6, I discussed the PRISM trial and the feasibility of standard fractionation treatment with the MR-Linac. Further work has been carried out estimating the delivered dose with this MR-guided radiotherapy compared to the expected dose with a standard linac [6] for the first five patients. Further dosimetric analysis will allow evaluation of the potential therapeutic gains and toxicity reductions.

8.2.1 Extreme hypofractionation

The biggest gains with the MRI-guided workflow however, would be expected from treatment where a higher target dose would be beneficial, but harder to achieve in order to maintain OAR constraints. This includes dose escalation to the dominant nodule (Section 1.2.4) in higher risk patients and supporting the

move towards extreme hypofractionated schedules (Section 1.3) in low and intermediate risk patients.

During my period of research, I was awarded a fellowship to the '*ECCO-AACR-EORTC-ESMO Workshop on Methods in Clinical Cancer Research*', submitting a protocol on 'Ultra-hypofractionated prostate stereotactic body radiotherapy (SBRT) on the MR-linac'. Further work will focus on reducing the number of fractions to two, with a recent grant application awarded for the 'The 5 vs. 2 study: A phase II randomised study of ultrahypofractionated stereotactic body radiotherapy in men with localised prostate cancer', chief investigator Dr Alison Tree, with myself as a co-investigator.

Ultimately, rather than treating each fraction individually, the use of daily dose reconstruction [7-9], ideally in conjunction with MLC tracking [9] would allow calculation of the dose delivered and dose to OAR, therefore allowing compensation in the remaining fractions [4]. This is especially pertinent for hypofractionated treatment. There are various steps required for this including rapid and accurate contour deformation, re-optimisation and dose accumulation as discussed above. The online and real-time adaptive workflow with MRI guidance has the capability to support several indications.

8.2.2 Anatomical variation

With limited availability of MR-guided systems and treatment slots, due to the longer duration of each fraction and considering the volume of patients requiring prostate radiotherapy, it will be difficult to treat all such patients on the MR-Linac. Furthermore, as most patients have limited toxicity and excellent

biochemical control it may not be necessary to do so. Thus informed patient selection for treatment on the MR-Linac is essential and illustrated in the early results from the PRISM study, where several patients may have had limited dosimetric benefit.

However, the second patient treated within the PRISM trial had bowel adjacent to the target on initial CT planning causing significant compromise to the target dose (Figure 6.5). This patient represents a subset of patients who would benefit from MRI-guided daily online replanning, to enable dosimetric advantages when daily imaging shows more favourable anatomy. The follow on work has shown an average estimated improvement of 4.6 Gy to the prostate CTV D98, from 49.9 Gy to 54.5 Gy [6], in a patient who would not be able to achieve optimal radical target doses on a conventional linear accelerator. Further work assessing the feasibility of delivering a different dose each day according to anatomy should be pursued testing the hypothesis that greater than 3Gy (in a 20 fraction schedule) can be delivered on the days of favourable anatomy safely, which would improve the CTV D98.

A key target for future work would be how best to identify those patients who would benefit from daily online replanning on the MR-Linac. Patients with unfavourable anatomy for achieving optimal dosimetric parameters may be recognised during standard radiotherapy planning or potentially on their diagnostic imaging. Similarly, patients receiving treatment on a conventional linac displaying variable anatomy on cone-beam CT with concerns about target

coverage or dose to OAR, could also be referred for MR-guided radiotherapy for the remainder of the treatment course.

8.2.3 Margin reduction

With daily online adaptive radiotherapy, there is potential to reduce the margins required for the PTV, as discussed previously, this needs to be done with caution to allow a minimum required margin [10]. PTV margin reduction will also be dependent on the treatment delivery, i.e. whether real-time adaption is possible. The work on automatic fiducial tracking from Chapter 2 was consistent with previous studies, showing an overall translation trend of 1.0 mm posteriorly and 0.9 mm caudally. Review of individual cine-MR imaging from this study as well as daily MRI from patients treated within the PRISM study show, as expected, variability between patients, with some patients displaying relatively stable anatomy and others showing larger fluctuations. This could be incorporated using data from the first fractions to allow patient individualised margins for optimal treatment delivery.

The concept of the PTV may become redundant with MR-guided radiotherapy, with corrections made for interfractional and/or intrafractional motion. An internal target volume (ITV) becomes more relevant, where movement outside of a threshold margin triggers a change in treatment delivery or re-optimisation.

8.3 Further roles of MR-guided radiotherapy for prostate patients

8.3.1 Oligometastatic disease

We know that oligometastatic prostate cancer, where there are limited distant metastatic sites (fewer than 3 to 5), differs in biological behaviour to the patients with more extensive metastatic disease. In addition there is interest in oligoprogression, that is, patients with more diffuse metastatic disease having progression in a limited number of sites. Stereotactic body radiotherapy (SBRT) is an effective local treatment [11] which can improve outcome and delay systemic treatment in prostate cancer [12]. In a multi-institutional analysis, SBRT to oligometastases was found to be safe and associated with favourable progression free survival (PFS) rates. However, PFS is limited by the biological effective dose (BED) that can delivered [13]. It would therefore be attractive to harness the advantages of MRI-guided radiotherapy to allow a sufficiently ablative dose to areas in close proximity to organs at risk, such as lymph nodes and spinal metastases.

8.3.2 Re-irradiation

Another application where MRI-guided radiotherapy would have benefits, would be for the challenge of re-irradiation. Local recurrence of prostate cancer is managed depending on the fitness of the patient with the more radical options of salvage prostatectomy or re-irradiation, understandably associated with increased risk. Several groups have reported salvage brachytherapy to the prostate, although there is limited data with small patient series [14, 15].

Understandably re-irradiation requires minimal margins to mitigate OAR dose and therefore toxicity. Initial conformal EBRT re-irradiation studies were associated with high toxicity rates [16]. Salvage treatment with SBRT appears promising [17-21] but again with limited data.

The outcome is dependent on many factors in this heterogenous group of patients, including risk group [22], whether androgen deprivation is employed, time to recurrence and PSA at recurrence [18, 19]. Although SBRT can be safely delivered, there are limitations to the dose that can delivered, leading to higher recurrence rates in some studies, again dependent on the BED [19].

As patients live longer with multifocal metastatic disease, re-irradiation of bone or soft tissue metastatic disease is increasingly common. Total dose is limited by adjacent normal tissue toxicity such as spinal cord tolerance when re-irradiating vertebral metastases [23]. Although not the focus of trials, there is a population of patients who would benefit from the palliative effects of radiotherapy to sites previously treated [24].

The population of patients for re-irradiation of any site must be considered carefully, but we would expect that with online adaptive radiotherapy, with cautious margin reduction and accurate delivery, ideally with dose accumulation to assess target and OAR dose, MR-guided radiotherapy would provide a suitable delivery technique.

8.4 Conclusion

With MR-guided radiotherapy now being delivered within the UK and early data showing this treatment is safe, there are exciting times ahead. The sophisticated pathway requires additional training, resources and time. There are challenges involved in the different steps and constant evolution to create a more practical and streamlined process.

MR-guided radiotherapy may be applied to indications such as unfavourable anatomy, extreme hypofractionation, oligometastatic disease and re-irradiation, to name but a few. There are many advantages highlighted here for this novel technique as we explore more avenues to improve the outcomes for our prostate cancer patients.

8.5 References

1) Pathmanathan A, Bower L, Creasey H et al. EP-1566 MR-guided online adaptive radiotherapy: First experience in the UK. Radiotherapy and Oncology 2019; 133: S845.
2) de Muinck Keizer DM, Kerkmeijer LGW, Maspero M et al. Soft-tissue prostate intrafraction motion tracking in 3D cine-MR for MR-guided radiotherapy. Physics in Medicine & Biology 2019; 64: 235008.
3) Tetar SU, Bruynzeel AME, Lagerwaard FJ et al. Clinical implementation of magnetic resonance imaging guided adaptive radiotherapy for localized prostate cancer. Physics and Imaging in Radiation Oncology 2019; 9: 69-76.
4) Kontaxis C, Bol GH, Lagendijk JJW, Raaymakers BW. Towards adaptive IMRT sequencing for the MR-linac. Physics in Medicine and Biology 2015; 60: 2493.
5) Fast MF, Kamerling CP, Ziegenhein P et al. Assessment of MLC tracking performance during hypofractionated prostate radiotherapy using real-time dose reconstruction. Physics in Medicine and Biology 2016; 61: 1546.
6) Alex Dunlop AM, Alison Tree, Helen Barnes, Lorna Bower, Joan Chick, Edmund Goodwin, Trina Herbert, Rebekah Laws, Helen McNair, Dualta McQuaid, Jonathan Mohajer, Rahul Nilawar, Angela Pathmanathan, Gillian Smith, Ian Hanson, Simeon Nill, Uwe Oelfke. Daily adaptive radiotherapy for patients with prostate cancer using the Elekta MR-linac: initial clinical experiences and assessment of delivered doses compared to a C-arm linac. Submitted for publication August 2019 2019.
7) Ghilezan MJ, Jaffray DA, Siewerdsen JH et al. Prostate gland motion assessed with cine-magnetic resonance imaging (cine-MRI). International Journal of Radiation Oncology, Biology and Physics 2005; 62: 406-417.
8) Mohan R, Zhang X, Wang H et al. Use of deformed intensity distributions for on-line modification of image-guided IMRT to account for interfractional anatomic changes. International Journal of Radiation Oncology, Biology and Physics 2005; 61: 1258-1266.
9) Kamerling C, Fast M, Ziegenhein P et al. TH-CD-202-12: Online Inter-Beam Replanning Based On Real-Time Dose Reconstruction. Medical Physics 2016; 43: 3879-3879.
10) Engels B, Soete G, Verellen D, Storme G. Conformal Arc Radiotherapy for Prostate Cancer: Increased Biochemical Failure in Patients With Distended Rectum on the Planning Computed Tomogram Despite Image Guidance by Implanted Markers. International Journal of Radiation Oncology, Biology and Physics 2009; 74: 388-391.
11) Tree AC, Khoo VS, Eeles RA et al. Stereotactic body radiotherapy for oligometastases. Lancet Oncol 2013; 14: e28-37.
12) Battaglia A, De Meerleer G, Tosco L et al. Novel Insights into the Management of Oligometastatic Prostate Cancer: A Comprehensive Review. Eur Urol Oncol 2019; 2: 174-188.
13) Ost P, Jereczek-Fossa BA, As NV et al. Progression-free Survival Following Stereotactic Body Radiotherapy for Oligometastatic Prostate Cancer Treatment-naive Recurrence: A Multi-institutional Analysis. European Urology 2016; 69: 9-12.

14) Kollmeier MA, McBride S, Taggar A et al. Salvage brachytherapy for recurrent prostate cancer after definitive radiation therapy: A comparison of low-dose-rate and high-dose-rate brachytherapy and the importance of prostate-specific antigen doubling time. Brachytherapy 2017; 16: 1091-1098.
15) Maenhout M, Peters M, van Vulpen M et al. Focal MRI-Guided Salvage High-Dose-Rate Brachytherapy in Patients With Radiorecurrent Prostate Cancer. Technology in cancer research & treatment 2017; 16: 1194-1201.
16) Zilli T, Benz E, Dipasquale G et al. Reirradiation of Prostate Cancer Local Failures After Previous Curative Radiation Therapy: Long-Term Outcome and Tolerance. International Journal of Radiation Oncology, Biology and Physics 2016; 96: 318-322.
17) Ingrosso G, Becherini C, Lancia A et al. Nonsurgical Salvage Local Therapies for Radiorecurrent Prostate Cancer: A Systematic Review and Meta-analysis. European Urology Oncology.
18) Fuller D, Wurzer J, Shirazi R et al. Retreatment for Local Recurrence of Prostatic Carcinoma After Prior Therapeutic Irradiation: Efficacy and Toxicity of HDR-Like SBRT. International Journal of Radiation Oncology, Biology and Physics 2020; 106: 291-299.
19) Jereczek-Fossa BA, Rojas DP, Zerini D et al. Reirradiation for isolated local recurrence of prostate cancer: Mono-institutional series of 64 patients treated with salvage stereotactic body radiotherapy (SBRT). British Journal Radiology 2019; 92: 20180494.
20) Janoray G, Reynaud-Bougnoux A, Ruffier-Loubiere A et al. Stereotactic body re-irradiation therapy for locally recurrent prostate cancer after external-beam radiation therapy: Initial report. Cancer Radiotherapy 2016; 20: 275-281.
21) Loi M, Di Cataldo V, Simontacchi G et al. Robotic Stereotactic Retreatment for Biochemical Control in Previously Irradiated Patients Affected by Recurrent Prostate Cancer. Clinical Oncology (R Coll Radiol) 2018; 30: 93-100.
22) Chang H, Fitzpatrick JM. A technique for accurate magnetic resonance imaging in the presence of field inhomogeneities. IEEE Trans Med Imaging 1992; 11: 319-329.
23) Sahgal A, Ma L, Weinberg V et al. Reirradiation human spinal cord tolerance for stereotactic body radiotherapy. International Journal of Radiation Oncology, Biology and Physics 2012; 82: 107-116.
24) Myrehaug S, Soliman H, Tseng C et al. Re-irradiation of Vertebral Body Metastases: Treatment in the Radiosurgery Era. Clinical Oncology (R Coll Radiol) 2018; 30: 85-92.

Publications arising from this thesis

International Journal of Radiation Oncology biology • physics

www.redjournal.org

Critical Review

Magnetic Resonance Imaging-Guided Adaptive Radiation Therapy: A "Game Changer" for Prostate Treatment?

Angela U. Pathmanathan, MA,[*,†] Nicholas J. van As, MD,[*,†] Linda G.W. Kerkmeijer, PhD,[‡] John Christodouleas, MD,[§] Colleen A.F. Lawton, MD,[‖] Danny Vesprini, MD,[¶] Uulke A. van der Heide, PhD,[#] Steven J. Frank, MD,[**] Simeon Nill, PhD,[*,†] Uwe Oelfke, PhD,[*,†] Marcel van Herk, PhD,[††,‡‡] X. Allen Li, PhD,[‖] Kathryn Mittauer, PhD,[§§] Mark Ritter, PhD,[§§] Ananya Choudhury, PhD,[††,‡‡] and Alison C. Tree, MD[*,†]

**The Institute of Cancer Research, London, United Kingdom; [†]The Royal Marsden National Health Service Foundation Trust, London, United Kingdom; [‡]University Medical Center Utrecht, Utrecht, The Netherlands; [§]Elekta, Inc, Philadelphia, Pennsylvania; [‖]Medical College of Wisconsin, Milwaukee, Wisconsin; [¶]Sunnybrook Health Sciences Centre, University of Toronto, Toronto, Ontario, Canada; [#]Department of Radiation Oncology, The Netherlands Cancer Institute, Amsterdam, The Netherlands; [**]The University of Texas MD Anderson Cancer Center, Houston, Texas; [††]Manchester Cancer Research Centre, University of Manchester, Manchester Academic Health Science Centre, The Christie National Health Service Foundation Trust, Manchester, United Kingdom; [‡‡]National Institute of Health Research, Manchester Biomedical Research Centre, Central Manchester University Hospitals National Health Service Foundation Trust, Manchester Academic Health Science Centre, Manchester, United Kingdom; and [§§]University of Wisconsin School of Medicine and Public Health, Madison, Wisconsin*

Received Sep 14, 2017, and in revised form Oct 9, 2017. Accepted for publication Oct 12, 2017.

Reprint requests to: Ananya Choudhury, PhD, The Royal Marsden National Health Service Foundation Trust, Wilmslow Rd, Withington, Manchester M20 4BX, United Kingdom. Tel: (161) 918-7939; E-mail: ananya.choudhury@christie.nhs.uk

A.C. and A.C.T. are joint last authors.

A.T., A.C., U.O., S.N., and A.P. have received research and educational travel support from Elekta. Elekta financially supports the MR-Linac Consortium and all member institutes, including research funding. Elekta supports travel costs for consortium meetings. A.T., A.P., N.V.A., U.O., and S.N. acknowledge the support of National Health Service funding to the National Institute of Health Research Biomedical Research Centre at The Royal Marsden and The Institute of Cancer Research. The views expressed in this paper are those of the authors and not necessarily those of the NHS, the NIHR or the Department of Health. Research at the Institute of Cancer Research is also supported by Cancer Research UK (CRUK) (program grant C33589/A19727).

Conflict of interest: L.K., J.C., C.L., D.V., U.A.H., S.F., S.N., U.O., M.H., A.L., A.C., and A.T. are part of the Elekta MR-Linac Research Consortium, which aims to coordinate international research into the magnetic resonance linear accelerator. Elekta and Philips are members of the MR-Linac Consortium. J.C. is an employee of Elekta. L.K. reports grants from Elekta to University Medical Center Utrecht, outside the submitted work. A.C. and M.V. acknowledge the support of the National Institute of Health Research Manchester Biomedical Research Centre. A.C. has received grants from Cancer Research UK, National Institute for Health Research, and Prostate Cancer UK outside the submitted work. N.V.A. has received grants and personal fees from Accuray outside the submitted work. S.J.F. acknowledges U19 National Institutes of Health/National Cancer Institute grant support, is a consultant/advisor for Varian, has received honoraria from IBA and Hitachi, is a board member of American Board of Radiology and American Brachytherapy Society, is a director of C4 Imaging, and has a patent for MRI markers licensed. A.T. has received honoraria from Janssen, Astellas, and Bayer and research funding from MSD outside the submitted work. K.M. has received honoraria from ViewRay, Inc.

Acknowledgments—Figure 5 was provided courtesy of Maria Schmidt, The Institute of Cancer Research.

Int J Radiation Oncol Biol Phys, Vol. 100, No. 2, pp. 361–373, 2018

https://doi.org/10.1016/j.ijrobp.2017.10.020

Radiation therapy to the prostate involves increasingly sophisticated delivery techniques and changing fractionation schedules. With a low estimated α/β ratio, a larger dose per fraction would be beneficial, with moderate fractionation schedules rapidly becoming a standard of care. The integration of a magnetic resonance imaging (MRI) scanner and linear accelerator allows for accurate soft tissue tracking with the capacity to replan for the anatomy of the day. Extreme hypofractionation schedules become a possibility using the potentially automated steps of autosegmentation, MRI-only workflow, and real-time adaptive planning. The present report reviews the steps involved in hypofractionated adaptive MRI-guided prostate radiation therapy and addresses the challenges for implementation.

Introduction

Prostate radiation therapy (RT) techniques have undergone a metamorphosis during the past 2 decades. We have transitioned from 2-dimensional to 3-dimensional (3D) techniques and, subsequently, to intensity modulated RT, image-guided RT (IGRT), and, more recently, to stereotactic body RT (SBRT). Localization strategies have evolved from external skin markings, to 2-dimensional/megavoltage-based bony localization, to complex techniques allowing localization of the target through implanted fiducial markers, electromagnetic beacons, or 3D/kilovoltage volumetric imaging with soft tissue capabilities of in-room computed tomography (CT) or cone beam CT.

However, another wave of technological refinements is fast approaching, with magnetic resonance imaging (MRI)-guided photon RT, modern particle therapy, and the prospect of ultrafast replanning, enabling treatment paradigms previously thought to be science fiction to become reality.

The improvement in precision delivered by these technical changes has synchronized with a change in our RT fractionation. The CHHiP (conventional or hypofractionated high dose intensity modulated radiotherapy for prostate cancer) trial (1) has shown that 60 Gy in 20 fractions is at least as good as 74 Gy in 37 fractions, which has changed the standard fractionation in many countries from 7.5 weeks to 4 weeks. The PACE (prostate advances in comparative evidence) trial (ClinicalTrials.gov identifier, NCT01584258) is randomizing between a similar 4-week schedule and 5-fraction SBRT. As the α/β ratio of prostate cancer is thought to be low (2-5), hypofractionation should improve the therapeutic ratio.

The purpose of the present review is to describe

1. The future implications of the existing evidence on the optimal fractionation for prostate cancer and, ultimately, whether single-fraction RT is feasible
2. How MRI-guided RT (MRgRT) could change the paradigms in prostate cancer RT
3. A road map to overcoming the obstacles to implementation

Search Strategy and Selection Criteria

Published studies for the present review were identified by conducting a search using PubMed, with the following words: "prostate," "radiotherapy," "radiation therapy," "MRI," "MR," "magnetic resonance image," "adaptive," "MR-guided," "MR-linac," "ViewRay," "autosegmentation," "automatic segmentation," "autocontouring," "pseudo-CT," and "substitute CT." The last PubMed search was performed on August 1, 2017. The search included meeting abstracts and was restricted to reports available in English. Further references were identified by a manual search of the reference list of the included studies. Identified studies were first screened by title and/or abstract, with a further full paper screening to generate the final list of studies relevant to the scope of the present review.

Hypofractionation—How Low Do We Go?

Although the ideal dose and fractionation of RT, allowing for maximum tumor control with acceptable toxicity, is far from certain, hypofractionation is increasingly favored (6-8). The α/β ratio for prostate cancer is estimated to be as low as 1.5 Gy (1, 2, 9, 10), suggesting that moderate hypofractionation can be as effective as standard fractionation for prostate RT. This has now been confirmed in large phase III trials (1, 11).

Extreme hypofractionation, using SBRT doses per fraction of $\geq$7.0 Gy, has many potential advantages, including improved clinical outcomes and fewer visits, improving patient convenience and departmental capacity. Prospective phase II studies of SBRT have focused on low- and intermediate-risk patients but have reported favorable biochemical outcomes for all risk groups (12, 13). The phase III PACE trial is testing 5-fraction SBRT against standard fractionation to establish whether the abbreviated schedule is noninferior. In advance of the randomized evidence, SBRT in 5 fractions appears to have promising efficacy and side effect profile.

To enhance personalized treatment, the dose can be escalated to the dominant intraprostatic lesion, which is the most common site of local recurrence (14, 15). This has been tested in the FLAME (investigate the benefit of a focal

lesion ablative microboost in prostate cancer) trial (ClinicalTrials.gov identifier, NCT01168479) (16) and the hypo-FLAME (hypofractionated focal lesion ablative microboost in prostate cancer) study (ClinicalTrials.gov identifier, NCT02853110). The concept of "biological conformality" (17) uses the additional information from functional sequences to target the dose to the area most likely to benefit from dose escalation. In particular, diffusion weighted imaging (DWI) can be used to generate apparent diffusion coefficient maps to identify more aggressive disease, which might benefit from boosting (18-20).

The direction has been towards progressively more abbreviated RT schedules; thus, if 5-fraction SBRT is safe and effective, it raises the question of how low can we go (Fig. 1). Hoskin et al (21, 22) reported the longer term outcomes for mainly intermediate- and high-risk patients who underwent high-dose-rate brachytherapy (HDR-BT) alone. A dose of either 3 fractions at 10.5 Gy or 2 fractions at 13 Gy gave acceptable toxicity rates, with 91% to 93% free of biochemical relapse at 4 years (22). The same group reported early toxicity data showing single-fraction prostate HDR-BT with 19 Gy is tolerable, although a significant increase in the need for catheterization was seen compared with the 2-fraction cohort, in particular, when 20 Gy was delivered to the whole gland (23). However, late toxicity and biochemical control were similar for a single 19- to 20-Gy fraction compared with 2 to 3 fractions (22). Other groups have reported favorable toxicity rates with single-fraction HDR-BT (24, 25). Prada et al (24) reported low morbidity in patients treated with single-fraction 19-Gy HDR-BT monotherapy with injections of transperineal hyaluronic acid into the perirectal fat. However, no margin was added to the prostate for the planning target volume, and the biochemical control rate was 66% at 6 years. The urethral dose can be a limiting factor to the total dose achieved, as seen when HDR-BT is used to plan an intraprostatic boost (26).

Low-dose-rate brachytherapy is also an option for dose escalation, with low toxicity rates and excellent biochemical control (27, 28) and without the need for a shielded room such as required for HDR-BT. In the ASCENDE-RT (an analysis of survival endpoints for a randomized trial comparing a low-dose-rate brachytherapy boost to a dose-escalated external beam RT) trial, the use of low-dose-rate BT as a boost improved biochemical progression-free survival compared with dose-escalated external beam RT alone (29); however, this was at the cost of higher genitourinary toxicity (30). Although brachytherapy might be considered the ultimate in conformal treatment, it is invasive and requires patients to meet anatomic criteria and is therefore not broadly available to all patients. In contrast, linear accelerator (linac)-based single-fraction treatment would potentially be feasible across the globe. It might even offer cost-effective benefits compared with brachytherapy or multiple-fraction treatment and allow higher patient throughput on a single machine.

Fig. 1. Progression of radiation therapy trials within the United Kingdom during the past 15 years. *Abbreviations:* CHHiP = conventional or hypofractionated high dose intensity modulated radiotherapy for prostate cancer; PACE = prostate advances in comparative evidence; RT01 = Medical Research Council RT01.

It is technically feasible to deliver similar target doses and meet the same constraints of HDR-BT using external beam RT (31). SBRT can be used to deliver an equivalent biologically effective dose without the need for a surgical procedure, general anesthesia, and associated potential complications. This is being assessed within the phase II PROSINT (phase II study of ultra-high-dose hypofractionated vs single-dose image-guided radiotherapy for prostate cancer) trial (ClinicalTrials.gov identifier, NCT02570919) randomizing between 45 Gy in 5 fractions and a single 24-Gy fraction.

Given the higher dose per fraction, highly conformal dose distribution, and steep dose gradient seen with SBRT, accurate delivery using direct tumor motion monitoring and online adaptive RT (ART) methods has become even more important. The ideal delivery system would consist of optimal image guidance (before treatment and intrafraction MRI), rapid delivery, and intrafraction ART.

Future of Image-Guided RT

MRgRT Platforms

MRgRT systems provide what has long been considered the "holy grail" of RT delivery, the integration of an MRI scanner that can provide clinical quality imaging with a modern linear accelerator (32). Several systems are in development for clinical use (33-36); these have been summarized in Table 1. Not only can the improved soft tissue contrast of MRI improve patient positioning before RT "on-line," but "real-time" imaging during treatment delivery itself can also help to detect the tumor and normal tissue position and deliver the radiation dose more precisely.

The MRIdian system (ViewRay Inc, Oakwood Village, OH), with integrated options of either tricobalt-60 or, more recently, a 6-megavoltage linac, has been treating patients since 2014, and the first patient was treated using the Elekta MR-Linac (Elekta AB, Stockholm, Sweden) in May 2017. Despite the potential effect on dose distribution by the magnetic field (37), which increases with higher field strength (38), treatment plan quality equivalency to standard linacs is

Table 1 Magnetic resonance imaging-guided radiation platforms existing or in development

Variable	Type of system	Magnetic field orientation	Research/ clinical status	Adaptive capabilities
Elekta MR-Linac (29)	1.5-T, 7-MV; 70-cm closed bore; single-focused Agility MLC providing 5-mm resolution for nominal 100-cm SSD, projecting to 7 mm at the isocenter	B_0 magnetic field perpendicular to delivery	First patient treated May 2017 in Utrecht as part of First In Man protocol	ART capabilities include 1. Shifting plan to overlay anatomy—simple dose shift 2. Offline ART 3. Library of plans 4. Online ART—segment-weight optimization and full reoptimization available 5. Visual tracking of target
ViewRay MRIdian cobalt-60 system (30)	0.35-T Cobalt system, 3 ^{60}Co heads on rotating gantry ring; split magnet 70-cm closed bore	B_0 magnetic field perpendicular to delivery	FDA 510(k) cleared for cobalt systems; treated patients since 2014 on cobalt system	ART capabilities include 1. Shifting plan to overlay anatomy—couch shift 2. Offline ART 3. Library of plans 4. Online ART—segment-weight optimization and full reoptimization available 5. Tracking with exception gating for target
ViewRay MRIdian Linac system	Newer system with 6-MV linac, split magnet 70-cm bore "Razor" MLC is a double-stacked, double-focused MLC, 8-mm leaf width, providing 4-mm resolution and allowing field sizes down to 2×4 mm	B_0 magnetic field perpendicular to delivery	FDA 510(k) cleared for linac system; treated patients since 2017 on linac system	ART capabilities include 1. Shifting plan to overlay anatomy—couch shift 2. Offline ART 3. Library of plans 4. Online ART—segment-weight optimization and full reoptimization available 5. Tracking with exception gating for target
Sydney Inline Australian MRI-LINAC system (31)	1.0 T 6-MV 82-cm open bore	B_0 magnetic field perpendicular and parallel to delivery	Currently, a research system	NA
MagnetTx Aurora RT Linac-MR (32)	0.5 T, 6-MV	B_0 magnetic field parallel to delivery	Currently, a research system	NA

Abbreviations: ART = adaptive radiation therapy; FDA = Food and Drug Administration; linac = linear accelerator; MR = magnetic resonance; MRI = magnetic resonance imaging; MV = megavoltage; NA = not available; SSD = solid-state drive.

achievable (39, 40). The dosimetric effect of the Lorentz force can be accounted for and mitigated through Monte Carlo dose calculations and inverse planning techniques.

Benefits and Challenges of MRI

MRI in RT planning provides superior soft tissue differentiation with the added capability of functional imaging. Improved image contrast has also been demonstrated with MRgRT systems, with which even low field strength from an on-board 0.35 T MRI can give improved anatomic visualization compared with on-board CT (41), with a reduction in radiation exposure. Figure 2 shows clinical true fast imaging with steady-state precision MR sequence from ViewRay MRIdian system of the prostate.

MRI sequences could also be used as an indicator of tumour response. Some preliminary results of DWI with MRgRT have been reported (42), although, currently, no validated MRI biomarkers are available for prostate RT. MR images acquired throughout a course of MRgRT could allow the dose distribution to be adjusted based on the tumor response. Adaptive dose painting can target the index lesion, where local relapse is most likely to occur (14, 20), or areas of more aggressive disease (18, 19). Currently, a paucity of data assessing imaging changes during and directly after treatment is available; however, studies have shown that the apparent diffusion coefficient values from DWI increase after treatment (43-45), with the greatest changes seen in patients with better outcomes (44).

The integration of MRI into the different stages of RT from target identification to planning to delivery is clearly attractive. However, limitations exist, including the limited availability of MRI scanners, medical contraindications to MRI, and the relatively reduced familiarity with MRI by radiation oncologists compared with CT. In addition, MRI introduces technical hurdles within the planning process, including the lack of direct electron density information, organ motion between the CT and MRI scans, and geometric distortion. Conventional immobilization with MR receiver coils presents additional challenges. Obstacles also include culture changes when a radiation oncology department houses an MRI scanner. Although integration of MR simulators is becoming more commonplace in radiation oncology departments, the need to incorporate MRI safety poses unique challenges.

Daily Adaptive Replanning

Benefits of Daily Adaptive Replanning

With standard IGRT, no method is available to compensate for the independent movements of the 4 potential RT targets—prostate, seminal vesicles, pelvic lymph nodes, and intraprostatic boost. RT can induce an initial increase in the size of the prostate, followed by constriction at the end of RT (46, 47). With SBRT, the swelling can persist even after the end of treatment (48).

Despite daily IGRT to compensate for interfraction movement, residual deformation of the prostate and the organs at risk (OAR) (47, 49) with ongoing intrafraction motion of the prostate continues to be a challenge (50). Offline adaptation can adjust for systematic changes; however, Peng et al (51) showed that when the original treatment plan is superimposed on daily in-room CT scans, approximately one-third of the fractions would need online replanning owing to the discrepancy in the planned and delivered dose.

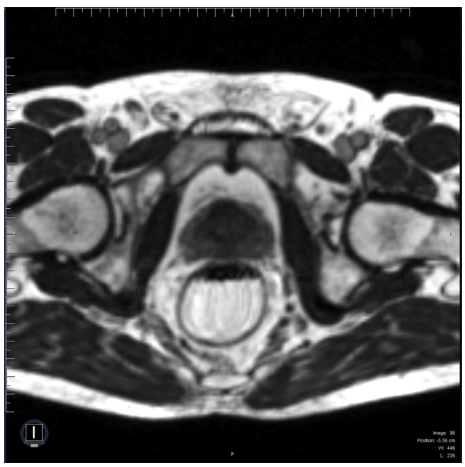

Fig. 2. A clinical true fast imaging with steady-state precision magnetic resonance sequence from ViewRay MRIdian system with acquisition in 25 seconds.

The implications of this disparity become more significant with a shorter ultrafractionated treatment course. On-table, online ART is now feasible with MRgRT and represents an attractive solution for ultrahypofractionated prostate RT. Online ART has the ability to account for not only systematic anatomic changes of prostate swelling, but also random anatomic changes, such as inter- and intrafraction bladder and rectal filling, in addition to independent movement and deformation of multiple targets.

Daily Adaptive Replanning—Obstacles and Solutions

The solution for optimal delivery of a planned dose is real-time planning and daily online adaptation. A number of steps are involved in using the newly acquired images to adjust for changes in anatomy (Fig. 3).

We have defined 6 strategies for ART:

1. Shifting the plan to overlay anatomy: The dose is adapted by shifting the plan relative to the anatomy (3-dimensional or 6-dimensional correction) or vice versa. This is equivalent to standard IGRT.
2. Dynamic shifting of a plan with tracking: This requires intrafraction motion monitoring and has been shown to be feasible with prostate cancer with Calypso beacons (52).
3. Offline ART: This is correct for systematic deformations of the targets (53) or OARs that occur slowly during the RT course, plus shifting the plan on the day of treatment as in strategy 2.
4. Library of plans: Selection is from plans for varying patient anatomy and to deliver the best fit for the anatomy of the day (54, 55).
5. Online ART: This is used to adapt the plan on a daily basis after imaging and to re-optimize or create a new treatment plan.
6. Real-time (intrafraction) ART: This is used to adapt the planned dose during an RT fraction.

The strategies most relevant to prostate MRgRT (strategies 1, 5, and 6) are discussed in the subsequent sections and summarized in Figure 4. The offline strategies 3 and 4 can be performed in lieu of strategy 5, when departmental resources limit the ability to perform on-table ART. All 6 strategies can be used with MRgRT gating in the presence of accurate beam-on imaging.

Shifting the Plan to Overlay Anatomy

IGRT repositioning

Online approaches (56) adjust for interfraction displacements of 1 selected RT target using a couch shift technique and keeping the treatment plan the same.

Simple dose shift

The pretreatment dose distribution itself is translated and rotated according to the change in anatomy (57). This

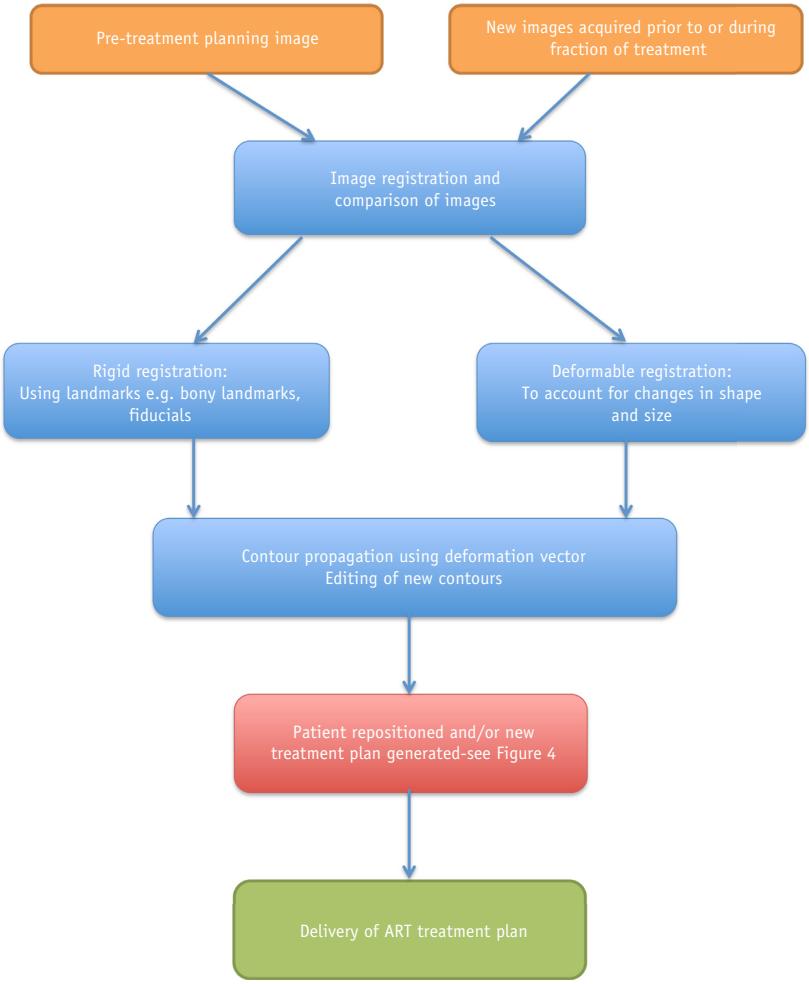

Fig. 3. Flow chart summarizing the steps in adaptive radiation therapy (ART).

method does not require full reoptimization of a plan and is therefore a rapid IGRT solution. A similar method has been described for online rotational correction by adjusting the gantry and collimator angles (58).

Real-time imaging with gated delivery

The challenge of intrafraction motion can be mitigated using gating strategies, whereby tumor motion monitoring is used in conjunction with visual inspection or an automated algorithm to adjust treatment delivery. "Exception gating" uses a specified threshold, eg, with a 2-mm/5-s threshold, if the movement of the prostate exceeds 2 mm from baseline for >5 seconds, treatment delivery is paused to allow for a return of the prostate to the initial position, adaptation of patient position, or a simple dose shift.

At present, prostate motion can be monitored using x-ray tracking of implanted radiopaque markers (seeds) (59, 60) or the Calypso system using electromagnetic transponders (52). MRgRT using soft tissue matching, however, does not require the implantation of seeds or additional radiation exposure and allows visualization of target and normal tissue motion and deformation. The accuracy of target localization is dependent on the speed of image acquisition. Gating through MRI in a clinical setting has been demonstrated with the MRIdian system, where motion monitoring is performed on a sagittal plane acquired at 4 frames per second, followed by real-time deformation and segmentation of the region of interest (61). However, this would be further improved using 3D imaging and patient individualization of the threshold margin, which might include motion prediction algorithms (62).

Online adaptive replanning

A number of methods with various levels of complexity are available for adaptive replanning. Most studies to date have

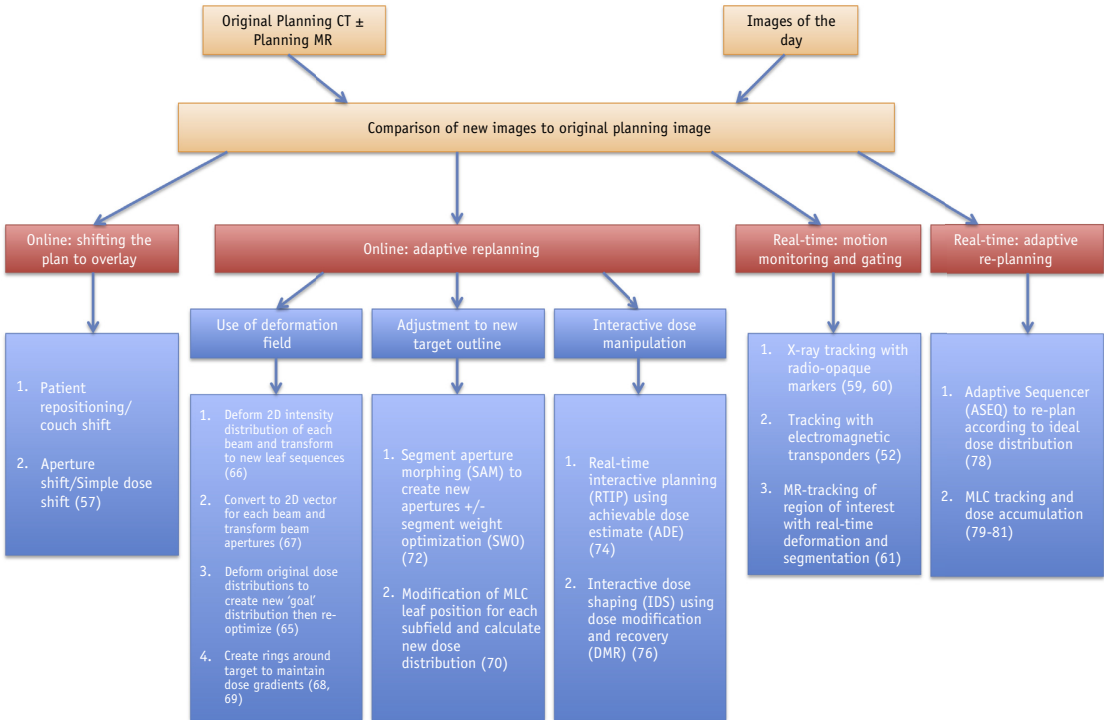

Fig. 4. Flow chart summarizing the spectrum of adaptive radiation therapy (ART). *Abbreviations:* CT = computed tomography; MLC = multileaf collimator; MR = magnetic resonance.

used cone beam CT for daily imaging, which provides a poorer image quality (compared with planning CT and MRI) for new contours, followed by plan adaptation.

The "Blue Sky" aim would be eventually to dispense with pretreatment planning completely and create an online plan from the beginning each day to reflect the current anatomy. This can be in tandem with dose painting based on the distribution of the tumor load as described previously (63). Online MRgRT has been demonstrated clinically with daily MRI by reoptimizing using the original beam angles and objectives used if the constraints were not met (64). Just greater than one-half of the fractions were treated using an adapted plan. The median time for ART was 26 minutes and was well tolerated.

Because this process needs to be completed in a timely manner, several approaches have described adjusting the initial plan, without full optimization, for expediency. Rapid replanning is especially important because increased organ motion over time could negate any benefit from ART.

Use of the deformation field

The deformation matrix created by registering the daily verification images to the planning images can be used to alter the original plan accordingly. Comparison of the whole target or points on the target (65) in the beam's eye view can be used to modify each segment (66) or beam aperture (67). Alternatively, the method of gradient maintenance (68) creates a series of partial concentric rings around the target with the aim of retaining the dose gradients toward each OAR. A similar method has been described with the MRIdian system, whereby rings control the gradients and autosegmentation through deformation, to minimize the recontouring required (69).

Adjustment to new target outline

To avoid the complexities of deformable image registration (DIR), methods to simply compare the target outline are available (70, 71). Segment aperture morphing can adjust the segment shapes to the new target contour (72), with a further step of segment weight optimization for larger deformations. Online replanning methods that are suitable for implementation with the Elekta MR-Linac have also been reported (71, 73).

Interactive dose manipulation

This approach enables the clinician to use tools to click on or select a part of the plan and "drag" the isodose curves or

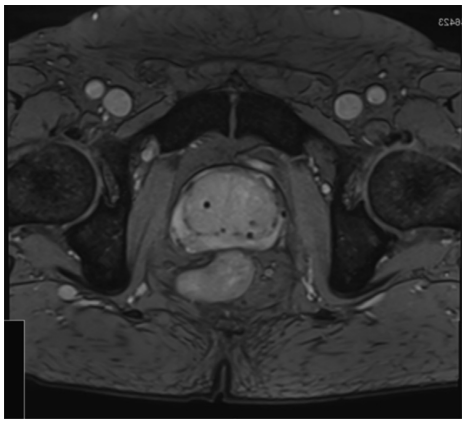

Fig. 5. Magnetic resonance image using adaptation of the "medic" T2-weighted Siemens sequence showing prostate capsule and fiducial markers (image courtesy of Maria Schmidt, Institute of Cancer Research).

and the resultant "intrapatient" autocontours are more accurate (84, 96, 97) and time efficient.

MRI-Only Workflow

Benefits of MRI-only workflow

RT planning currently uses CT imaging, which provides the relevant electron density required for dose calculations. A mixed CT-MRI workflow requires image coregistration, which incurs the risk of introducing inaccuracy as a result of discrepancies in patient positioning, imaging information, and anatomic changes between scans. The latter is particularly relevant for prostate cancer patients, in whom bladder and rectal filling can vary between scans, although minimizing the time between CT and MRI acquisitions can reduce this problem.

The registration error has been estimated to be approximately 2 mm (98) and remains a problem even when using gold fiducial markers to coregister the CT and MRI scans (99), although the "real truth" of image registration inaccuracy is unknown. However, the ultimate goal of the MRgRT system would be to avoid the need for fiducial markers, which require extra resources for insertion and have associated risks for the patients.

Planning directly on an MRI scan removes the systematic error of coregistration (100), which might be large enough to counteract any advantage from the addition of MRI into the process. MRI-only workflow requires a synthetic CT or pseudo-CT scan (101, 102) to give the electron density information required for dose calculations. A major challenge when using MRI is geometric distortion, which can result from either machine-related or patient-related factors. Geometric distortion is greater at a distance from the center of the field; however, for accurate dose calculation, the spatial integrity maintained to the skin surface is essential. This should be minimized using postprocessing before the use of images for planning (102). Efforts have been made to characterize correction maps; however, further work is needed to quantify and develop methods for mitigating geometric distortion (103).

Obstacles to MRI-only workflow and solutions

A number of methods are available to create a pseudo- or synthetic CT scan. These include tissue segmentation, atlas mapping method, and voxel method.

Tissue segmentation

After manual or automatic segmentation of an MRI data set, assigning separate densities to air, soft tissue, and bone is more accurate than applying a single electron density equivalent to water to the whole body (104, 105) and gives comparable results to the standard method of a planning CT scan (105, 106). However, bone segmentation is time consuming using standard MRI sequences, and the value used for the assigned densities must also be relevant (105, 107, 108).

Atlas mapping method

The first step for the atlas mapping method (109, 110) involves the generation of MRI and pseudo-CT atlases from patient data. When MRI data from a new patient is acquired, the same deformations required to register the compiled MRI atlas to the new MR images are applied to the pseudo-CT atlas to map the electron density information to the new patient. A comparison of the standard planning CT scan to the pseudo-CT scan gave a dose difference of $<2\%$ (109, 111), in agreement with data from other MRI planning studies (104, 112). This method can also be used to propagate contours (109, 110); however, it does have limitations, with atypical patient anatomy and the initial step of atlas formation requiring DIR, with the potential errors as described in previous sections.

Voxel method

Statistical models to differentiate the attenuation of tissue types have been investigated to allow the automatic conversion of the MRI intensity in each voxel to a Hounsfield unit (113-115). Using the information from all voxels, a greater spectrum of attenuation coefficients is obtained for a more accurate dose calculation, rather than the limited number used with tissue segmentation (115, 116).

Ultimately, an automated approach for pseudo-CT generation, combining the described methods, will be more clinically useful. The now commercially available Philips MRCAT (MR for calculation attenuation) creates a pseudo-CT scan from an mDIXON sequence, acquired with 2 echo times. The initial step comprises model-based automatic tissue segmentation into the 5 classes of air, fat, water-rich tissue, spongy bone, and compact bone. In the second step,

each voxel is assigned a pseudo-Hounsfield unit value based on density values. A number of factors contribute to dose calculations in this process (117); however, the workflow appears to be dosimetrically accurate compared with CT-based planning (118) and has been implemented clinically in prostate RT (119).

MRI-only workflow is now a realistic prospect in the near future and could improve the accuracy of RT planning.

Conclusions

The technological revolution in RT planning now allows us to ask questions, which a decade ago would have been impossible to answer. The increased precision in every step might allow us to further hypofractionate prostate cancer RT, perhaps even down to a single fraction, such as has been demonstrated with brachytherapy. Although this could be delivered using CT guidance, the ideal technology would be MRgRT. Intrafraction MRI, automatic contouring, and fast online and real-time adaptive replanning allow us to challenge the accepted dogma of the RT planning workflow.

To achieve this vision, many hurdles lie ahead, and high quality clinical research is necessary. The challenges are clear and the benefit is yet to be realized. As a wise man once said, "a journey of a thousand miles starts with a single step."

References

1. Dearnaley D, Syndikus I, Mossop H, et al. Conventional versus hypofractionated high-dose intensity-modulated radiotherapy for prostate cancer: 5-Year outcomes of the randomised, non-inferiority, phase 3 CHHiP trial. *Lancet Oncol* 2016;17:1047-1060.
2. Dasu A, Toma-Dasu I. Prostate alpha/beta revisited—an analysis of clinical results from 14 168 patients. *Acta Oncol* 2012;51:963-974.
3. Brenner DJ, Martinez AA, Edmundson GK, et al. Direct evidence that prostate tumors show high sensitivity to fractionation (low α/β ratio), similar to late-responding normal tissue. *Int J Radiat Oncol Biol Phys* 2002;52:6-13.
4. Tree AC, Alexander EJ, Van As NJ, et al. Biological dose escalation and hypofractionation: What is there to be gained and how will it best be done? *Clin Oncol* 2013;25:483-498.
5. Tree AC, Khoo VS, van As NJ, et al. Is biochemical relapse-free survival after profoundly hypofractionated radiotherapy consistent with current radiobiological models? *Clin Oncol (R Coll Radiol)* 2014;26:216-229.
6. Dearnaley DP, Jovic G, Syndikus I, et al. Escalated-dose versus control-dose conformal radiotherapy for prostate cancer: Long-term results from the MRC RT01 randomised controlled trial. *Lancet Oncol* 2014;15:464-473.
7. Viani GA, Stefano EJ, Afonso SL. Higher-than-conventional radiation doses in localized prostate cancer treatment: A meta-analysis of randomized, controlled trials. *Int J Radiat Oncol Biol Phys* 2009;74:1405-1418.
8. Zietman AL, DeSilvio ML, Slater JD, et al. Comparison of conventional-dose vs high-dose conformal radiation therapy in clinically localized adenocarcinoma of the prostate: A randomized controlled trial. *JAMA* 2005;294:1233-1239.
9. Fowler J, Chappell R, Ritter M. Is α/β for prostate tumors really low? *Int J Radiat Oncol Biol Phys* 2001;50:1021-1031.
10. Miralbell R, Roberts SA, Zubizarreta E, et al. Dose-fractionation sensitivity of prostate cancer deduced from radiotherapy outcomes of 5,969 patients in seven international institutional datasets: $\alpha/\beta = 1.4$ (0.9-2.2) Gy. *Int J Radiat Oncol Biol Phys* 2012;82:e17-e24.
11. Incrocci L, Wortel RC, Alemayehu WG, et al. Hypofractionated versus conventionally fractionated radiotherapy for patients with localised prostate cancer (HYPRO): Final efficacy results from a randomised, multicentre, open-label, phase 3 trial. *Lancet Oncol* 2016;17:1061-1069.
12. Loblaw A, Cheung P, D'Alimonte L, et al. Prostate stereotactic ablative body radiotherapy using a standard linear accelerator: Toxicity, biochemical, and pathological outcomes. *Radiother Oncol* 2013;107:153-158.
13. King CR, Brooks JD, Gill H, et al. Long-term outcomes from a prospective trial of stereotactic body radiotherapy for low-risk prostate cancer. *Int J Radiat Oncol Biol Phys* 2012;82:877-882.
14. Cellini N, Morganti AG, Mattiucci GC, et al. Analysis of intraprostatic failures in patients treated with hormonal therapy and radiotherapy: Implications for conformal therapy planning. *Int J Radiat Oncol Biol Phys* 2002;53:595-599.
15. Arrayeh E, Westphalen AC, Kurhanewicz J, et al. Does local recurrence of prostate cancer after radiation therapy occur at the site of primary tumor? Results of a longitudinal MRI and MRSI study. *Int J Radiat Oncol Biol Phys* 2012;82:e787-e793.
16. Lips IM, van der Heide UA, Haustermans K, et al. Single blind randomized phase III trial to investigate the benefit of a focal lesion ablative microboost in prostate cancer (FLAME-trial): Study protocol for a randomized controlled trial. *Trials* 2011;12:255.
17. Ling CC, Humm J, Larson S, et al. Towards multidimensional radiotherapy (MD-CRT): Biological imaging and biological conformality. *Int J Radiat Oncol Biol Phys* 2000;47:551-560.
18. deSouza NM, Riches SF, Van As NJ, et al. Diffusion-weighted magnetic resonance imaging: A potential non-invasive marker of tumour aggressiveness in localized prostate cancer. *Clin Radiol* 2008;63:774-782.
19. van As NJ, de Souza NM, Riches SF, et al. A study of diffusion-weighted magnetic resonance imaging in men with untreated localised prostate cancer on active surveillance. *Eur Urol* 2009;56:981-988.
20. Pathmanathan AU, Alexander EJ, Huddart RA, et al. The delineation of intraprostatic boost regions for radiotherapy using multimodality imaging. *Future Oncol* 2016;12:2495-2511.
21. Hoskin P, Rojas A, Ostler P, et al. High-dose-rate brachytherapy with two or three fractions as monotherapy in the treatment of locally advanced prostate cancer. *Radiother Oncol* 2014;112:63-67.
22. Hoskin P, Rojas A, Ostler P, et al. Single-dose high-dose-rate brachytherapy compared to two and three fractions for locally advanced prostate cancer. *Radiother Oncol* 2017;124:56-60.
23. Hoskin P, Rojas A, Ostler P, et al. High-dose-rate brachytherapy alone given as two or one fraction to patients for locally advanced prostate cancer: Acute toxicity. *Radiother Oncol* 2014;110:268-271.
24. Prada PJ, Jimenez I, González-Suárez H, et al. High-dose-rate interstitial brachytherapy as monotherapy in one fraction and transperineal hyaluronic acid injection into the perirectal fat for the treatment of favorable stage prostate cancer: Treatment description and preliminary results. *Brachytherapy* 2012;11:105-110.
25. Krauss DJ, Ye H, Martinez AA, et al. Favorable preliminary outcomes for men with low- and intermediate-risk prostate cancer treated with 19-Gy single-fraction high-dose-rate brachytherapy. *Int J Radiat Oncol Biol Phys* 2017;97:98-106.
26. Dankulchai P, Alonzi R, Lowe GJ, et al. Optimal source distribution for focal boosts using high dose rate (HDR) brachytherapy alone in prostate cancer. *Radiother Oncol* 2014;113:121-125.
27. Morris WJ, Keyes M, Spadinger I, et al. Population-based 10-year oncologic outcomes after low-dose-rate brachytherapy for low-risk and intermediate-risk prostate cancer. *Cancer* 2013;119:1537-1546.

28. Zaorsky NG, Davis BJ, Nguyen PL, et al. The evolution of brachytherapy for prostate cancer. *Nat Rev Urol* 2017;14:415-439.
29. Morris WJ, Tyldesley S, Rodda S, et al. Androgen suppression combined with elective nodal and dose escalated radiation therapy (the ASCENDE-RT trial): An analysis of survival endpoints for a randomized trial comparing a low-dose-rate brachytherapy boost to a dose-escalated external beam boost for high- and intermediate-risk prostate cancer. *Int J Radiat Oncol Biol Phys* 2017;98:275-285.
30. Rodda S, Tyldesley S, Morris WJ, et al. ASCENDE-RT: An analysis of treatment-related morbidity for a randomized trial comparing a low-dose-rate brachytherapy boost with a dose-escalated external beam boost for high- and intermediate-risk prostate cancer. *Int J Radiat Oncol Biol Phys* 2017;98:286-295.
31. Henderson D, Tree A, van As N. Single fraction external beam radiotherapy for localised prostate cancer: A planning study. *Clin Oncol* 2017;29:e87.
32. Choudhury A, Budgell G, MacKay R, et al. The future of image-guided radiotherapy. *Clin Oncol* 2017;29:662-666.
33. Raaymakers BW, Lagendijk JJW, Overweg J, et al. Integrating a 1.5 T MRI scanner with a 6 MV accelerator: Proof of concept. *Phys Med Biol* 2009;54:N229.
34. Mutic S, Dempsey JF. The ViewRay System: Magnetic resonance-guided and controlled radiotherapy. *Semin Radiat Oncol* 2014;24:196-199.
35. Keall PJ, Barton M, Crozier S. The Australian magnetic resonance imaging-linac program. *Semin Radiat Oncol* 2014;24:203-206.
36. Fallone BG, Murray B, Rathee S, et al. First MR images obtained during megavoltage photon irradiation from a prototype integrated linac-MR system. *Med Phys* 2009;36(6 Pt 1):2084-2088.
37. Raaijmakers AJE, Raaymakers BW, van der Meer S, et al. Integrating a MRI scanner with a 6 MV radiotherapy accelerator: Impact of the surface orientation on the entrance and exit dose due to the transverse magnetic field. *Phys Med Biol* 2007;52:929-939.
38. Raaijmakers AJE, Raaymakers BW, Lagendijk JJW. Magnetic-field-induced dose effects in MR-guided radiotherapy systems: Dependence on the magnetic field strength. *Phys Med Biol* 2008;53:909-923.
39. Wooten HO, Green O, Yang M, et al. Quality of intensity modulated radiation therapy treatment plans using a ^{60}Co magnetic resonance image guidance radiation therapy system. *Int J Radiat Oncol Biol Phys* 2015;92:771-778.
40. Pathmanathan A, Nill S, Oelfke U, et al. Stereotactic body radiotherapy (SBRT) for localised prostate cancer on the magnetic resonance linac. *Clin Oncol* 2017;29:141-204.
41. Noel CE, Parikh PJ, Spencer CR, et al. Comparison of onboard low-field magnetic resonance imaging versus onboard computed tomography for anatomy visualization in radiotherapy. *Acta Oncol* 2015;54:1474-1482.
42. Yang Y, Cao M, Sheng K, et al. Longitudinal diffusion MRI for treatment response assessment: Preliminary experience using an MRI-guided tri-cobalt 60 radiotherapy system. *Med Phys* 2016;43:1369-1373.
43. Park SY, Kim CK, Park BK, et al. Early changes in apparent diffusion coefficient from diffusion-weighted MR imaging during radiotherapy for prostate cancer. *Int J Radiat Oncol Biol Phys* 2012;83:749-755.
44. Liu L, Wu N, Ouyang H, et al. Diffusion-weighted MRI in early assessment of tumour response to radiotherapy in high-risk prostate cancer. *Br J Radiol* 2014;87:20140359.
45. Decker G, Mürtz P, Gieseke J, et al. Intensity-modulated radiotherapy of the prostate: Dynamic ADC monitoring by DWI at 3.0 T. *Radiother Oncol* 2014;113:115-120.
46. King BL, Butler WM, Merrick GS, et al. Electromagnetic transponders indicate prostate size increase followed by decrease during the course of external beam radiation therapy. *Int J Radiat Oncol Biol Phys* 2011;79:1350-1357.
47. Nichol AM, Brock KK, Lockwood GA, et al. A magnetic resonance imaging study of prostate deformation relative to implanted gold fiducial markers. *Int J Radiat Oncol Biol Phys* 2007;67:48-56.
48. Gunnlaugsson A, Kjellén E, Hagberg O, et al. Change in prostate volume during extreme hypo-fractionation analysed with MRI. *Radiat Oncol* 2014;9:1-6.
49. Kerkhof EM, van der Put RW, Raaymakers BW, et al. Variation in target and rectum dose due to prostate deformation: An assessment by repeated MR imaging and treatment planning. *Phys Med Biol* 2008;53:5623-5634.
50. McPartlin AJ, Li XA, Kershaw LE, et al. MRI-guided prostate adaptive radiotherapy—a systematic review. *Radiother Oncol* 2016;119:371-380.
51. Peng C, Ahunbay E, Chen G, et al. Characterizing interfraction variations and their dosimetric effects in prostate cancer radiotherapy. *Int J Radiat Oncol Biol Phys* 2011;79:909-914.
52. Kupelian P, Willoughby T, Mahadevan A, et al. Multi-institutional clinical experience with the Calypso system in localization and continuous, real-time monitoring of the prostate gland during external radiotherapy. *Int J Radiat Oncol Biol Phys* 2007;67:1088-1098.
53. Nijkamp J, Pos FJ, Nuver TT, et al. Adaptive radiotherapy for prostate cancer using kilovoltage cone-beam computed tomography: First clinical results. *Int J Radiat Oncol Biol Phys* 2008;70:75-82.
54. Chen W, Gemmel A, Rietzel E. A patient-specific planning target volume used in "plan of the day" adaptation for interfractional motion mitigation. *J Radiat Res* 2013;54(Suppl 1):i82-i90.
55. Xia P, Qi P, Hwang A, et al. Comparison of three strategies in management of independent movement of the prostate and pelvic lymph nodes. *Med Phys* 2010;37:5006-5013.
56. Létourneau D, Martinez AA, Lockman D, et al. Assessment of residual error for online cone-beam CT-guided treatment of prostate cancer patients. *Int J Radiat Oncol Biol Phys* 2005;62:1239-1246.
57. Bol GH, Lagendijk JJW, Raaymakers BW. Virtual couch shift (VCS): Accounting for patient translation and rotation by online IMRT re-optimization. *Phys Med Biol* 2013;58:2989-3000.
58. Rijkhorst E-J, Lakeman A, Nijkamp J, et al. Strategies for online organ motion correction for intensity-modulated radiotherapy of prostate cancer: Prostate, rectum, and bladder dose effects. *Int J Radiat Oncol Biol Phys* 2009;75:1254-1260.
59. Shimizu S, Nishioka K, Suzuki R, et al. Early results of urethral dose reduction and small safety margin in intensity-modulated radiation therapy (IMRT) for localized prostate cancer using a real-time tumor-tracking radiotherapy (RTRT) system. *Radiat Oncol* 2014;9:118.
60. Keall PJ, Ng JA, Juneja P, et al. Real-time 3D image guidance using a standard LINAC: Measured motion, accuracy, and precision of the first prospective clinical trial of kilovoltage intrafraction monitoring-guided gating for prostate cancer radiation therapy. *Int J Radiat Oncol Biol Phys* 2016;94:1015-1021.
61. Bohoudi O, Bruynzeel A, Senan S, et al. SP-0494: Using a MRI-guided radiation therapy system for prostate cancer patients. ESTRO 36. *Radiother Oncol* 2017;123(Suppl 1):S263.
62. Seregni M, Paganelli C, Lee D, et al. Motion prediction in MRI-guided radiotherapy based on interleaved orthogonal cine-MRI. *Phys Med Biol* 2016;61:872.
63. van Schie MA, Steenbergen P, Dinh CV, et al. Repeatability of dose painting by numbers treatment planning in prostate cancer radiotherapy based on multiparametric magnetic resonance imaging. *Phys Med Biol* 2017;62:5575-5588.
64. Acharya S, Fischer-Valuck BW, Kashani R, et al. Online magnetic resonance image guided adaptive radiation therapy: First clinical applications. *Int J Radiat Oncol Biol Phys* 2016;94:394-403.
65. Wu QJ, Danthai T, Zhiheng W, et al. On-line re-optimization of prostate IMRT plans for adaptive radiation therapy. *Phys Med Biol* 2008;53:673-691.
66. Mohan R, Zhang X, Wang H, et al. Use of deformed intensity distributions for on-line modification of image-guided IMRT to account for interfractional anatomic changes. *Int J Radiat Oncol Biol Phys* 2005;61:1258-1266.

67. Feng Y, Castro-Pareja C, Shekhar R, et al. Direct aperture deformation: An interfraction image guidance strategy. *Med Phys* 2006; 33:4490-4498.
68. Ahunbay EE, Li XA. Gradient maintenance: A new algorithm for fast online replanning. *Med Phys* 2015;42:2863-2876.
69. Bohoudi O, Bruynzeel AME, Senan S, et al. Fast and robust online adaptive planning in stereotactic MR-guided adaptive radiation therapy (SMART) for pancreatic cancer. *Radiother Oncol* 2017 [e-pub ahead of print]. http://dx.doi.org/10.1016/j.radonc.2017.07.028.
70. Fu W, Yang Y, Yue NJ, et al. A cone beam CT-guided online plan modification technique to correct interfractional anatomic changes for prostate cancer IMRT treatment. *Phys Med Biol* 2009;54:1691-1703.
71. Ahunbay EE, Ates O, Li XA. An online replanning method using warm start optimization and aperture morphing for flattening-filter-free beams. *Med Phys* 2016;43:4575-4584.
72. Ahunbay EE, Peng C, Chen G-P, et al. An on-line replanning scheme for interfractional variations. *Med Phys* 2008;35:3607-3615.
73. Ates O, Ahunbay EE, Moreau M, et al. Technical note: A fast online adaptive replanning method for VMAT using flattening filter free beams. *Med Phys* 2016;43:2756-2764.
74. Otto K. Real-time interactive treatment planning. *Phys Med Biol* 2014;59:4845-4859.
75. Kamerling CP, Ziegenhein P, Sterzing F, et al. Interactive dose shaping part 2: Proof of concept study for six prostate patients. *Phys Med Biol* 2016;61:2471-2484.
76. Ziegenhein P, Kamerling CP, Oelfke U. Interactive dose shaping part 1: A new paradigm for IMRT treatment planning. *Phys Med Biol* 2016;61:2457-2470.
77. Colvill E, Booth J, Nill S, et al. A dosimetric comparison of real-time adaptive and non-adaptive radiotherapy: A multi-institutional study encompassing robotic, gimbaled, multileaf collimator and couch tracking. *Radiother Oncol* 2016;119:159-165.
78. Kontaxis C, Bol GH, Lagendijk JJW, et al. Towards adaptive IMRT sequencing for the MR-linac. *Phys Med Biol* 2015;60:2493-2509.
79. Colvill E, Booth JT, O'Brien RT, et al. Multileaf collimator tracking improves dose delivery for prostate cancer radiation therapy: Results of the first clinical trial. *Int J Radiat Oncol Biol Phys* 2015;92:1141-1147.
80. Fast MF, Kamerling CP, Ziegenhein P, et al. Assessment of MLC tracking performance during hypofractionated prostate radiotherapy using real-time dose reconstruction. *Phys Med Biol* 2016;61:1546-1562.
81. Kamerling C, Fast M, Ziegenhein P, et al. TH-CD-202-12: Online inter-beam replanning based on real-time dose reconstruction. *Med Phys* 2016;43:3879.
82. Wang Y, Mazur TR, Park JC, et al. Development of a fast Monte Carlo dose calculation system for online adaptive radiation therapy quality assurance. *Phys Med Biol* 2017;62:4970-4990.
83. Tao C-J, Yi J-L, Chen N-Y, et al. Multi-subject atlas-based auto-segmentation reduces interobserver variation and improves dosimetric parameter consistency for organs at risk in nasopharyngeal carcinoma: A multi-institution clinical study. *Radiother Oncol* 2015; 115:407-411.
84. Hwee J, Louie AV, Gaede S, et al. Technology assessment of automated atlas based segmentation in prostate bed contouring. *Radiat Oncol* 2011;6:110.
85. Warfield SK, Zou KH, Wells WM. Simultaneous truth and performance level estimation (STAPLE): An algorithm for the validation of image segmentation. *IEEE Trans Med Imaging* 2004;23:903-921.
86. Wong WKH, Leung LHT, Kwong DLW. Evaluation and optimization of the parameters used in multiple-atlas-based segmentation of prostate cancers in radiation therapy. *Br J Radiol* 2016;89:20140732.
87. Velker VM, Rodrigues GB, Dinniwell R, et al. Creation of RTOG compliant patient CT-atlases for automated atlas based contouring of local regional breast and high-risk prostate cancers. *Radiat Oncol* 2013;8:188.
88. Greenham S, Dean J, Fu CKK, et al. Evaluation of atlas-based auto-segmentation software in prostate cancer patients. *J Med Radiat Sci* 2014;61:151-158.
89. Klein S, van der Heide UA, Lips IM, et al. Automatic segmentation of the prostate in 3D MR images by atlas matching using localized mutual information. *Med Phys* 2008;35:1407-1417.
90. Pasquier D, Lacornerie T, Vermandel M, et al. Automatic segmentation of pelvic structures from magnetic resonance images for prostate cancer radiotherapy. *Int J Radiat Oncol Biol Phys* 2007;68: 592-600.
91. Morrow NV, Lawton CA, Qi XS, et al. Impact of computed tomography image quality on image-guided radiation therapy based on soft tissue registration. *Int J Radiat Oncol Biol Phys* 2012;82:e733-e738.
92. Simmat I, Georg P, Georg D, et al. Assessment of accuracy and efficiency of atlas-based autosegmentation for prostate radiotherapy in a variety of clinical conditions. *Strahlenther Onkol* 2012;188:807-815.
93. Beasley WJ, McWilliam A, Slevin NJ, et al. An automated workflow for patient-specific quality control of contour propagation. *Phys Med Biol* 2016;61:8577-8586.
94. Altman MB, Kavanaugh JA, Wooten HO, et al. A framework for automated contour quality assurance in radiation therapy including adaptive techniques. *Phys Med Biol* 2015;60:5199-5209.
95. Feng Y, Kawrakow I, Olsen J, et al. A comparative study of automatic image segmentation algorithms for target tracking in MR-IGRT. *J Appl Clin Med Phys* 2016;17:441-460.
96. Li W, Vassil A, Zhong Y, et al. Daily dose monitoring with atlas-based auto-segmentation on diagnostic quality CT for prostate cancer. *Med Phys* 2013;40:111720.
97. Godley A, Sheplan Olsen LJ, Stephans K, et al. Combining prior day contours to improve automated prostate segmentation. *Med Phys* 2013;40:021722.
98. Roberson PL, McLaughlin PW, Narayana V, et al. Use and uncertainties of mutual information for computed tomography/magnetic resonance (CT/MR) registration post permanent implant of the prostate. *Med Phys* 2005;32:473-482.
99. Huisman HJ, Fütterer JJ, van Lin EN, et al. Prostate cancer: Precision of integrating functional MR imaging with radiation therapy treatment by using fiducial gold markers. *Radiology* 2005;236:311-317.
100. Nyholm T, Nyberg M, Karlsson MG, et al. Systematisation of spatial uncertainties for comparison between a MR and a CT-based radiotherapy workflow for prostate treatments. *Radiat Oncol* 2009; 4:54.
101. Nyholm T, Jonsson J. Counterpoint: Opportunities and challenges of a magnetic resonance imaging-only radiotherapy work flow. *Semin Radiat Oncol* 2014;24:175-180.
102. Schmidt AM, Payne SG. Radiotherapy planning using MRI. *Phys Med Biol* 2015;60:R323-R361.
103. Price RG, Kadbi M, Kim J, et al. Technical note: Characterization and correction of gradient nonlinearity induced distortion on a 1.0 T open bore MR-SIM. *Med Phys* 2015;42:5955-5960.
104. Chen L, Price RA Jr, Wang L, et al. MRI-based treatment planning for radiotherapy: Dosimetric verification for prostate IMRT. *Int J Radiat Oncol Biol Phys* 2004;60:636-647.
105. Jonsson JH, Karlsson MG, Karlsson M, et al. Treatment planning using MRI data: An analysis of the dose calculation accuracy for different treatment regions. *Radiat Oncol* 2010;5:62.
106. Korsholm ME, Waring LW, Edmund JM. A criterion for the reliable use of MRI-only radiotherapy. *Radiat Oncol* 2014;9:16.
107. Kim J, Garbarino K, Schultz L, et al. Dosimetric evaluation of synthetic CT relative to bulk density assignment-based magnetic resonance-only approaches for prostate radiotherapy. *Radiat Oncol* 2015;10:239.
108. Hu Y, Zhao W, Du D, et al. Magnetic resonance imaging-based treatment planning for prostate cancer: Use of population average

tissue densities within the irradiated volume to improve plan accuracy. *Pract Radiat Oncol* 2015;5:248-256.
109. Dowling JA, Lambert J, Parker J, et al. An atlas-based electron density mapping method for magnetic resonance imaging (MRI)-alone treatment planning and adaptive MRI-based prostate radiation therapy. *Int J Radiat Oncol Biol Phys* 2012;83:e5-e11.
110. Burgos N, Guerreiro F, McClelland J, et al. Iterative framework for the joint segmentation and CT synthesis of MR images: Application to MRI-only radiotherapy treatment planning. *Phys Med Biol* 2017;62:4237-4253.
111. Guerreiro F, Burgos N, Dunlop A, et al. Evaluation of a multi-atlas CT synthesis approach for MRI-only radiotherapy treatment planning. *Phys Med* 2017;35:7-17.
112. Uh J, Merchant TE, Li Y, et al. MRI-based treatment planning with pseudo CT generated through atlas registration. *Med Phys* 2014;41:051711.
113. Catana C, van der Kouwe A, Benner T, et al. Towards implementing an MR-based PET attenuation correction method for neurological studies on the MR-PET brain prototype. *J Nucl Med* 2010;51:1431-1438.
114. Berker Y, Franke J, Salomon A, et al. MRI-based attenuation correction for hybrid PET/MRI systems: A 4-class tissue segmentation technique using a combined ultrashort-echo-time/Dixon MRI sequence. *J Nucl Med* 2012;53:796-804.
115. Johansson A, Karlsson M, Nyholm T. CT substitute derived from MRI sequences with ultrashort echo time. *Med Phys* 2011;38:2708-2714.
116. Kapanen M, Tenhunen M. T1/T2*-weighted MRI provides clinically relevant pseudo-CT density data for the pelvic bones in MRI-only based radiotherapy treatment planning. *Acta Oncol* 2013;52:612-618.
117. Maspero M, Seevinck PR, Schubert G, et al. Quantification of confounding factors in MRI-based dose calculations as applied to prostate IMRT. *Phys Med Biol* 2017;62:948-965.
118. Tyagi N, Fontenla S, Zhang J, et al. Dosimetric and workflow evaluation of first commercial synthetic CT software for clinical use in pelvis. *Phys Med Biol* 2017;62:2961-2975.
119. Tyagi N, Fontenla S, Zelefsky M, et al. Clinical workflow for MR-only simulation and planning in prostate. *Radiat Oncol* 2017;12:119.

REVIEW
Special Focus Issue: Prostate Imaging

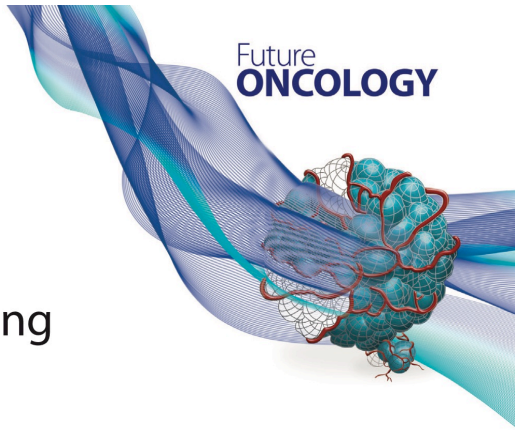

The delineation of intraprostatic boost regions for radiotherapy using multimodality imaging

Angela U Pathmanathan*[1], Emma J Alexander[2], Robert A Huddart[1] & Alison C Tree[2]

Dose escalation to the prostate improves tumor control but at the expense of increased rectal toxicity. Modern imaging can be used to detect the most common site of recurrence, the intraprostatic lesion (IPL), which has led to the concept of focusing dose escalation to the IPL in order to improve the therapeutic ratio. Imaging must be able to detect lesions with adequate sensitivity and specificity to accurately delineate the IPL. This information must be carefully integrated into the radiotherapy planning process to ensure the dose is targeted to the IPL. This review will consider the role and challenges of multiparametric MRI and PET computed tomography in delineating a tumor boost to be delivered by external beam radiotherapy.

First draft submitted: 18 March 2016; Accepted for publication: 1 May 2016; Published online: 20 June 2016

KEYWORDS
• boost • dose escalation
• intraprostatic lesion • MRI
• PET-CT • prostate cancer

Background: the rationale behind the intraprostatic boost

• Dose escalation

Increasing the dose to the prostate during radical radiotherapy (RT) has consistently shown improvement in biochemical control [1–6]. A meta-analysis showed that the postulated improvement in biochemical control rate at 5 years was an increase of 19.2% in high-risk patients between the dose ranges of 70 and 80 Gy [3]. However, dose escalation to the whole prostate is associated with an increase in bladder and rectal toxicity [4–7].

• Patterns of recurrence

Although prostate cancer tends to be multifocal, histopathology from prostatectomy specimens commonly reveals a larger focus or intraprostatic lesion (IPL), also referred to as the dominant intraprostatic lesion (DIL). Local recurrence following radical RT largely occurs at the site of the IPL [8–10]. Cellini *et al.* reported on 12 patients who had an intraprostatic recurrence, following EBRT and androgen-deprivation therapy (ADT) [8]. For all 12 patients, clinical examination and imaging findings showed recurrence was at the site of the primary tumor. Pucar *et al.* reviewed pathology from salvage radical prostatectomy in nine patients with locally recurrent disease [9]. Visual comparison of pathology, together with pre- and post-RT MRI showed that all significant recurrent lesions occurred at the site of the primary tumor.

Therefore a higher dose to the IPL may reduce biochemical prostate-specific antigen failure and it is suggested that improving local control may translate into a reduction in distant metastases [11].

[1]The Institute of Cancer Research, 123 Old Brompton Road, London, SW7 3RP, UK
[2]The Royal Marsden NHS Foundation Trust, Downs Road, Sutton, SM2 5PT, UK
*Author for correspondence: angela.pathmanathan@icr.ac.uk

Future Medicine part of fsg

• Improved therapeutic ratio

The demonstration of disease recurrence within the DIL has led to the proposal of boosting this region, while maintaining a standard dose to the rest of the prostate, in order to improve the therapeutic ratio [12]. The boost dose needs to be at least 80–90 Gy in 2 Gy fractions, to reach the top of the tumor control probability (TCP) curve [3,5]. The aim of treatment would be to increase the TCP without increasing the normal tissue complication probability (NTCP) for the bladder and rectum.

• Multifocality

Prostatectomy specimens reveal the multifocality of prostate cancer [13] and when more than one tumor is identified on imaging, boosting several dominant nodules is technically possible [14]. The significance of smaller, incidental tumors, however, is unclear. Noguchi *et al.* reported that the secondary tumors identified following radical prostatectomy did not predict for biochemical failure [15]. In a disease where we know some low-risk cancers can safely be observed [16,17], stratification systems have been produced which help to determine intraprostatic disease which can be considered insignificant on template-mapping biopsy procedures [18]. This is an important concept to consider when discussing IPL boost.

• Dose painting

Focal therapies to an IPL include the different techniques of external beam RT, brachytherapy, high-intensity focused ultrasound or cryotherapy. With RT techniques such as intensity-modulated radiation therapy (IMRT) and volumetric-modulated arc therapy (VMAT), more complex dose distributions are possible, allowing an increase in dose to a particular volume, while limiting the dose to the organs at risk. To deliver this dose accurately and improve the therapeutic ratio, prostate movement needs to be accounted for by image-guided radiotherapy (IGRT). The boost may be delivered sequentially, following standard treatment to the prostate, or as a simultaneous integrated boost (SIB). The optimal boost dose and RT planning method is unclear – this is beyond the scope of this review and will not be debated here. Most studies to date have used static field IMRT [14,19–23]. Planning studies have also assessed VMAT [24–26] and stereotactic body radiation therapy techniques [27,28]. **Figure 1** shows an example of an IPL boost plan for Cyberknife delivered stereotactic body radiation therapy.

Also unclear is which patients would benefit from an intraprostatic boost. Given the excellent control rates seen from studies such as the CHHiP trial [29], it may be that only higher risk patients need to be treated with a boost.

• Identification of IPL

Although imaging techniques have previously been reviewed for detection of an IPL, whether an image is sufficient to accurately define the tumor boundary is a separate question. An accurate IPL boost involves several stages, from optimal imaging, accurately transferring this information to the planning computed tomography (CT), correct identification and delineation of the lesion, and then delivering the RT as intended.

In this article, we will be looking at the use of imaging when delineating a boost for external beam RT modalities, specifically concentrating on multiparametric MRI (mp-MRI) and PET. For each of these, we consider the limitations, practicalities and challenges of IPL delineation under the following sections:

- Type of imaging;
- Limitations and challenges of imaging;
- Histopathological correlation of contours for boost techniques;
- Feasibility of boost delivery;
- Integration of imaging during RT.

MRI

There are clear benefits for the addition of MRI when contouring the prostate as a whole, with the improved soft tissue contrast providing better definition of the prostate boundary and subsequent reduced interobserver variability [30–33].

• Multiparametric imaging

The accuracy of MRI in staging prostate cancer has been extensively studied. Conventional MRI consists of anatomical T2-weighted images (T2W) with prostate cancer exhibiting low T2 signal intensity. Multiparametric MRI (mp-MRI) includes functional data from dynamic contrast-enhanced (DCE), magnetic resonance spectroscopy (MRS) and/or diffusion-weighted imaging (DWI), which can all provide additional information on the tumor to improve the sensitivity and specificity of tumor detection [34–39].

DCE-MRI acquires images while contrast is administered and therefore provides information

on the perfusion and vascular permeability of a tumor. DWI assesses the motion of water molecules, with tumors showing a restricted diffusion due to increased cellularity. This restriction of diffusion is expressed as the apparent diffusion coefficient (ADC) and has been found to be a predictor of the aggressiveness of a prostate cancer [40,41]. MRS is a form of metabolic imaging that detects prostate cancer due to the lower levels of intracellular citrate and higher levels of choline compared with benign prostate tissue. There is increased sensitivity for detection of prostate cancer with the addition of MRS [36]; however, spatial resolution is poor, limiting accurate tumor delineation.

Combining modalities improves the sensitivity compared with T2W images alone [37–39]. Pooled results from studies using the combination of T2W, DWI and DCE-MRI show a sensitivity of 0.74 (95% CI: 0.66–0.81) with specificity of 0.88 (95% CI: 0.82–0.92) [42]. Of the three multiparametric modalities (DWI, MRS and DCE), two appear to be sufficient for maximal sensitivity and adding in the third modality may not be of additional benefit [43]. Current recommendations suggest the use of two functional MRI techniques in addition to standard T2W images [44]. **Figure 2** shows an IPL on mp-MRI and PET imaging with an IMRT plan depicting the boost dose for the DELINEATE trial (UKCRN ID 10309).

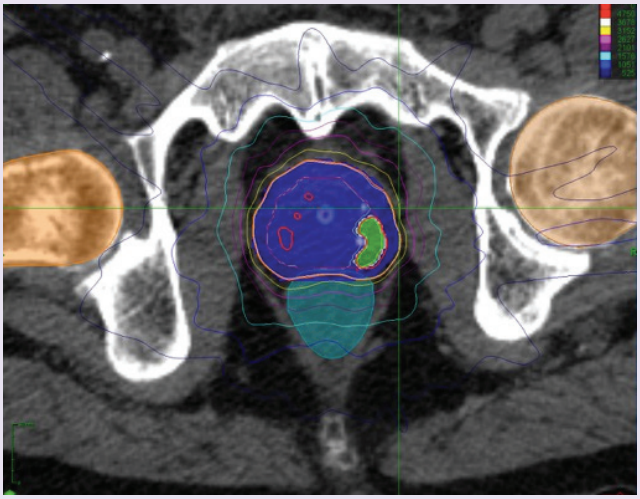

Figure 1. An example of an intraprostatic lesion boost delivered using Cyberknife within the SPARC trial (NCT02145494). Purple shading represents prostate planning target volume, green shading represents intraprostatic lesion boost.

• Limitations & challenges of MRI for delineation of IPL

Accuracy

The reported accuracy of MRI for IPL delineation is variable and dependent on a number of imaging factors as well as tumor characteristics. Technical factors include field strength, b values (which assess the strength of the gradients for DWI), signal to noise ratio and whether an endorectal coil (ERC) is used. The latter improves the spatial resolution and has been found to improve the sensitivity, specificity and staging accuracy of prostate cancer [45] but the presence of the coil causes distortion of the prostate, which limits its use in planning RT.

Low signal on T2W can be seen with prostatitis, hemorrhage, post-RT change and scarring, and distinguishing these from tumor nodules can be challenging.

MRI is limited in the detection of small volume tumors, for example, <0.5 cm^3 [46], particularly those of lower Gleason score. This is due to histological characteristics of the tumor focus, such as the ratio of malignant epithelium-to-stroma, which are inherently different in lesions picked up on MRI compared with those that are not detected [47,48].

Interobserver variability

The delineated shape and size of the IPL should be consistent, aiming to minimize inter- and intra-observer variability. Steenbergen *et al.* compared the delineated tumors using mp-MRI from six teams from three different centers [49]. These were compared with the histological findings from prostatectomy to assess the accuracy of tumor delineation and interobserver variability. Using the combination of T2W, DWI and DCE images, 18 out of 20 dominant lesions were detected by all groups. However, parts of the dominant lesion were missed and 66 out of 69 satellite lesions were undetected. As discussed previously, the clinical significance of these satellite lesions, most of which were smaller than 0.4 cm^3, is unclear [15]. Although these data are consistent with the high sensitivity of detecting tumors with mp-MRI, there was discrepancy of the shape and size of the dominant lesion to be boosted. This may have an impact on local control if the dose to the remaining prostate were

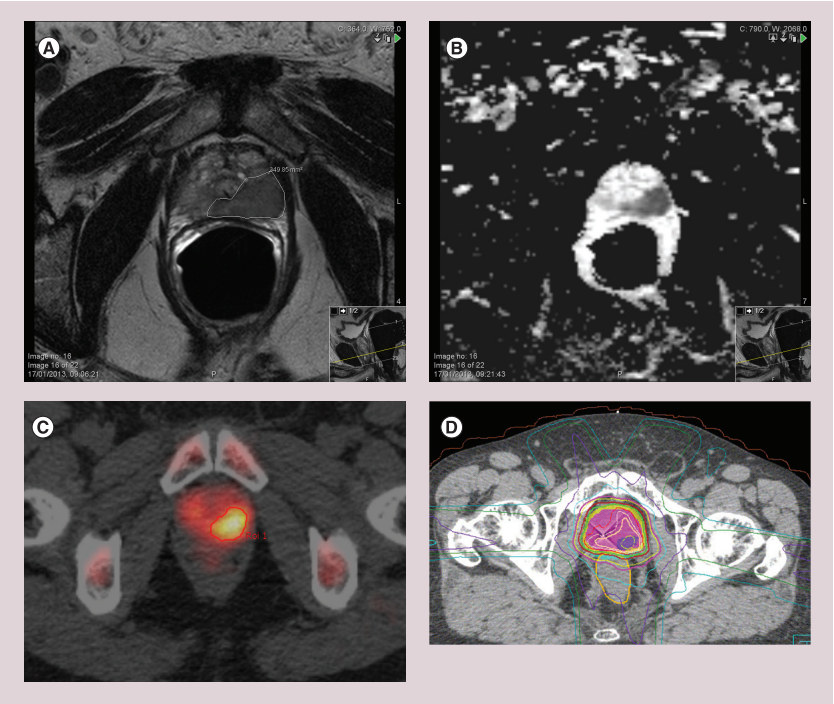

Figure 2. An intensity-modulated radiation therapy delivered intraprostatic lesionboost to a left sided tumor with corresponding MRI and PET computed tomography imaging.
(A) T2-weighted imaging. **(B)** Diffusion-weighted MRI. **(C)** PET computed tomography imaging. **(D)** Intensity-modulated radiation therapy delivered boost in the context of the DELINEATE study – pink shading represents prostate clinical target volume, yellow shading represents prostate planning target volume, purple shading represents intraprostatic lesion boost.

to be reduced, or focal therapy techniques used in isolation. However, overall there was good agreement (kappa statistic of 0.61) between observers.

Image interpretation

The variation and discrepancy in IPL delineation is a significant limitation in allowing accurate RT boost and subsequent introduction to routine practice. There are scoring systems to allow a more standardized method of reporting, such as the Prostate Imaging Reporting and Data System score [44,50] but the experience of the reporting radiologist remains important. A significant hurdle can be combining the information from multiparametric datasets. A comparison of the IPL delineation from DWI and DCE-MRI [51] showed a large variation in the overlap with particularly poor agreement in certain patients. This adds to the uncertainty of the IPL volume, with the same group suggesting a pathologically validated statistical model to predict the risk of tumor presence on a voxel level [52]. Computer-aided delineation techniques such as this and others [53,54] use quantitative features from images to assess whether each voxel is classified as tumor or normal tissue. Further validation is required but these programs could help to reduce uncertainty in delineation and reduce interobserver variation [55].

Effect of androgen-deprivation therapy

The timing of the imaging to be used for definition of the boost is particularly relevant in prostate cancer. Dominant nodules may be easily defined on initial diagnostic imaging, however most patients then receive ADT, which decreases the size of the IPL, and reduces tumor conspicuity [56]. Imaging for DIL delineation for RT planning could therefore be acquired

prior to starting ADT with immediate irradiation, thus necessitating a change in the treatment paradigm. Alternatively, the information from pre-ADT imaging can be 'mapped' onto post-ADT imaging using deformable registration techniques. Additionally, it is unknown whether the optimal target is in fact the pre- or post-ADT lesion. The latter would require further investigation into the effect of ADT on mp-MRI images and may become clearer when the exact benefits of an IPL boost are confirmed.

• Histopathological correlation of contours with MRI

The gold standard of any imaging technique is correlation with histopathology; however, accurate comparison with imaging is extremely challenging. Even with studies comparing imaged IPLs with 'whole-mount prostate' reference histology there are certain limitations such as shrinkage of tissue during fixation and coregistration errors, which may be introduced when aligning histopathology specimens to the equivalent imaging slice. To reduce the impact of such errors one group have used individualized MRI-based custom moulds to aid accurate coregistration of the specimens following prostatectomy [57].

Variability of tumor volume estimation

Data show a positive correlation between the tumor volume derived from histopathology and the MRI defined volume, with the accuracy of MRI estimation improving with a higher tumor volume [46,58]. However, even for lesions greater than 0.5 cm^3, there is still variability [46]. Coakley *et al.* found the MRI defined tumor volume ranged from 3 to 433% of the actual volume on histopathology [46]. However, this study looked at any Gleason grade of tumor in the specimen and as discussed above, Gleason grade 3 + 3 may be less distinct on MRI.

Several studies show tumor volume may be under- rather than over-estimated on MRI [59–62]. One such study comparing the volume seen on MRI compared with histology in 50 tumors [59], showed underestimation by mp-MRI with the volume being lower by a mean of 47% compared with histopathology. Interestingly, this group found that the underestimation was worse for lesions with a high Gleason score [59,62], which has the potential to severely impact the outcome for these patients.

Consideration of margins required to cover tumor

Groenendaal *et al.* found that the use of mp-MRI for IPL delineation gave a tumor coverage of 44–89% of the corresponding lesion on whole mount histopathology [60]. The addition of a margin of two voxels (~5 mm) improved coverage to 85% or more. Similar results for the margin required have been suggested by other studies. Anwar *et al.* identified prostate foci using MRS and subsequently contoured these lesions using T2W images in patients about to undergo prostatectomy (mp-MRI was not used) [61]. When compared with whole mount histopathology, they found that in order to cover the 'MRI undercall' (i.e., the areas underestimated by the readers) that expansion by 5 mm at the noncapsular margin would cover 95% of the actual tumor volume.

A similar study comparing MRI contouring to histopathology concluded that a 9 mm margin would be adequate to cover all 46 tumors analyzed [62]. This differed from the studies above by looking at which margin would be required to cover the entire tumor. The authors suggested 9 mm as the noncapsular margin and 3 mm for the capsular margin, to take into account extraprostatic extension. However, the maximum Hausdorff distance, looking at the difference between the magnetic resonance delineated lesion and histology, was significantly greater for high-grade lesions. It must be considered that the 9 mm margin suggested, included coverage of Gleason 6 tumors (10/46 lesions). Margins could therefore be stratified based on tumor characteristics, especially as in the absence of de-escalation to the whole prostate gland, coverage of low-risk disease is not the objective. For example the same study showed that a smaller margin of 5 mm covered 73.9% of tumors, 7 mm covered 93.5% of tumors.

From an RT planning point of view, these studies indicate an intraprostatic margin of 5 mm around the MRI-defined IPL would be suitable [60,61]. A further factor to be considered is the administration of ADT, which would shrink the IPL and surrounding prostate, so a smaller margin may subsequently be appropriate.

• Feasibility of MRI-defined boost delivery: theoretical

There have been a number of planning studies estimating the TCP, NTCP and investigating the factors that would make an IPL boost feasible. These are outlined in **Table 1**.

Table 1. Planning studies delivering a boost to an MRI-defined intraprostatic lesion.

Study (year)	Patients	Imaging techniques	Radiotherapy treatment	Findings	Ref.
Van Lin *et al.* (2006)	n = 5	1.5 T MRI with ERC T2W, MRS, DCE MR and CT fusion using fiducials IPL delineation by radiologist	Step and shoot IMRT with SIB Plan 1 (boost to IPL): – Prostate + 7 mm 70 Gy/35 fractions – IPL + 5 mm 90 Gy/35 fractions Plan 2 (no boost to IPL): – Prostate + 7 mm 78 Gy/39 fractions	In 5/5 patients, increased therapeutic ratio with boost plan due to a reduction in rectal NTCP with maintained TCP	[63,64]
Housri *et al.* (2011)	n = 42 overall n = 24 had visible IPL	MRI with ERC T2W, DCE, ADC, MRS Treatment planning MR without ERC in 14/24 patients with IPL Manual transfer of MRI information	Step and shoot IMRT with SIB Prostate + 9 mm (5 mm post) 75.6 Gy/42 fractions IPL + 3 mm 151.2 Gy/42 fractions Dose escalation to 151.2 Gy achieved in 12/24 and between 94.5–136.1 Gy in 9/24	SIB infeasible lesions less than 4.2 mm from rectum SIB more feasible with greater hip–hip width >37.22 cm	[64]
Ost *et al.* (2011)	n = 12	T2W and/or MRS MR and CT fusion	Step and shoot IMRT (3, 5, 7 field) compared with VMAT Prostate + 4 mm D_{50} ≥78Gy IPL + 0 mm D_{50} ≥85 Gy	SIB feasible with 5, 7 field IMRT and VMAT VMAT superior to IMRT for rectal volumes receiving 20–50 Gy	[24]
Tree *et al.* (2013)	n = 15	T2W MR and CT fusion IPL delineation by oncologist and radiologist	Stereotactic body radiation therapy with SIB Planned for both Cyberknife and Rapid Arc IPL + 0 mm 47.5 Gy/5 fractions Prostate + 5 mm (3 mm post) 36.25 Gy/5 fractions	Boost feasible with both treatment methods If margins increased to 8 mm (5 mm post) 37/75 compared with 11/75 of constraints missed	[28]
Riches *et al.* (2014)	n = 23 overall n = 20 had visible IPL	1.5 T MRI with ERC T2W, MRS, DCE (pre-ADT) MR and CT fusion using fiducials	Step and shoot IMRT IPL + 2 mm 82 Gy/37 fractions Prostate + 3 mm (0 mm post) 74 Gy	TCP significantly higher in boost plan Rectal NTCP significantly lower in boost plan	[65]
Murray *et al.* (2014)	n=10	1.5 T MRI T2W, DWI, DCE IPL delineation by radiologist MR and CT fusion	VMAT Prostate + 6 mm 42.7 Gy/7 fractions (alternate days) IPL + 4 mm, prescription dose increased by 5% increments starting at 115% Plans with proximal seminal vesicles 32.4–36.5 Gy/7 fractions	For prostate alone plus boost – median SIB 53.4 Gy/7 fractions (125%) Rectal NTCP increased with IPL boost	[26]
Feng *et al.* (2015)	n = 14 n = 7 planned (smaller IPL)	1.5 T MRI T2W IPL delineation by radiologist	VMAT (dual arc) Prostate + 5 mm (3 mm post) 36.25 Gy/5 fractions IPL + 3 mm 47.5 Gy/5 fractions	SIB feasible in all seven patients Standard rigid registration not clinically acceptable	[66]

ADC: Apparent diffusion coefficient; ADT: Androgen-deprivation therapy; CT: Computed tomography; DCE: Dynamic contrast-enhanced; DWI: Diffusion-weighted imaging; ERC: Endorectal coil; IMRT: Intensity-modulated radiation therapy; IPL: Intraprostatic lesion; MR: Magnetic resonance; MRS: Magnetic resonance spectroscopy; NTCP: Normal tissue complication probability; SIB: Simultaneous integrated boost; T2W: T2-weighted; TCP: Tumor control probability; VMAT: Volumetric-modulated arc therapy.

The largest of these was published by Housri *et al.* Nine-field IMRT plans were designed with the aim of delivering a total dose of 151.2 Gy to the IPL without violating dose constraints [64]. This was possible in 12 out of 24 patients and in particular, they reported the distance between the IPL and rectum was predictive of whether high-dose radiation could be delivered to the IPL, with a plan being infeasible with a distance of less than 4.2 mm from the IPL to the rectum.

Riches *et al.* planned IMRT at a dose of 74 Gy to the whole prostate with an additional 8 Gy SIB in 20 patients with an IPL identified using mp-MRI [65]. A planned boost was feasible in all patients while meeting dose constraints. Radiobiological modeling suggested a significant improvement for the TCP and a significantly lower rectal NTCP for the boosted plan. The latter has also been reported in other studies [25,63] and may be due to the redistribution

of dose, including hotspots, when a boost is planned.

• Feasibility of MRI-defined boost delivery: clinical

Acknowledging the limitations described above, and with the aspiration that MRI will continue to increase its accuracy in delineating IPLs, several investigators have assessed the practicalities of delivering RT with focal dose escalation. There have been several studies confirming that an MRI-planned RT boost is practically feasible, can be delivered within dose constraints and is possible without an increase in acute toxicity. These are summarized in **Table 2**.

The studies in **Table 2** have generally shown that an IPL can be selectively dose-escalated with no obvious toxicity penalty. Further randomized studies are needed to confirm this hypothesis.

• Integration of imaging

Optimal boost delineation requires imaging to be carefully integrated into the planning process [65,72]. At present, an RT planning CT provides the electron density data required for dose calculation and hence any additional boost imaging needs to be precisely coregistered with the planning CT to allow fidelity of the boost volume transcription. Even if imaging were to have 100% accuracy, if it is not precisely coregistered into the RT planning pathway, the IPL will not be faithfully represented.

At present, the optimal method for incorporating the information from MRI, is to 'fuse' the CT and MRI dataset. Although this process can be performed manually, software provides deformation algorithms to aid this complicated process, these programs differ in the steps used to match the images and the degree of flexibility. Given the variability in rectal and bladder volumes and movement of the prostate, as expected, deformable image registration is more accurate than rigid techniques [73]. Image registration can introduce a systematic anatomical error although the presence of gold seeds improves this process [72,74]. Additional complications include MRI artifacts, limitations with the geometric fidelity of MRI and the distortion of the prostate seen when an ERC is used, all of which make accurate delineation of an IPL challenging. The discrepancy introduced by these MRI factors should be limited where possible, for example an endorectal balloon (ERB) can be used for the planning scan and throughout treatment to compensate for the ERC [63], but may not be practical.

The ease of image registration is also dependent on whether the patient was scanned in the RT treatment position for the secondary image set (in this case MRI) with identical immobilization including knee wedges, foot stocks and with the same bladder filling protocol and rectal preparation.

If fusion is not possible, images are reviewed side by side to delineate the boost area, known as 'visual cognitive fusion'. This will add a further uncertainty to this process although this manual transfer method has been used in planning studies [19,64].

• Implementation of tumor dose escalation

Adequate margins must be added to take into account coregistration and delineation errors plus motion during the treatment course (intra- and interfraction motion). Even taking into account the margin required to cover the IPL adequately, given the discrepancy seen with delineation as discussed earlier, the optimal intraprostatic margin for the boost is unclear and is dependent on the mode of delivery with some studies using a 0 mm margin and relying on a relatively shallow dose fall off within the prostate clinical target volume (CTV) [19,23–24,28]. Treatment must be delivered accurately with the use of in-room IGRT, with fiducial markers as the current gold standard.

Although the studies detailed here confirm the feasibility of delivering focal dose escalation, with the potential for increased tumor control with decreased NTCP, additional information is needed. Prospective clinical trials such as the Phase III randomized controlled trial FLAME [75], HEIGHT (clinicaltrials.gov: NCT01411332) and the Phase II DELINEATE (UKCRN ID 10309) and SPARC trials (clinical trials.gov: NCT02145494) will provide the vital information on clinical outcome, toxicity and feasibility of boosting to decide whether focal dose escalation should become standard practice.

PET-CT imaging

• Acquisition of images

PET-CT is a form of molecular imaging, requiring injection of a radio-labeled tracer which accumulates based on tissue characteristics. For prostate cancer, differences in choline metabolism have been most frequently exploited for PET imaging. In particular, research has focused

Table 2. Clinical studies delivering a boost to an intraprostatic lesion.

Study (year)	Patients	Imaging	Radiotherapy treatment	Summary of toxicity	Ref.
De Meerleer *et al.* (2005)	n = 15 ADT 87% L/I/H: not specified	1.5 T MRI with ERC T2W 9/15 patients had ERC	Step and shoot IMRT with SIB Verification with daily ultrasound Prostate + 7–10 mm 74 Gy IPL + 0 mm dose 80 Gy	Long-term follow-up not specified Acute: (RTOG): – GI: 20% grade 2, 0% grade 3 – GU: 40% grade 2, 7% grade 3	[19]
Singh *et al.* (2007)	n = 3 ADT not specified L/I/H: not specified	3 T MRI with ERC T2W, MRS, DCE MR and CT fusion using fiducials	Step and shoot IMRT with SIB Fiducials Prostate + 7 mm 75.6 Gy/42 fractions IPL + 3 mm dose 94.5 Gy/42 fractions	Follow-up at 18, 6 and 3 months 2/3 patients grade 2 acute GU (RTOG) 1/3 patients grade 1 acute GI All symptoms resolved at 3 months	[14]
Fonteyne *et al.* (2008)	n = 230 overall n = 118 had SIB ADT 98% L/I/H: 2/40/58%	1.5 T MRI with ERC T2W, MRS (in 49%) MR and CT fusion	Step and shoot IMRT with daily ultrasound verification Prostate + 4 mm dose 78 Gy/38 fractions IPL + 8 mm dose 80 Gy/38 fractions	Median follow-up 12 months No increase in acute toxicity with SIB (RTOG)	[67]
Miralbell *et al.* (2010)	n = 50 ADT 66% L/I/H: 10/24/66%	MRI with ERC T2W and DCE MR and CT fusion (endorectal balloon used for planning CT)	Sequential hypofractionated boost, infrared markers. Prostate dose 64–64.4 Gy 28/50 patients 50.4 Gy/28 fractions to pelvic nodes 21/50 patients two fractions of 5–7 Gy boost 29/50 patients received two fractions of 8 Gy boost	Late (at 5 years): (RTOG): – GI: 10% grade 2, 10% grade 3 – GU: 12% grade 2, 0% grade 3	[27]
Ippolito *et al.* (2012)	n = 40 ADT 100% L/I/H: 10/42/48%	1.5 T MRI with ERC	Step and shoot IMRT with SIB Prostate + 10 mm 72 Gy/40 fractions IPL + 5 mm 80 Gy/40 fractions	Median follow-up 19 months Late: (RTOG/EORTC): – GI 5% grade 2, 2.5% grade 3 – GU 5% grade 2, 2.5% grade 4	[68]
Aluwini *et al.* (2013)	n = 50 (n = 14 had SIB) ADT 0% L/I/H: 60/40/0%	1.5 T MRI (no ERC) T2W MR and CT fusion using fiducials and foley catheter	Stereotactic body radiation therapy SIB in patients with visible tumor Prostate + 3 mm 38 Gy/4 fractions (daily) IPL up to 44 Gy/4 fractions (daily)	Late (at 24 months): (RTOG/EORTC): – GI: 3% grade 2 GI, 0% grade 3 – GU: 10% grade 2 GU, 6% grade 3 GU No difference in toxicity with SIB	[69]
Pinkawa *et al.* (2012)	n = 67 (n = 46 had SIB) ADT 17% L/I/H: not specified	^{18}F-choline PET-CT IPL defined by tumor to background ratio of >2.0	Prostate + 4–8 mm 76 Gy/38 fractions IPL + 4 mm (3 mm post) 80 Gy/38 fractions Verification with daily ultrasound	Median follow-up 19 months No significant difference in QoL with addition of SIB	[70,71]
Wong *et al.* (2011)	n = 71 overall n = 51 scans positive ADT 24% L/I/H: 44/42/14%	Indium-111-capromab pendetide imaging Coregistration with planning scan	Step and shoot IMRT Verification with daily ultrasound Prostate + 6 mm 75.6 Gy/42 fractions IPL + 0 mm 82 Gy/42 fractions	Median follow-up 66 months Late: (Mayo modification of RTOG): – GI: 21% grade 2, 0% grade 3 – GU: 39% grade 2, 4% grade 3, 1% grade 4 (hematuria)	[23]

ADT: Androgen-deprivation therapy; CT: Computed tomography; DCE: Dynamic contrast-enhanced; EORTC: European Organization for Research and Treatment of Cancer; ERC: Endorectal coil; GU: Genitourinary; GI: Gastrointestinal; IMRT: Intensity-modulated radiation therapy; IPL: Intraprostatic lesion; L/I/H: Percentage of patients in low/intermediate/high-risk groups; MR: Magnetic resonance; MRS: Magnetic resonance spectroscopy; QoL: Quality of life; RTOG: Radiation Therapy Oncology Group; SIB: Simultaneous integrated boost; T2W: T2-weighted.

on [^{11}C]- and [^{18}F]-labeled choline derivatives, taking advantage of the increased turnover of choline in prostate cancer, which is required for phospholipids in the cell membrane. Although ^{11}C-Choline PET-CT has the advantage of nonurinary excretion, it has a short half life (20 min) and requires an onsite cyclotron, which limits it usage. ^{11}C-acetate has also been explored, however seems less favorable [76]. There are further investigations into other radiotracers

including those targeting prostate-specific membrane antigen (PSMA), the synthetic amino acid analog anti-1-amino-3-F18-fluorocyclobutane-1-carboxylic acid (FACBC) and F-18-fluoro-5α-dihydrotestosterone (FDHT) which targets the androgen receptor.

PET imaging is not routinely obtained for patients being treated for prostate cancer, although is increasingly used to enhance staging in locally advanced or relapsed disease.

• Limitations & challenges of PET-CT

There have been several studies assessing the role of PET-CT in defining IPLs in prostate cancer, the majority of these use ^{11}C- or ^{18}F-choline [77–81]. For example, a study with ^{11}C-choline PET-CT showed a sensitivity of 66% and specificity of 81% [77]. However, the uptake of lesions can be variable and the studies are limited by conflicting results and small sample sizes. As a result, there continue to be concerns over the use of PET-CT in RT planning [82]. As with MRI, false positives can be seen with prostatitis and inflammation secondary to biopsy or treatment [77]. Van den Bergh *et al.* reported that when multiparametric MRI is used, there is no additional benefit of PET-CT [83], with the accuracy of detecting lesions dependent on the SUV used.

Image interpretation

There are two main methods that have been used for identifying the target in prostate cancer with PET-CT; manual interpretation of the images or the use of automated threshold techniques. The latter has the benefit of defining a target volume without observer bias and therefore maintaining consistency. However, there are a number of factors that will alter the SUV and therefore IPL volume including inhomogeneity within an IPL, lesion size and motion artefact [84]. Using an absolute SUV value to define the target volume does not take into account the variable background activity of the prostate. Therefore, the two main threshold methods are using a tumor-to-background ratio or percentage of the maximum SUV (SUV_{max}). Values have been derived from histopathological studies and are discussed further below.

Spatial resolution

PET-CT has limited spatial resolution, being unable to detect lesions smaller than 5 mm. The SUV_{max} of smaller tumors is less than that of larger ones [81]. The partial volume effect (PVE) leads to smaller lesions either being lost or appearing larger (and therefore encompassing normal tissues) but dimmer [85].

• Histopathological correlation of delineation using PET-CT

Variability of studies

The accuracy of IPL delineation using PET-CT has been assessed by studies using histopathological correlation. Sensitivity and specificity can vary significantly depending on whether studies use voxel, segments or whole prostate level of analysis as the area of interest. Studies also vary depending on the patient population, the standardized uptake value (SUV) threshold used and the acquisition of images. As noted earlier, there are limitations of these histopathological studies, which must be considered when interpreting results. Among the issues to be considered are the accuracy and type of pathology (biopsy or whole mount specimens), the optimal timing of the imaging following tracer injection and the most appropriate segmentation or thresholding level for defining the IPL.

Timing of PET Imaging

Kwee *et al.* analyzed the change in maximum SUV (SUV_{max}) in malignant and benign areas in prostate cancer using additional delayed scanning at 1 h [78]. SUV_{max} for malignant areas increased from the initial to delayed scan, whereas the mean SUV_{max} for benign areas decreased. The difference between areas marked as 'dominant malignant' and 'probably benign' was only statistically significant on delayed imaging with the mean malignant-to-benign ratio increasing from 1.4 on the initial images to 1.8 on the delayed images. The additional challenge of using delayed imaging with this modality, however, is that ^{18}F-choline is renally excreted with accumulation of radioactivity within the bladder, which can complicate image interpretation of the prostate base.

Methods for IPL delineation

A mean tumor-to-background ratio of approximately 2 has been identified in several studies as a method for IPL delineation [77–78,81] and was used by Pinkawa *et al.* for delineation of a clinically delivered boost volume [70]. In this study, definition of the IPL was based on a slightly increased tumor to background ratio of >2 in order to increase specificity, although this would

lead to a decreased sensitivity with smaller tumors excluded.

An autocontour method based on 60% of the maximum SUV (SUV_{60}) has been reported by several groups as having the best correlation with histopathology [79–80,86]. However, in these studies, the SUV_{60} was not found to be significantly better when compared with the other threshold contours [80,86]. It is also unclear as to which correlation indices are best to compare contours and whether the dice similarity co-efficient and Youden Index adequately assess the clinical significance of overlap. Therefore, although SUV_{60} had the highest correlation indices (as per dice similarity co-efficient and Youden Index), this requires prospective clinical validation before implementation.

As the percentage of SUV_{max} threshold increases, specificity increases but sensitivity decreases as used by Pinkawa *et al.* to increase the specificity for dose escalation [20].

Comparison of PET-CT with MRI for delineation accuracy

Chang *et al.* [86] used reference contours defined from prostatectomy pathology in 21 patients to compare the accuracy of manual contours from ^{11}C-choline PET-CT to manual contours using DW-MRI. They found that PET-CT had significantly better correlation to the reference contours compared with T2W/DW-MRI. A limitation of this study however, was that multiparametric sequences of DCE-MRI or MRS were not included, as per the Barentz recommendations [44] therefore the comparison did not include the optimal set of MRIs. This group also found, as previously shown [79,80], that the SUV_{60} had the best correlation to the reference contours and in fact performed significantly better compared with manual delineation by a radiologist using the PET-CT.

• Feasibility of boost delivery using specific tracers

There have been several studies investigating the feasibility of delivering a dose-escalated boost to the delineated IPL using various specific PET tracers. The clinical study by Pinkawa is outlined in **Table 2**, with planning studies summarized in **Table 3**.

^{11}C-choline PET-CT

Chang *et al.* [21] generated IMRT plans for eight patients using the contouring methods described above [80] to deliver two boost doses within a single plan. $PLAN_{78–90}$ delivered 78, 84 and 90 Gy and $PLAN_{72–90}$ delivered 72, 84 and 90 Gy to the whole prostate, $SUV_{60\%}$ and $SUV_{70\%}$, respectively. All plans were feasible while meeting dose constraints, with the rectal NTCP being non-significantly lower in the boost plan. Both boost plans had a significantly higher TCP for the PET defined volume (TCP_{PET}) and the prostatectomy specimen defined volume (TCP_{path}) compared with the standard plan where 78 Gy was planned to the whole prostate alone. However, the risk of de-escalating the non-DIL prostate was demonstrated for one of the patients where the TCP_{path} was lower in the $PLAN_{72–90}$ boost plan compared with $PLAN_{78}$. Overall, using the histopathology from prostatectomy, they were able to demonstrate increased population TCP with this method.

^{18}F-choline PET-CT

Kuang *et al.* concluded ^{18}F-choline PET-CT can be used to localize a boost volume for VMAT plans [25]. Using a similar method to Chang, RT plans had a two dose level boost of 105 Gy defined using the 70% of the SUV_{max} threshold (labeled $IDL_{SUV70\%}$) 'nested' inside a larger boost of 100 Gy defined by 60% of the SUV_{max} (labeled $IDL_{SUV60\%}$) with the aim of delivering the higher dose to the area of greater tumor specificity, while maintaining a dose of 79 Gy to the whole gland. They reported a higher TCP and a slightly lower rectal NTCP with the addition of a boost compared with a plan delivering 79 Gy alone to the prostate.

^{11}C-acetate PET-CT

^{11}C-acetate PET-CT was used by Seppala *et al.* to define the IPL using an absolute SUV of 2.0 in a planning study of 12 patients [22]. They similarly confirmed an improved TCP with IMRT plans delivering a SIB up to 90 Gy, without increasing the NTCP. However, a meta-analysis has concluded that ^{11}C-acetate should not be used for IPL localization due to poor sensitivity and specificity [76].

Just as for MRI planning, the higher TCP seen with dose escalation to the IPL is on the assumption that the imaging perfectly defines the target. Dose modeling has demonstrated that any additional benefit in TCP due to a SIB will be dependent on the sensitivity of imaging [87].

• Integration of imaging

With combined PET-CT images, the process of image registration is simpler compared with that

Table 3. Planning studies delivering a boost to a PET-computed tomography defined intraprostatic lesion.

Study (year)	Patients	Imaging techniques	Radiotherapy treatment	Findings	Ref.
Kuang *et al.* (2015)	n = 30	^{18}F-choline PET/CT Boost defined by 60 and 70% of SUV_{max} threshold (labeled $IDL_{SUV60\%}$ and $IDL_{SUV70\%}$, respectively)	VMAT Plan1: – Prostate + 3–6 mm 79 Gy/39 fractions Plan 2: Prostate + 3–6 mm 79 Gy/39 fractions $IDL_{SUV60\%}$ + 3–6 mm 100 Gy/39 fractions $IDL_{SUV70\%}$ + 3–6 mm 105 Gy/39 fractions	SIB feasible in all patients TCP significantly higher in boost plan Slightly lower rectal NTCP in boost plan	[25]
Seppala *et al.* (2009)	n = 12	11C-Acetate PET/CT Coregistration with planning scan SUV of 2.0 used for IPL delineation	Step and shoot IMRT Plan 1: – Prostate + 6 mm 77.9 Gy/41 fractions Plan 2: – Prostate + 6 mm 72.2 Gy/41 fractions – IPL + 6 mm 77.9–90 Gy/41 fractions	TCP increased for all boost plans Average dose of 82.1 Gy to IPL gave the highest probability of uncomplicated control	[22]
Chang *et al.* (2012)	n = 8	^{11}C-choline PET/CT Coregistration with planning scan Boost defined by 60 and 70% of SUV_{max} threshold (labeled $SUV_{60\%}$ and $SUV_{70\%}$, respectively)	Step and shoot IMRT Plan 1 (standard): – Prostate + 6 mm 78 Gy/39 fractions Plan 2 (boost plan): – Prostate + 6 mm 78 Gy/39 fractions – IPL ($SUV_{60\%}$) + 6 mm 84 Gy/39 fractions – IPL ($SUV_{70\%}$) + 6 mm 90 Gy/39 fractions Plan 3 (boost plan, de-escalation to prostate): – Prostate + 6 mm 72 Gy/39 fractions – IPL ($SUV_{60\%}$) + 6 mm 84 Gy/39 fractions – IPL ($SUV_{70\%}$) + 6 mm 90 Gy/39 fractions	SIB feasible in all patients TCP significantly higher for both boost plans compared with standard plan No significant difference in TCP comparing boost plans 2 and 3 No significant difference in rectal NTCP for all three plans	[21]

CT: Computed tomography; IMRT: Intensity-modulated radiation therapy; IPL: Intraprostatic lesion; NTCP: Normal tissue complication probability; SIB: Simultaneous integrated boost; TCP: Tumor control probability; VMAT: Volumetric-modulated arc therapy.

needed for CT-MRI fusion. However, the PET imaging component is acquired in several phases so there will still be some discrepancy with bladder and bowel filling and prostate position. PET-CT images are obtained without the distortion from ERC discussed previously and can be used for patients when MRI is contraindicated.

• Implementation of tumor dose escalation

The importance of accurate delivery with IGRT has already been discussed. The optimal technique for tumor segmentation and delineation with PET-CT is not yet clear. Further investigation and validation of proposed methods such as tumor to background and SUV_{60} is required with rigorous histopathological assessments and robust follow-up of outcomes. An expansion margin may be additionally required to cover the IPL adequately, similar to those described above for MRI [60–62].

Other imaging

An Indium-111-capromab pendetide scan (ProstaScint) uses a US FDA-approved monoclonal antibody to target upregulated PSMA receptors on prostate cancer cells. This tracer shows much promise in both the staging of *de novo* prostate cancer and in detecting recurrent disease. It has been used in a prospective trial to localize an IMRT planned boost (see **Table 2**) [23]. Results including biochemical control and toxicity were reported as favorable but further studies are needed to confirm the accuracy of localization. The study used a prostate/muscle ratio of signal intensity 3:1, but similar to the choline studies, the optimal threshold for contouring would need further investigation. There are conflicting results on the reliability of localizing prostate cancer [88,89]; however, research continues into other agents that target PSMA.

Future perspective

• Combining imaging modalities

A combination of imaging may be helpful, which would optimally use one modality with high sensitivity and a second with high specificity. Imaging techniques are constantly evolving and refinements in magnetic resonance or PET technique may increase our confidence in IPL delineation. Combining several modalities may further increase the fidelity of our contouring.

• Patient stratification

The studies discussed here have demonstrated the technical feasibility of dose escalation to an IPL but follow-up is required from randomized prospective trials to determine the benefit and effect on toxicity. There is significant heterogeneity in prostate cancers, which will complicate the decision as to whether a boost is required and the appropriate dose to be used. Tumors of the same size can have a different risk of relapse dependent on tumor biology and other pathological predictive factors [90]. Ideally, utilizing information from a combination of sources including imaging, pathology and biomarkers will allow stratification of patients to reflect the heterogeneity of tumors in the RT dose distribution. The use of hypoxic markers can be considered for dose escalation combined with prognostic markers for personalized RT.

In addition, imaging patients during an RT course for an early response assessment may predict those likely to fail biochemically, identifying patients who would benefit from further dose escalation. This escalation could then be given using adaptive RT to the existing plan or as a hypofractionated boost at the end of treatment. Further research is ongoing to search for such imaging biomarkers.

• Differential dose

Rather than having a single dose to the entire IPL, several planning studies discussed here have demonstrated how more than one boost dose can be delivered to the IPL using PET-CT [21,25]. This can maintain the maximum dose within the area of higher specificity, while having a fall off for the dose closer to organs at risk. The same approach could be used with mp-MRI, based on guidelines for the interpretation of MRI [44] or validated models which predict tumor presence [52]. This model by Groenendaal *et al.* for example suggests three levels; a GTV, a high-risk CTV and low-risk CTV (i.e., standard prostate dose) based on high, intermediate and low tumor probability, respectively. Alternatively a multiple dose level approach could be considered when imaging is used to identify a subvolume of more aggressive or radio-resistant disease within the IPL.

• MRI workflow

Magnetic resonance currently is the preferred modality for boost delineation. As there are some limitations of image registration with CT, an MRI only workflow would eliminate this systemic error. RT planning using MRI images alone has its own challenges, including geometric distortion and the lack of electron density information required for dose calculations, however, there are several methods described and being developed for this such as 'pseudo' or 'synthetic' CT [91,92].

IGRT improves accuracy of RT delivery, but most commonly used methods, such as CBCT and gold seeds do not take into account intrafraction movement, which contributes to the margin to be added and impacts the therapeutic ratio. Imaging during treatment further improves the accuracy of treatment, allowing gating or adaptation. Development of combinations of a linear accelerator or cobalt machine with on board MRI [93,94] may further improve inter- and intrafraction imaging. Furthermore, acquisition of magnetic resonance images during treatment may mean the boost regions could be directly visualized during beam delivery, increasing accuracy, calculation of delivered dose and facilitating adaptive planning strategies.

• What is the objective of imaging a dominant lesion?

Prostate cancer comprises a wide spectrum of disease, ranging from what could be considered a variant of normal ageing (organ confined Gleason 6 disease) to a life-limiting aggressive disease. Current stratification is inadequate to identify patients who would most benefit from dose-escalated local treatment. For those with low to low–intermediate-risk disease, conventional doses are sufficient to cure the vast majority of patients and a boost is unlikely to be required. For those with intermediate- or high-risk disease, a boost to the IPL may increase TCP with little or no effect on toxicity. In this case, the optimal imaging modality may not need to be sensitive to low-risk Gleason 6 disease, which will be adequately treated with conventional dose. A deficit of the current literature is the lack of understanding of the correlation between imaging findings with high-risk pathology only. In addition, mp-MRI and PET imaging have not been robustly compared, to help determine the optimal imaging modality for IPL delineation.

If the identification of the IPL is a prelude to de-escalating or even not treating the rest of the prostate gland, then there is still some way to go before we can be confident that our chosen imaging modality identifies all intraprostatic disease or indeed that which requires treatment.

Conclusion

Dose escalation to an MRI or PET-CT defined IPL is theoretically feasible, but further studies are needed to confirm the optimal imaging techniques which will faithfully represent the IPL in the RT planning process. Early clinical data suggest acceptable toxicity when DIL boosts are delivered with sophisticated RT techniques and state-of-the-art IGRT. Prospective clinical data are required to confirm which patient groups would benefit and to quantify any improvement in the therapeutic index.

Acknowledgements

The authors thank David Dearnaley and Nicholas van As for kindly providing images from the DELINEATE and SPARC studies. The authors gratefully acknowledge the support of the Royal Marsden Hospital and the Institute for Cancer Research work in partnership as a National Institute for Health Research (UK) Biomedical Research Centre.

Financial & competing interests disclosure

The authors have no relevant affiliations or financial involvement with any organization or entity with a financial interest in or financial conflict with the subject matter or materials discussed in the manuscript. This includes employment, consultancies, honoraria, stock ownership or options, expert testimony, grants or patents received or pending, or royalties.

No writing assistance was utilized in the production of this manuscript.

EXECUTIVE SUMMARY

Rationale behind intraprostatic boost

- Dose escalation to the whole prostate improves biochemical control but at the expense of increased toxicity.
- Local recurrence occurs at the site of the primary tumor, therefore a boost to the intraprostatic lesion (IPL) may improve the therapeutic ratio.

MRI for IPL delineation

- Although multiparametric MRI improves the accuracy of tumor detection, there are a number of limitations including a mismatch between different MRI techniques, false-positive findings and the effect of androgen deprivation therapy on imaging.
- The interpretation of magnetic resonance images is operator and training dependent and prone to interobserver variation, even in the presence of published scoring systems.
- Histopathological correlation studies indicate that IPL volumes delineated by MRI tend to underestimate the true tumor volume, with studies suggesting a margin of 5–9 mm to cover the 'undercall.'
- Clinical and planning studies have shown that a boost to an IPL is feasible, with acceptable levels of toxicity and the potential to improve the tumor control probability.
- The IPL must be accurately transferred through the radiotherapy planning process by using the fusion of images, and treatment must be delivered using high-quality image-guided radiotherapy.

PET-computed tomography for IPL delineation

- PET-computed tomography can be used for tumor delineation but sensitivity and specificity is variable, with fewer studies confirming histopathological correlation.
- Image interpretation is variable; IPL delineation can be manual or automated, with methods used to define the IPL based on a percentage of the SUV_{max} or a tumor to background ratio.
- The limited clinical and planning studies indicate that a boost is feasible to a PET-computed tomography defined IPL, with the possibility of using differing SUV thresholds to varying dose levels.
- The IPL must be faithfully represented throughout the planning process and treatment delivered accurately with image-guided radiotherapy.

Future perspective

- Data are needed from prospective trials to confirm the benefits of delivering a boost to the IPL and to confirm the best imaging, contouring methods, boost dose and radiotherapy techniques.
- A combination of imaging, pathology and biomarkers could be used to stratify patients and individualize treatment to identify those patients who will benefit from focal dose escalation.

References

Papers of special note have been highlighted as:
• of interest

1 Pollack A, Zagars GK, Starkschall G *et al.* Prostate cancer radiation dose response: results of the M. D. Anderson Phase III randomized trial. *Int. J. Radiat. Oncol. Biol. Phys.* 53(5), 1097–1105 (2002).

2 Peeters STH, Heemsbergen WD, Koper PCM *et al.* Dose-response in radiotherapy for localized prostate cancer: results of the dutch multicenter randomized Phase III trial comparing 68 Gy of radiotherapy with 78 Gy. *J. Clin. Oncol.* 24(13), 1990–1996 (2006).

3 Viani GA, Stefano EJ, Afonso SL. Higher-than-conventional radiation doses in localized prostate cancer treatment: a meta-analysis of randomized, controlled trials. *Int. J. Radiat. Oncol. Biol. Phys.* 74(5), 1405–1418 (2009).

4 Kuban DA, Tucker SL, Dong L *et al.* Long-term results of the M. D. Anderson randomized dose-escalation trial for prostate cancer. *Int. J. Radiat. Oncol. Biol. Phys.* 70(1), 67–74 (2008).

5 Zietman AL, Desilvio ML, Slater JD *et al.* Comparison of conventional-dose vs high-dose conformal radiation therapy in clinically localized adenocarcinoma of the prostate: a randomized controlled trial. *JAMA* 294(10), 1233–1239 (2005).

6 Dearnaley DP, Jovic G, Syndikus I *et al.* Escalated-dose versus control-dose conformal radiotherapy for prostate cancer: long-term results from the MRC RT01 randomised controlled trial. *Lancet Oncol.* 15(4), 464–473 (2014).

• **Long-term follow-up confirming the benefit of dose escalation.**

7 Peeters ST, Heemsbergen WD, Van Putten WL *et al.* Acute and late complications after radiotherapy for prostate cancer: results of a multicenter randomized trial comparing 68 Gy to 78 Gy. *Int. J. Radiat. Oncol. Biol. Phys.* 61(4), 1019–1034 (2005).

8 Cellini N, Morganti AG, Mattiucci GC *et al.* Analysis of intraprostatic failures in patients treated with hormonal therapy and radiotherapy: implications for conformal therapy planning. *Int. J. Radiat. Oncol. Biol. Phys.* 53(3), 595–599 (2002).

9 Pucar D, Hricak H, Shukla-Dave A *et al.* Clinically significant prostate cancer local recurrence after radiation therapy occurs at the site of primary tumor: magnetic resonance imaging and step-section pathology evidence. *Int. J. Radiat. Oncol. Biol. Phys.* 69(1), 62–69 (2007).

10 Arrayeh E, Westphalen AC, Kurhanewicz J *et al.* Does local recurrence of prostate cancer after radiation therapy occur at the site of primary tumor? Results of a longitudinal MRI and MRSI study. *Int. J. Radiat. Oncol. Biol. Phys.* 82(5), e787–e793 (2012).

11 Kuban DA, Levy LB, Cheung MR *et al.* Long-term failure patterns and survival in a randomized dose-escalation trial for prostate cancer. Who dies of disease? *Int. J. Radiat. Oncol. Biol. Phys.* 79(5), 1310–1317 (2011).

12 Nutting CM, Corbishley CM, Sanchez-Nieto B, Cosgrove VP, Webb S, Dearnaley DP. Potential improvements in the therapeutic ratio of prostate cancer irradiation: dose escalation of pathologically identified tumour nodules using intensity modulated radiotherapy. *Br. J. Radiol.* 75(890), 151–161 (2002).

• **Early planning study showing an improved therapeutic ratio with intraprostatic boost.**

13 Villers A, Mcneal JE, Freiha FS, Stamey TA. Multiple cancers in the prostate. Morphologic features of clinically recognized versus incidental tumors. *Cancer* 70(9), 2313–2318 (1992).

14 Singh AK, Guion P, Sears-Crouse N *et al.* Simultaneous integrated boost of biopsy proven, MRI defined dominant intra-prostatic lesions to 95 Gray with IMRT: early results of a Phase I NCI study. *Radiat. Oncol.* 2, 36–36 (2007).

15 Noguchi M, Stamey TA, Mcneal JE, Nolley R. Prognostic factors for multifocal prostate cancer in radical prostatectomy specimens: lack of significance of secondary cancers. *J. Urol.* 170(2, Part 1), 459–463 (2003).

16 Selvadurai ED, Singhera M, Thomas K *et al.* Medium-term outcomes of active surveillance for localised prostate cancer. *Eur. Urol.* 64(6), 981–987 (2013).

17 Klotz L, Vesprini D, Sethukavalan P *et al.* Long-term follow-up of a large active surveillance cohort of patients with prostate cancer. *J. Clin. Oncol.* 33(3), 272–277 (2015).

18 Ahmed HU, Hu Y, Carter T *et al.* Characterizing clinically significant prostate cancer using template prostate mapping biopsy. *J. Urol.* 186(2), 458–464 (2011).

19 Meerleer GD, Villeirs G, Bral S *et al.* The magnetic resonance detected intraprostatic lesion in prostate cancer: planning and delivery of intensity-modulated radiotherapy. *Radiother. Oncol.* 75(3), 325–333 (2005).

20 Pinkawa M, Attieh C, Piroth MD *et al.* Dose-escalation using intensity-modulated radiotherapy for prostate cancer – evaluation of the dose distribution with and without 18F-choline PET-CT detected simultaneous integrated boost. *Radiother. Oncol.* 93(2), 213–219 (2009).

21 Chang JH, Lim Joon D, Lee ST *et al.* Intensity modulated radiation therapy dose painting for localized prostate cancer using 11C-choline positron emission tomography scans. *Int. J. Radiat. Oncol. Biol. Phys.* 83(5), e691–e696 (2012).

22 Seppälä J, Seppänen M, Arponen E, Lindholm P, Minn H. Carbon-11 acetate PET/CT based dose escalated IMRT in prostate cancer. *Radiother. Oncol.* 93(2), 234–240 (2009).

23 Wong WW, Schild SE, Vora SA *et al.* Image-guided radiotherapy for prostate cancer: a prospective trial of concomitant boost using indium-111-capromab pendetide (ProstaScint) imaging. *Int. J. Radiat. Oncol. Biol. Phys.* 81(4), e423–e429 (2011).

24 Ost P, Speleers B, De Meerleer G *et al.* Volumetric arc therapy and intensity-modulated radiotherapy for primary prostate radiotherapy with simultaneous integrated boost to intraprostatic lesion with 6 and 18 MV: a planning comparison study. *Int. J. Radiat. Oncol. Biol. Phys.* 79(3), 920–926 (2011).

25 Kuang Y, Wu L, Hirata E, Miyazaki K, Sato M, Kwee SA. Volumetric modulated arc therapy planning for primary prostate cancer with selective intraprostatic boost determined by 18F-choline PET/CT. *Int. J. Radiat. Oncol. Biol. Phys.* 91(5), 1017–1025 (2015).

26 Murray LJ, Lilley J, Thompson CM *et al.* Prostate stereotactic ablative radiation therapy using volumetric modulated arc therapy to dominant intraprostatic lesions. *Int. J. Radiat. Oncol. Biol. Phys.* 89(2), 406–415 (2014).

27 Miralbell R, Mollà M, Rouzaud M *et al.* Hypofractionated boost to the dominant tumor region with intensity modulated stereotactic radiotherapy for prostate cancer: a sequential dose escalation pilot study. *Int. J. Radiat. Oncol. Biol. Phys.* 78(1), 50–57 (2010).

• **Demonstrates feasibility of intraprostatic lesion (IPL) boost with 5 years follow-up and disease-free survival.**

28 Tree A, Jones C, Sohaib A, Khoo V, Van As N. Prostate stereotactic body radiotherapy with simultaneous integrated boost: which is the best planning method? *Radiat. Oncol.* 8, 228–228 (2013).

29 Dearnaley D, Syndikus I, Mossop H *et al.* Comparison of hypofractionated high-dose intensity modulated radiotherapy schedules for prostate cancer: results from the Phase III randomized CHHiP trial (CRUK/06/016). *J. Clin. Oncol.* 34(Suppl. 2), Abstract 2 (2016).

30 Khoo VS, Padhani AR, Tanner SF, Finnigan DJ, Leach MO, Dearnaley DP. Comparison of MRI with CT for the radiotherapy planning of prostate cancer: a feasibility study. *Br. J. Radiol.* 72(858), 590–597 (1999).

31 Villeirs GM, Vaerenbergh K, Vakaet L *et al.* Interobserver delineation variation using ct versus combined ct + MRI in intensity-modulated radiotherapy for prostate cancer. *Strahlenther. Onkol.* 181(7), 424–430 (2005).

32 Debois M, Oyen R, Maes F *et al.* The contribution of magnetic resonance imaging to the three-dimensional treatment planning of localized prostate cancer. *Int. J. Radiat. Oncol. Biol. Phys.* 45(4), 857–865 (1999).

33 Rasch C, Barillot I, Remeijer P, Touw A, Van Herk M, Lebesque JV. Definition of the prostate in CT and MRI: a multi-observer study. *Int. J. Radiat. Oncol. Biol. Phys.* 43(1), 57–66 (1999).

34 Fütterer JJ, Heijmink SWTPJ, Scheenen TWJ *et al.* Prostate cancer localization with dynamic contrast-enhanced MR imaging and proton MR spectroscopic imaging. *Radiology* 241(2), 449–458 (2006).

35 Haider MA, Van Der Kwast TH, Tanguay J *et al.* Combined T2-weighted and diffusion-weighted MRI for localization of prostate cancer. *AJR Am. J. Roentgenol.* 189(2), 323–328 (2007).

36 Scheidler J, Hricak H, Vigneron DB *et al.* Prostate cancer: localization with three-dimensional proton MR spectroscopic imaging – clinicopathologic study. *Radiology* 213(2), 473–480 (1999).

37 Isebaert S, Van Den Bergh L, Haustermans K *et al.* Multiparametric MRI for prostate cancer localization in correlation to whole-mount histopathology. *J. Magn. Reson. Imaging* 37(6), 1392–1401 (2013).

38 Wu L-M, Xu J-R, Ye Y-Q, Lu Q, Hu J-N. The clinical value of diffusion-weighted imaging in combination with T2-weighted imaging in diagnosing prostate carcinoma: a systematic review and meta-analysis. *AJR Am. J. Roentgenol.* 199(1), 103–110 (2012).

39 Turkbey B, Pinto PA, Mani H *et al.* Prostate cancer: value of multiparametric mr imaging at 3 T for detection – histopathologifc correlation. *Radiology* 255(1), 89–99 (2010).

40 Desouza NM, Riches SF, Van As NJ *et al.* Diffusion-weighted magnetic resonance imaging: a potential non-invasive marker of tumour aggressiveness in localized prostate cancer. *Clin. Radiol.* 63(7), 774–782 (2008).

41 Henderson DR, De Souza NM, Thomas K *et al.* Nine-year follow-up for a study of diffusion-weighted magnetic resonance imaging in a prospective prostate cancer active surveillance cohort. *Eur. Urol.* doi:10.1016/j.eururo.10.010 (2016) (Epub ahead of print).

42 De Rooij M, Hamoen EHJ, Fütterer JJ, Barentsz JO, Rovers MM. Accuracy of multiparametric MRI for prostate cancer detection: a meta-analysis. *AJR Am. J. Roentgenol.* 202(2), 343–351 (2014).

43 Riches SF, Payne GS, Morgan VA *et al.* MRI in the detection of prostate cancer: combined apparent diffusion coefficient, metabolite ratio, and vascular parameters. *AJR Am. J. Roentgenol.* 193(6), 1583–1591 (2009).

44 Barentsz JO, Richenberg J, Clements R *et al.* ESUR prostate MR guidelines 2012. *Eur. Radiol.* 22(4), 746–757 (2012).

- **Guidelines discussing the multiparametric MRI sequences required and scoring techniques.**

45 Fütterer JJ, Engelbrecht MR, Jager GJ *et al.* Prostate cancer: comparison of local staging accuracy of pelvic phased-array coil alone versus integrated endorectal-pelvic phased-array coils. *Eur. Radiol.* 17(4), 1055–1065 (2006).

46 Coakley FV, Kurhanewicz J, Lu Y *et al.* Prostate cancer tumor volume: measurement with endorectal MR and MR spectroscopic imaging. *Radiology* 223(1), 91–97 (2002).

47 Rosenkrantz AB, Mendrinos S, Babb JS, Taneja SS. Prostate cancer foci detected on multiparametric magnetic resonance imaging are histologically distinct from those not detected. *J. Urol.* 187(6), 2032–2038 (2012).

48 Langer DL, Kwast THVD, Evans AJ *et al.* Intermixed normal tissue within prostate cancer: effect on mr imaging measurements of apparent diffusion coefficient and T2 – sparse versus dense cancers. *Radiology* 249(3), 900–908 (2008).

49 Steenbergen P, Haustermans K, Lerut E *et al.* Prostate tumor delineation using multiparametric magnetic resonance imaging: inter-observer variability and pathology validation. *Radiother. Oncol.* 115(2), 186–190 (2015).

50 Weinreb JC, Barentsz JO, Choyke PL *et al.* PI-RADS Prostate Imaging – Reporting and Data System: 2015, Version 2. *Eur. Urol.* 69(1), 16–40 (2016).

51 Groenendaal G, Van Den Berg CaT, Korporaal JG *et al.* Simultaneous MRI diffusion and perfusion imaging for tumor delineation in prostate cancer patients. *Radiother. Oncol.* 95(2), 185–190 (2010).

52 Groenendaal G, Borren A, Moman MR *et al.* Pathologic validation of a model based on diffusion-weighted imaging and dynamic contrast-enhanced magnetic resonance imaging for tumor delineation in the prostate peripheral zone. *Int. J. Radiat. Oncol. Biol. Phys.* 82(3), e537–e544 (2012).

- **Statistical voxel-based model for prediction of tumor.**

53 Viswanath SE, Bloch NB, Chappelow JC *et al.* Central gland and peripheral zone prostate tumors have significantly different quantitative imaging signatures on 3 Tesla endorectal, *in vivo* T2-weighted magnetic resonance imagery. *J. Magn. Reson. Imaging* 36(1), 213–224 (2012).

54 Vos PC, Barentsz JO, Karssemeijer N, Huisman HJ. Automatic computer-aided detection of prostate cancer based on multiparametric magnetic resonance image analysis. *Phys. Med. Biol.* 57(6), 1527 (2012).

55 Dinh CV, Steenbergen P, Ghobadi G *et al.* Magnetic resonance imaging for prostate cancer radiotherapy. *Phys. Med.* 32(3), 446–451 (2016).

56 Groenendaal G, Van Vulpen M, Pereboom SR *et al.* The effect of hormonal treatment on conspicuity of prostate cancer: implications for focal boosting radiotherapy. *Radiother. Oncol.* 103(2), 233–238 (2012).

57 Turkbey B, Mani H, Shah V *et al.* Multiparametric 3T prostate magnetic resonance imaging to detect cancer: histopathological correlation using prostatectomy specimens processed in customized magnetic resonance imaging based molds. *J. Urol.* 186(5), 1818–1824 (2011).

58 Turkbey B, Mani H, Aras O *et al.* Correlation of magnetic resonance imaging tumor volume with histopathology. *J. Urol.* 188(4), 1157–1163 (2012).

59 Le Nobin J, Orczyk C, Deng F-M *et al.* Prostate tumour volumes: evaluation of the agreement between magnetic resonance imaging and histology using novel co-registration software. *BJU Int.* 114(0), E105–E112 (2014).

60 Groenendaal G, Moman MR, Korporaal JG *et al.* Validation of functional imaging with pathology for tumor delineation in the prostate. *Radiother. Oncol.* 94(2), 145–150 (2010).

- **Comparison of tumor delineation on MRI with histopathology findings.**

61 Anwar M, Westphalen AC, Jung AJ *et al.* Role of endorectal MR imaging and MR spectroscopic imaging in defining treatable intraprostatic tumor foci in prostate cancer: quantitative analysis of imaging contour

compared with whole-mount histopathology. *Radiother. Oncol.* 110(2), 303–308 (2014).

- **Considers the discrepancy between MRI delineation and pathology and margins that could be used.**

62 Le Nobin J, Rosenkrantz AB, Villers A *et al.* Image guided focal therapy of magnetic resonance imaging visible prostate cancer: defining a 3-dimensional treatment margin based on magnetic resonance imaging-histology co-registration analysis. *J. Urol.* 194(2), 364–370 (2015).

63 Van Lin ENJT, Fütterer JJ, Heijmink SWTPJ *et al.* IMRT boost dose planning on dominant intraprostatic lesions: gold marker-based three-dimensional fusion of CT with dynamic contrast-enhanced and 1H-spectroscopic MRI. *Int. J. Radiat. Oncol. Biol. Phys.* 65(1), 291–303 (2006).

64 Housri N, Ning H, Ondos J *et al.* Parameters favorable to intraprostatic radiation dose escalation in men with localised prostate cancer. *Int. J. Radiat. Oncol. Biol. Phys.* 80(2), 614–620 (2011).

65 Riches SF, Payne GS, Desouza NM *et al.* Effect on therapeutic ratio of planning a boosted radiotherapy dose to the dominant intraprostatic tumour lesion within the prostate based on multifunctional MR parameters. *Br. J. Radiol.* 87(1037), 20130813 (2014).

66 Feng Y, Welsh D, Mcdonald K *et al.* Identifying the dominant prostate cancer focal lesion using image analysis and planning of a simultaneous integrated stereotactic boost. *Acta Oncol.* 54(9), 1543–1550 (2015).

67 Fonteyne V, Villeirs G, Speleers B *et al.* Intensity-modulated radiotherapy as primary therapy for prostate cancer: report on acute toxicity after dose escalation with simultaneous integrated boost to intraprostatic lesion. *Int. J. Radiat. Oncol. Biol. Phys.* 72(3), 799–807 (2008).

68 Ippolito E, Mantini G, Morganti AG *et al.* Intensity-modulated radiotherapy with simultaneous integrated boost to dominant intraprostatic lesion: preliminary report on toxicity. *Am. J. Clin. Oncol.* 35(2), 158–162 (2012).

69 Aluwini S, Van Rooij P, Hoogeman M, Kirkels W, Kolkman-Deurloo I-K, Bangma C. Stereotactic body radiotherapy with a focal boost to the MRI-visible tumor as monotherapy for low- and intermediate-risk prostate cancer: early results. *Radiat. Oncol.* 8, 84–84 (2013).

70 Pinkawa M, Piroth MD, Holy R *et al.* Dose-escalation using intensity-modulated radiotherapy for prostate cancer – evaluation of quality of life with and without ^{18}F-choline PET-CT detected simultaneous integrated boost. *Radiat. Oncol.* 7 14–14 (2012).

71 Pinkawa M, Holy R, Piroth MD *et al.* Intensity-modulated radiotherapy for prostate cancer implementing molecular imaging with ^{18}F-choline PET-CT to define a simultaneous integrated boost. *Strahlenther. Onkol.* 186(11), 600–606 (2010).

72 Huisman HJ, Fütterer JJ, Lin ENJTV *et al.* Prostate cancer: precision of integrating functional MR imaging with radiation therapy treatment by using fiducial gold markers. *Radiology* 236(1), 311–317 (2005).

73 Thornqvist S, Petersen JB, Hoyer M, Bentzen LN, Muren LP. Propagation of target and organ at risk contours in radiotherapy of prostate cancer using deformable image registration. *Acta Oncol.* 49(7), 1023–1032 (2010).

74 Parker CC, Damyanovich A, Haycocks T, Haider M, Bayley A, Catton CN. Magnetic resonance imaging in the radiation treatment planning of localized prostate cancer using intra-prostatic fiducial markers for computed tomography co-registration. *Radiother. Oncol.* 66(2), 217–224 (2003).

75 Lips IM, Van Der Heide UA, Haustermans K *et al.* Single blind randomized Phase III trial to investigate the benefit of a focal lesion ablative microboost in prostate cancer (FLAME-trial): study protocol for a randomized controlled trial. *Trials* 12, 255–255 (2011).

- **Trial protocol for a prospective study delivering a simultaneous integrated boost.**

76 Mohsen B, Giorgio T, Rasoul ZS *et al.* Application of 11C-acetate positron-emission tomography (PET) imaging in prostate cancer: systematic review and meta-analysis of the literature. *BJU Int.* 112(8), 1062–1072 (2013).

77 Farsad M, Schiavina R, Castellucci P *et al.* Detection and localization of prostate cancer: correlation of 11C-choline PET/CT with histopathologic step-section analysis. *J. Nucl. Med.* 46(10), 1642–1649 (2005).

78 Kwee SA, Wei H, Sesterhenn I, Yun D, Coel MN. Localization of primary prostate cancer with dual-phase ^{18}F-fluorocholine PET. *J. Nucl. Med.* 47(2), 262–269 (2006).

79 Park H, Meyer CR, Wood D *et al.* Validation of automatic target volume definition as demonstrated for ^{11}C-Choline PET/CT of human prostate cancer using multi-modality fusion techniques. *Acad. Radiol.* 17(5), 614–623 (2010).

80 Chang JH, Joon DL, Lee ST *et al.* Histopathological correlation of ^{11}C-choline PET scans for target volume definition in radical prostate radiotherapy. *Radiother. Oncol.* 99(2), 187–192 (2011).

81 Reske SN, Blumstein NM, Neumaier B *et al.* Imaging prostate cancer with ^{11}C-Choline PET/CT. *J. Nucl. Med.* 47(8), 1249–1254 (2006).

82 Picchio M, Giovannini E, Crivellaro C, Gianolli L, Muzio ND, Messa C. Clinical evidence on PET/CT for radiation therapy planning in prostate cancer. *Radiother. Oncol.* 96(3), 347–350 (2010).

83 Van Den Bergh L, Koole M, Isebaert S *et al.* Is There an additional value of ^{11}C-choline PET-CT to T2-weighted MRI images in the localization of intraprostatic tumor nodules? *Int. J. Radiat. Oncol. Biol. Phys.* 83(5), 1486–1492 (2012).

84 Zaidi H, El Naqa I. PET-guided delineation of radiation therapy treatment volumes: a survey of image segmentation techniques. *Eur. J. Nucl. Med. Mol. Imaging* 37(11), 2165–2187 (2010).

85 Soret M, Bacharach SL, Buvat I. Partial-volume effect in PET tumor imaging. *J. Nucl. Med.* 48(6), 932–945 (2007).

86 Chang JH, Lim Joon D, Davis ID *et al.* Comparison of [^{11}C]choline positron emission tomography with T2- and diffusion-weighted magnetic resonance imaging for delineating malignant intraprostatic lesions. *Int. J. Radiat. Oncol. Biol. Phys.* 92(2), 438–445 (2015).

87 Niyazi M, Bartenstein P, Belka C, Ganswindt U. Choline PET based dose-painting in prostate cancer – modelling of dose effects. *Radiat. Oncol.* 5, 23–23 (2010).

88 Ellis RJ, Kim EY, Conant R *et al.* Radioimmunoguided imaging of prostate cancer foci with histopathological correlation. *Int. J. Radiat. Oncol. Biol. Phys.* 49(5), 1281–1286 (2001).

89 Mouraviev V, Madden JF, Broadwater G *et al.* Use of ^{111}In-capromab pendetide immunoscintigraphy to image localized prostate cancer foci within the prostate gland. *J. Urol.* 182(3), 938–948 (2009).

90 Chopra S, Toi A, Taback N *et al.* Pathological predictors for site of local recurrence after radiotherapy for prostate cancer. *Int. J. Radiat. Oncol. Biol. Phys.* 82(3), e441–e448 (2012).

91 Jonsson JH, Karlsson MG, Karlsson M, Nyholm T. Treatment planning using MRI data: an analysis of the dose calculation accuracy for different treatment regions. *Radiat. Oncol.* 5, 62–62 (2010).

92 Dowling JA, Lambert J, Parker J *et al.* An Atlas-based electron density mapping method for magnetic resonance imaging (MRI)-alone treatment planning and adaptive MRI-based prostate radiation therapy. *Int. J. Radiat. Oncol. Biol. Phys.* 83(1), e5–e11 (2012).

93 Lagendijk JJW, Raaymakers BW, Raaijmakers AJE *et al.* MRI/linac integration. *Radiother. Oncol.* 86(1), 25–29 (2008).

94 Mutic S, Dempsey JF. The ViewRay System: magnetic resonance-guided and controlled radiotherapy. *Sem. Radiat. Oncol.* 24(3), 196–199 (2014).

IOP Publishing Phys. Med. Biol. 64 (2019) 07NT02 (10pp) https://doi.org/10.1088/1361-6560/ab09a6

Physics in Medicine & Biology

IPEM Institute of Physics and Engineering in Medicine

NOTE

Fiducial marker based intra-fraction motion assessment on cine-MR for MR-linac treatment of prostate cancer

D M de Muinck Keizer[1,4,5], A U Pathmanathan[2,4], A Andreychenko[1,3], L G W Kerkmeijer[1], J R N van der Voort van Zyp[1], A C Tree[2], C A T van den Berg[1] and J C J de Boer[1]

[1] Department of Radiotherapy, University Medical Center Utrecht, PO Box 85500, 3508 GA, Utrecht, The Netherlands
[2] Royal Marsden Hospital NHS Foundation Trust and Institute of Cancer Research, Fulham Road, SW3 6JJ, London, United Kingdom
[3] ITMO University, 49 Kronverksky Pr., St. Petersburg, 197101, Russia
[4] Joint first author.
[5] Author to whom any correspondence should be addressed.

E-mail: D.M.deMuinckKeizer@umcutrecht.nl

RECEIVED 11 October 2018

REVISED 4 February 2019

ACCEPTED FOR PUBLICATION 22 February 2019

PUBLISHED 4 April 2019

Keywords: prostate cancer, intrafraction motion, hypofractionation, fiducial marker, tracking, cine-MR

Supplementary material for this article is available online

Abstract

We have developed a method to determine intrafraction motion of the prostate through automatic fiducial marker (FM) tracking on 3D cine-magnetic resonance (MR) images with high spatial and temporal resolution. Twenty-nine patients undergoing prostate stereotactic body radiotherapy (SBRT), with four implanted cylindrical gold FMs, had cine-MR imaging sessions after each of five weekly fractions. Each cine-MR examination consisted of 55 sequentially obtained 3D datasets ('dynamics'), acquired over a 11 s period, covering a total of 10 min. FM locations in the first dynamic were manually identified by a clinician, FM centers in subsequent dynamics were automatically determined. Center of mass (COM) translations and rotations were determined by calculating the rigid transformations between the FM template of the first and subsequent dynamics. The algorithm was applied to 7315 dynamics over 133 scans of 29 patients and the obtained results were validated by comparing the COM locations recorded by the clinician at the halfway-dynamic (after 5 min) and end dynamic (after 10 min). The mean COM translations at 10 min were *X*: 0.0 $\pm$ 0.8 mm, *Y*: 1.0 $\pm$ 1.9 mm and *Z*: 0.9 $\pm$ 2.0 mm. The mean rotation results at 10 min were *X*: 0.1 $\pm$ 3.9°, *Y*: 0.0 $\pm$ 1.3° and *Z*: 0.1 $\pm$ 1.2°. The tracking success rate was 97.7% with a mean 3D COM error of 1.1 mm. We have developed a robust, fast and accurate FM tracking algorithm for cine-MR data, which allows for continuous monitoring of prostate motion during MR-guided radiotherapy (MRgRT). These results will be used to validate automatic prostate tracking based on soft-tissue contrast.

1. Introduction

In present-day external beam radiotherapy (RT) for prostate cancer, accurate targeting is often based on kilovoltage (kV) and megavoltage (MV) imaging of implanted gold fiducial markers (FM). The implantation of FM prior to prostate RT allows accurate patient set-up verification prior to each fraction of the treatment (van der Heide *et al* 2007, Mutanga *et al* 2012). In addition, co-registration of planning computed tomography (CT) and magnetic resonance imaging (MRI) images is more accurate with the use of FM (Parker *et al* 2003). However although this image-guided RT (IGRT) permits margin reduction (Litzenberg *et al* 2006, Beltran *et al* 2008), online images acquired prior to the RT fraction do not adjust for intrafraction movement of the prostate, which can be significant and is dependent on patient movement, bladder and rectal filling (Padhani *et al* 1999, Mah *et al* 2002, Ghilezan *et al* 2005, Ogino *et al* 2011).

MRI provides several benefits during the RT planning process including increased soft tissue contrast for delineation of the prostate (Khoo *et al* 1999, Rasch *et al* 1999, Villeirs *et al* 2005), seminal vesicles and organs at

risk (OAR) without the use of additional radiation exposure. MR-guided systems (Raaymakers *et al* 2009, Mutic and Dempsey 2014) harness the advantages of MRI for intrafractional imaging with the potential for tumour tracking, gated treatment and adaptive radiotherapy (Pathmanathan *et al* 2018). For these to occur, a realistic assessment of prostate motion is required to determine the planning margins added to the prostate clinical target volume (CTV). Specifically, techniques for fast adaptation to the anatomy of the moment based on continuous MR imaging (Kontaxis *et al* 2017a), require reliable motion information to be automatically extracted from the image stream.

Inter- and intrafractional prostate motion has been extensively studied (Langen and Jones 2001, McPartlin *et al* 2016). In particular, the use of cine-MR images can be used to reflect the prostate motion during a treatment fraction with previous studies using defined points of interest (Ghilezan *et al* 2005, Nichol *et al* 2010, Ogino *et al* 2011, Terashima *et al* 2013), the prostate boundaries (Mah *et al* 2002) or measurement of movement compared to a baseline contour (Padhani *et al* 1999). These provide data on drift of the prostate as well as transient movements of varying magnitude, however do not consider the entire prostate volume. Continuous motion data during radiotherapy treatment itself is provided by tracking electromagnetic markers (Langen *et al* 2008) and reporting the frequency and magnitude of displacements using the geometric center of the markers.

FM have become the standard for accurate registration of the prostate in kV imaging. We therefore first focus on FM tracking in MR images to obtain results that can be compared to the literature. FM's create a high signal on CT images (Meyer *et al* 2010) and are therefore easily identified, however, specific sequences are required to visualize FMs properly on MR images such as spin echo, gradient echo and balanced steady-state free precession (bSSFP) sequences imaging (Fernandes *et al* 2017, Maspero *et al* 2018). More recent work has focused on automatic FM detection using these sequences (Schieda *et al* 2015, Ghose *et al* 2016, Fernandes *et al* 2017, Gustafsson *et al* 2017, Maspero *et al* 2017). There are a number of methods including template matching to detect FM (Maspero *et al* 2017, Zijlstra *et al* 2017), feature extraction from MR intensities (Fernandes *et al* 2017, Gustafsson *et al* 2017) or even a combination of approaches (Ghose *et al* 2016).

Here we use an extensive dataset of three dimensional (3D) bSSFP cine-MR scans with sufficient temporal resolution to assess the accuracy of an automatic fiducial detection method. We assess the detailed characteristics of prostate motion, including rotations, over the ten minute period of the cine-MR, reflecting the duration of a RT fraction. We have developed the automatic fiducial detection method to obtain ground truth intrafraction motion in preparation of soft-tissue MR-guided RT of the prostate. To our knowledge, this is the first data using automatic FM tracking on cine-MR to assess intrafraction motion. The obtained results will be used in the development of a FM-free soft-tissue tracking method of the prostate.

2. Materials and methods

2.1. Patient selection

Twenty-nine patients undergoing prostate SBRT within the HypoFLAME trial (NCT02853110) with four implanted cylindrical gold FM (5 mm length, 1 mm diameter), had repeated cine-MR imaging sessions at the University Medical Center Utrecht after each of five weekly fractions. During these imaging sessions, patient set-up was similar to that during prostate RT. Apart from drinking 400 ml water prior to scanning or treatment, no specific rectal or bladder preparations were applied.

2.2. Image acquisition

Each cine-MR examination consisted of 55 sequentially obtained 3D datasets ('dynamics') that were acquired with a 3D bSSFP sequence using fat suppression (repetition time (TR) = 4 ms, echo time (TE) = 1.98 ms, flipangle = 30°, B_0 = 3 T) that provided good anatomical as well as FM contrast. Each dynamic was acquired over a 11 s period, with a voxel size of $0.96 \times 0.96 \times 2$ mm^3 and a $384 \times 384 \times 120$ mm^3 field of view. Each cine-MR exam therefore covered a 10 min period.

2.3. Manual FM identification

The locations of the FM in the first dynamic were manually determined by a clinician, who marked the top and bottom location of each FM according to the method described by Maspero *et al* (2018), from which the FM center was obtained. The FM template containing the 3D-positions of all markers on the first dynamic was then stored. An example of manually segmented markers on cine-MR images is provided in figure 1. The marking of the FM top and bottom was performed without reference to the CT of the patient. The found marker template of the FM by the clinician was compared with available FM templates obtained from CT scans of the patients. The FM centers in subsequent dynamics were automatically determined using in-house developed Python code as described in the next section.

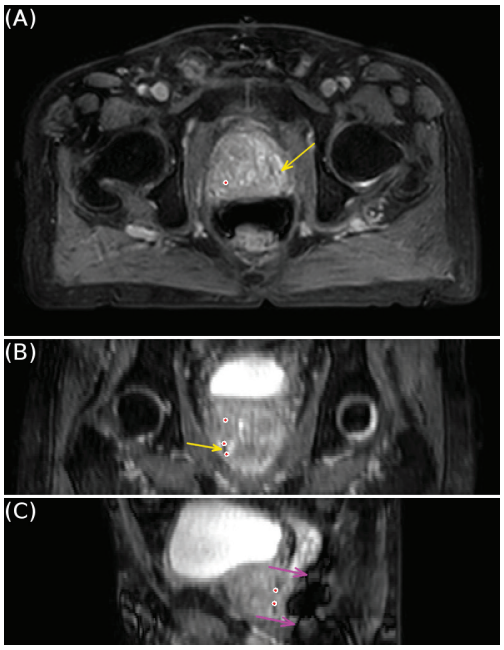

Figure 1. Overview of cine-MR images with manually segmented markers by the clinician. Images A, B and C show the respectively transversal, coronal and sagittal slices of a patient. Manually segmented marker top or bottom locations are visualized as the dots. The (yellow) arrows in image A and B show the effect of a signal void caused by a fiducial marker. The highlighted signal void in image A has no dot as this void is in the center of a marker located in the cranial-caudal plane. The effect of the banding artifact caused by rectal gas is highlighted by the (magenta) arrows in image C.

2.4. Automatic FM identification

All dynamics were resampled to a voxel spacing of 0.25 mm^3 to improve the accuracy and resolution of the automatic tracking results. Automatic determination of the FMs in subsequent frames was then performed by defining a local kernel of voxels with a diameter of 7 mm and height of 14 mm around each fiducial center in the first dynamic. The defined kernels were individually correlated to subsequent dynamics using the Pearson correlation to determine the current location of all FM, in a radius of 15 mm around the initial FM position of the first dynamic.

To reduce the influence of outliers from wrongly determined FM locations and increase robustness, the found FM locations of all subsequent dynamics were rigidly mapped to the marker template of the first dynamic using a leave-one-out strategy. All four possible combinations of three markers from the current dynamic were used to calculate a rigid transformation to the marker template of the first dynamic. The transformation with the lowest intra-marker difference between the mapped and original FM points was used for the determination of the final Euler transformation. The calculated transformation is thus based on three markers and describes the translation and rotation between the first and current dynamic and these variables are stored as the center of mass (COM) translation and rotation.

The results from the algorithm were verified by comparing the automatically found COM locations with the locations manually identified by the clinician at the halfway (27th) dynamic (after approximately 5 min) and end (55th) dynamic (after approximately 10 min). The grid system used in this paper defines X as left–right (where positive denotes right), Y as anterior–posterior (where positive denotes posterior) and Z as the caudal-cranial axis (where positive denotes cranial).

2.5. Statistics

Different statistical analyses were used to assess the results. The analyzed statistical metrics include the systematic error per patient per time point, the group mean displacement per time point, population systematical error per time point and the population random error per time point. The systematical error per patient (Sp) can be seen as the mean error over the patient's treatment, and is calculated on time point t_i by:

$$S_p(t_i) = \frac{1}{N_c(p)} \sum_{c=1}^{N_c(p)} \Delta_{p,c}(t_i). \quad (1)$$

With $N_c(p)$ as the number of total cine-MR scans per patient (p), c as the cine-MR scan number and Δ as the translation per direction in X, Y or Z. The group mean displacement (M) on time point t_i can then be calculated with:

$$M(t_i) = \frac{1}{N_p} \sum_{p=1}^{N_p} S_p(t_i). \quad (2)$$

With N_p as the total number of included patients. Using equations (1) and (2), the population systematical error can be seen as a measure for the mean displacement in all patients and is calculated by:

$$\Sigma(t_i) = \left(\frac{1}{N_p - 1} \sum_{p=1}^{N_p} \left(S_p(t_i) - M(t_i) \right)^2 \right)^{1/2}. \quad (3)$$

The population random error is calculated by using:

$$\sigma(t_i) = \left(\frac{1}{N_p} \sum_{p=1}^{N_p} \frac{1}{N_c(p) - 1} \sum_{c=1}^{N_c(p)} \left(\Delta_{p,c}(t_i) - S_p(t_i) \right)^2 \right)^{1/2}. \quad (4)$$

The population random error can be denoted as the effective random displacement, as it provides a measure for the mean fluctuations in the found result of the population (de Boer and Heijmen 2007).

The algorithm's success rate was determined by calculating the mean absolute intramarker distance between the FMs found in the current dynamic, and the FMs of the first dynamic, transformed to the current dynamic. The transformation of the FMs from the first to the current dynamic was performed by applying the inverse of the obtained transformation between the current and first dynamic. The intramarker distance was defined as the difference between the found position of a FM in the current dynamic and the transformed position of the same FM from the first to the current dynamic. If the mean absolute intramarker distance was equal to or less than 0.25 mm (equal to the resampled voxel spacing), the identification of the individual FMs and the registration between the dynamics was considered a success.

3. Results

The algorithm was applied to 7315 dynamics over 133 scans of 29 patients and a graphical representation of these results is summarized in figures 2 and 3. Figure 2 provides an overview of the population mean translation results. The population mean rotation results are provided in figure 3. Patients spent on average 2.4 ± 0.7 min on the scanner table before the start of the cine-MR imaging sequence. The mean 3D error in the COM position found by the algorithm compared with the clinician on dynamic 27 and 55 is 1.1 ± 0.7 mm with the largest 3D error being 3.8 mm. The mean 3D error in the FM positions provided by the clinician based on MR images compared with the 3D positions obtained from CT scans is 1.6 ± 1.2 mm. Linear regression analysis between the COM of the validation points by the clinician and the found COM positions by the algorithm returned a correlation value of 0.92. The success rate of the algorithm's tracking and registration was 97.7%.

The found COM translations at 10 min were 0.0 ± 0.8 mm (maximum 3.4 mm) for X, 1.0 ± 1.9 mm (maximum 9.7 mm) for Y (posterior direction) and 0.9 ± 2.0 mm (maximum 8.0 mm) for Z (caudal direction). The rotation results at 10 min were 0.1 ± 3.9° (maximum 30.3°) for X (towards anterior), 0.0 ± 1.3° (maximum 4.0°) for Y and 0.1 ± 1.2° (maximum 3.8°) for Z. Cumulative 3D translation occurrences of the COM of at least 2, 4 and 5 mm are provided in figure 4. These results indicate the cumulative fraction of scans in which the 3D COM translation was larger than the thresholds from the start of the imaging sequence up to the time intervals of 1, 3, 5, 7, 9 and 10 min. Results on the cumulative occurrences of COM rotations of at least 2, 4 and 5 degrees in the X direction are presented in figure 5. Figure 6 provides an overview of the population systematic translation error. The population random translation error is given in figure 7. An overview of individual motion paths of a single imaging session of a patient is given in figure 8. The graphs show the difference in results for the cases when using three markers versus all four markers.

Full automatic analysis of a single dynamic took 10 s, which is sufficiently fast to analyze an incoming cine-MR data stream without lag.

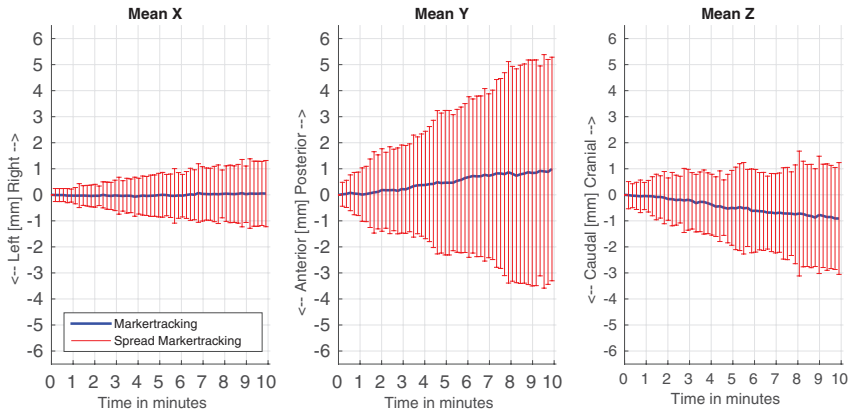

Figure 2. Overview of the population translation results, which show the found translation trends of 1 mm in the posterior and 0.9 mm in the caudal direction with the found spread (95 percentile) at each time point (over patients and fractions) as error bars. No translation trend was observed for the left–right direction.

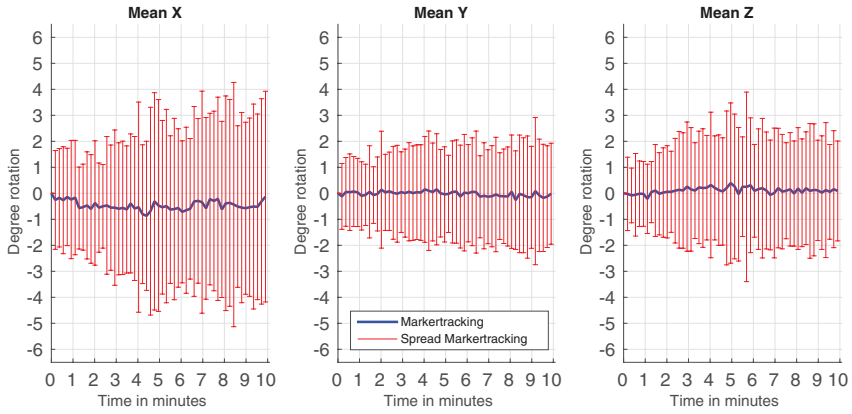

Figure 3. Overview of the population rotation results. The mean anterior–posterior rotation (about the *X*-axis) is provided on the left hand side and shows a small mean rotation trend of 0.5 degree in the anterior direction during the 10 min time period with the found spread (95 percentile) at each time point (over patients and fractions) as error bars. No rotational trend was observed for the *Y* and *Z* axis.

4. Discussion

Linear regression analysis indicated a good agreement between the COM of the validation points by the clinician and the found COM positions by the algorithm. To our knowledge, this is the first fully 3D cine-MR analysis of prostate intrafraction motion. This makes comparison to literature difficult and we can only compare to algorithms which are optimized for automatic fiducial marker detection in non-cine-MR sequences. An example of automatic fiducial detection is described by Ghose *et al* who reported a mean centroid difference of 0.5 ± 0.5 mm while using a voxel spacing of $0.6 \times 0.6 \times 2$ mm with non-cine-MR sequences specifically optimized for FM detection (Ghose *et al* 2016). The success rate of our tracking method for registrations was 97.7% based on an independent conservative measure as described in the material and methods section. On the other hand, we have detected prostate intrafraction motion of up to 9.7 mm, significantly larger than the obtained 3D error of 1.1 ± 0.7 mm. Therefore, the accuracy of our tracking method is sufficient for clinical application.

While using three instead of all four available FM may seem sub-optimal at first, determining the Euler transformation on the best three fitting markers to the marker template of the first dynamic result in lower errors for the found translation and rotation. All FM are individually tracked and used to determine the rigid Euler transformation. Therefore, a single wrongly localized marker can result in particularly large rotation errors as shown

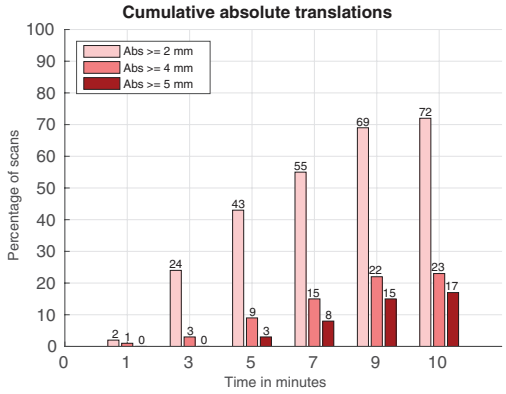

Figure 4. Overview of the cumulative percentage of scans, in which the found 3D COM translations is at least 2, 4 or 5 mm.

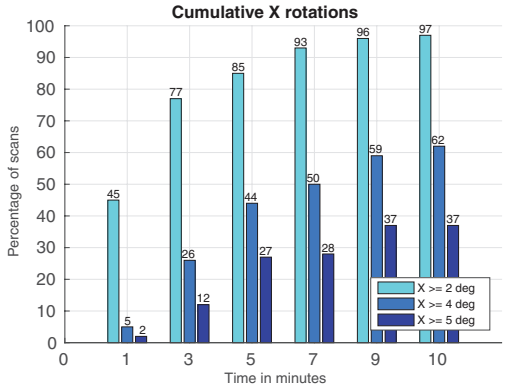

Figure 5. Overview of the cumulative percentage of scans, in which the found *X* rotation is at least 2, 4 or 5 degrees.

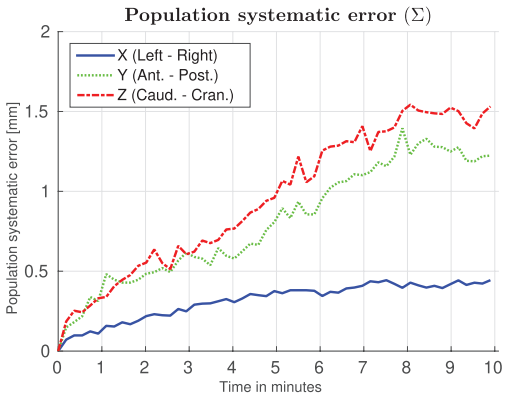

Figure 6. The development of the systematic translation errors (Σ) over time, for the three main directions.

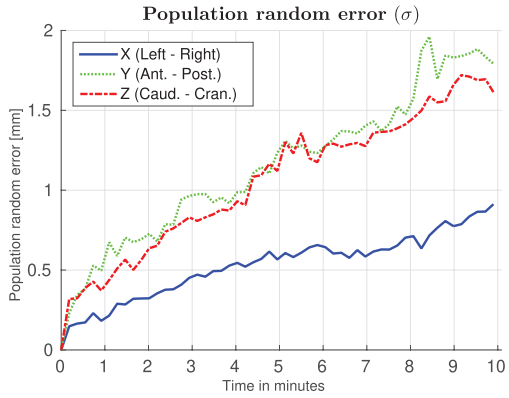

Figure 7. The development of the random translation errors (σ) over time, for the three main directions.

in figure 8. In this figure, large rotation values can be observed for the *X* and *Z* rotation when using four markers around the 7 and 8.5 min mark. To reduce the influence of outliers and obtain robust motion results, the three best fitting markers to the marker template of the first dynamic were used to obtain the translation and rotation motion.

A marker tracking simulation was performed to identify the effect of single voxel marker mis-locations in the anterior–posterior direction on the obtained rotation results. In this simulation, a fiducial marker model was used based on the group mean fiducial marker positions of all patients, obtained from the CT scan of patients. The simulation showed that the marker tracking left–right rotation results have a mean measurement step size of 0.67 degrees.

Two scans were excluded from the analysis based on visual inspection of the cine-MR data and the performance of the marker tracking algorithm. These scans were excluded due to an excessive banding artifact caused by local B_0 distortions due to rectal gas and are typical for bSSFP sequences. The banding artifact overlapped on large portions of the prostate, which made it nearly impossible to find marker locations in the prostate with confidence. The effect of the banding artifact is shown in figure 1, image Fernandes *et al* (2017) had previously reported the impact on fiducial detection of gas within the rectum causing a signal drop-off. Use of a different MR sequence (e.g. spoiled gradient echo) in future image acquisition can help to eliminate the influence of banding artifacts. Apart from these rare artifacts, we have shown that fast and accurate FM tracking on 3D cine-MR is feasible and may be applied on an MR-linac.

A maximum 3D error of 3.8 mm in the COM position found by the algorithm compared with the clinician was found. This error is visualized in figures 1 and 2 in the supplementary material (stacks.iop.org/PMB/64/07NT02/mmedia). In this particular case, two markers were identified which were placed relatively close together in the prostate. Further inspection showed that the signal void of both markers seemed to partially overlap in the cranial-caudal direction. It is a possibility that the clinician segmented the markers differently in the first dynamic, from which the template for the marker tracking is extracted. The error of 3.8 mm could then originate from deviations in the manual segmentations. An investigation with multiple observers could specify if this is the case, or that the difference originates from an error in the algorithm.

The population results in figures 2 and 3 show that the magnitude of intrafraction displacements continuously increased over the 10 min interval. Next to the small overall trends, the spread of the displacements increased consistently. The growth of the displacements is visualized by the figures and suggests that the prostate will continue to move after 10 min, consistent with the random walk model of Ballhausen *et al* (2014).

Figure 4 shows that the translations continue to increase over time, which is also reflected by figure 2. A majority of the scans (72%) showed a COM translation of at least 2 mm during the 10 min, while a COM translation of at least 5 mm was found in 17% of the scans during the 10 min. Only the *X* rotations were shown in figure 5, as significant rotations about the *X*-axis were most commonly observed. More than one-third of the scans (37%) showed an *X* rotation of at least 5 degrees during the 10 min. *Z* and *Y* rotations are less common with at least 5 degrees *Z* rotation in 9% and at least 5 degrees *Y* rotation in 3% of the scans during the 10 min. The maximum *X* rotation of 30.3° was found in a case where a gas pocket passing by caused severe intrafraction motion in the period of a single dynamic.

The presented results are consistent with published results. Results from this research reflect that the largest rotation occurs about the left–right (LR) axis, while the translation motions are mainly found in the anterior–

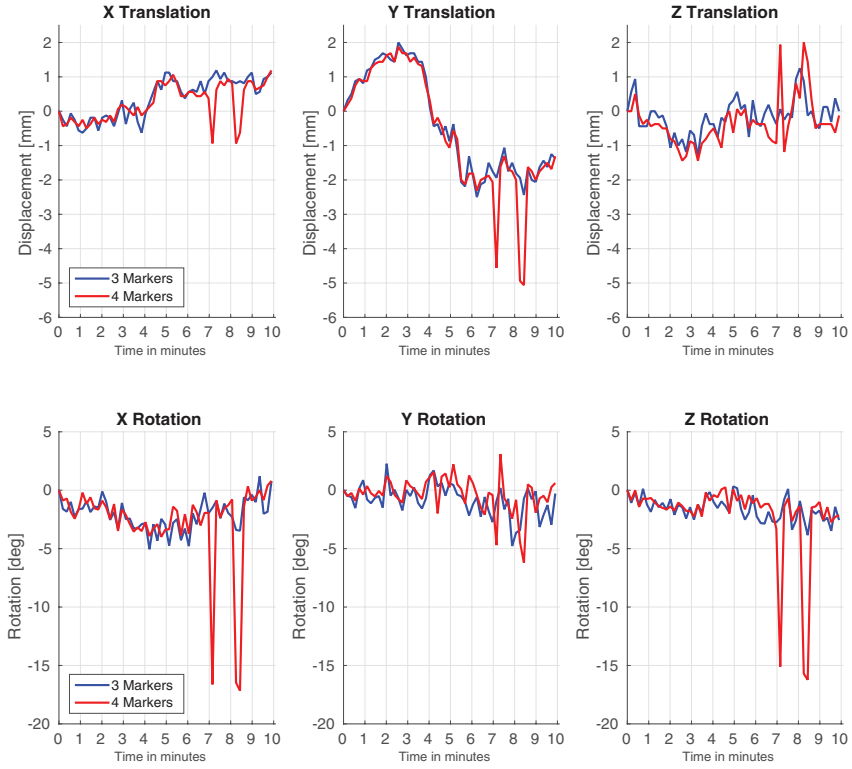

Figure 8. Overview of individual motion paths during a single imaging session of a patient. The results are shown for the case when using the best three markers (blue), and using all four markers (red). From the *X* and *Z* rotation graphs can be observed that using all four markers can result in large rotation values.

posterior (AP) and cranial-caudal (CC) direction (Padhani *et al* 1999, Huang *et al* 2002, Mah *et al* 2002, Sihono *et al* 2018). The population average trends can be described as a group mean displacement of 1 mm in both the posterior and caudal direction and an 0.5 degree rotational trend in the anterior direction over the *X* axis over a 10 min time period. This may be due to a gradual increase in bladder filling. The effect of breathing on prostate intrafraction motion was not taken into account, as influence of breathing on prostate motion was found to be very small (Terashima *et al* 2013). When considering prostate displacements, both the magnitude and duration are relevant. Our findings of increased movement over time are consistent with tracking data from electromagnetic markers (Langen *et al* 2008, Cramer *et al* 2013), cine-MR studies (Ghilezan *et al* 2005) and transperineal ultrasound imaging (Sihono *et al* 2018). As stated before, our findings indicate a monotonously increasing displacement with an increasing variance over time, consistent with findings reported in literature (Ballhausen *et al* 2014). Similar results obtained with the Calypso Localization System over an 8 min time period are reported by Olsen *et al* (2012), where the findings indicate prostate displacement trends in the *Y* (0.64 ± 0.5 mm) and *Z* (0.96 ± 0.6 mm) direction and rotation over the *X* axis ($5.7 \pm 5°$). Huang *et al* (2015) reported an *X*-axis rotation of at least 5 degrees in 35% of all scans at 8 min time interval, in agreement with our findings. Comparable motion characteristics within the same order of magnitude have been reported by other groups (Willoughby *et al* 2006, Li *et al* 2009, Tehrani *et al* 2013).

Clearly, a shorter treatment time results in less prostate motion and so effort should be put in reducing time between patient positioning and treatment if no strategies for countering intrafraction motion are available. This claim is supported by Ballhausen *et al* (2018) who found that the 3D prostate displacement significantly reduced from 1.31 ± 1.28 mm for intensity modulated radiotherapy (IMRT) at 6 min to 0.96 ± 1.04 mm for volumetric arc therapy (VMAT) of under 3 min. Similar conclusions were reported by Cramer *et al* (2013), who advise to reposition the patient for treatment durations over 4–6 min when no correction protocol for intrafraction motion is used. However, the picture dramatically changes if cine-MR data will be used to drive real-time plan adaptation on an MR-linac (Kontaxis *et al* 2017a, 2017b). Then, in principle, overall treatment time will not be

vital anymore to treatment accuracy but only to patient comfort and treatment costs. The cine-MR datasets analysed here incorporate a ten minute period, with the aim of representing the duration of treatment delivery. With the recent implementation of MR-guided radiotherapy at our institutions, the workflow encompasses acquiring daily MRI and online re-planning. The patient is therefore on the treatment couch for a longer duration, however repeat verification imaging is carried out prior to treatment delivery to ensure the coverage of the prostate remains adequate. The data we have presented here remains highly relevant, as the evaluation of prostate motion during the MR-guided workflow is paramount, particularly with the aim of real-time adaptive radiotherapy during treatment delivery in the future. In addition, using FM tracking will just be a first step in this process as the full potential of 3D cine-MR data for soft-tissue tracking and hence optimal dose adaptation can then be exploited.

Therefore, our next aim is soft tissue motion monitoring of the prostate, without the use of FM. Our current research therefore involves the development of a FM-free tracking method of the prostate, where the results of the presented study will be used for validation.

5. Conclusion

We have developed a robust, fast and accurate FM tracking algorithm in cine-MR data, which allows for continuous monitoring of intrafraction motion and validation of FM-free soft-tissue tracking methods in MR-guided radiotherapy. As stated before, to our knowledge this is the first data using automatic FM tracking on cine-MR to assess prostate intrafraction motion. We obtained six degrees of freedom prostate intrafraction motion based on volumetric cine-MR images only. The results include rotational analysis for which there is considerably less data available in literature than prostate translation. We found a continuous increase with time in intrafraction motion magnitude (translations and rotations) over a ten minute period, which hardly flattened. The amplitude and temporal behavior of the found intrafraction motion stresses the importance of real-time MR-guidance by fast imaging and dose re-optimization for prostate SBRT.

Acknowledgments

This paper represents independent research support by the National Institute for Health Research (NIHR) Biomedical Research Centre at the Royal Marsden NHS Foundation Trust and the Institute of Cancer Research. The views expressed are those of the author(s) and not necessarily those of the NHS, the NIHR or the Department of Health.

References

Ballhausen H, Li M, Ganswindt U and Belka C 2018 Shorter treatment times reduce the impact of intra-fractional motion *Strahlentherapie Onkol.* **194** 664–74

Ballhausen H, Li M, Hegemann N, Ganswindt U and Belka C 2014 Intra-fraction motion of the prostate is a random walk *Phys. Med. Biol.* **60** 549

Beltran C, Herman M G and Davis B J 2008 Planning target margin calculations for prostate radiotherapy based on intrafraction and interfraction motion using four localization methods *Int. J. Radiat. Oncol. Biol. Phys.* **70** 289–95

Cramer A K *et al* 2013 Real-time prostate motion assessment: image-guidance and the temporal dependence of intra-fraction motion *BMC Med. Phys.* **13** 4

de Boer H C and Heijmen B J 2007 eNAL: an extension of the NAL setup correction protocol for effective use of weekly follow-up measurements *Int. J. Radiat. Oncol. Biol. Phys.* **67** 1586–95

Fernandes C D, Dinh C V, Steggerda M J, ter Beek L C, Smolic M, van Buuren L D, Pos F J and van der Heide U A 2017 Prostate fiducial marker detection with the use of multi-parametric magnetic resonance imaging *Phys. Imaging Radiat. Oncol.* **1** 14–20

Ghilezan M J *et al* 2005 Prostate gland motion assessed with cine-magnetic resonance imaging (cine-MRI) *Int. J. Radiat. Oncol. Biol. Phys.* **62** 406–17

Ghose S, Mitra J, Rivest-Hénault D, Fazlollahi A, Stanwell P, Pichler P, Sun J, Fripp J, Greer P B and Dowling J A 2016 MRI-alone radiation therapy planning for prostate cancer: automatic fiducial marker detection *Med. Phys.* **43** 2218–28

Gustafsson C, Korhonen J, Persson E, Gunnlaugsson A, Nyholm T and Olsson L E 2017 Registration free automatic identification of gold fiducial markers in MRI target delineation images for prostate radiotherapy *Med. Phys.* **44** 5563–74

Huang C Y, Tehrani J N, Ng J A, Booth J and Keall P 2015 Six degrees-of-freedom prostate and lung tumor motion measurements using kilovoltage intrafraction monitoring *Int. J. Radiat. Oncol. Biol. Phys.* **91** 368–75

Huang E, Dong L, Chandra A, Kuban D A, Rosen I I, Evans A and Pollack A 2002 Intrafraction prostate motion during IMRT for prostate cancer *Int. J. Radiat. Oncol. Biol. Phys.* **53** 261–8

Khoo V S, Padhani A R, Tanner S F, Finnigan D J, Leach M O and Dearnaley D P 1999 Comparison of MRI with CT for the radiotherapy planning of prostate cancer: a feasibility study *The Br. J. Radiol.* **72** 590–7

Kontaxis C, Bol G H, Kerkmeijer L G, Lagendijk J J and Raaymakers B W 2017 Fast online replanning for interfraction rotation correction in prostate radiotherapy *Med. Phys.* **44** 5034–42

Kontaxis C, Bol G, Stemkens B, Glitzner M, Prins F M, Kerkmeijer L G, Lagendijk J J and Raaymakers B W 2017b Towards fast online intrafraction replanning for free-breathing stereotactic body radiation therapy with the MR-linac *Phys. Med. Biol.* **62** 7233

Langen K and Jones D 2001 Organ motion and its management *Int. J. Radiat. Oncol. Biol. Phys.* **50** 265–78

Langen K M, Willoughby T R, Meeks S L, Santhanam A, Cunningham A, Levine L and Kupelian P A 2008 Observations on real-time prostate gland motion using electromagnetic tracking *Int. J. Radiat. Oncol. Biol. Phys.* **71** 1084–90

Li J S, Jin L, Pollack A, Horwitz E M, Buyyounouski M K, Price R A and Ma C M 2009 Gains from real-time tracking of prostate motion during external beam radiation therapy *Int. J. Radiat. Oncol. Biol. Phys.* **75** 1613–20
Litzenberg D W, Balter J M, Hadley S W, Sandler H M, Willoughby T R, Kupelian P A and Levine L 2006 Influence of intrafraction motion on margins for prostate radiotherapy *Int. J. Radiat. Oncol. Biol. Phys.* **65** 548–53
Mah D, Freedman G, Milestone B, Hanlon A, Palacio E, Richardson T, Movsas B, Mitra R, Horwitz E and Hanks G E 2002 Measurement of intrafractional prostate motion using magnetic resonance imaging *Int. J. Radiat. Oncol. Biol. Phys.* **54** 568–75
Maspero M, Seevinck P R, Willems N J, Sikkes G G, de Kogel G J, de Boer H C, van der Voort van Zyp J R and van den Berg C A 2018 Evaluation of gold fiducial marker manual localisation for magnetic resonance-only prostate radiotherapy *Radiat. Oncol.* **13** 105
Maspero M, van den Berg C A, Zijlstra F, Sikkes G G, de Boer H C, Meijer G J, Kerkmeijer L G, Viergever M A, Lagendijk J J and Seevinck P R 2017 Evaluation of an automatic MR-based gold fiducial marker localisation method for MR-only prostate radiotherapy *Phys. Med. Biol.* **62** 7981–8002
McPartlin A J *et al* 2016 MRI-guided prostate adaptive radiotherapy—a systematic review *Radiother. Oncol.* **119** 371–80
Meyer E, Raupach R, Lell M, Schmidt B and Kachelrieß M 2010 Normalized metal artifact reduction (nmar) in computed tomography *Med. Phys.* **37** 5482–93
Mutanga T F, de Boer H C, Rajan V, Dirkx M L P, Incrocci L and Heijmen B J 2012 Day-to-day reproducibility of prostate intrafraction motion assessed by multiple kV and MV imaging of implanted markers during treatment *Int. J. Radiat. Oncol. Biol. Phys.* **83** 400–7
Mutic S and Dempsey J F 2014 The viewray system: magnetic resonance—guided and controlled radiotherapy *Semin. Radiat. Oncol.* **24** 196–9
Nichol A M *et al* 2010 A cinematic magnetic resonance imaging study of milk of magnesia laxative and an antiflatulent diet to reduce intrafraction prostate motion *Int. J. Radiat. Oncol. Biol. Phys.* **77** 1072–8
Ogino I, Kaneko T, Suzuki R, Matsui T, Takebayashi S, Inoue T and Morita S 2011 Rectal content and intrafractional prostate gland motion assessed by magnetic resonance imaging *J. Radiat. Res.* **52** 199–207
Olsen J R, Noel C E, Baker K, Santanam L, Michalski J M and Parikh P J 2012 Practical method of adaptive radiotherapy for prostate cancer using real-time electromagnetic tracking *Int. J. Radiat. Oncol. Biol. Phys.* **82** 1903–11
Padhani A R, Khoo V S, Suckling J, Husband J E, Leach M O and Dearnaley D P 1999 Evaluating the effect of rectal distension and rectal movement on prostate gland position using cine MRI *Int. J. Radiat. Oncol. Biol. Phys.* **44** 525–33
Parker C C, Damyanovich A, Haycocks T, Haider M, Bayley A and Catton C N 2003 Magnetic resonance imaging in the radiation treatment planning of localized prostate cancer using intra-prostatic fiducial markers for computed tomography co-registration *Radiother. Oncol.* **66** 217–24
Pathmanathan A U *et al* 2018 Magnetic resonance imaging-guided adaptive radiation therapy: a game changer for prostate treatment? *Int. J. Radiat. Oncol. Biol. Phys.* **100** 361–73
Raaymakers B W *et al* 2009 Integrating a 1.5 T MRI scanner with a 6 MV accelerator: proof of concept *Phys. Med. Biol.* **54** N229
Rasch C, Barillot I, Remeijer P, Touw A, van Herk M and Lebesque J V 1999 Definition of the prostate in CT and MRI: a multi-observer study *Int. J. Radiat. Oncol. Biol. Phys.* **43** 57–66
Schieda N, Avruch L, Shabana W M and Malone S C 2015 Multi-echo gradient recalled echo imaging of the pelvis for improved depiction of brachytherapy seeds and fiducial markers facilitating radiotherapy planning and treatment of prostatic carcinoma *J. Magn. Reson. Imaging* **41** 715–20
Sihono D S K, Ehmann M, Heitmann S, von Swietochowski S, Grimm M, Boda-Heggemann J, Lohr F, Wenz F and Wertz H 2018 Determination of intrafraction prostate motion during external beam radiation therapy with a transperineal 4-dimensional ultrasound real-time tracking system *Int. J. Radiat. Oncol. Biol. Phys.* **101** 136–43
Tehrani J N, OBrien R T, Poulsen P R and Keall P 2013 Real-time estimation of prostate tumor rotation and translation with a kV imaging system based on an iterative closest point algorithm *Phys. Med. Biol.* **58** 8517
Terashima K *et al* 2013 Can a belly board reduce respiratory-induced prostate motion in the prone position? -assessed by cine-magnetic resonance imaging *Technol. Cancer Res. Treatment* **12** 447–53
van der Heide U A, Kotte A N, Dehnad H, Hofman P, Lagenijk J J and van Vulpen M 2007 Analysis of fiducial marker-based position verification in the external beam radiotherapy of patients with prostate cancer *Radiother. Oncol.* **82** 38–45
Villeirs G M, Van Vaerenbergh K, Vakaet L, Bral S, Claus F, De Neve W J, Verstraete K L and De Meerleer G O 2005 Interobserver delineation variation using CT versus combined CT+MRI in intensity–modulated radiotherapy for prostate cancer *Strahlentherapie Onkol.* **181** 424–30
Willoughby T R *et al* 2006 Target localization and real-time tracking using the Calypso 4D localization system in patients with localized prostate cancer *Int. J. Radiat. Oncol. Biol. Phys.* **65** 528–34
Zijlstra F, Moerland M A, van der Voort van Zyp J R, Noteboom J L, Viergever M A and Seevinck P R 2017 Challenges in MR-only seed localization for postimplant dosimetry in permanent prostate brachytherapy *Med. Phys.* **44** 5051–60

Received: 7 August 2018 | Revised: 6 November 2018 | Accepted: 10 December 2018

DOI: 10.1002/acm2.12529

RADIATION ONCOLOGY PHYSICS

WILEY

Improving fiducial and prostate capsule visualization for radiotherapy planning using MRI

Angela U. Pathmanathan[1,2]* | Maria A. Schmidt[1,2]* | Douglas H. Brand[1,2] | Evanthia Kousi[1,2] | Nicholas J. van As[1,2] | Alison C. Tree[1,2]

[1]The Royal Marsden Hospital NHS Foundation Trust, London, UK

[2]The Institute of Cancer Research, London, UK

Author to whom correspondence should be addressed. Angela U. Pathmanathan
E-mail: angela.pathmanathan@icr.ac.uk

Funding information
National Institute for Health Research Biomedical Research Centre; Cancer Research UK, Grant/Award Number: C33589/A19727; National Institute for Health Research; Elekta

Abstract

Background and purpose: Intraprostatic fiducial markers (FM) improve the accuracy of radiotherapy (RT) delivery. Here we assess geometric integrity and contouring consistency using a T2*-weighted (T2*W) sequence alone, which allows visualization of the FM.

Material and methods: Ten patients scanned within the Prostate Advances in Comparative Evidence (PACE) trial (NCT01584258) had prostate images acquired with computed tomography (CT) and Magnetic Resonance (MR) Imaging: T2-weighted (T2W) and T2*W sequences. The prostate was contoured independently on each imaging dataset by three clinicians. Interobserver variability was assessed using comparison indices with Monaco ADMIRE (research version 2.0, Elekta AB) and examined for statistical differences between imaging sets. CT and MR images of two test objects were acquired to assess geometric distortion and accuracy of marker positioning. The first was a linear test object comprising straight tubes in three orthogonal directions, the second was a smaller test object with markers suspended in gel.

Results: Interobserver variability for prostate contouring was lower for both T2W and T2*W compared to CT, this was statistically significant when comparing CT and T2*W images. All markers are visible in T2*W images with 29/30 correctly identified, only 3/30 are visible in T2W images. Assessment of geometric distortion revealed in-plane displacements were under 0.375 mm in MRI, and through plane displacements could not be detected. The signal loss in the MR images is symmetric in relation to the true marker position shown in CT images.

Conclusion: Prostate T2*W images are geometrically accurate, and yield consistent prostate contours. This single sequence can be used to identify FM and for prostate delineation in a mixed MR-CT workflow.

PACS
87.57.nm

KEY WORDS
geometric distortion, MR-guided RT, MRI, prostate, segmentation

*Joint first author.

1 | INTRODUCTION

Accurate co-registration of magnetic resonance (MR) and computed tomography (CT) images is essential in radiotherapy (RT) planning using both modalities. MR-CT fusion combines the superior soft tissue contrast of MR images and the electron density from CT images, which is currently required for planning.[1] However, CT and MR examinations take place at different times and over different timescales; the acquisition of detailed MR images covering the tumor volume may require a few minutes, while CT is considerably faster. Physiological motion may thus affect MR and CT images differently, and this is detrimental to the accuracy of MR-CT fusion. In addition, inter- and intra-fraction motion may be significant at the time of RT delivery, introducing further errors.[2,3] In order to mitigate this, fiducial markers can be placed into relatively mobile tumors (or their vicinity), enabling more precise image co-registration to be performed for MR-CT fusion during the planning process[4] and position verification prior to each fraction.[5,6] A more accurate MR-CT co-registration will enable better targeting, therefore markers must be visible, both in MR and CT.

Metallic markers appear bright on CT, often surrounded by reconstruction and beam hardening artifacts,[7,8] but do not yield MR signals and are seen as dark "void" areas on MR. Their susceptibility cause variations in the magnetic field in their vicinity, and they are often better visualized in T2*-weighted (T2*W) images where the signal loss around the markers is emphasized.[9] The design of MR protocols for RT planning thus requires not only geometric accuracy but also that the markers are clearly visible and the image contrast provides confidence in target outlining. Uncertainties and variation in target delineation during RT planning adds a further systematic error. MRI allows a reduction in interobserver variability for prostate contours compared to CT,[10] however, this is dependent on the sequence used.[11] Previously it has not been possible to provide one single sequence that enables both visualization of the markers and target outlining, and this adds a degree of complexity to the RT planning workflow.

This work investigates a sequence suitable for MR-CT fusion for prostate RT using fiducial markers; in our institution, a set of three gold seeds is implanted in each patient. The MR protocol we implemented consists of two sequences; one standard T2-weighted (T2W) sequence used in diagnostic prostate scans, thus optimized for visualization of intra-prostatic structures, and a second T2*W sequence optimized for marker visualization using the combination of several gradient-echoes with different echo-times (TE) which follow each excitation. The second sequence maximizes visualization of the markers for RT planning fusion.

Studies so far for similar sequences have focused on accuracy of fiducial detection.[12–17] In this article we examine the T2*W sequence and investigate whether it is possible to use this sequence alone in prostate studies, considering geometric integrity, the ability to locate marker positions and the ability to provide enough contrast for prostate volume outlining.

2 | MATERIALS AND METHODS

2.A | Patient population

Patients were scanned at 1.5 T (Siemens Aera, Erlangen, Germany) as part of the Prostate Advances in Comparative Evidence (PACE) trial (NCT01584258). PACE A randomizes patients between prostatectomy and stereotactic body radiotherapy (SBRT) to a dose of 36.25 Gy in five fractions, and PACE B randomizes patients between SBRT and conventionally fractionated RT, either 62 Gy in 20 fractions or 78 Gy in 39 fractions. Patients do not receive androgen deprivation therapy. A minimum of 1 week prior to planning imaging, three 1.0 × 3.0 mm knurled gold markers are inserted into the prostate. Fiducial positions are used to fuse the CT and MR scans and for position verification prior to each treatment.

2.B | Planning CT acquisition

At the Royal Marsden Hospital, all patients receiving RT in PACE have a RT planning CT followed, on the same day, by a planning MRI scan. Patients are scanned with bladder filling and rectal preparation as per institutional guidelines and no intravenous contrast is used. Patients receive 2 days of rectal preparation with enemas prior to planning, and an enema just before their planning CT scan. The CT scan incorporates axial slices of 1.5 mm from mid lumbar spine to below the obturator foramen.

2.C | Planning MRI acquisition

Prostate MRI examinations were undertaken with two two-dimensional (2D) sequences, covering the prostate volume in 28 adjacent slices (2.5 mm thickness). The first one is a standard T2W pulse sequence used in diagnostic MRI of the prostate. This sequence is based on fast spin-echoes and allows visualization of internal structure of the prostate (central and peripheral zone and urethra). The second sequence is applied to the same locations, but it is gradient-echo-based and maximizes the signal loss surrounding the markers. For that purpose, we employed a sequence, which combines several gradient-echo signals, with a range of echo-times (TE), into one single image. This strategy maintains the signal-to-noise ratio in T2*W acquisitions and has been used for other clinical applications.[18,19] Both sequences cover the same volume, centered on the prostate and including at least part of the pelvic bones. Both sequences use the same shimming volume to optimize the magnetic field homogeneity and the manufacturer's own distortion correction software (in 2D). Parameters of both sequences are provided in Table 1.

2.D | Geometric integrity

The field inhomogeneity of the main magnet and the non-uniformity of gradient fields are known to progressively affect the MR images as the distance from the magnet isocenter increases. Although it is unlikely that the local MR-CT co-registration could

TABLE 1 Parameters of MRI sequences for prostate RT Planning.

	T2W acquisition (2D T2W FSE)	T2*W acquisition (2D "medic")
FOV readout (phase)	240 mm (100%)	240 mm (100%)
PE oversampling	60%	60%
Number of Slices	28	28
Slice thickness/gap	2.5 mm/0	2.5 mm/0
Acquisition matrix (phase)	320 (75%)	256 (75%)
TE/TR	110 ms/7210 ms	24 ms/550 ms
Averages	3	2
Orientation	Transaxial	Transaxial
PE direction	Left/right	Left/right
Reconstruction matrix	320 × 320	512 × 512
Receiver bandwidth	200 Hz/pixel Fat-water shift = 0.84 mm	230 Hz/pixel Fat-water shift = 0.92 mm
Pixel size	0.75 mm × 0.75 mm	0.46875 mm × 0.46875 mm
Other	Echo-train length 25, echo spacing 9.98 ms, echo-trains per slice 16	Combined echoes 5, flip Angle 28 degrees
Filters	PrescanNormalize/DistCorrection 2D	PrescanNormalize/DistCorrection 2D
Coil arrangement	Spine coil & body array	Spine coil & body array
Total acquisition time	2 min 46 s Parallel imaging = 2 (GRAPPA)	6 min 4 s Parallel imaging = 2 (GRAPPA)

FSE: fast spin echo; FOV: field of view; TE: echo time; TR: relaxation time; GRAPPA: GeneRalized Autocalibrating Partial Parallel Acquisition.

be affected by geometric distortion at the prostate location, close to the isocenter, we characterized the hardware-related geometric distortion over the imaging volume. For that purpose we acquired CT and MR images of a previously described test object consisting of straight tubes in three orthogonal directions, known as "Linear Test Object."[20] Images were co-registered and evaluated using the three-dimensional (3D) slicer software package (www.slicer.org).[21] Displacements of test object structures between CT and MR images can be easily detected if they reach half of the voxel size — a level of accuracy that is sufficient for the purposes of this study.

In addition a second test object was built by suspending the markers in a gel volume comparable with a prostate (porcine gel, Sigma-Aldricht, St. Louis, MI, 100 g/L, approximately 90 cm^3) to verify whether the position of the markers is correctly depicted in the MR images with the sequences used. This step is necessary because the markers themselves disturb the field inhomogeneity, and the associated signal loss is not necessarily symmetric in relation to the true marker position.[22] Therefore, in marker-based registration, it is important to verify that systematic errors are not being introduced.

The markers were orientated approximately in the superior/inferior direction, which most closely resembles their orientation in clinical examinations (Fig. 1). However, the object was rotated by 90° for a second MR acquisition, to evaluate how the susceptibility-related signal loss depends on orientation, and also scanned at different orientations. In order to verify whether systematic errors were introduced, two CT-MR registrations were produced. The first gold standard registration employs the outline of the test object volume, visible in MR and CT. The second registration employs only the marker information, and registration coordinates are compared. In addition, a capsule of cod liver oil was placed on top of the test object to provide a standard for displacements associated with chemical shift. The fat-water chemical shift is known to be 3.5 ppm (225 Hz at 1.5 T), and fat-water displacement was measured by using a readout gradient reversal.[23]

2.E | Clinical studies

2.E.1 | Patient population

Ten patients with localized prostate cancer treated consecutively within the PACE trial with SBRT at the Royal Marsden Hospital, Sutton, from January 2015 to December 2016 were selected. Each patient had three imaging datasets- RT planning CT, T2W and T2*W MRI sequences as described. Examples are seen in Fig. 2.

2.E.2 | Visibility of fiducials

Without reference to the CT images, T2W and T2*W images were reviewed to assess the number of fiducial markers visible.

2.E.3 | Volume definition

Using Research Monaco 5.19.02 (Elekta AB, Stockholm, Sweden), the prostate contour was delineated on each of the three

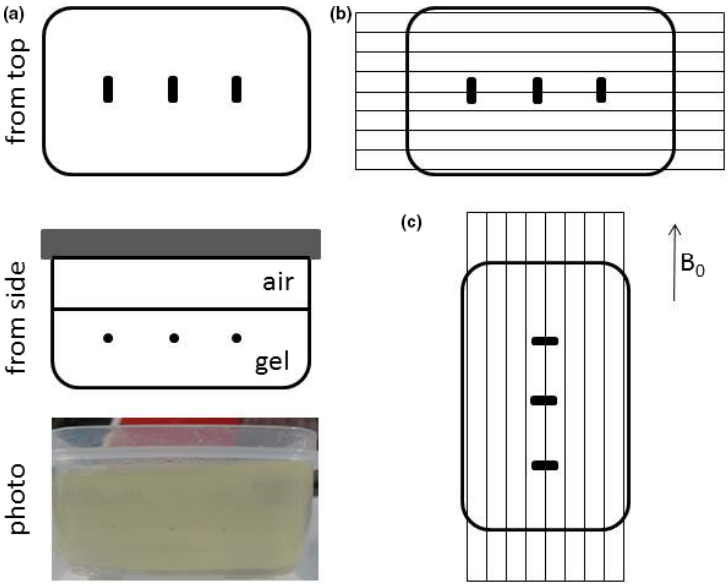

FIG. 1. (a) Gel test object containing gold seeds (schematic diagram and photo showing gold seeds suspended in gel), (b) Standard test object position, gold seeds approximately lined up with main magnetic field as in most clinical examinations, and transaxial slices acquired, (c) Alternative orientation, gold seeds at 90° with static magnetic field B_0. Images for slices A, B, and C are shown in Fig. 3.

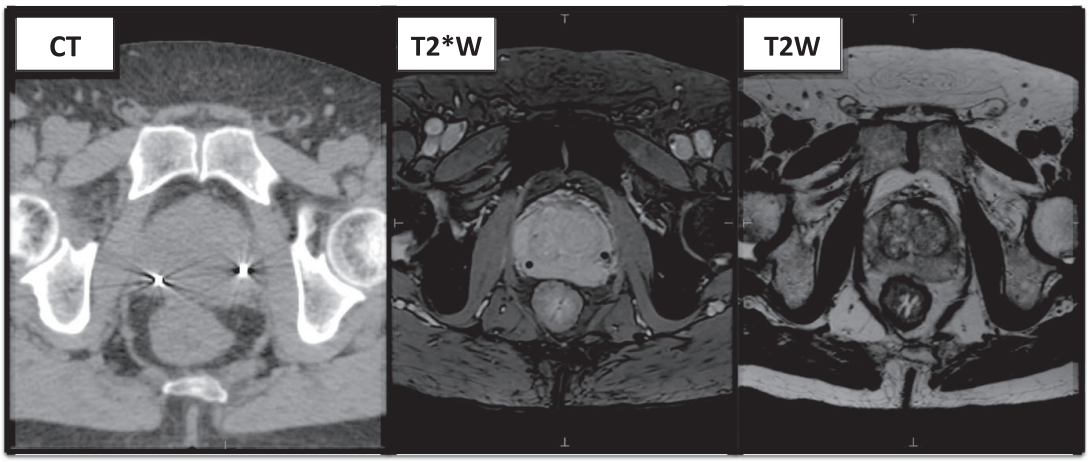

FIG. 2. The three imaging sequences used for prostate contours showing the corresponding levels for the same patient. From left to right (a) CT imaging- fiducials seen as bright markers with surrounding artifact (b) T2*W MRI sequence- fiducials seen as dark void areas (c) T2W MRI sequence- fiducials not visible.

sequences for all ten patients by three clinicians from the same institution (AP, AT, and DB) experienced with prostate contouring on both CT and MRI. The clinicians were instructed to contour the prostate alone; that is, excluding the seminal vesicles (SV). Contouring was completed on each dataset independently, without reference to the other two types of imaging. The three sequences for each patient were contoured during three separate sessions, with at least 2 weeks between each session to minimize recall bias.

2.E.4 | Contour variability

Inter-observer variability, as a measure of consistency, was assessed for each sequence by comparing each individual clinician contour to a Simultaneous Truth and Performance Level Estimation (STAPLE) contour[24] formed from all three clinician contours.

Monaco ADMIRE software version 2.0 was used to generate a combination of contour comparison indices[25,26] to analyze the

difference between clinician contours for the same imaging dataset. Distance measurements included the Hausdorff distance (HD) and mean distance between contours. Overlap measures included Dice similarity co-efficient (DSC) and Cohen's Kappa. A shorter distance between contours or higher overlap index indicates higher agreement between observers. The Shapiro–Wilk test confirmed non-normality of the data using SPSS Statistics, version 23. Therefore a separate Freidman's test was performed for all four delineation metrics, examining for differences across the three imaging modalities. Where significant, pair-wise group comparison was undertaken using Wilcoxon's signed rank testing with Bonferroni correction.

3 | RESULTS

3.A | Geometric integrity

Figure 3 shows Maximum Intensity Projections (MIPs) of the Linear Test Object dataset, and a 3D view for the T2W and T2*W sequences. All lines appear straight within the volume studied ($240 \times 240 \times 70$ mm^3). Displacements from true position were estimated to be smaller than half of the voxel size (i.e., under 0.375 mm in the Left/Right and Anterior/Posterior direction). In the Superior/Inferior direction the slice thickness is 2.5 mm and no significant distortion could be detected. Using the T2*W sequences several imperfections of the test object become apparent as areas of signal loss associated with localized field inhomogeneity, but all tubes still appear straight.

Considering the test object with markers suspended in gel, the markers are always clearly visible in T2*W images; in T2W images the signal loss is much smaller, as expected (Fig. 4). MR and CT images were co-registered and displacements were shown to be smaller than half pixel size. The signal loss in MR images was thus shown to be symmetric in relation to the true marker position shown in CT images. For both sequences the displacement of fat signals in relation to water signals due to chemical shift was confirmed to be less than 1 mm, as expected.

Figure 5 shows an example of a clinical examination, with markers in different orientations. Both test object and clinical examinations show different levels of signal loss around the gold seeds.

A larger area of signal loss associated with the marker in the center of the gel test object was obtained irrespective of test object orientation, and was therefore investigated; the three markers appear identical in CT and ultrasound images and there are no visible air bubbles in the gel preparation. In order to gain further insight, the gel test object was rebuilt: the gold seeds were removed from the gel and cleaned with ethanol and placed in a new batch of gel in the same container, but in different positions. This resulted in almost identical images, the signal loss around one particular gold seed persisted being much larger than the signal loss surrounding the others, for any orientation. Therefore, although the signal loss pattern is expected to depend on seed orientation and position, it is also quite possible that one particular gold seed has a different magnetic susceptibility.

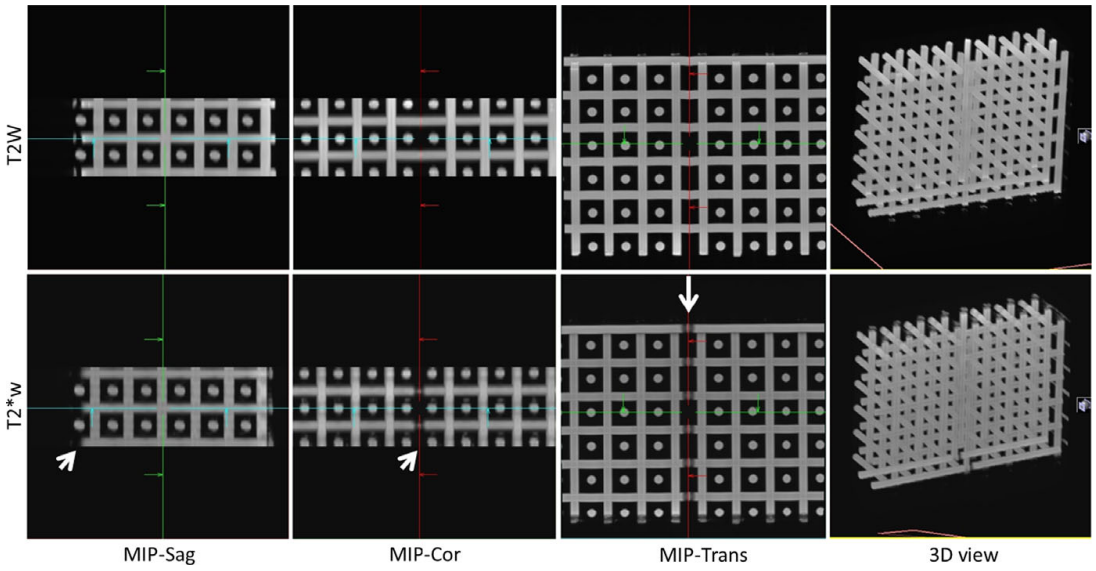

FIG. 3. T2W (top) and T2*W (bottom) images of the Linear Test Object comprising straight tubes in three orthogonal directions. The maximum intensity projections (MIPs) show the brightest pixel along a given direction, in a three-dimensional volume. All tubes appear straight (3D view) and overlap in the MIPs in all three directions. Signal loss associated with susceptibility-related field inhomogeneity is visible in T2*W images (arrows), as expected.

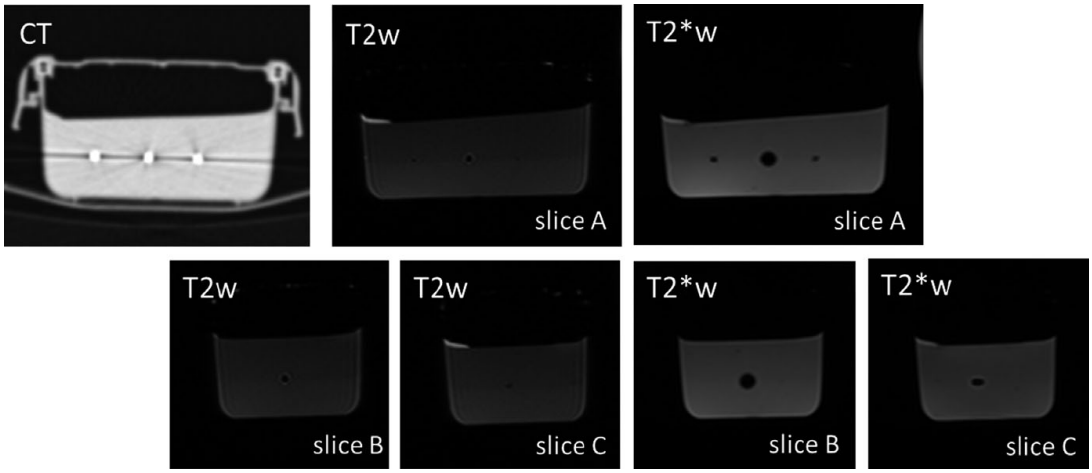

FIG. 4. Gel test object images showing signal loss around marker positions, which is larger on T2*W images as expected. The signal loss is symmetric in relation to the true position of the marker. The level of signal loss associated with the markers varies, and is much larger for the central marker, irrespective of test object orientation. Ultrasound and CT images confirm there is no air gap or any imperfection at the markers. Image intensity differences within the gel in T2W images are due to the test object construction technique, in two layers; the second layer is built after the bottom layer has hardened sufficiently to hold the weight of the seeds.

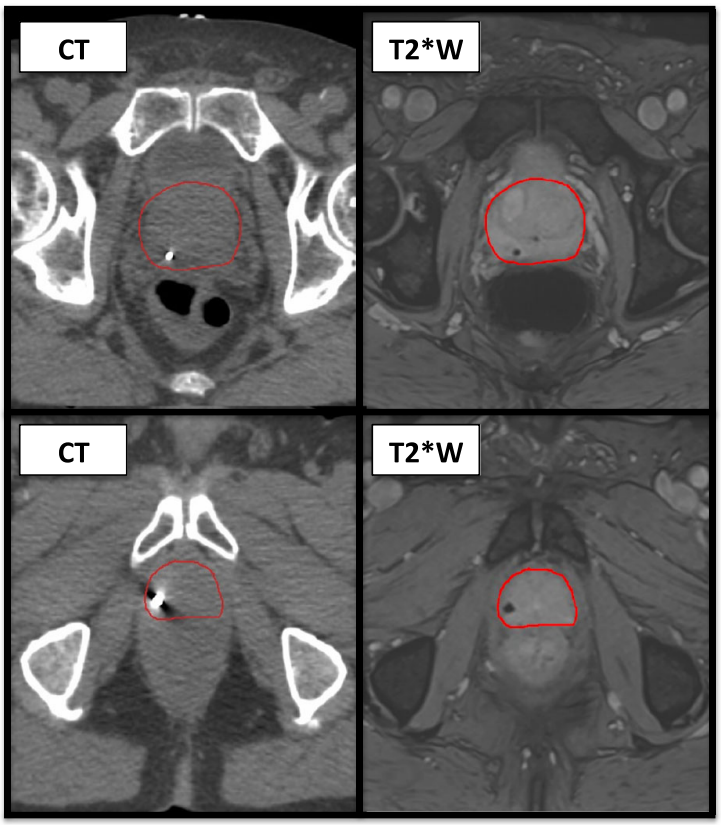

FIG. 5. Clinical example of the variation in signal loss. Top line-CT (left) and T2*W (right) imaging displaying the usual signal loss associated with a fiducial marker in the cranio-caudal position. Bottom line-CT (left) and T2*W (right) imaging for the same patient showing the altered signal loss seen with the inferior fiducial marker which in this case is angled more in the transverse plane.

3.B | Clinical studies

3.B.1 | Visibility of fiducials

Review of only the T2W imaging of all patients revealed three out of 30 fiducials were correctly identified. Fig. 6(a) shows an example of the fiducial appearance on T2W MRI. On T2*W imaging, all 30 fiducial markers were visible. However, only 29 out of 30 markers were correctly identified due to the presence of calcifications creating a similar signal loss. Such calcifications were variable in number and size but were seen in eight out of the ten patients, an example is seen in Fig. 6(b).

3.B.2 | Contour variability

Image review shows that the prostate has a high contrast appearance in relation to the surrounding tissues in T2*W images, and internal structures are not demonstrated as clearly as in T2W sequences. Summary of the comparison metrics for all ten patients for each imaging modality is seen in Table 2.

There is good agreement between the three observers for all imaging modalities. Distance measurements between contours were greater and overlap indices lower for CT compared to both MR sequences, indicating a poorer interobserver variability for CT imaging compared to MRI. This was statistically significant when comparing CT with T2*W, as indicated in Table 2.

4 | DISCUSSION

Test object images demonstrated that prostate MR images are not significantly distorted, and that the T2*W sequence produces a signal void that is symmetric in relation to the true marker position. This indicates that the signal loss is sufficiently large to obscure the volume immediately adjacent to the seeds where significant image distortion could otherwise be detected.[15] Detected differences in the size of the signal void associated with markers are expected to relate to the marker orientation in relation to the static magnetic field and transaxial image plane,[22,27] but small variations in the

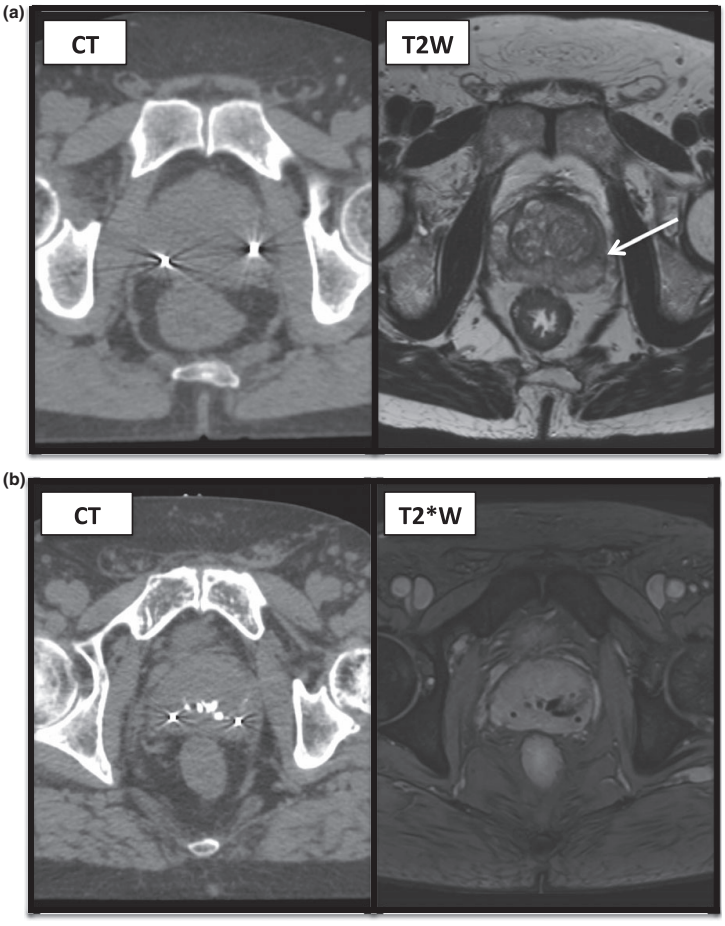

FIG. 6. (a) Corresponding CT (left) and T2W (right) images for a patient showing the appearance of a fiducial marker on standard T2W imaging, as indicated by the arrow. The second fiducial marker visible on CT imaging could not be identified on T2W images here. (b) Corresponding CT (left) and T2*W (right) images for a patients showing two fiducials with surrounding artifact on CT images and central calcifications, all showing as signal loss on T2*W imaging.

TABLE 2 Summary of the median comparison metrics for three observers contouring all ten patients for each imaging type (with interquartile range in brackets). * Denotes a statistically significant difference when compared to T2*W using a significance level of $P = 0.0167$ (Bonferroni correction).

Imaging modality	Hausdorff distance (mm)	Mean distance (mm)	Cohen's kappa	Dice similarity co-efficient
CT	5.01* (4.68–5.71)	0.77* (0.69–0.86)	0.92* (0.89–0.93)	0.95* (0.94–0.96)
T2W	4.09 (3.57–4.89)	0.53 (0.48–0.61)	0.94 (0.93–0.96)	0.97 (0.96–0.97)
T2*W	3.61 (3.16–3.73)	0.45 (0.43–0.48)	0.95 (0.94–0.96)	0.97 (0.96–0.97)

magnetic susceptibility of the seeds cannot be ruled out as a contributing factor.

There is a high agreement for prostate contouring on all image sets, likely to reflect the high level of experience of all clinicians, from the same institution and familiar with using MRI for contouring. The higher agreement for contours on MRI compared to CT is consistent with previous studies as a result of the improved soft tissue contrast with MRI.[28,29] Despite the visual appearance of a more defined prostate capsule on the T2*W sequence, there was no significant difference in interobserver variability when compared to T2W imaging, which again may reflect the users' experience with MR sequences. For this group of observers, the T2*W sequence is similar to standard T2W imaging, but with the added benefit of fiducial identification.

The more recent development of MR-guided RT allows the use of continuous MRI during treatment for motion monitoring and gating.[30] Ultimately the aim would be for an MR-only workflow[31] without the need for markers, using soft tissue visualization alone. In this context the T2*W sequence may be advantageous in comparison to the standard diagnostic T2W sequence as the prostate has a high intensity appearance and fewer internal structures are clearly depicted. The performance of automated contouring software based on machine learning and artificial intelligence techniques should therefore be investigated for the T2*W sequence. However, at present, MR-guided delivery mostly relies on a mixed MR-CT workflow with fiducials allowing more accurate fusion of images[4] and further used for position verification prior to treatment.

There have been a number of studies investigating dedicated MRI sequences for fiducial detection.[12–17] Both balanced steady-state free precession sequences[13] and sequences based on spoiled gradient-echoes have been employed in 2D[12–15] and 3D[16,17] acquisitions, relying on T2*-related signal loss to create a detectable signal void in the vicinity of the fiducials. The averaging of consecutive echoes in multi-echo recalled sequences, such as the one used here is an attractive mechanism to increase the signal-to-noise ratio. Previous investigations of pulse sequences of this type focused on seed depiction capabilities; Shieda et al.[12] report superior image sharpness, but did not perform contouring studies. We demonstrated a successful combination of prostate contouring and correct seed localization with one single sequence. Furthermore, we demonstrated the absence of geometric distortions which could lead to systematic registration errors. We believe this is a valuable advance toward MR-only prostate RT planning.

The accuracy of fiducial detection is paramount and can be either manual[12] or automatic.[13–17] However, ultimately, this must be performed automatically, especially if intrafractional imaging is to be used. Different methods have been described for automatic algorithms including feature extraction[13,15] and template matching.[14,16,17] The fiducial detection is dependent on the signal loss, which varies with factors including seed orientation and TE.[22,27] We demonstrated that calcifications in prostate are a common source of signal voids in T2*W images, and they have been shown to mimic fiducial voids.[32] Although Gustafsson et al.[15] proposed to detect fiducials automatically by considering images at different TEs and the progressive increase in signal loss in multiple-echo pulse sequences, it is unclear whether calcifications will be a significant confounding factor. Further investigation is required to determine whether false positive detection as a result of calcifications is a significant issue and whether calcifications can contribute towards MR-CT co-registration.[32] The full potential of artificial intelligence techniques in fiducial detection has not yet been realized.[33]

With progressively more targeted treatment delivery, the accuracy of delineation becomes even more essential.[34] For the prostate, this requires adequate tissue contrast of the capsule to improve confidence in contouring and reduce inter-observer variability. With the development of prostate motion monitoring in MR-guided RT, the prostate contour can be used for gated treatment.[35] This requires easy and accurate identification of the target either visually or using automated algorithms. The latter may either rely on registration of images and propagation of contours or *de novo* auto-delineation of the prostate on new images.[36–38] The sequence described here would therefore be an attractive solution for detailing seeds and the prostate capsule. Further work of significance to MR-guided RT, will be assessment of prostate contouring by treatment radiographers[39] and auto-contouring software on the sequences used here.

5 | CONCLUSION

We have described here a single T2*W MR sequence suitable for fiducial depiction and prostate contouring. These MR images were demonstrated to be geometrically accurate, the MR signal loss surrounding the fiducial was shown to be symmetric in relation to the true marker position shown in CT and all markers are visible. Prostate contours on MR are more consistent than CT-based contours with good agreement between prostate RT clinicians. We expect

T2*W sequences to be useful for a mixed MR-CT workflow and furthermore for MR-guided RT.

ACKNOWLEDGMENTS

The authors wish to thank Dr Elly Castellano and Dr Tuathan O'Shea for help with CT and US test object scanning, and Craig Cummings and team at the ICR/RMH workshop for the work on the LTO test object. The authors acknowledge the support of NHS funding to the NIHR Biomedical Research Centre and the Clinical Research Facility in Imaging at the Royal Marsden NHS Foundation Trust and the Institute of Cancer Research. The views expressed are those of the authors and not necessarily those of the NHS, the NIHR or the Department of Health. Research at the Institute of Cancer Research is also supported by Cancer Research UK (CRUK) under program grant C33589/A19727. CRUK and EPSRC support to the Cancer Imaging Centre at ICR and RMH in association with MRC and Department of Health C1060/A10334, C1060/A16464. Douglas Brand acknowledges personal fellowship funding from the National Institute for Health Research (NIHR) and Cancer Research UK.

CONFLICTS AND DISCLOSURE

The Royal Marsden Hospital NHS Foundation Trust and Institute of Cancer Research are part of the Elekta MR-Linac research consortium, which aims to coordinate international research into the MR-Linac. Elekta and Philips are members of the MR-Linac Consortium. Elekta financially supports the MR-linac Consortium and all member institutes, including research funding. AT and AP have received research and educational travel support from Elekta. Elekta supports travel costs for consortium meetings. AT has received honoraria from Janssen, Astellas, Ferring and Bayer and research funding from MSD outside of the submitted work.

REFERENCES

1. Schmidt AM, Payne SG. Radiotherapy planning using MRI. *Phys Med Biol*. 2015;60:R323.
2. Langen KM, Jones DTL. Organ motion and its management. *Int J Radiat Oncol Biol Phys*. 2001;50:265–278.
3. McPartlin AJ, Li XA, Kershaw LE, et al. MRI-guided prostate adaptive radiotherapy – a systematic review. *Radiother Oncol*. 2016;119:371–380.
4. Parker CC, Damyanovich A, Haycocks T, Haider M, Bayley A, Catton CN. Magnetic resonance imaging in the radiation treatment planning of localized prostate cancer using intra-prostatic fiducial markers for computed tomography co-registration. *Radiother Oncol*. 2003;66:217–224.
5. van der Heide UA, Kotte AN, Dehnad H, Hofman P, Lagenijk JJ, van Vulpen M. Analysis of fiducial marker-based position verification in the external beam radiotherapy of patients with prostate cancer. *Radiother Oncol*. 2007;82:38–45.
6. Beltran C, Herman MG, Davis BJ. Planning target margin calculations for prostate radiotherapy based on intrafraction and interfraction motion using four localization methods. *Int J Radiat Oncol Biol Phys*. 2008;70:289–295.
7. Meyer E, Raupach R, Lell M, Schmidt B, Kachelriess M. Normalized metal artifact reduction (NMAR) in computed tomography. *Med Phys*. 2010;37:5482–5493.
8. Boas FE, Fleischmann D. Evaluation of two iterative techniques for reducing metal artifacts in computed tomography. *Radiology*. 2011;259:894–902.
9. Callaghan PT. *Principles of Nuclear Magnetic Resonance Microscopy*. Oxford: Clarendon Press; 1991:208–217.
10. Rasch C, Barillot I, Remeijer P, Touw A, van Herk M, Lebesque JV. Definition of the prostate in CT and MRI: a multi-observer study. *Int J Radiat Oncol Biol Phys*. 1999;43:57–66.
11. Nyholm T, Jonsson J, Söderström K, et al. Variability in prostate and seminal vesicle delineations defined on magnetic resonance images, a multi-observer, -center and -sequence study. *Radiat Oncol (London, England)*. 2013;8:126.
12. Schieda N, Avruch L, Shabana WM, Malone SC. Multi-echo gradient recalled echo imaging of the pelvis for improved depiction of brachytherapy seeds and fiducial markers facilitating radiotherapy planning and treatment of prostatic carcinoma. *J Magnet Reson Imaging*. 2015;41:715–720.
13. Dinis Fernandes C, Dinh CV, Steggerda MJ, et al. Prostate fiducial marker detection with the use of multi-parametric magnetic resonance imaging. *Phys Imaging Radiat Oncol*. 2017;1:14–20.
14. Ghose S, Mitra J, Rivest-Henault D, et al. MRI-alone radiation therapy planning for prostate cancer: automatic fiducial marker detection. *Med Phys*. 2016;43:2218.
15. Gustafsson C, Korhonen J, Persson E, Gunnlaugsson A, Nyholm T, Olsson LE. Registration free automatic identification of gold fiducial markers in MRI target delineation images for prostate radiotherapy. *Med Phys*. 2017;44:5563–5574.
16. Zijlstra F, Moerland MA, van der Voort van Zyp JRN, Noteboom JL, Viergever MA, Seevinck PR. Challenges in MR-only seed localization for postimplant dosimetry in permanent prostate brachytherapy. *Med Phys*. 2017;44:5051–5060.
17. Maspero M, van den Berg CAT, Zijlstra F, et al. Evaluation of an automatic MR-based gold fiducial marker localisation method for MR-only prostate radiotherapy. *Phys Med Biol*. 2017;62:7981–8002.
18. Martin N, Malfair D, Zhao Y, et al. Comparison of MERGE and axial T2-weighted fast spin-echo sequences for detection of multiple sclerosis lesions in the cervical spinal cord. *AJR Am J Roentgenol*. 2012;199:157–162.
19. Held P, Dorenbeck U, Seitz J, Frund R, Albrich H. MRI of the abnormal cervical spinal cord using 2D spoiled gradient echo multiecho sequence (MEDIC) with magnetization transfer saturation pulse. A T2* weighted feasibility study. *J Neuroradiol* (Journal de neuroradiologie). 2003;30:83–90.
20. Doran SJ, Charles-Edwards L, Reinsberg SA, Leach MO. A complete distortion correction for MR images: I. Gradient warp correction. *Phys Med Biol*. 2005;50:1343–1361.
21. Fedorov A, Beichel R, Kalpathy-Cramer J, et al. 3D Slicer as an image computing platform for the quantitative imaging network. *Magn Reson Imaging*. 2012;30:1323–1341.
22. Jonsson JH, Garpebring A, Karlsson MG, Nyholm T. Internal fiducial markers and susceptibility effects in MRI-simulation and measurement of spatial accuracy. *Int J Radiat Oncol Biol Phys*. 2012;82:1612–1618.
23. Chang H, Fitzpatrick JM. A technique for accurate magnetic resonance imaging in the presence of field inhomogeneities. *IEEE Trans Med Imaging*. 1992;11:319–329.
24. Warfield SK, Zou KH, Wells WM. Simultaneous truth and performance level estimation (STAPLE): an algorithm for the validation of image segmentation. *IEEE Trans Med Imaging*. 2004;23:903–921.
25. Hanna GG, Hounsell AR, O'Sullivan JM. Geometrical analysis of radiotherapy target volume delineation: a systematic review of

reported comparison methods. *Clin Oncol (Royal College of Radiologists (Great Britain))*. 2010;22:515–525.
26. Fotina I, Lutgendorf-Caucig C, Stock M, Potter R, Georg D. Critical discussion of evaluation parameters for inter-observer variability in target definition for radiation therapy. *Strahlenther Onkol*. 2012;188:160–167.
27. Schenck JF. The role of magnetic susceptibility in magnetic resonance imaging: MRI magnetic compatibility of the first and second kinds. *Med Phys*. 1996;23:815–80.
28. Villeirs GM, Vaerenbergh K, Vakaet L, et al. Interobserver delineation variation using CT versus combined CT + MRI in intensity–modulated radiotherapy for prostate cancer. *Strahlenther Onkol*. 2005;181:424–430.
29. Debois M, Oyen R, Maes F, et al. The contribution of magnetic resonance imaging to the three-dimensional treatment planning of localized prostate cancer. *Int J Radiat Oncol Biol Phys*. 1999;45:857–865.
30. Pathmanathan AU, van As NJ, Kerkmeijer LGW, et al. Magnetic resonance imaging-guided adaptive radiation therapy: a "game changer" for prostate treatment? *Int J Radiat Oncol Biol Phys*. 2018;100:361–373.
31. Nyholm T, Jonsson J. Counterpoint: opportunities and challenges of a magnetic resonance imaging–only radiotherapy work flow. *Sem Radiat Oncol*. 2014;24:175–180.
32. Zeng GG, McGowan TS, Larsen TM, et al. Calcifications are potential surrogates for prostate localization in image-guided radiotherapy. *Int J Radiat Oncol Biol Phys*. 2008;72:963–966.
33. LeCun Y, Bengio Y, Hinton G. Deep learning. *Nature*. 2015;521:436–444.
34. Njeh C. Tumor delineation: the weakest link in the search for accuracy in radiotherapy. *J Med Phys*. 2008;33:136–140.
35. Bohoudi O, Bruynzeel A, Senan S, Slotman B, Palacios M, Lagerwaard F. Using a MRI-guided radiation therapy system for prostate cancer patients. ESTRO 36; 2017:SP-0494.
36. Greenham S, Dean J, Fu CKK, et al. Evaluation of atlas-based autosegmentation software in prostate cancer patients. *J Med Radiat Sci*. 2014;61:151–158.
37. Klein S, van der Heide UA, Lips IM, van Vulpen M, Staring M, Pluim JPW. Automatic segmentation of the prostate in 3D MR images by atlas matching using localized mutual information. *Med Phys*. 2008;35:1407–1417.
38. Pasquier D, Lacornerie T, Vermandel M, Rousseau J, Lartigau E, Betrouni N. Automatic segmentation of pelvic structures from magnetic resonance images for prostate cancer radiotherapy. *Int J Radiat Oncol Biol Phys*. 2007;68:592–600.
39. Pathmanathan AU, McNair HA, Schmidt MA, et al. Comparison of prostate delineation on multimodality imaging for MR-guided radiotherapy. *Br J Radiol*. 2019;92:20180948.

BJR https://doi.org/10.1259/bjr.20180948

Received: 06 November 2018 | Revised: 14 December 2018 | Accepted: 18 December 2018

Cite this article as:
Pathmanathan AU, McNair HA, Schmidt MA, Brand DH, Delacroix L, Eccles CL, et al. Comparison of prostate delineation on multimodality imaging for MR-guided radiotherapy. *Br J Radiol* 2019; **92**: 20180948.

FULL PAPER

Comparison of prostate delineation on multimodality imaging for MR-guided radiotherapy

[1,2]ANGELA U PATHMANATHAN, [1]HELEN A MCNAIR, [1,2]MARIA A SCHMIDT, [1,2]DOUGLAS H BRAND, [1]LOUISE DELACROIX, [1,2]CYNTHIA L ECCLES, [1]ALEXANDRA GORDON, [1]TRINA HERBERT, [1,2]NICHOLAS J VAN AS, [1,2]ROBERT A HUDDART and [1,2]ALISON C TREE

[1]The Royal Marsden Hospital NHS Foundation Trust, Downs Road, Sutton, United Kingdom
[2]The Institute of Cancer Research, 15 Cotswold Road, Sutton, United Kingdom

Address correspondence to: Dr Angela U Pathmanathan
E-mail: *angela.pathmanathan@icr.ac.uk*

Objective: With increasing incorporation of MRI in radiotherapy, we investigate two MRI sequences for prostate delineation in radiographer-led image guidance.
Methods: Five therapeutic radiographers contoured the prostate individually on CT, T_2 weighted (T_2W) and T_2* weighted (T_2*W) imaging for 10 patients. Contours were analysed with Monaco ADMIRE (research v. 2.0) to assess interobserver variability and accuracy by comparison with a gold standard clinician contour. Observers recorded time taken for contouring and scored image quality and confidence in contouring.
Results: There is good agreement when comparing radiographer contours to the gold-standard for all three imaging types with Dice similarity co-efficient 0.91–0.94, Cohen's κ 0.85–0.91, Hausdorff distance 4.6–7.6 mm and mean distance between contours 0.9–1.2 mm. In addition, there is good concordance between radiographers across all imaging modalities. Both T_2W and T_2*W MRI show reduced interobserver variability and improved accuracy compared to CT, this was statistically significant for T_2*W imaging compared to CT across all four comparison metrics. Comparing MRI sequences reveals significantly reduced interobserver variability and significantly improved accuracy on T_2*W compared to T_2W MRI for DSC and Cohen's κ. Both MRI sequences scored significantly higher compared to CT for image quality and confidence in contouring, particularly T_2*W. This was also reflected in the shorter time for contouring, measuring 15.4, 9.6 and 9.8 min for CT, T_2W and T_2*W MRI respectively.
Conclusion:
Therapeutic radiographer prostate contours are more accurate, show less interobserver variability and are more confidently and quickly outlined on MRI compared to CT, particularly using T_2*W MRI.
Advances in knowledge:
Our work is relevant for MRI sequence choice and development of the roles of the interprofessional team in the advancement of MRI-guided radiotherapy.

INTRODUCTION

MRI provides a number of benefits in radiotherapy (RT) of the prostate, including improved soft tissue resolution for prostate and organs at risk delineation and multiparametric imaging for intraprostatic lesion identification and response assessment. There has been increasing interest in MR-guided systems[1,2] to encompass these advantages and permit intrafractional imaging without additional radiation exposure.[3] With variability in prostate and seminal vesicles contouring dependent on the sequence used,[4] sequence optimisation is vital to maintain accuracy. In addition, prostate delineation must be completed in a timely manner when used in an online or real-time adaptive setting.

Dedicated MRI sequences can enhance the signal void of fiducials,[5,6] required for accurate MRI and CT fusion[7] and position verification prior to treatment. One such sequence, T_2*-weighted (T_2*W) MRI, uses multiple echo times[8] resulting in a more defined prostate capsule as well as a reliable depiction of fiducials; geometric accuracy and clinician contouring consistency on this type of sequence has previously been assessed.[9]

With relative unfamiliarity of MRI compared to CT, MRI must be introduced carefully into the RT planning process involving all members of the interprofessional team, together with appropriate training.[10] Therapeutic radiographers at our centre are experienced in reviewing the prostate position on cone beam CT (CBCT) for image

guidance prior to treatment delivery. RT services benefit from the expanded role of therapeutic radiographers including radiographer-led delineation of the target or organs at risk[11] which can shorten the treatment planning process.[12] At our institution, following a training programme, specialised therapeutic radiographers outline the prostate and seminal vesicles on the RT planning CT, prior to clinician review and final approval.

However, with the emergence of new technologies, this must be extended to prostate identification on MRI for MRI-guided RT. With the installation of the Elekta MR-Linac[1] at our centre and treatment of our first patient in September 2018, we wish to extend the therapeutic radiographer role to include delineation of the prostate on MRI. This will be particularly relevant for adaptive online replanning where recontouring and intrafraction monitoring of the target is required.

With RT workflow changing, the work we present here addresses an important area which has not been well studied to date. Despite the evolving role of therapeutic radiographers, to our knowledge there are no publications demonstrating the accuracy and consistency of radiographer-derived contours which is an essential part of treatment quality assurance. Our study assesses the interobserver variability and accuracy of prostate delineation by therapeutic radiographers using three imaging types; CT, T_2 weighted (T_2W) and T_2*W MRI.

METHODS AND MATERIALS

Patient population

The patient population and image acquisition have previously been described.[9] 10 patients receiving treatment within the Prostate Advances in Comparative Evidence (PACE) trial (NCT01584258) at the Royal Marsden Hospital NHS Foundation Trust, Sutton, had RT planning CT and MRI scans acquired on the same day. The PACE trial has two parallel randomisations; PACE A randomises between prostatectomy or stereotactic body radiotherapy (SBRT) to a dose of 36.25 Gy in five fractions, and PACE B randomised patients between SBRT or conventionally fractionated RT, either 62 Gy in 20 fractions or 78 Gy in 39 fractions. Patients do not receive androgen deprivation therapy.

Image acquisition

At least 1 week prior to planning imaging, three 1.0 × 3.0 mm knurled gold fiducial markers are inserted under transrectal ultrasound guidance. Patients are instructed regarding bladder filling and rectal preparation as per departmental guidelines prior to their imaging sessions. The latter consists of two days of rectal preparation with microenemas prior to their CT planning appointment, and an enema just before their planning CT scan. The treatment set-up position is replicated for planning imaging. The CT extends in 1.5 mm axial slices from the mid-lumbar spine to below the obturator foramen. This is followed, on the same day, by the planning MRI scan at 1.5 T (Siemens Aera, Erlangen, Germany) with 2 two-dimensional sequences, covering the prostate volume using 28 adjacent slices (at 2.5 mm thickness). Firstly, a standard T_2W pulse sequence used in diagnostic prostate MRI and based on fast spin echoes, allowing visualisation of the internal structure of the prostate, is acquired. The second sequence is T_2*W combining several gradient echo signals, with a range of echo-times into a single image, thereby maximising the signal loss related to the fiducial markers. Examples of images are shown in Figure 1.

Contouring

The contouring and analysis methods have previously been described in published abstract format.[13] Three clinicians

Figure 1. A–C are examples of CT, T_2W and T_2*W imaging at corresponding levels for the same patient, without contours. D–F demonstrate the same imaging with superimposed radiographer contours. Reproduced from published abstract format with permission.[13]

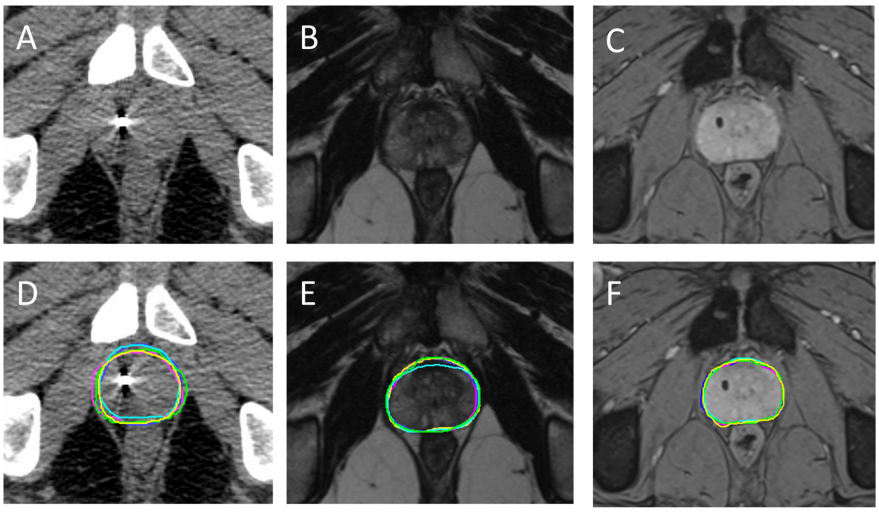

experienced in prostate RT delineated the prostate on each of the three imaging data sets—CT, T_2W and T_2*W MRI using Monaco v.5.19.02 (research version, Elekta AB, Stockholm, Sweden). All contours were created individually, without reference to other types of imaging. A minimum of 2 weeks was left between contouring images of the same patient to avoid recall bias. A simultaneous truth and performance level estimate (STAPLE)[14] contour was created from all three clinician contours for each imaging set to create the "gold-standard" for comparison. The interobserver variability for these clinician contours has previously been reported with median Dice similarity co-efficient (DSC) of 0.95 (interquartile range 0.94–0.96), 0.97 (0.96–0.97) and 0.97 (0.96–0.97) for CT, T_2W and T_2*W imaging respectively.[9]

Five therapeutic radiographers experienced in delineation and/or registration of the prostate on CT and CBCT, completed a single training session, delivered by a clinical oncologist. The training included review of the anatomy on each of the three imaging types and access to CT, T_2W and T_2*W "atlases" with axial contours to refer to. The radiographers then delineated the prostate on CT, T_2W and T_2*W MRI for the same 10 patients using the same instructions. In addition, the time taken for delineation was recorded and images were scored from 0 to 10 for "image quality" and "confidence in contouring", where a higher score indicates an improvement.

Analysis of contours

Assessment was made of;

(1) *Interobserver variability*—a STAPLE contour was created from the contours of all five radiographers. Each individual contour was then compared to this STAPLE contour to assess radiographer interobserver variability.
(2) *Accuracy*—by comparison of radiographer contours to the gold standard' clinician STAPLE.

Contours were assessed using Monaco ADMIRE software v.2.0 (research version, Elekta AB, Stockholm, Sweden). For each comparison, the overlap measures DSC and Cohen's kappa (κ) were recorded, (where higher values indicate greater agreement). In addition, the distance measures of Hausdorff distance and mean distance between contours were recorded (where lower values indicate greater agreement).

Using GraphPad Prism v7.0d, non-parametric Friedman testing was performed with Dunn's test for multiple comparisons. The three imaging comparisons—CT *vs.* T_2W, CT *vs.* T_2*W and T_2W *vs.* T_2*W were pre-planned. Values were defined as statistically different if the adjusted p-value was <0.05.

RESULTS

Examples of radiographer contours are shown in Figure 1, reproduced from published abstract format with permission.[13]

Median (interquartile range) comparisons for each imaging type, delineation times and imaging scores are summarised in Table 1. Results of statistical testing are summarised in Figure 2.

The high overlap values, with all DSC and Cohen's κ ≥0.85, illustrate the good agreement between radiographers and between radiographers and the gold-standard across all imaging types.

On comparison of MRI to CT, both T_2W and T_2*W contours show higher overlap values and lower distance values, indicating reduced interobserver variability and improved accuracy when compared to the gold standard. This was statistically significant for T_2*W contours compared to CT across all four comparison metrics.

In addition, comparison of the two MRI sequences reveals that prostate contours delineated using T_2*W MRI show significantly decreased interobserver variability for all measurements excluding Hausdorff distance, and significantly improved accuracy for DSC and Cohen's κ when compared to T_2W MRI. (Table 1/ Figure 2).

Table 1. Summary of median (interquartile range) comparison values for each imaging type

		CT	T_2W MRI	T_2*W MRI
Interobserver variability	DSC	0.93 (0.91–0.95)	0.94 (0.93–0.95)	0.96 (0.95–0.96)
	Cohen κ	0.90 (0.87–0.91)	0.91 (0.89–0.92)	0.93 (0.92–0.94)
	HD (mm)	6.5 (5.7–7.9)	4.8 (4.2–5.8)	4.7 (3.9–5.4)
	Mean d (mm)	0.9 (0.8–1.1)	0.8 (0.7–1.0)	0.7 (0.6–0.7)
Comparison to gold-standard	DSC	0.91 (0.89–0.92)	0.93 (0.91–0.94)	0.94 (0.93–0.95)
	Cohen κ	0.85 (0.83–0.88)	0.89 (0.86–0.90)	0.91 (0.89–0.93)
	HD (mm)	7.6 (6.6–9.1)	5.2 (4.4–6.2)	4.6 (4.0–5.5)
	Mean d (mm)	1.2 (1.2–1.4)	1.0 (0.9–1.2)	0.9 (0.7–1.0)
Assessment of contouring efficiency	Time taken to contour (min)	15.4 (12.0–16.3)	9.6 (8.3–12.6)	9.8 (8.9–10.9)
	Image quality (0–10)	5.3 (5.2–5.8)	7.8 (7.4–8.1)	8.5 (8.2–8.8)
	Confidence in contour (0–10)	5.5 (5.2–5.6)	6.8 (6.7–7.3)	7.8 (7.5–7.9)

DSC, Dice similarity co-efficient; HD, Hausdorff distance; d, distance.
Values are reported to one decimal place apart from overlap measures reported to two decimal places.

Figure 2. Summary of *p*-values (reported to two decimal places) from statistical testing for comparison between imaging modalities. Values are adjusted for multiple comparisons and statistically significant if p<0.05. Abbreviations: Cohen,Cohen's κ; mean d, mean distance between contours; confid, confidence in contouring score; image, image quality score; .

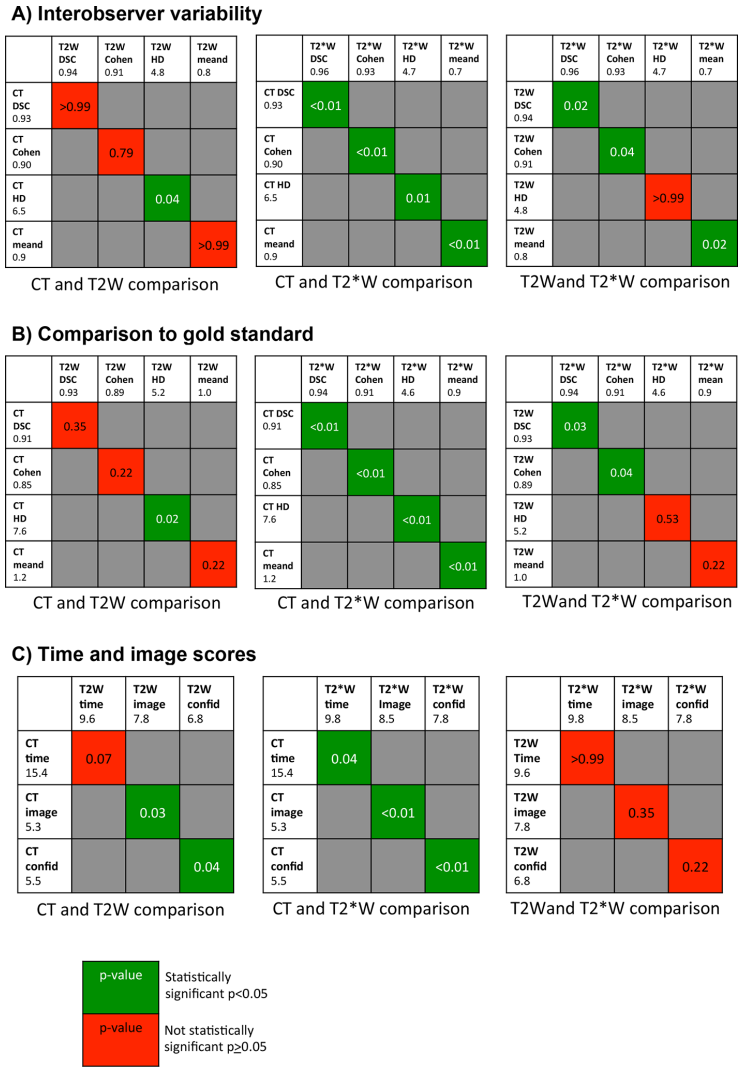

Greater quality images and confidence in contouring were reported for both MRI types but especially T_2*W MRI, reflected in the shorter time to complete contours, with a median of 9.6–9.8 min for MRI compared to 15.4 min for CT.

DISCUSSION

We have demonstrated that despite the unfamiliarity of MRI, interobserver variability and accuracy of therapeutic radiographer prostate contours improved with both MRI sequences, in particular the T_2*W sequence.

We have considered both consistency and accuracy of contours. The reduced interobserver variability on MRI is in keeping with previous results from clinician contouring[15–17] as a result of improved soft tissue contrast, reflected in the higher scores for image quality and confidence in contouring. However, this was only statistically significant across all four measures for T_2*W *vs.* CT.

For accuracy of contouring, a gold-standard for RT planning is difficult to define; here we have used the STAPLE of three

experienced clinicians to reduce the effect of interobserver variability for the gold-standard contour. All observers, both clinicians and radiographers, are from the same institution, which will influence both consistency and accuracy, as assessed by the overlap and distance measurements here and previously.[9]

With regards to time, the prostate was delineated on both MR sequences more quickly compared to CT. There was a reduction in the median time for contouring by 5.6 and 5.8 min for T_2*W and T_2W MRI respectively. This is particularly relevant for contouring in an online adaptive workflow, where shortening this step is beneficial to minimise intrafractional motion. Although the time improvement with MRI is mirrored in the higher confidence in contouring and image quality of MRI compared to CT, note must be made of the differing slice thickness of the images—1.5 mm for CT and 2.5 mm for MRI. As a result, there were a greater number of slices over the length of the prostate for contouring on CT compared to MRI. Although observers were allowed to use interpolation of contours if desired on any of the image sets, the time taken must be interpreted with caution for this reason.

There is no consensus on the best method for contour comparison,[18,19] we have therefore used a combination of comparison values here to encompass the overlap and distance between contours. Although we have carried out statistical testing here, we have not assessed the clinical impact of a significant difference in these comparisons. For example, the clinical implication of a DSC of 0.93 *vs* 0.95 may be negligible although this will also be dependent on where the discrepancy lies and the margins added during planning. The resulting dosimetric effect, not assessed here, would be more relevant.[20]

Our findings are particularly important as we have commenced MR-guided RT at the Royal Marsden Hospital with daily online replanning, which requires recontouring on images acquired each day. The process either involves manual contouring from the beginning or amending propagated contours produced by deformable registration of the reference image to the new daily acquired image. To begin with, this is clinician led with the aim of expanding the role of our radiographers to encompass this step. This is an essential progression of the extended role which has developed from evaluating treatment portal images,[21] evaluating verification images for hypofractionated treatments,[22] and to more recently, choosing the "plan of the day".[23] Accurate target identification is also required for motion monitoring of the target prostate during treatment delivery. Contributing to current literature, our study has considered the practical points of "confidence in contouring" and the time taken, both highly relevant in the time pressured online adaptive RT setting.

Most relevant literature to date makes use of T_2W images which are the mainstay of MRI for diagnosis and staging. We have proposed the T_2*W sequence, which not only allows visualisation of the fiducials, particularly important for a mixed CT-MR workflow, but also provides improved contrast between the prostate and surrounding tissues. MRI for delineation is not used routinely outside of a trial setting in our institution but implanted fiducial markers are used for image guidance prior to each fraction. Our study shows that sequences such as T_2*W MRI, allowing improved prostate capsule visualisation and contour accuracy, can continue to be useful even if fiducials are no longer required, such as with the clinical use of MR only workflow.

The work we have presented here is novel, in addition to establishing the accuracy and consistency of contours for this professional group, we have demonstrated the relevance of sequence selection and validated the use of the T_2*W sequence. Our work will be expanded further to assess the dosimetric impact of any differences in contours and consider the use of the T_2*W sequence for automatic contouring. A formal training programme will also be designed for therapeutic radiographer training as the role of MR-guided RT develops.

CONCLUSIONS

Despite unfamiliarity with MRI for treatment verification, therapeutic radiographer prostate contours are more accurate, show less interobserver variability and are more confidently and quickly outlined on MRI compared to CT. In addition, this improvement is consistently statistically significant for the T_2*W MRI sequence. This is particularly relevant for MRI sequence choice and development of the roles of the interprofessional team in the advancement of MRI-guided RT.

ACKNOWLEDGEMENT

The authors acknowledge the support of NHS funding to the NIHR Biomedical Research Centre and the Clinical Research Facility in Imaging at the Royal Marsden NHS Foundation Trust and the Institute of Cancer Research. The views expressed are those of the authors and not necessarily those of the NHS, the NIHR or the Department of Health. Research at the Institute of Cancer Research is also supported by Cancer Research UK (CRUK) under programme grant C33589/A19727. CRUK and EPSRC support to the Cancer Imaging Centre at ICR and RMH in association with MRC and Department of Health C1060/A10334, C1060/A16464. Douglas Brand acknowledges personal research fellowship funding from the National Institute for Health Research (NIHR), Cancer Research UK and the Wellcome Trust.

DISCLOSURES

The Royal Marsden Hospital NHS Foundation Trust and Institute of Cancer Research are part of the Elekta MR-Linac research consortium, which aims to coordinate international research into the MR-Linac. Elekta and Philips are members of the MR Linac Consortium. Elekta financially supports the MRlinac Consortium and all member institutes, including research funding and travel costs for consortium meetings. AT and AP have received research and educational travel support and honoraria from Elekta. AT has received honoraria from Janssen, Astellas, Ferring and Bayer and research funding from Accuray and MSD outside of the submitted work. NVA has received grants and personal fees from Accuray, outside this submitted work.

REFERENCES

1. Raaymakers BW, Lagendijk JJW, Overweg J, Kok JGM, Raaijmakers AJE, Kerkhof EM, et al. Integrating a 1.5 T MRI scanner with a 6 MV accelerator: proof of concept. *Phys Med Biol* 2009; **54**: N229–N237. doi: https://doi.org/10.1088/0031-9155/54/12/N01
2. Mutic S, Dempsey JF. The ViewRay system: magnetic resonance-guided and controlled radiotherapy. *Semin Radiat Oncol* 2014; **24**: 196–9. doi: https://doi.org/10.1016/j.semradonc.2014.02.008
3. Pathmanathan AU, van As NJ, Kerkmeijer LGW, Christodouleas J, Lawton CAF, Vesprini D, et al. Magnetic Resonance Imaging-Guided Adaptive Radiation Therapy: A "Game Changer" for Prostate Treatment? *International Journal of Radiation Oncology*Biology*Physics* 2018; **100**: 361–73. doi: https://doi.org/10.1016/j.ijrobp.2017.10.020
4. Nyholm T, Jonsson J, Söderström K, Bergström P, Carlberg A, Frykholm G, et al. Variability in prostate and seminal vesicle delineations defined on magnetic resonance images, a multi-observer, -center and -sequence study. *Radiat Oncol* 2013; **8**: 126. doi: https://doi.org/10.1186/1748-717X-8-126
5. Schieda N, Avruch L, Shabana WM, Malone SC. Multi-echo gradient recalled echo imaging of the pelvis for improved depiction of brachytherapy seeds and fiducial markers facilitating radiotherapy planning and treatment of prostatic carcinoma. *J Magn Reson Imaging* 2015; **41**: 715–20. doi: https://doi.org/10.1002/jmri.24590
6. Ghose S, Mitra J, Rivest-Hénault D, Fazlollahi A, Stanwell P, Pichler P, et al. MRI-alone radiation therapy planning for prostate cancer: Automatic fiducial marker detection. *Med Phys* 2016; **43**: 2218–28. doi: https://doi.org/10.1118/1.4944871
7. Parker CC, Damyanovich A, Haycocks T, Haider M, Bayley A, Catton CN. Magnetic resonance imaging in the radiation treatment planning of localized prostate cancer using intra-prostatic fiducial markers for computed tomography co-registration. *Radiother Oncol* 2003; **66**: 217–24. doi: https://doi.org/10.1016/S0167-8140(02)00407-3
8. Held P, Dorenbeck U, Seitz J, et al. MRI of the abnormal cervical spinal cord using 2D spoiled gradient echo multiecho sequence (MEDIC) with magnetization transfer saturation pulse. A T2* weighted feasibility study. *J Neuroradiol* 2003; **30**: 83–90.
9. Pathmanathan A, Schmidt M, Brand D, et al. Improving fiducial and prostate capsule visualisation for radiotherapy planning using MRI. *Journal of Applied Clinical Medical Physics* 2019; Accepted for publication December 2018.
10. Pötter R, Eriksen JG, Beavis AW, Coffey M, Verfaillie C, Leer JW, et al. Competencies in radiation oncology: a new approach for education and training of professionals for Radiotherapy and Oncology in Europe. *Radiother Oncol* 2012; **103**: 1–4. doi: https://doi.org/10.1016/j.radonc.2012.03.006
11. Jefferies S, Taylor A, Reznek R, .Radiotherapy Planning Working Party Results of a national survey of radiotherapy planning and delivery in the UK in 2007. *Clin Oncol* 2009; **21**: 204–17. doi: https://doi.org/10.1016/j.clon.2008.11.017
12. Boston S, Scrase C, Hardy V. 140 Implementation of radiographer led planning target delineation for prostate cancer. *Radiother Oncol* 2005; **76**: S73. doi: https://doi.org/10.1016/S0167-8140(05)81116-8
13. Pathmanathan A, Schmidt M, Brand D, Delacroix L, Eccles C, Gordon A, et al. EP-1613: Comparison of prostate delineation on multi-modality imaging for MR-guided radiotherapy. *Radiother Oncol* 2018; **127**: S868–S869. doi: https://doi.org/10.1016/S0167-8140(18)31922-4
14. Warfield SK, Zou KH, Wells WM. Simultaneous Truth and Performance Level Estimation (STAPLE): An Algorithm for the Validation of Image Segmentation. *IEEE Transactions on Medical Imaging* 2004; **23**: 903–21. doi: https://doi.org/10.1109/TMI.2004.828354
15. Khoo VS, Padhani AR, Tanner SF, Finnigan DJ, Leach MO, Dearnaley DP. Comparison of MRI with CT for the radiotherapy planning of prostate cancer: a feasibility study. *Br J Radiol* 1999; **72**: 590–7. doi: https://doi.org/10.1259/bjr.72.858.10560342
16. Villeirs GM, Van Vaerenbergh K, Vakaet L, Bral S, Claus F, De Neve WJ, et al. Interobserver delineation variation using CT versus combined CT + MRI in intensity-modulated radiotherapy for prostate cancer. *Strahlenther Onkol* 2005; **181**: 424–30. doi: https://doi.org/10.1007/s00066-005-1383-x
17. Rasch C, Barillot I, Remeijer P, Touw A, van Herk M, Lebesque JV. Definition of the prostate in CT and MRI: a multi-observer study. *International Journal of Radiation Oncology*Biology*Physics* 1999; **43**: 57–66. doi: https://doi.org/10.1016/S0360-3016(98)00351-4
18. Hanna GG, Hounsell AR, O'Sullivan JM. Geometrical analysis of radiotherapy target volume delineation: a systematic review of reported comparison methods. *Clin Oncol* 2010; **22**: 515–25. doi: https://doi.org/10.1016/j.clon.2010.05.006
19. Fotina I, Lütgendorf-Caucig C, Stock M, Pötter R, Georg D. Critical discussion of evaluation parameters for inter-observer variability in target definition for radiation therapy. *Strahlenther Onkol* 2012; **188**: 160–7. doi: https://doi.org/10.1007/s00066-011-0027-6
20. Vinod SK, Jameson MG, Min M, Holloway LC. Uncertainties in volume delineation in radiation oncology: A systematic review and recommendations for future studies. *Radiother Oncol* 2016; **121**: 169–79. doi: https://doi.org/10.1016/j.radonc.2016.09.009
21. Suter B, Shoulders B, Maclean M, Balyckyi J. Machine verification radiographs: an opportunity for role extension? *Radiography* 2000; **6**: 245–51. doi: https://doi.org/10.1053/radi.2000.0275
22. Hudson J, Doolan C, McDonald F, Locke I, Ahmed M, Gunapala G, et al. Are therapeutic radiographers able to achieve clinically acceptable verification for stereotactic lung radiotherapy treatment (SBRT)? *J Rad in Prac* 2015; **14**: 10–17. doi: https://doi.org/10.1017/S1460396914000478
23. McNair HA, Hafeez S, Taylor H, Lalondrelle S, McDonald F, Hansen VN, et al. Radiographer-led plan selection for bladder cancer radiotherapy: initiating a training programme and maintaining competency. *Br J Radiol* 2015; **88**: 20140690. doi: https://doi.org/10.1259/bjr.20140690